Michael Rosenlund Lodahl

INFLUENCE *of* **SMECTITE CONTENT**
on the **DEFORMATION BEHAVIOUR** *of* **CLAY**

Influence of smectite content on the deformation behaviour of clay

PhD Dissertation

Michael Rosenlund Lodahl

July 2017

COWI

Abstract

A number of structures are planned to be constructed on or in the Palaeogene clays in Denmark, e.g. the re-development of Aarhus Ø and the construction of the Femern Fixed Link. The Palaeogene clays are generally of very high plasticity, hold low strengths and have high deformation potentials despite being previously compressed by past glaciations. When unloaded the clay adsorbs water and swells profoundly. These geotechnical traits pose a challenge and must be accounted for when designing a structure situated on high plasticity clays. When not considered, the features of the Palaeogene clay may pose a safety concern for the building and settlements may develop over time.

Previous studies on Palaeogene clays in Denmark have shown, that the well-known index relations used in Danish geotechnical practice are generally not valid for the in situ behaviour of high plasticity clays. Moreover, several studies illustrates how the vertical yield stress derived from the compression curves of high plasticity clays does not reflect the previously sustained overburden, which normally is the case for clays of low to medium plasticity. The feature have been described as "lack of stress memory".

The present thesis investigates the 1D deformation behaviour of high plasticity clays. The effects of the clay mineral smectite on the deformation and swelling potential of the high plasticity clays are of special focus. Based on 1D compression tests the deformation potential of a range of artificial specimens made from mixtures of kaolinite and smectite minerals were investigated. Features typically observed for Danish Palaeogene clays were also observed for the artificial mixtures, e.g. high plasticity and low stiffness, which have both been related to the smectite content in the tested, artificial specimens.

Based on a number of tests, conducted following different loading programmes, a deformation model framework is presented which captures the essential features of the high plasticity clays. The model reproduces the compression curves obtained from testing of artificial specimens quite well and have also successfully been applied to reproduce compression curves from oedometer tests on intact natural highly plastic clays presented in literature. Based on the conducted tests it was observed that the lack of stress memory was related to the void ratio increase on a former unloading step, and thus directly affected by the smectite content of the specimen and the extent of unloading. It was also found that the compression potential in normally and overconsolidated conditions is dictated by smectite content but also affected by the length of the stress path followed during testing.

Resumé

Flere bygge- og anlægsprojekter er planlagt opført på de danske palæogene lere, f.eks. udviklingen af Aarhus Ø og etableringen af den faste forbindelse over Femern Bælt. De palæogene lere har generelt meget høj plasticitet, lave styrker og høje deformationspotentialer, selvom de tidligere er blevet belastet af isen under forgangne istider. Når leren aflastes, f.eks. ved udgravning, absorberer den vand og sveller kraftigt op. Disse geotekniske egenskaber er en udfordring, som skal behandles, når et bygværk planlægges udført på ler af høj plasticitet. Såfremt egenskaberne af de højplastiske lere ikke inddrages i designfasen, kan de udgøre en sikkerhedsrisiko for bygværket, som kan udvikle store sætninger over tid.

Tidligere studier af palæogent ler i Danmark viser, at de velkendte indeksrelationer, som ofte bruges i dansk geoteknisk praksis, generelt set ikke gælder, når in situ egenskaberne af leren søges. Desuden viser flere studier, hvordan forkonsolideringsspændingen, bestemt via. arbejdskurver fra oedometer forsøg, ikke svarer til lerens tidligere belastning, hvilket ellers normalt forventes for ler med lav eller middel plasticitet. Denne egenskab er blevet beskrevet som "tab af spændingshukommelse".

I nærværende afhandling undersøges de en-dimensionale deformationsegenskaber for høj-plastisk ler. Specielt er fokus lagt på effekten af lermineralet smektit på deformations- og svelleopførelse af de højplastiske lere. På baggrund af konsolideringsforsøg er deformationsegenskaberne blevet undersøgt for en række kunstige prøver, blandet af kaolin- og smektitmineraler. De egenskaber, som typisk observeres for de danske palæogene lere, f.eks. høj plasticitet og lav stivhed, kan relateres til smektitindholdet i de testede kunstige prøver.

På baggrund af en række forsøg, udført efter forskellige belastningsprogrammer, er der opstillet en deformationsmodel, som afspejler de essentielle egenskaber af den højplastiske ler. Således reproducerer modellen arbejdskurverne fra forsøgene på de kunstige prøver på tilfredsstillende vis. Ligeledes er modellen blevet anvendt til at reproducere arbejdskurver, præsenteret i litteraturen, fra forsøg på naturligt, intakt, højplastisk ler. På baggrund af de udførte forsøg er det observeret, at tabet af spændingshukommelse kan relateres til størrelsen af poretalsforøgelsen under en tidligere aflastning, hvilket er en direkte konsekvens af smektitindholdet og graden af aflastningen. Det er også påvist, at deformationspotentialet i såvel normal- som forkonsolideret tilstand er bestemt af smektitindholdet og længden af fulgte spændingssti under forsøgene.

Thesis Details

Thesis Title:	Influence of smectite content on the deformation behaviour of clays
PhD Student:	Michael Rosenlund Lodahl
Supervisors:	Professor (Docent) Dr. Kenny Kataoka Sørensen, Aarhus University
	Chief Specialist Dr. Helle Trankjær, COWI A/S, Aarhus
	Technical Director Niels Mortensen, nmGeo ApS, Allerød

This dissertation has been submitted for assessment in partial fulfilment of the PhD degree. The thesis is formed as a monograph. However, selected side studies, carried out along with the main findings, were published as individual papers. The papers are enclosed in the appendix. Other side studies, which were undertaken to confirm validity of the applied methods, are also enclosed in the appendix.

The present thesis is based on results from a total of 76 oedometer tests performed by the author and a total of 37 tests performed during MSc-projects, where the author was involved as secondary supervisor. Where the results from the tests carried out during the MSc-projects are presented in the thesis, it is clearly stated in the text.

All soil element tests carried out during the project period are documented in individual test reports which have been compiled into a global laboratory report, which is enclosed in electronic form. The laboratory report also contains results from other tests, e.g. XRD-analyses and hydrometer tests, along with calibration factors for the applied test equipment. The laboratory report may be downloaded from the following repository. Login-details for the repository may be obtained by emailing the author: mirl@cowi.dk.

`http://projects.cowiportal.com/psc/A058934/Documents/Externals/`
`Data%20report`

The following collection of scientific papers have been published by the author of the present dissertation in collaboration with other co-authors:

> M. R. Lodahl and K. K. Sørensen. 2015. "Influence of Smectite Content on the One-Dimensional Deformation Behavior of Reconstituted High Plasticity Clay." In *Deformation Characteristics of Geomaterials - Proceedings of the 6th International Symposium on Deformation Characteristics of Geomaterials, IS-Burnos Aires 2015.* Edited by V. A. Rinaldi et al. doi:`10.3233/978-1-61499-601-9-1057`

> M. R. Lodahl et al. 2016. "Oedometer tests with measurements of internal friction between oedometer ring and clay specimen." In *NGM 2016 Reykjavik - Proceedings of the 17th Nordic Geotechnical Meeting - Challenges in Nordic Geotechnics 25th - 28th of May*, 289–298. ISBN: 978-9935-24-002-6. `http://www.ngm2016.com/papers.html`

> M. R. Lodahl and K. K. Sørensen. 2017. "Effects of pore water chemistry on the unloading-reloading behaviour of reconstituted clays." *European Journal of Environmental and Civil Engineering.* Submitted. ISSN: 2116-7214

As part of the assessment, co-author statements have been made available to the assessment committee and are also available at the Faculty. The published papers are discussed further in the thesis along with other results obtained during the study.

Preface

This thesis summarises the industrial PhD-project "Influence of smectite content on the deformation behaviour of clays" carried out from August 2014 to July 2017 in collaboration between Aarhus University, Department of Engineering and COWI A/S.

It would not have been possible to carry out the work presented in this dissertation without the help and support from several people. I would like to thank my supervisors: Professor (Docent) at Aarhus University, Department of Engineering Dr. Kenny Kataoka Sørensen, Chief Specialist at COWI A/S Dr. Helle Trankjær, and Technical Director at nmGeo ApS Niels Mortensen for their tireless support, valuable technical discussions and excellent guidance during the past three years.

Furthermore, I owe special thanks to my managers in COWI Vice Presidents Jørgen Pedersen (–2017) and Mette Thomsen (2017–), and Head of sections Dr. Kim André Larsen (2014–2016) and Kristian Thoustrup Brødbæk (2016–) for giving their blessing for me to pursue a PhD-degree. The project was partly funded by Innovation Fund Denmark and COWIfonden, for which I am grateful.

During my studies I was granted access to the Femern database, for which I am very grateful. I have also received cores obtained from the Femern boring campaign near the Little Belt bridge of 1935, for which I wish to express gratitude towards Banedanmark. The company Geo I also owe thanks for allowing the use of laboratory test data obtained from construction project at the harbour of Aarhus. Any interpretations, conclusions and suggestions presented in the present thesis, based on the data from the bodies presented above, are my opinions and responsibility. Thus, they do not necessarily comply with the opinions of Femern A/S, Banedanmark and Geo.

I also visited the Schmertmann Research Lab at the Norwegian Geotechnical Institute, NGI in Oslo. I am truly thankful for the kind atmosphere and for all the help I received from the highly skilled staff. I would like specifically to express my gratitude to Head of Section for laboratory and model testing Morten Andreas Sjursen and Technical Lead at the geotechnical laboratory Dr. Rune Dyvik for their help and kindness during my stay.

My fellow PhD-students at Aarhus University, Thomas and Jakub, and my colleagues at COWI in Aalborg and Aarhus I also owe thanks for providing a great and stimulating working environment. Special thanks goes to Chief Specialist Dr. Anders Hust Augustesen for reading my manuscript and providing inputs and to Chief Specialist Dr.

Contents

Nomenclature

Definitions

Fabric   Internal arrangement of clay minerals, spatial distribution, particle size and orientation in particles and their particle-to-particle relationship

Sample   Entire artificial slurry after preconsolidation. Specimens are cut from the samples

Specimen Trimmed from sample. Used as soil element in element tests

Structure   The combined effect of fabric, fissures, cementation and slickensides. Obtained during or after sedimentation of natural clays (e.g. due to diagenesis). Inherent structure of clay specimens affects deformation behaviour and strength

Swelling   Response of specimen during unloading, i.e. void ratio increase from the decrease of vertical load

Roman Symbols

a Parabolic index after Hansen and Mise (1964). Controls shape of curved swelling curves

b Parabolic index after Hansen and Mise (1964). Controls shape of curved recompression curves

b^* Modified parabolic index. Controls shape of curved recompression curves in the model proposed in the present thesis

c Fitting parameter after Hansen and Mise (1964), used to calculate the parabolic index b

C_α Coefficient of secondary consolidation (based on void ratio)

$C_{\alpha\varepsilon}$ Coefficient of secondary consolidation (based on strain)

C_b Secant parameter used in log-parabolic framework presented in the current work (based on void ratio)

C_C^*	Intrinsic compression index. $C_C^* = e_{100}^* - e_{1000}^*$
C_C	Compression index (based on void ratio)
$C_{C\varepsilon}$	Modified compression index (based on strain)
C_R	Recompression index (based on void ratio)
$C_{R\varepsilon}$	Modified recompression index (based on strain)
C_S	Swelling index (based on void ratio)
C_S^*	Swelling index for reconstituted specimens (based on void ratio)
$C_{S,lcs}$	Secant swelling index (based on void ratio) over the first logarithmic decade of stress during unloading
$C_{S\varepsilon}$	Modified swelling index (based on strain)
c_v	Coefficient of consolidation
C_C	Compression index for deionised water conditions
C_C	Compression index for saline conditions
CEC	Cat-ion Exchange Capacity. Measure of reactivity of clay minerals
CRS	Constant Rate of Strain. Oedometer testing with loading applied with a constant strain rate
D	Equivalent diameter of clay particle (Grain size distribution tests)
d	Diameter of specimen or sample
d_s	Particle density of soil
d_w	Density of water
DDL	Diffuse Double Layer.
e	Void ratio
e_{max}	Maximum void ratio prior to unloading
e_{min}	Minimum void ratio obtained during unloading (at σ_{min}')
e_0	Initial void ratio, e.g. prior to oedometer test
e_{100}	Void ratio at end of primary consolidation
e_{100}^*	Intrinsic void ratio at $\sigma_v' = 100\,\text{kPa}$. Determined for a reconstituted soil
e_{1000}^*	Intrinsic void ratio at $\sigma_v' = 1000\,\text{kPa}$. Determined for a reconstituted soil
e_{end}	Void ratio at end of test

$E_{oed,sec}$ Secant stiffness determined on oedometer compression curves

E_{oed} Tangent stiffness determined on oedometer compression curves

F Sum of squared residuals from fitting procedure

FEM   Finite Element Method

G_{max} Maximal shear modulus at very small shear strains

h Height of specimen

$\bar{H}$ Average drainage path for specimen

h_0 Initial height of specimen before oedometer test

h_C Parameter in the proposed model for upwards concave virgin curves in $\log(\sigma'_v)$. May be compared with C_C for linear virgin curves (in $\log(\sigma'_v)$)

h_f Final height of specimen after oedometer test

i Exponent in the proposed model for upwards concave virgin curves in $\log(\sigma'_v)$-space.

I_v^* Modified void index. Void ratio of a specimen related the void ratio at σ'_{max} and σ'_{min} on an unloading-reloading loop

I_p Plasticity index. $I_p = w_L - w_p$

I_v Void index. Void ratio of a specimen related to the intrinsic void ratio at $\sigma'_v = 100\,\text{kPa}$ and at $1000\,\text{kPa}$

ICL Intrinsic Compression Line. Common normalised compression curve for reconstituted specimens. Presented by Burland (1990)

IL   Incrementally loaded. Oedometer test with load applied in increments left for a certain amount of time

k Exponent in the proposed model for calculating b^*

K_0 Coefficient of earth pressure at rest. Ratio of horizontal and vertical effective stresses

K_p Coefficient of passive earth pressure

K_t Tangent stiffness. Determined for the initial part of the recompression curves

k_{Darcy} Coefficient of permeability in the framework presented by Darcy (1856)

m Exponent used in framework by Hansen and Mise (1964), used to calculate the parabolic index a

m_0 Initial mass of specimen prior to oedometer test

m_{ring} Mass of oedometer ring

m_{end} $m_{\mathrm{ring}} + m_f$. Final mass of specimen and oedometer ring after test

m_f Final mass of specimen after oedometer test

m_{NC} Modulus number for the normally consolidated stress regime

m_{OC} Modulus number for the overconsolidated stress regime

N Number of observations

n Exponent used in framework by Hansen and Mise (1964), used to calculate the parabolic index b

OCR OverConsolidation Ratio based on stresses induced during testing. Defined as $OCR = \sigma'_{\mathrm{max}}/\sigma'_{\mathrm{min}}$ in the present study. Note that this parameter is defined differently in the present project than normally in Danish geotechnical engineering. The ratio is illustrated in figure 1

p' Triaxial mean stress, $p' = (\sigma'_v + 2\sigma'_h)/3$

q Deviator stress, $q = \sigma'_v - \sigma'_h$

q_{net} Cone resistance from CPTu-testing, corrected for area effects on the CPT-cone

R Parameter describing interval during unloading to be modelled using a polynomial. Used in the Femern Fixed Link project. Unloading below $R\sigma'_{\mathrm{max}}$ is modelled using a straight line (Femern 2014e). $R = 0.95$ is proposed by Femern (2014e)

R^2 Regression coefficient. Indicator of goodness of fit

S Degree of saturation

S_0 Initial saturation, e.g. prior to oedometer testing

S_t Sensitivity of clay. $S_t = \sigma'_{vy}/\sigma^*_{ey}$

SCL Sedimentation Compression Line. Common normalised virgin compression curve for sedimented specimens. Presented by Burland (1990)

SSA Specific Surface Area of clay minerals

T Dimensionless time factor $T = t\, c_v/h^2$

t Time

t_{50} Time for 50 % consolidation

t_{90} Time for 90 % consolidation

t_{100} Time for 100 % consolidation

U	Degree of consolidation
u	Excess pore pressure
V	Volume
V_0	Initial volume, prior to testing
w	Water content
w_0	Water content of specimen before oedometer test
w_L	Liquid limit, i.e. water content when clay-water mixture turns liquid
w_p	Plastic limit, i.e. water content when clay-water mixture turns plastic
w_f	Final water content of specimen after oedometer test
x, y, z	Variables. Explained in text where used
XRD	X-Ray Diffraction analysis
YSR	Yield Strength Ratio. Defined as $YSR = \sigma'_{vy}/\sigma'_{min}$ in the present study. The ratio is illustrated in figure 1.
CF	Clay Fraction of clay sample or specimen

Greek Symbols

β	Model parameter from E_{oed} model (reloading) presented by Femern (2014e). β links the parameters q_{net} to E_{oed}
$\Delta\sigma'_v$	Operator indicating change of a value. E.g. Δe is change in void ratio
δ_v	Vertical displacement
$\dot{\varepsilon}$	Strain rate
ε	Strain
ε_v	Vertical strain (normal or axial)
ε_0	Vertical strain at beginning of a load step
ε_{50}	Vertical strain at 50 % of primary consolidation
ε_{90}	Vertical strain at 90 % of primary consolidation
ε_{100}	Vertical strain at end of primary consolidation
ε_{creep}	Vertical strain from creep in the specimen
ε_{end}	Vertical strain at end of a load step
ε_{vol}	Volumetric strain

γ_w — Unit weight of water

κ — Parameter from the Cam Clay model (Roscoe et al. 1958). Slope on the unloading and reloading curves when plotted in $\ln(\sigma_v')$-space

κ_R — Curvature of a curve. Defined as the inverse of the radius

λ — Parameter from the Cam Clay model (Roscoe et al. 1958). Slope on the virgin curve when plotted in $\ln(\sigma_v')$

ν — Specific volume. $\nu = e + 1$

ψ — Electric potential field near clay platelet surface

σ_{ey}^* — Effective stress sustained by a reconstituted specimen, corresponding to void index, I_v at σ_{vy}' for a natural NC specimen

σ_h' — Horizontal effective stress

σ_v' — Vertical effective stress

$\sigma_{\max}'$ — Maximal vertical effective stress. Stress sustained by specimen prior to unloading. See figure 1

$\sigma_{\min}'$ — Minimum vertical effective stress. Stress sustained by specimen prior to reloading. See figure 1

σ_m' — Mean effective stress

σ_{pc}' — Vertical effective preconsolidation pressure. Related to actual maximal stress sustained by specimens, which is often uncertain (or unknown) for natural specimens. In the present work σ_{pc}' is thus related to the stress path, not the behaviour of the specimen, but may be viewed as a geological $\sigma_{\max}'$-value.

σ_s' — Reference effective stress state used for log-parabolic framework presented in the current work

σ_{v0}' — Vertical effective in situ stress

σ_{vy}' — Vertical effective yield stress. See figure 1. The yield stress causes a shift in specimen behaviour and is identified by the methods of Janbu and Casagrande. The yield stress level may be influence by structure, which may cause $\sigma_{vy}' > \sigma_{pc}'$. In the present work however, $\sigma_{vy}' < \sigma_{pc}'$ was observed for specimens of very high plasticity

σ_{sw} — Vertical effective swell stress

σ_v — Total vertical stress

XX

Definition sketches

The concepts of YSR and OCR are illustrated in figure 1 for a typical unloading-reloading curve in an oedometer test. σ'_{max} is the maximal stress previously sustained by the specimen and thus changes during primary loading. When the specimen is unloaded, the parameter σ'_{min} is changed during unloading until reloading is initiated (During unloading $\sigma'_{max} = \sigma'_{pc}$). The vertical yield stress identified along the reloading curve, by the method of e.g. Casagrande (1936) is defined as σ'_{vy}. For laboratory testing, the OCR and YSR are defined as illustrated in figure 1 and may not necessarily be equal.
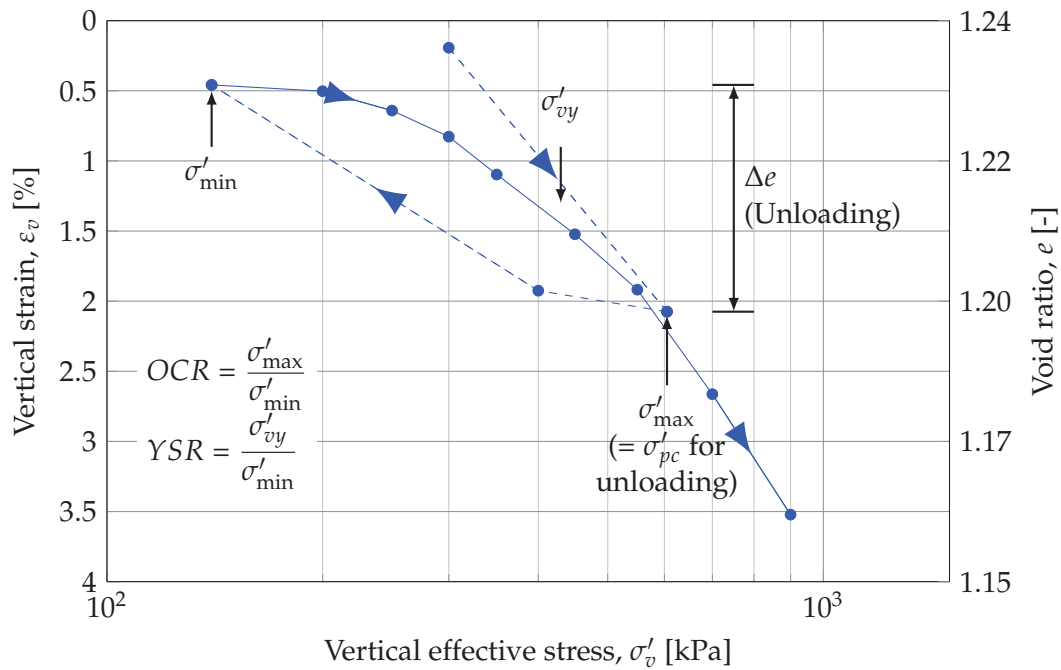
Figure 1: Definition of parameters used for assessing stress memory of high plasticity clays.

Introduction

The present dissertation deals with the deformation behaviour of high plasticity clays, with special focus on the influence of the clay mineral composition. In Denmark, a significant amount of money goes into building structures founded on high plasticity clays, yet the behaviour of the clays is not well-understood. The current study presents a range of consistently performed, incrementally loaded oedometer tests on clays of varying plasticity. Based on the obtained test results a deformation model was derived which is capable of reproducing key features of the deformation behaviour of the Palaeogene clay. The number of construction projects, where structures are founded on high plasticity Palaeogene clays, have increased over the latest five to ten years. In the years to come, a number of large-scale buildings are to be constructed on or in the Palaeogene clays. One of the construction projects are the re-development of Aarhus harbour front as the new urban district "Aarhus Ø", where a 110 m high-rise block, Lighthouse* is planned (Aarhus Stiftstidende 2016). Another is the construction of the Femern Fixed link between Denmark and Germany. The link is planned as a submerged tunnel spanning 18 km across Femern Belt, linking railway and highway infrastructure on Zealand, Denmark and in northern Germany (Femern A/S 2016). Illustrations of the Lighthouse* and the Femern tunnel are presented in figure 1.1.

Figure 1.1: *Visualization of the Lighthouse* on the harbour of Aarhus and of one of the tunnel elements of the Femern Fixed Link. After (Lighthouse* 2017; Femern A/S 2016).*

The Palaeogene clays as a group are characterised by their (extremely) high plasticity, fine grained nature, slickensides and fissures, along with relative poor bearing capacity and high volume change potential. In a number of cases inadequate attention to the traits of the high plasticity clays have caused excessive settlements of the structures, leading to costly strengthening projects. In 2014 the foundation of the Little Belt Bridge from 1935 were strengthened in a project amounting approx. 100 MDKK as settlements of up to 70 cm of the four offshore piers have accumulated during the lifetime of the bridge (Banedanmark 2013). Multiple cases are seen, where the high plasticity clays are unloaded and hence swell after construction of a building. During the swelling process, large stresses may be transferred to the structure, which may develop cracks in the façades, uneven floors or tilting of the entire building. As the Palaeogene clays are highly impermeable, the volume changes due the construction works may continue for decades.

Planning and construction of structures, such as a high-rise block or a long tunnel, are demanding tasks. The design process must ensure that loads from the environment and daily use of the structure are safely transferred to the soil, which in turn must be able to carry the applied load with an acceptable safety margin. Low strength of a deposit must be accounted for during the design phase. However, the large compressibility of the Palaeogene clays is an equally important factor to include. For initial assessments in a construction project (or for small projects) the plasticity index is often used to assess strength and deformation potential for clay beds. However, for high plasticity clays, the commonly applied relations, which were derived for clays of low or medium plasticity (Sørensen and Okkels 2015), rarely perform satisfactory. Thus, the in situ deformation potential are lower than proposed from the well-known relations and the effective strength parameters show scatter due to cracks and fissures (Sørensen and Okkels 2013).

For Femern Fixed Link, the planned alignment for the tunnel includes an approximately 4 km long stretch founded directly in high plasticity Palaeogene clay from seabed to large depth. Thus, a significant test programme was initiated in 2009 (Femern 2014c). Parts of this program showed that a traditional clay, e.g. a glacial clay till, "remembers" the maximum pressure sustained in the past, which is why an indication of the stress sustained during past glaciations may be deduced from oedometer tests, i.e. the vertical yield stress approximates the previous maximal vertical stress. However, it was also shown that the vertical yield stresses identified for high plasticity Palaeogene clays, do not reflect the previously sustained maximal stress (Femern 2014a). Similar "lack of stress memory" was identified by Krogsbøll et al. (2012) and Mortensen (2012). Thus, contrary to clays of low or medium plasticity, the normally and overconsolidated stress regions are not well-defined for the Palaeogene clays, which may pose a challenge during design.

Standard framework for estimating deformation for structures often relies on the use of simple models, which are essentially linear relationships with the logarithm of vertical effective stress, σ_v'. For the high plasticity clays however, a linear relationship is not obtained from testing. On the contrary, the compression curves are highly curved. This observation combined with the ill-defined normally and overconsolidated stress regimes, requires extreme care to be taken when traditional models are applied to model the behaviour of the Palaeogene clays to assess settlements for structures.

The large content of smectite minerals has been offered as an explanation for the

difference in behaviour between the high plasticity Palaeogene clay and other clays (Femern 2014c). However, no systematic studies have so far been carried out with the aim to achieve an understanding of the influence of soil mineralogy and especially the smectite content on the observed deformation behaviour of Danish Palaeogene clays. To increase the knowledge on this matter for Danish Palaeogene clays, the present PhD project investigates the effects of smectite mineral content on the deformation behaviour of artificial clays. The use of artificial clays allows for variation of a single parameter at the time, which enables a detailed study. Moreover, unwanted effects of sample disturbance, recent stress history etc. which may be introduced with the use of natural, intact clays are avoided by using artificial specimens. The present study thus will illustrate the effect of smectite content on the consistency characteristics and the deformation behaviour. Particularly, a great deal of focus have been placed on the deformation behaviour in an overconsolidated stress state, and on the "loss of stress memory" observed for the natural clays.

1.1 Aims of study

The overall aim of the current studies was to acquire more knowledge on the deformation behaviour of high plasticity clays, specifically targeting the influence of the clay mineral composition. Specific aims of the study were formulated as follows:

> To achieve a deeper knowledge on the significant parameters that influences the deformation behaviour of high plasticity clays through review of literature and laboratory tests.

> To develop a framework capable of modelling the deformation behaviour of high plasticity clays. The framework is to be based on the significant parameters identified from the first objective, and should eventually be applied for modelling natural Palaeogene clays.

1.2 Methodology

Through a series of incrementally loaded, oedometer tests carried out on reconstituted, artificial specimens, the effect of the smectite content on the deformation behaviour will be documented. By use of artificial specimens, the mineralogical composition and the stress history of the oedometer specimens is well-known, and can be varied in a controlled manner during testing. The main study will comprise specimens of different mixtures of kaolin and bentonite, to cover a large interval of specimen plasticities, which will be subjected to multiple loading programmes. During the tests, the effects of clay mineralogical composition and the applied stress path during loading on the deformation behaviour will be evaluated.

Based on the performed oedometer tests, an empirical model is to be derived, which is capable of reproducing the essential features of the tested clays. The derived deformation model will be formulated to account for both normally consolidated and overconsolidated conditions, and to allow stress paths covering both unloading and reloading to be modelled. As the model is based on oedometer tests, the limitations of this test

type is inherited by the proposed deformation model. Thus, the model may be assumed to be valid for conditions close to the conditions in the oedometer cell, and does not account for e.g. small strain behaviour. Due to time constraints no strength-related tests on the artificial mixtures were carried out, which is why only deformation properties are discussed in the present dissertation.

The main aim of the study is supported by a number of secondary objectives, which were undertaken during the PhD-project. These comprised analyses of the effects of frictional stress loss in the oedometer cell during testing and the effects of pore fluid salinity on the deformation behaviour. These studies were carried out as sub-studies besides the main objectives, and for some of the sub-studies, the tests were performed by MSc-students. Finally, a few simple tests were identified, which may be used to assess whether the smectite content of a specimen will govern the deformation behaviour.

1.3 Thesis outline

The present dissertation is structured as outlined below:

> Chapter 2 introduces the features of the two main clay minerals included in the present project, namely kaolinite and smectite. The atomic structures and electro-chemical abilities of single clay minerals are introduced and related to the Danish Palaeogene deposits, based on information published in literature.

> Chapter 3 deals with previous studies on high plasticity clays, with special focus on the behaviour of Danish Palaeogene clays, as published in literature. In this chapter a number of concepts are introduced, which are vital for the following analysis of the test data from the PhD-project.

> Chapter 4 present the properties and characteristics for the materials used for the tests performed within the present project.

> Chapter 5 introduces the applied procedures for performing index testing, preparation of slurry samples, trimming of oedometer specimens and execution and analysis of oedometer tests.

> Chapter 6 highlights key observations from the main laboratory tests. These observations provide the main features of the tested clays to be modelled using the proposed deformation model.

> Chapter 7 introduces the proposed deformation model, and accounts for the calibration procedures. Moreover, some analyses of the model are presented, which aid the understanding of the behaviour of the artificial specimens. Specifically, the discordance between maximal stress sustained by the specimen and vertical yield stress on recompression branch after unloading is discussed.

> Chapter 8 presents the validation studies carried out to assess the performance of the deformation model proposed in chapter 7. Moreover, the effects of specific test conditions on the shape of the unloading-reloading loops are discussed.

4

> Chapter 9 illustrates, how the proposed deformation model may be applied to oedometer tests on natural Palaeogene clays. The chapter presents data from literature for Danish Palaeogene clays, and illustrates the performance of the proposed model, based on three case studies.

> Chapter 10 sums up and concludes the present study. Moreover, a few recommendations for further research areas are presented.

Mineralogy of clays

As the present dissertation deals with the influence of clay mineralogy on the mechanical behaviour of clays, the basic properties of the two main minerals investigated in the present project, are introduced in the following chapter. The presentation introduces the structure of the clay minerals, and briefly touches on their behaviour. Ultimately, the chapter discusses the main characteristics on clay minerals in Danish Palaeogene deposits. The following chapter will focus on the behaviour of clays, where a mixtures of clay minerals contribute to the mechanical properties.

2.1   Composition of natural clays

Natural clays often consist of a mix of particles in different sizes. In natural Danish clay in general, boulders, rocks, sand and silt can be found along with the clay particles. In the glacial clay tills the most varying mix of different diameters is found, whereas the Danish Palaeogene clays often consist almost only of particles from the clay fraction. A comparison of the grain size distribution of a typical glacial clay till and a typical Palaeogene clay is presented in figure 2.1. The two clays may be considered two extremes of the natural Danish clays in terms of grain size distribution.

In general sand and silt particles consist of minerals with 3D lattices, e.g. Quartz or Feldspar, whereas the clay fraction consists of different clay minerals which are composed of sheet-like lattices. The focus of the present chapter is a short presentation of two of the common clay minerals and their features, to give an overall idea of the behaviour of the minerals used for the investigations presented in the present thesis. Understanding the behaviour of the pure clay minerals may be considered the first step in understanding the wide range of mixtures of clay minerals and non-clay particles in natural soils.

2.2   Structure of clay minerals

The clay minerals are built of layers or sheets of atomic units, i.e. the octahedral and tetrahedral units. A single octahedral unit consists of six hydroxyl groups or oxygens ordered around an aluminium, iron or magnesium atom. The octahedral units are ordered into sheets, where three of the hydroxyls are shared between two individual units
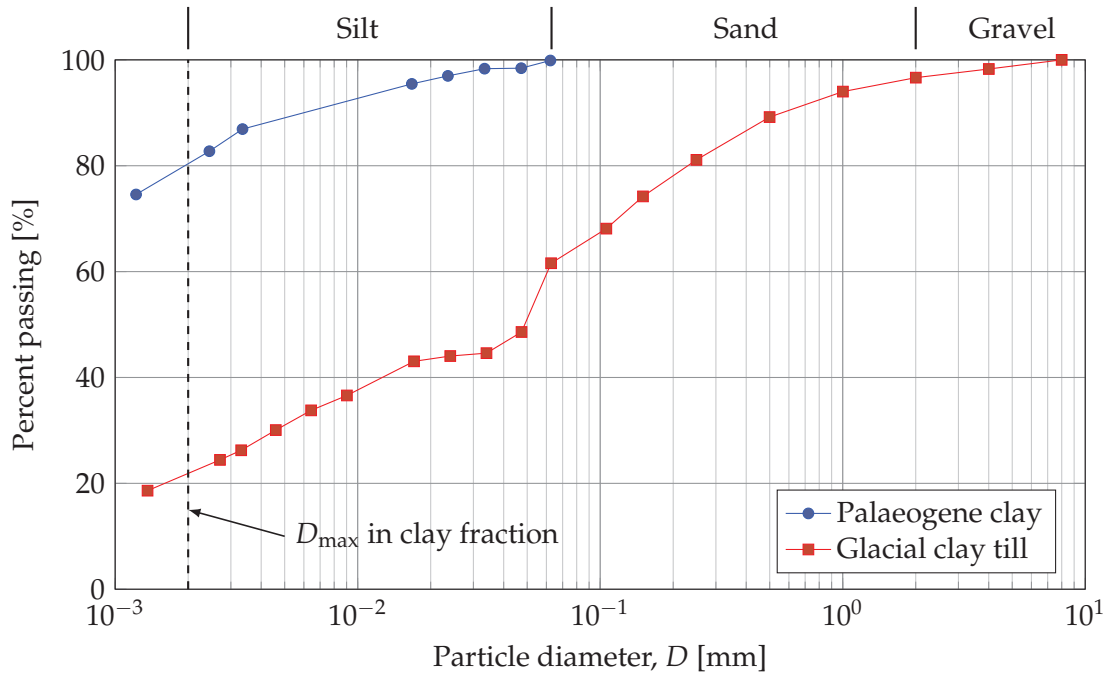
Figure 2.1: *Comparison of grain size distribution for a typical glacial clay till (specimen 09.A.003 09-101869) and a typical Danish Palaeogene clay (specimen 09.A.002 09-101436). After Femern (2014a).*

(Grim 1962). The atomic formula for the sheet structure is $Al_2(OH)_6$ and the thickness of a sheet of octahedral units are about $5.05\,\text{Å}$. The single octahedral unit and the sheet structure are illustrated in figure 2.2.

The second atomic unit is the tetrahedral unit. In a single unit the oxygens are positioned in a tetrahedron with a silicon atom positioned with equal distances to the oxygen atoms. The single tetrahedral units form sheets by sharing three of the oxygens with three neighbouring units, forming a plane of hydroxyls structured in "hexagons". The sheets are continued indefinitely in the horizontal direction, where the fourth oxygens (i.e. the tips on the units) all points in the same direction, as illustrated in figure 2.3. The structured network of the tetrahedrons can be formulated with the atomic formula $Si_4O_6(OH)_4$. The thickness of a sheet is about $4.93\,\text{Å}$ (Grim 1962).

○ and ○ = Hydroxyls   ● = Aluminium, Magnesium, etc.
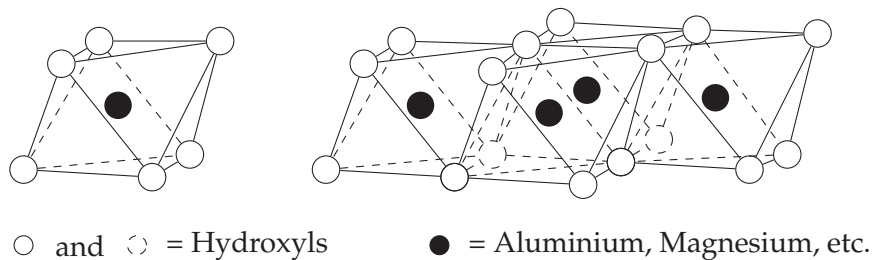
Figure 2.2: *Illustration of the octahedral unit (left) and the sheet structure (right). After Grim (1962).*

○ and ◌ = Oxygens   ● = Silicon
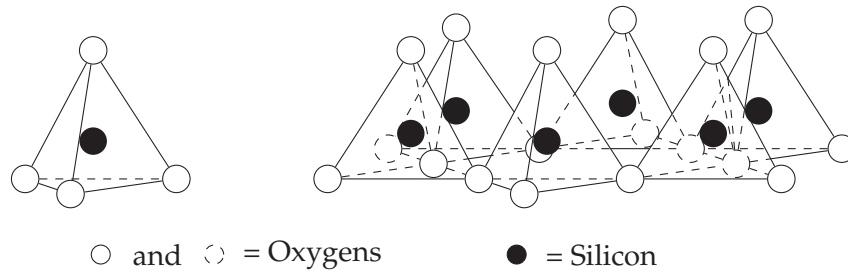
Figure 2.3: Illustration of the tetrahedral unit (left) and the sheet structure (right). After Grim (1962).

2.3 Kaolinite minerals

The kaolinite mineral is composed of a sheet of tetrahedral units placed, with the tips facing downwards, on a sheet of octahedral units, and is hence denoted a 1:1 clay mineral (Holtz et al. 2011). The hydroxyls on one of the sides of the octahedral sheet form the tips in the tetrahedral sheet layer. The combined thickness of the two sub-layers in the kaolinite mineral is about 7.2 Å. The atomic charge of the kaolinite mineral structure is well-balanced, which does not allow for substitutions of the minerals in the structure (Grim 1962). The structural formula for the kaolinite mineral is $(OH)_8Si_4Al_4O_{10}$.

The size of the kaolinite mineral flakes is limited by the dimensions of the sheets of octahedrals and tetrahedrals, but multiple sheets are often stacked, one on top of the other. The particles of kaolinite minerals may consist of up to hundred sheets stacked on top of each other (Terzaghi et al. 1996). The basal structure of the kaolinite minerals is presented in figure 2.4.

○ = Hydroxyl
○ = Oxygen
● = Silicon
● = Aluminium
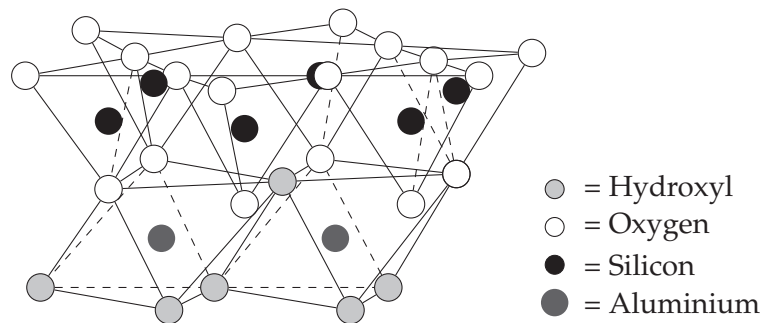
Figure 2.4: Illustration of the structure of the kaolinite mineral. The sheets are stacked above and below the sheet and are all oriented in the same way. After Grim (1962).

Geologically, the kaolinite minerals are formed from weathering of Mica and Feldspar in granitic rocks under moist but well-drained conditions, which have allowed for leaching of cations such as Ca^{++}, Mg^{++} and Fe^{+++} in the soil (Mitchell and Soga 2005). Most of the Palaeogene clays in Denmark contain kaolinite minerals in varying amounts (Femern 2014a; Awadalkarim 2011). In other Danish clay deposits kaolinite is usually found to constitute up to 40 % of the clay mineral group, where the rest primarily consists of smectite and illite (Trankjær and Christensen 2012).

Due to strong hydrogen bonds between the individual kaolinite sheets, the expansion of kaolinite usually is quite limited when exposed to water (Taylor and Smith 1986;

White 1955). Thus, kaolinite minerals exhibit quite small plasticity indices compared to other clay minerals (White 1955; Trankjær and Christensen 2012). The plastic limit, w_p, and liquid limit, w_L, for pure kaolinite minerals, are approximately 30 % and 60 %, respectively, yielding a plasticity index of approximately $I_p = 30$ %.

Kaolinite minerals are relative insensitive to the type and valence of an adsorbed cation in terms of the Atterberg limits, however an effect of the pore fluid salinity has been identified in some literature. It has been reported that w_L increases marginally with increasing concentration of ions in the pore water. Increasing the concentration and the valence of the ions in the pore fluid causes coagulation of the minerals, which leads to a higher liquid limit (Horpibulsuk et al. 2011; Sridharan and Venkatappa Rao 1975; Sridharan et al. 1986, 1988).

2.4 Smectite minerals

Smectite minerals are composed of two tetrahedral sheets, one on either side of a single octahedral sheet. The minerals are hence categorized as a 2:1 clay mineral. The tips of the tetrahedral sheets share oxygens with the octahedral layer and forms the 2:1 layered mineral sheet. In the smectite weak bonds exists between the individual sheets, which are formed between the hexagonal lattices of the tetrahedral sheets. The weak bonds, combined with the unbalanced elementary charge of the smectite sheet, allow water and dissolved cations to freely enter and react with the lattice, as illustrated in figure 2.5. The theoretical atomic formula for montmorillonite (which is part of the smectite group) is $(OH)_4Si_8Al_4O_{20}\cdot nH_2O$ (where n denotes an integer), however, montmorillonite always


$n\,H_2O$ layers with ions
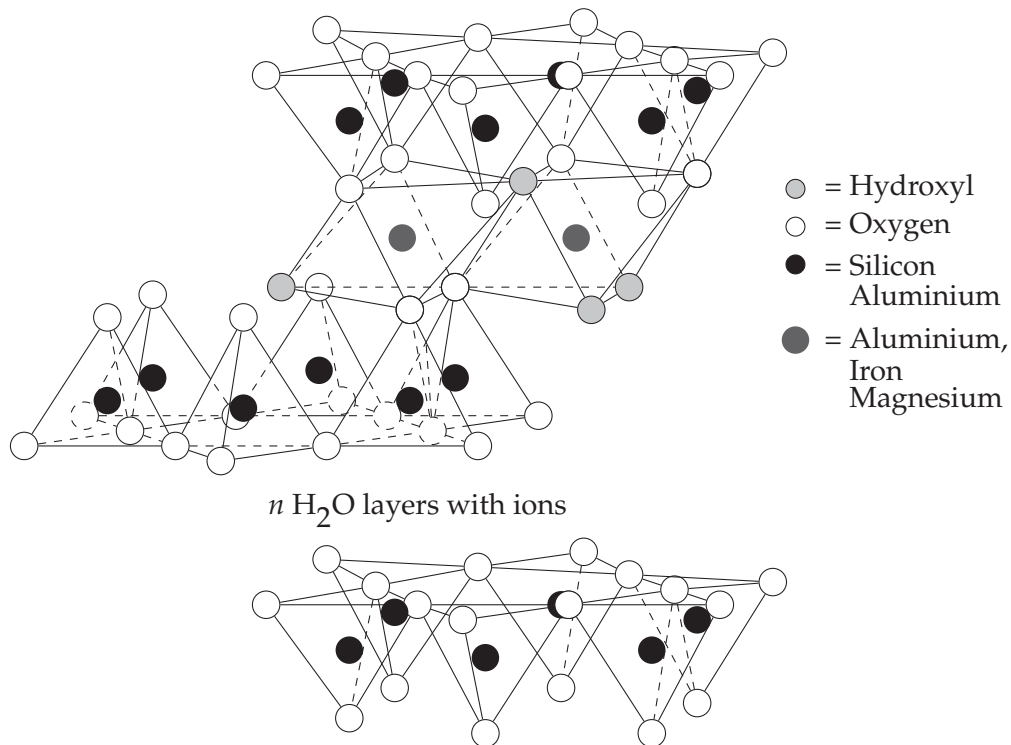
Figure 2.5: Illustration of the montmorillonite structure. After Grim (1962).

differ from the formula because of substitutions in the crystal lattice (Grim 1962).

The penetration of water molecules between the smectite mineral sheets causes the lattice to expand. In total dehydrated state the thickness of the mineral sheet is about 9.6 Å. However, when water is absorbed, the thickness depends not only on the number of water molecules between the sheets, but also on the adsorbed cations (Holtz et al. 2011). During a XRD-analysis the clay samples are treated with glycol which causes a full expansion of the crystal lattice to approx. 17 Å. Hence, comparing XRD-results for glycol treated and dried specimens, smectite can be identified by the shift in the intensity peaks corresponding to the thickness of the mineral in the two states.

The substitution in the crystal lattice introduces an electronic charge deficiency, which attracts cations. For mono-valent cations, like Na^+, the effect of the electric potential may reach a distance from the clay platelet surface of 100 Å (Morris and Żbik 2009). In montmorillonite with Ca^{++} as the adsorbed cation, the individual sheets are limited to adsorb a water layer with a thickness up to four water molecules (Terzaghi et al. 1996). This difference between clays with different cations influences the volume change behaviour. It has been estimated that Na^+-smectite has a swelling potential up to 200 times larger than what is found for Ca^{++}-smectite (Trankjær and Christensen 2012; Popescu 1986).

Montmorillonite and smectites in general, are formed from weathering of basic igneous rocks, i.e. basalt and volcanic ash in arid environments where both pH and concentration of the electrolytes are high (Mitchell and Soga 2005; Popescu 1986). Leaching effects may change the concentration of cations in the pore water of a deposited smectite-rich clay, which may alter the adsorbed cations (Horpibulsuk et al. 2011), and hence the properties of the clay after sedimentation.

2.5 Diffuse double layers of clay particles

The adsorption of cations significantly affect the behaviour of smectite clay minerals. As previously presented, Na^+-smectite has a significantly higher volume change potential compared to Ca^{++}-smectite. Thus, the Atterberg limits and deformation properties are found to greatly depend on the adsorbed cations (White 1955; Sridharan et al. 1986). The change in behaviour can be explained by the diffuse double layer theory (Olphen 1977), which is briefly outlined in the present section.

The net elementary charge caused by the substitutions in the clay particle lattice attracts the cations in the pore fluid. Moreover, the polar water molecules are electrostatically attracted to, and adsorbed on, the clay surface. Thus, the concentration of the cations is high near the surface of the clay particles, but is balanced by diffusion, which creates a layer with decreasing concentration of cations with distance from the clay platelet surface (Holtz et al. 2011; Mitchell and Soga 2005; Olphen 1977). The electric potential at the clay surface and the layer of cations form the diffuse double layer, which explains the sensitivity related to the type of adsorbed cations for smectite. An illustration of the electric potential near the clay platelet surface is presented in figure 2.6a for different concentrations of mono-valent cations. The full black dots denote the electric potential, which may be defined as the limit of the diffuse double layer (DDL) in simple models. Based on the theoretical framework for the diffuse double layer a relationship between effective stress and void ratio may be derived (Bharat and Sridharan

2015; Sridharan 2014). A comparison of test data provided by Bolt (1956) on Wyoming bentonite in 10^{-3} M NaCl and $CaCl_2$ solutions and theoretical model proposed by Bharat and Sridharan (2015) are presented in figure 2.6b. As may be noted from the figure, a fairly accurate fit between measured and calculated void ratios are obtained.

(a) Electric potential in near platelets

(b) Comparison of DDL-model and tests
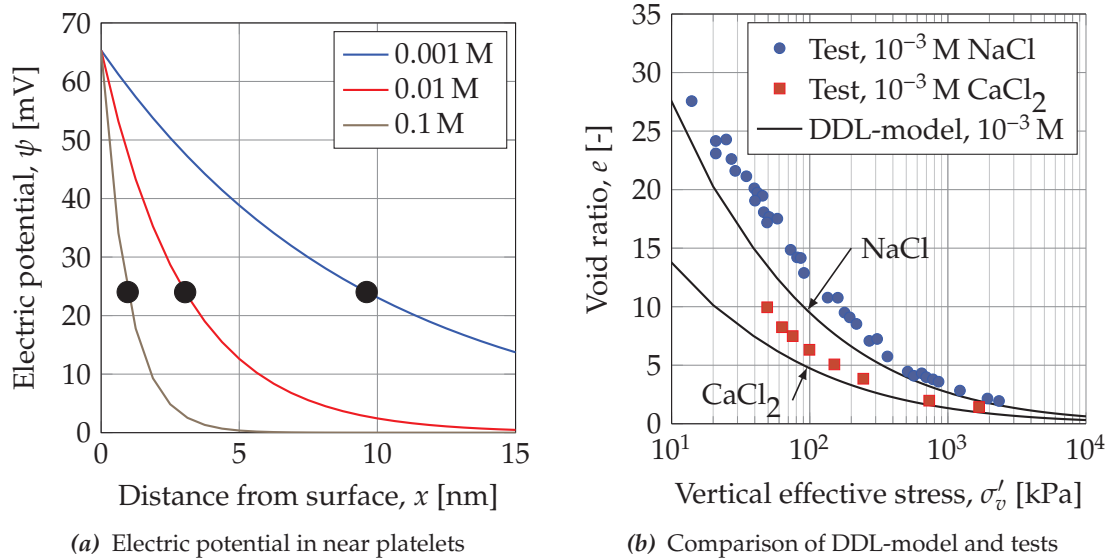
Figure 2.6: *Illustration of the electric potential near a clay platelet surface for different concentrations of mono-valent cations (Figure 2.6a). After Himenz and Rajagopalan (1997). In figure 2.6b the void ratio of a Wyoming bentonite is presented as a function of stress. Test data after (Bolt 1956) and model after (Bharat and Sridharan 2015).*

The cations in the mineral lattice can be exchanged if the mineral is exposed to a higher concentration of another cation (Rhoades 1982). The ability of the clay minerals to exchange cations is expressed by the Cations Exchange Capacity, CEC. Generally, the higher valence of ions, the tighter the ions are held by the lattice (Thøgersen 2001; Grim 1962). Thus, substituting Na^+-ions with Ca^{++}-ions is easier than vice versa.

The diffuse double layer thickness changes with the concentration of pore fluid and the electrostatic charge of the cations, which change the strength of the attraction (i.e. the electric potential field) as illustrated in figure 2.6a. High concentration of e.g. NaCl in saline waters causes the thickness of the diffuse double layer to shrink, limiting the volume change behaviour (Thøgersen 2001; Sridharan and Venkatappa Rao 1973). Thus, the w_L decreases with an increase of salinity for smectite-rich clays (Horpibulsuk et al. 2011; Sridharan and Venkatappa Rao 1975; Sridharan et al. 1986, 1988). The liquid limit, plastic limit, undrained shear strength and deformation potential, etc. are all depended on the dielectric constant of the pore fluid (i.e. pore fluid electrolyte type and concentration), generally forming a stiffer and stronger response with increasing salinity (Spagnoli et al. 2010).

Generally, very large swelling potentials are found for the smectites due to large CEC-values and small particles sizes, which cause a very large specific surface area, SSA of the clay minerals (Mitchell and Soga 2005). The lowest volume change potential is usually found for Ca^{++}-smectite and the highest for Na^+-smectite (Taylor and Smith

1986). Determining the plastic limit and liquid limit of smectite yields approximately w_p = 60–100 % and w_L = 125–700 %, respectively, which results in a plasticity index, I_p in the range of 50 % to 600 % (White 1955). The large variability in the consistency indices, which may be identified even between two smectites with the same adsorbed cation, may be caused by differences in the crystal lattice, as presented in section 2.4. As seen from the range of I_p, the effect of adsorbed cation on the smectite mineral is profound for the consistency characteristics (Grim 1962; White 1955).

Smectites are generally characterised by very low permeabilities, where the adsorbed cation also dictates the behaviour of the clays. Thus, sodium smectite is less permeable than calcium smectite (Mesri and Olson 1971). Due to the very low permeability, smectite is often used as barriers for e.g. waste disposal sites or for encapsulating of nuclear waste (Pusch et al. 2010; Dueck and Nilsson 2010; Hueckel 2002).

2.6 Mineralogy of Danish Palaeogene clays

In Denmark the Palaeogene clays are typically found close to the surface in eastern Jutland and in the southern parts of Funen and Zealand. Thus, in these parts of Denmark, the clays are highly relevant for construction projects. A map of the surface-near Palaeogene deposits in Denmark is presented in figure 2.7. The Epochs in the Palaeogene period are presented in different colouring in figure 2.7. South-west of the indicated bands, the Palaeogene clays are covered by younger sediments, whereas they are eroded by glaciations north-east of the band.

The geological models suggest that Denmark in the Palaeogene period were covered by deep seas with very limited deposition of material from the shores (Heilmann-Clausen 1995). Thus, the very fine-grained Palaeogene clay had time to settle. Analyses of the Niger Delta have shown that illite and kaolinite minerals tends to flocculate in larger particles than smectite, and will hence settle sooner (Porrenga 1966). Taking into account the deep waters above Denmark in the Palaeogene period, this sorting mechanism may be part of the explanation of the high content of smectite minerals in the Palaeogene clay deposits, as kaolinite and illite may have been deposited closer to the shore (e.g. over present day London, where the London clay typically contains a significant proportion of illite). A sedimentation rate of as little as a few mm clay material per 1000 years has been suggested for the Danish deposits (Heilmann-Clausen 1995), which may help to grasp the extreme fine-grained nature of the Danish Palaeogene clays. In the Quaternary period, following the Palaeocene and Neogene periods, a number of glaciations covered present day Denmark followed by ice retreats, which is why the Danish Palaeogene clays have been overconsolidated by ice caps.

The Danish deposits of Palaeogene clay, which have a significant content of smectite minerals (Pusch et al. 2015; Heilmann-Clausen 1995; Nielsen and Heilmann-Clausen 1988), are formed from weathering of volcanic ash, deposited from volcanic eruptions in present-day Norway (Heilmann-Clausen 1995). The weathering may have been completed onshore or in the sea as the fine particles may have been carried over large distances by the currents. In some of the Danish Palaeogene deposits thin layers of ash can still be found, in which clay mineralogical analyses reveal a very high content of smectite minerals (Nielsen 1974). This observation seems to verify the proposed volcanic origin
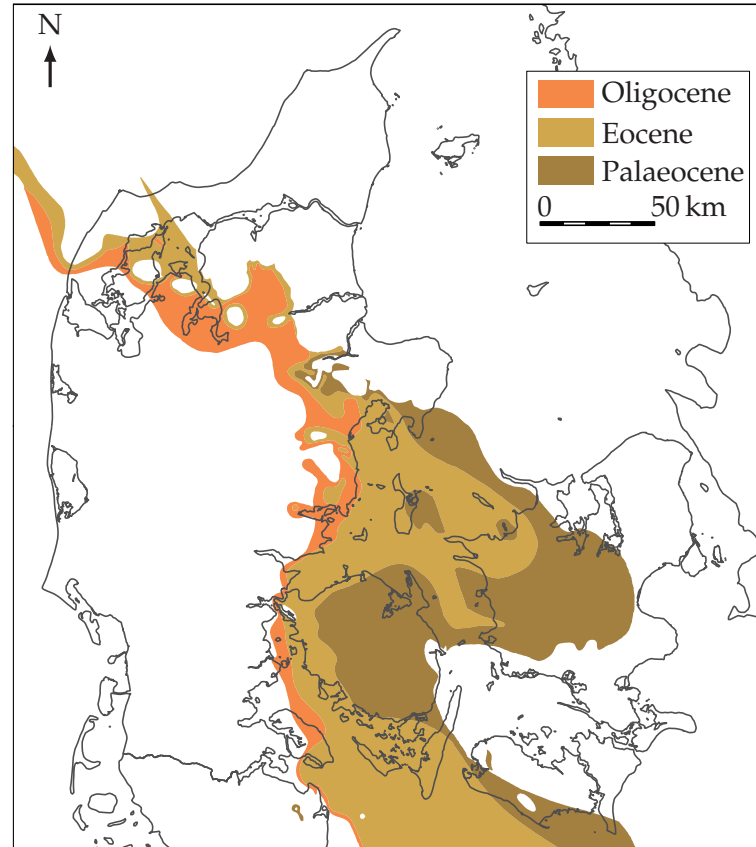
Figure 2.7: *Locations of Palaeogene deposits near the surface in Denmark. After Varv (1992).*

of the smectite minerals.

In Denmark only little work has been carried out to investigate the most common cation adsorbed to the smectite minerals. Thus, a general description of the dominating adsorbed cation, based on geographical location, cannot be given. However, for some locations the adsorbed cation ion of the smectite has been examined. At the harbour of Rødbyhavn some investigations were carried out to investigate whether the smectite-rich deposits were of sufficient quality to be used for industrial bentonite. It was, based on mineralogical analyses, concluded that the adsorbed cations of the smectite at Rødbyhavn were primarily Na^+ (Foged and Baumann 1999). However, the commercially exploited smectite-rich deposits at Tåsinge are found to be a natural Ca^{++}-bentonite (Dantonit A/S 2014). This seems to be supported by general findings in Europe, that most smectites have adsorbed Ca^{++}-cations (Pusch and Yong 2005). This has also been reported to be the case on other locations in Denmark (Holmboe 2001; Trankjær and Christensen 2012). A number of authors suggest that the most commonly found smectite has absorbed a mixture of Ca^{++} and Na^+-ions (Nielsen 2014; Graff-Petersen 1955). Thus, a part of the explanation for the very varying I_p that are often identified for a natural clay (Femern 2014a) may be a varying ratio of smectites with adsorbed sodium and calcium cations.

Based on the varying statements from literature it seems that the adsorbed cation on the smectite minerals depends on the location of the deposit. A deposit in saline

waters is subjected to a high concentration of sodium ions, which is why the predominately adsorbed cation presumably is Na^+. For deposits on-shore, calcareous ground water may flow near the smectite-rich layers, which will favour the development of Ca^{++}-smectite. Nielsen et al. (2015) suggests that the smectite minerals altered at the sedimentation location (offshore, after sedimentation of e.g. volcanic ash) is Na^+-smectite, whereas minerals weathered on-shore and transported prior to the final sedimentation is of the Ca^{++}-type. In the glacial periods in the Quaternary period the sea level were much lower than today due to the larger polar ice caps in this period. Thus, the Danish Palaeogene clays near the surface today, may all have been "on-shore" deposits at some point, which may have partly changed the adsorbed cations. In conclusion, it does not seem surprising that the natural Danish Palaeogene clays have varying adsorbed cations.

Previous studies of high plasticity clays

While chapter 2 dealt with the characteristics and formation conditions of the clay minerals of focus in the present thesis, the present chapter outlines the one-dimensional compression behaviour of natural high plasticity clays based on results from literature.

Clays have been studied intensively in the last century, covering a wide range of methods of investigation. In the present study, the main focus is the influence of clay mineralogy on the deformation behaviour of high plasticity clays as obtained from incrementally loaded oedometer tests. Thus, only a few selected topics, which are relevant for the analyses of the results presented later, are discussed below. The following topics are presented in the current chapter:

> The behaviour of the natural Danish Palaeogene clays.

> The influence of structure on the deformation behaviour of natural clays. The definition of structure applied in the present project are presented in the nomenclature on page XV.

> The normalisation of compression curves by the intrinsic properties framework.

> Previous studies of the influence of clay mineralogy on deformation behaviour of natural clays.

> Effects of pore water chemistry on the deformation behaviour of clay minerals and natural clays.

The literature presented within this chapter constitute the background for the methods developed and applied on the conducted tests in the present PhD-project, which are presented in chapter 5. Moreover, as the overall goal of the project is to add to the existing knowledge on the Danish Palaeogene clays, the objective of the present chapter is to identify and highlight the most essential features of the deformation behaviour.

3.1 Deformation behaviour of natural Danish Palaeogene clays

3.1.1 Geotechnical characteristics of Danish Palaeogene clays

The Palaeogene clays in Denmark are all sedimentary, marine clays and have high clay contents (usually between 60 % to 80 %), high plasticity indices, (I_p = 40 % to 210 %) and a significant content of smectite (15 % to 75 % of bulk mass) (Femern 2014a). The Palaeogene clays are very often fissured and slickensides may often be identified in laboratory specimens (Femern 2011a).

A very large testing programme was carried out and documented as a part of the tender for the Femern Fixed link, comprising in situ testing, laboratory testing and full scale tests. The laboratory programme comprised a range of classification tests, 1D compression tests, triaxial tests of various complexity and other more specialised tests as e.g. DSS-tests. Femern (2014c) describes the overall behaviour of the different units of Palaeogene clays found during the boring campaigns to be characterised by the content of smectite minerals in the clay. However, it was not possible to relate the secant stiffness parameters obtained from oedometer testing directly to smectite content (Femern 2014c). It should be noted that the influence of smectite content in relation to 1D deformation parameters were not specifically investigated as a part of the work related to the Femern Fixed link project.

Generally, the compression curves obtained from oedometer testing on the Palaeogene clays are highly non-linear – both during virgin loading and unloading-reloading loops. When performing stress reversals in the oedometer cell (e.g. going from virgin loading to unloading) a very high initial stiffness is identified from the oedometer tests (Femern 2014a). An example of a specimen showing large tangent stiffness, E_{oed}, after stress reversals are presented in figure 3.1. Indeed, the measured initial stiffness in the oedometer tests in some cases was higher than the G_{max}-value derived from small-strain tests on the Palaeogene clay. This behaviour is not what is to be expected, and may has been caused by reversal of flow gradients, reversal of the principal stresses or internal friction in the oedometer cell. The high initial stiffness enhances the non-linearity of the unloading and reloading curves and increases the hysteresis on the unloading-reloading loop.

During the oedometer testing programme for the Femern fixed link, it was noted that all specimens, when unloaded sufficiently, fell on a common unloading curve with a constant slope on a $\log(\sigma'_v)$-axis, i.e. a constant modified swelling index $C_{S\varepsilon} \approx 5.1$ % was observed across the majority of tests carried out on different Palaeogene clay units (Femern 2014a). This may suggest that the smectite content – once above a given threshold – does not significantly influence the 1D response of the natural clay, at least during unloading.

3.1.2 Yield stress of Danish Palaeogene clays

As discussed in section 2.6 the Danish Palaeogene clays are overconsolidated by glaciation and following erosion, which would be expected to be observed from the vertical yield stress, σ'_{vy} identified during oedometer tests. For natural Palaeogene clays σ'_{vy} is usually identified as low as σ'_{vy} = 280–490 kPa using the methods presented by Casagrande (1936) or Janbu (1969) (Thøgersen 2001; nmGeo 2013), compared to the load of

approximately 3000 kPa, assumed to subjected to the soil from the previous glaciations (Thøgersen 2001; Hansen and Mise 1964; Christensen and Hansen 1959). Grønbech et al. (2015) suggest a very high vertical yield stress, σ'_{vy} = 6850 kPa to 9100 kPa, which is related to the maximal stress sustained by the specimens on the geological time scale, but the deformation behaviour of the Danish Palaeogene clays does generally not reflect these high σ'_{vy}-values as the stiffness is too low (Thøgersen 2001; nmGeo 2013; Banedanmark 2013).
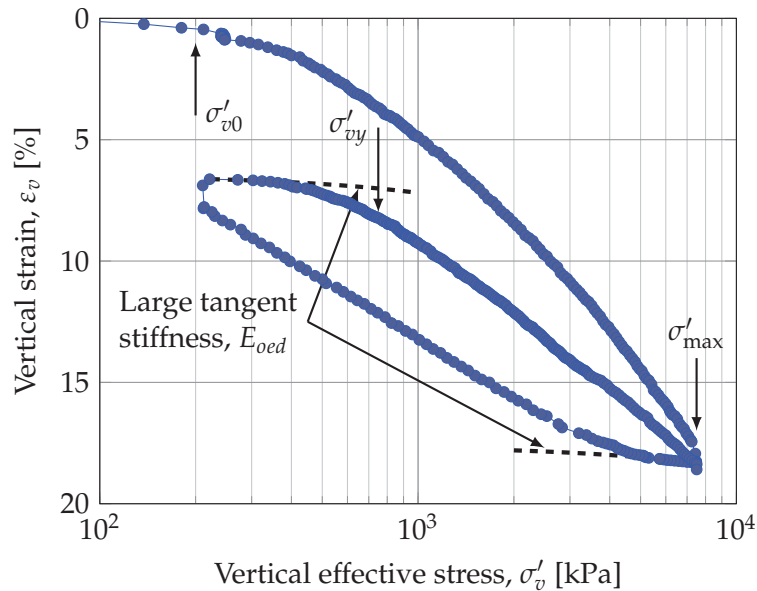
Figure 3.1: *Compression curve from CRS testing on a natural specimen of Røsnæs clay from 22.39 m depth. Note the low vertical yield stress identified on the reloading branch compared to the sustained maximal stress. After Femern (2014a), boring 09.A.002, test number 09-101477_19_21.*

For specimens of Danish Palaeogene clay, where the stress history is known from previous steps in the oedometer apparatus, the identified yield stress is not related to the maximal load sustained by the specimen (Sørensen and Okkels 2015; Femern 2014a; Mortensen 2012; Krogsbøll et al. 2012). The phenomenon is illustrated in figure 3.1 for a natural clay tested under the Femern fixed link project. As may be observed from the figure, $\sigma'_{vy} \approx 750$ kPa as identified along the recompression path (by both Casagrandes and Janbus methods) is far from the previously sustained stress, σ'_{max} = 7500 kPa. This behaviour may be caused by gradual destructuring of the specimens during unloading as observed by Krogsbøll et al. (2012) which is linked to the pronounced swelling during unloading causing an increase of the void ratio as reported by Mortensen (2012). Several authors suggest that the behaviour of the natural Palaeogene clay is governed by the high content of smectite (Krogsbøll et al. 2012; Mortensen 2012; Trankjær and Christensen 2012).

3.1.3 Yield stress of other Palaeogene clays

In a range of oedometer tests on different specimens of intact London clay ($I_p \approx 40\%$, smectite content up to approx. 50%), yielding was identified below the previously sus-

tained maximal stress on the recompression branches (Gasparre 2005), parallel to the behaviour observed for Danish natural Palaeogene clays. It should be noted, that a clear post-yield state was probably not achieved by Gasparre (2005), which may, to some extent, influence the determination of the yield stress – especially if the Casagrande approach is used. However, the maximal stresses sustained by the specimens were in the order of 20 000 kPa, which is why the relevance of a fully yielded state at even greater stresses is limited for practical engineering purposes.

Deng et al. (2012) performed a series of tests on the highly plastic Boom clay ($I_p \approx$ 40 %, smectite content up to 20 %, additionally up to 20 % illite-smectite) and found poor concordance between the maximal stress sustained prior to unloading in the oedometer cell and the yield stress inferred from the recompression branch, but did not further pursue the matter. Deng et al. (2012) identified essentially linear unloading paths when unloading sufficiently (Constant $C_{S\varepsilon}$ as described by Femern (2014c), see section 3.1), however the reloading curves were highly non-linear in the $\log(\sigma'_v)$-plot. Further works with the highly plastic Boom clay show similar tendencies (Cui et al. 2013; Nguyen et al. 2013). Cui et al. (2013) explained the curved shape of the unloading and reloading branches and the large observed hysteresis by two different responses during unloading and reloading. Below a threshold stress, the interlayer repulsion in the diffuse double layer is governing the deformation behaviour (i.e. a chemical response), whereas the mechanical response of the clay matrix governs the behaviour above the threshold stress (Cui et al. 2013).

Thus, the features observed for Danish Palaeogene clays are also observed on high plasticity clays elsewhere, even at lower plasticities. This seems to suggest that a common trait as e.g. the large proportion of smectite minerals in the clays, is responsible for the compression behaviour, and that a certain threshold value of smectite content triggers the behaviour discussed above.

3.1.4 Index relationships for Danish Palaeogene clays

The Danish Palaeogene clays are well-known for not following the empirical relations that exists between the index parameters, w_L, w_p and I_p and the compression index, C_C. As these relations are usually derived for soils with $I_p < 70$ % (Sørensen and Okkels 2015), the high plasticity indices may be to blame for the discrepancy. Several authors have analysed the validity of the many expressions presented in literature and have found reasonable correspondence between the shrinking index and compression index (Giasi et al. 2003; Sridharan and Nagaraj 2000), even for high plasticity clays ($w_L \leq$ 120 %). However, tests to determine shrinking index are rarely performed in Denmark.

As the pore fluid salinity affects the soil mechanical behaviour of the smectite minerals, the testing procedures may be to blame for the discrepancy between values calculated from empirical correlations and values found from laboratory testing. Many of the smectite-rich Danish Palaeogene clay are of marine origin and have saline pore fluids in the in situ conditions. When testing is performed using deionised water as proposed by DS/CEN ISO/TS 17892-12 (2004) the identified w_L does not reflect in situ conditions, as discussed in section 3.5, since the natural pore water is diluted. Thus, the state parameters used for establishing strength and stiffness correlations are not obtained correctly. The behaviour is caused by the interaction between the pore fluid and the smectite min-

erals diffuse double layers as discussed in section 2.5.

3.2 Intrinsic properties of clays

The compression curves for normally consolidated clays generally follow an unique line, when normalised using the void index as defined in equation (3.1) (Burland 1990). The Intrinsic Compression Line, ICL, is calculated using void ratios obtained from compression curves of reconstituted specimens, termed intrinsic properties. The intrinsic properties are marked by an asterisk, e.g. e^*_{100} for the intrinsic void ratio at $\sigma'_v = 100\,\mathrm{kPa}$. Burland (1990) recommended that reconstitution was performed at $w = 1.0\text{--}1.5w_L$, and in the present project, the main laboratory test specimens were reconstituted at $w = 1.5w_L$, as discussed in section 5.3.

$$I_v = \frac{e - e^*_{100}}{e^*_{100} - e^*_{1000}} = \frac{e - e^*_{100}}{C^*_C} \tag{3.1}$$
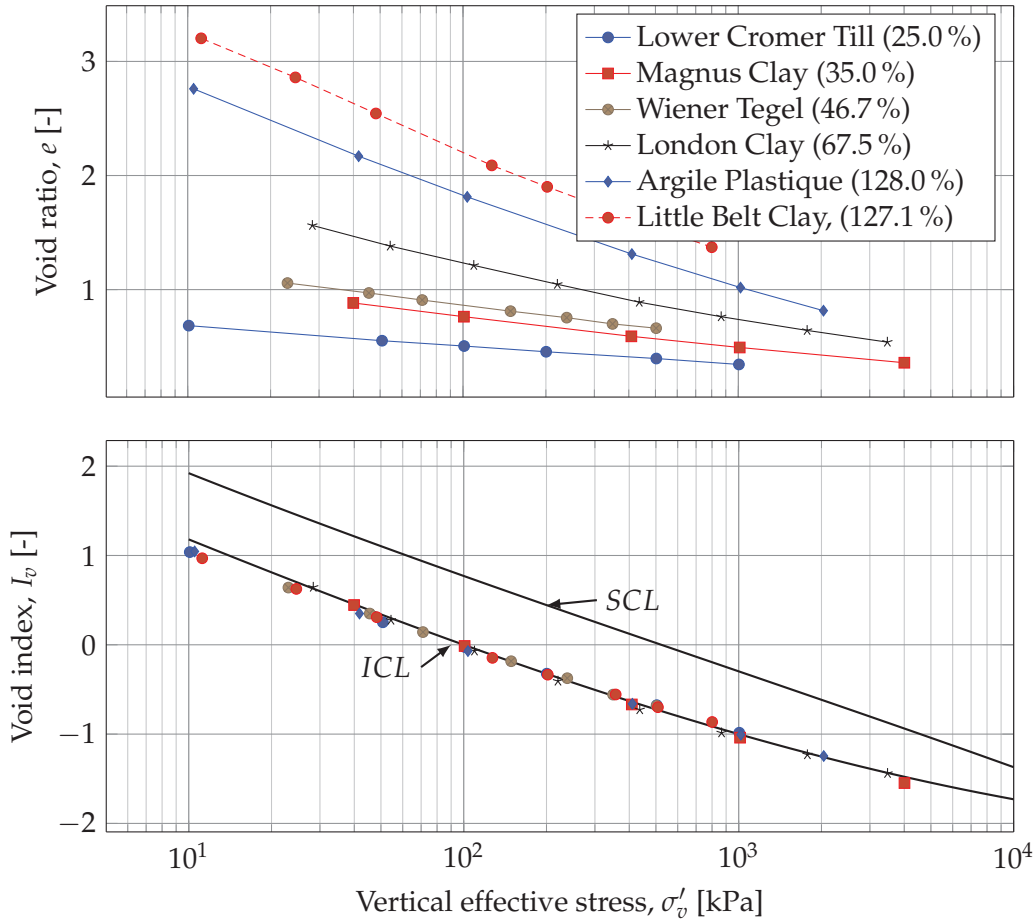
Figure 3.2: *Normalization of the compression curves obtained from a oedometer tests on six different reconstituted clays. Values in parenthesis denotes liquid limits of the specimens. The Intrinsic Compression Line ICL, and the Sedimentation Compression Line SCL are both presented along with normalised test data for the six clays. After (Burland 1990).*

Burland (1990) presented compression curves from literature obtained from tests on soils with a wide range of plasticity indices and showed the generality of the *ICL*, as indicated in figure 3.2. As may be noted from the figure the compression curves of the clays are different due to the different mineral composition of the tested clays. However, when the curves are normalised using equation (3.1) the curves lie within a fairly narrow band. The *ICL* fitted to the normalised virgin compression curves is presented in figure 3.2 and Burland (1990) derived the expression for the *ICL*, as presented in eq. (3.2).

$$I_v = 2.45 - 1.285 \log(\sigma'_v) + 0.015 \left(\log(\sigma'_v)\right)^3 \tag{3.2}$$

Both during sedimentation and post-sedimentation clays develop structure as discussed in section 3.3, which is why the *ICL* is rarely followed when intact, normally consolidated specimens are compressed. The effect of structure generally moves the compression line to the right in the stress-void index chart, i.e. for a given void ratio the yield stress increases due to structure, see figure 3.2, as the structure in sedimented specimens allows for higher void ratios compared to reconstituted specimens at a given stress. Burland (1990) presented the Sedimentation Compression Line, *SCL*, which most normally consolidated clays follow during compression due to the sedimentation structure. The sedimentation structure is influenced by the environment in which the clay is deposited, as discussed in section 3.3, which in turn affects the sensitivity, $S_t = \sigma'_{vy}/\sigma^*_{ey}$, of the clay. Burland (1990) developed the *SCL* based on soils with $S_t = 2$–9 which is why the *SCL*-curve presented in figure 3.2 may be considered valid for $S_t \approx 5$ as an average value (Cotecchia and Chandler 2000).

3.3 Influence of structure on deformation behaviour of clays

The structure in natural clays affects both strength and deformation behaviour (Coop et al. 1995). Overall effects of structure generally origins from two sources:

> Structure obtained during sedimentation, termed *sedimentation structure* (an effect of deposition environment and one-dimensional compression from deposition of overburden soils). During deposition of natural clays the specific conditions in the environment dictates the structure of the deposited clay. A specific salinity during sedimentation of marine clays causes a specific sedimentation structure due to flocculation of the individual clay minerals (Porrenga 1966).

> Structure obtained after sedimentation from e.g. unloading (increase in *OCR*), creep, folding and diagenesis, termed *post-sedimentation structure* (Cotecchia and Chandler 2000). Thus, the in situ structure of a clay is a product of mechanical and chemical history of the specific site.

3.3.1 Effect of structure in clays of low to moderate plasticity

The effects of structure on the compression behaviour are illustrated in figure 3.3. As seen from the figure, natural clays may show three types of behaviour during loading. The normally consolidated, sedimented clay follows the sedimentation compression line *SCL* during virgin compression (Burland 1990) as described in section 3.2. When the clay

is sampled (unloaded) and tested in the laboratory, the vertical yield stress is in concordance with the in situ stress for the intact specimen, Y_1 in figure 3.3 if the volume of the specimen remains constant during sampling and the specimens remain fully saturated (Cotecchia and Chandler 2000).
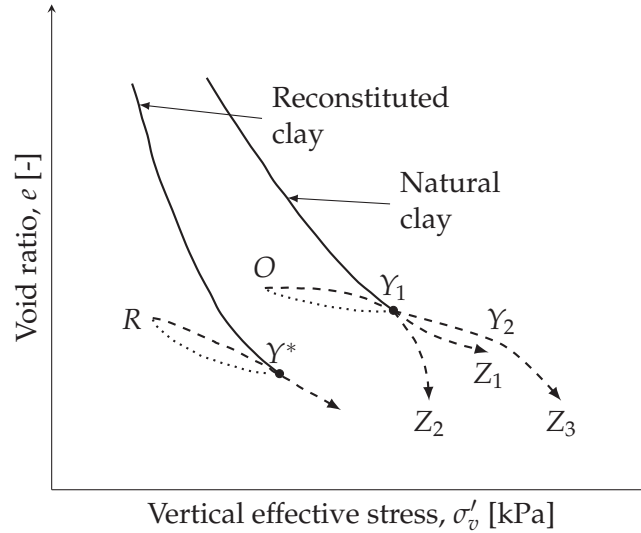
Figure 3.3: *Principle of compression curves for different natural and reconstituted clays of moderate plasticity. Reworked after Cotecchia and Chandler (2000).*

Upon further loading in the laboratory the compression curve may fall below the original virgin curve (Z_1 in figure 3.3) and follow the path Z_2 due to the higher strain rate in laboratory tests compared to geological processes or destructuring during compression. The same behaviour is to be expected for loading in engineering time scale e.g. when constructing a heavy building. If reloaded in situ on a geological time scale, the stress path Z_1 is followed, where the clay returns to the *SCL* with further compression (Cotecchia and Chandler 2000). Clays that develop a post-sedimentation structure e.g. due to diagenesis or creep reflect higher yield stresses (Y_2 in figure 3.3) and then follow a curve steeper than the *SCL* (Z_3 in figure 3.3) (Cotecchia and Chandler 2000).

Cotecchia and Chandler (2000) recommended a distinction to be made between preconsolidation stress and yield stress. The former is related to the actual stress sustained by the specimens during a previous loading and the latter to the mechanical behaviour of the clay during reloading. Thus, the *YSR* and *OCR* may be defined as the ratio between the yield stress and in situ stress (or minimum stress), and preconsolidation pressure and in situ stress, respectively:

$$YSR = \frac{\sigma'_{vy}}{\sigma'_{v0}} = \frac{\sigma'_{vy}}{\sigma'_{min}}, \quad OCR = \frac{\sigma'_{pc}}{\sigma'_{v0}} = \frac{\sigma'_{max}}{\sigma'_{min}} \tag{3.3}$$

The distinction proposed by Cotecchia and Chandler (2000) is rarely used in Danish geotechnical practice, where the term "preconsolidation pressure" (σ'_{pc}) is used for both geological preconsolidation stress and yield stress. E.g. Grønbech et al. (2015) denotes the yield stress (which she relates to the response of the system of fissures in the clay) "Lower σ'_{pc}" and the geological preconsolidation pressure "upper σ'_{pc}". However, the notation presented in eq. (3.3) is adopted in the present thesis.

3.3.2 Effect of structure in clays of high plasticity

Generally, only the case of $YSR \geq OCR$ is considered in literature as structure originated from diagenesis or creep typically increases the yield stress compared to the geological preconsolidation pressure for clays of low plasticity. However, the opposite behaviour is observed for Danish Palaeogene clays where the yield stress is often lower than the geological stress (Femern 2014a; Mortensen 2012; Krogsbøll et al. 2012), as described in section 3.1.2.

The Palaeogene, highly plastic London clay have been tested intensively, (Hight et al. 2003; Hight et al. 2007; Gasparre et al. 2007b; Gasparre et al. 2007a). London clay is structured with fissures, joints, bedding surfaces and shear surfaces (Hight et al. 2003), which may have been created by a large overburden of clay combined with small tectonic events followed by erosion of the overburden (Hight et al. 2007). Generally, the natural London clay shows some variability between the different units, however within a unit, e.g. the unit B2(c), the clay exhibits fairly constant compression behaviour, see figure 3.4 (Gasparre et al. 2007a). As may be noted from figure 3.4 the onset of yielding is not well-defined on the compression curves, as no clear onset of clay structure breakdown (distinct bend in the compression curve) can be identified on the curve (also reported by Hight et al. (2007)). The compression curves are generally located above the *ICL* which must be attributed to structure. Moreover, it may be seen from the figure that convergence between the intact specimens and the *ICL* is not achieved, which could be expected for complete destructuring at very high stresses (Burland 1990; Gasparre et al. 2007a). The fabric of the natural specimens thus seem to create a stable structure, which requires intense remoulding or very large strains to remove.
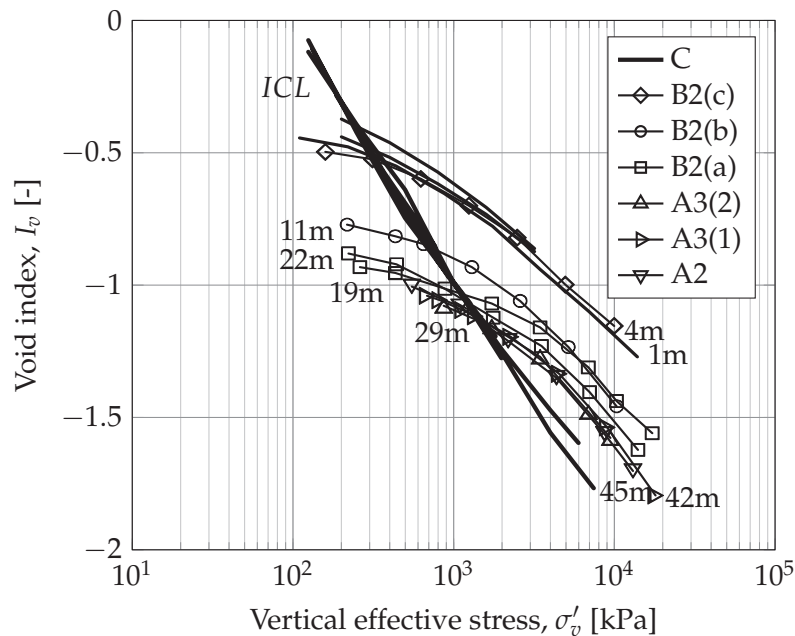
Figure 3.4: *Oedometer compression curves from intact, natural London clay compared with the intrinsic behaviour. The numbers presented near the curves denotes sample depth of the individual specimen. After (Gasparre et al. 2007a).*

The effects of structure on the soil mechanical behaviour in shearing and compression for natural London clay have been studied in detail at Imperial College, London (Gasparre et al. 2007b; Gasparre et al. 2007a; Hight et al. 2007; Gasparre 2005) and University College, London (Sørensen et al. 2007). During the tests a large effect of particular the post-sedimentation structure was found. Generally, the structure in the London clay causes a stiffer and stronger behaviour and thus a smaller swelling index. It was found that the structure may be damaged or destroyed by excessive swelling, which yields an increase in compressibility during following compression.

Gasparre et al. (2007a) investigated whether the effects of structure could be removed from a natural specimen by evaluating swelling sensitivity of specimens after loading to very high stress (8000 kPa to 18 000 kPa) and comparing the data with results obtained on specimens tested from in situ stress range. The specimens that were loaded to high stresses generally showed lower swelling sensitivity ($S_S = C_S^*/C_S$) compared to specimens tested from in situ stresses and were thus, to at least some extent, destructured. However, Gasparre et al. (2007a) concluded that even the very high load applied prior to testing was insufficient to completely erase structural effects in the specimens. This fact, combined with the lack of convergence with the *ICL* at very high stresses for the tested oedometer specimens, lead Gasparre et al. (2007a) to conclude that the structure of the natural London Clay primarily are on the micro-scale, originating from the inter-particle arrangements (fabric) rather than chemical bonding between particles (cementing or diagenesis).

3.3.3 Effects of structure in Danish Palaeogene clays

As the Danish Palaeogene clays are generally highly overconsolidated, a degree of destructuring during unloading to in situ stress might be expected for these clays which may – at least partly – influence the yield pressures identified during testing. However, only limited studies are available on Danish Palaeogene clays. The effects of structure of Danish Palaeogene clays were previously studied by Krogsbøll et al. (2012), who performed a test on Little Belt clay. During the test, the effects of destruction by swelling were studied and it was found that the swelling index, C_S, increased with increasing unloading of the Little Belt clay, even as complete destruction of the structure was probably not achieved. However, the effects of structure was not estimated by testing of a reconstituted clay sample.

3.3.4 Effects of fissures

Natural Palaeogene clays are often fissured. Cotecchia et al. (2011) showed – based on test on a naturally occurring Italian bentonite – that the compression curves of fissured high plasticity clays plot to the left of the *ICL* and only at very high pressures does the compression curves converge with the *ICL*. Based on a characterisation chart for fissured clays, developed by Vitone and Cotecchia (2011), clays with different intensity of fissuring were tested, all showing the above tendency, see figure 3.5. As may be observed from the figure, the yield points (denoted by an "Y" and an arrow) for the intact specimens are located below the *ICL* (dashed lines), which may be attributed to the fissures in the clays, yielding a softer response than the remoulded clay specimens.
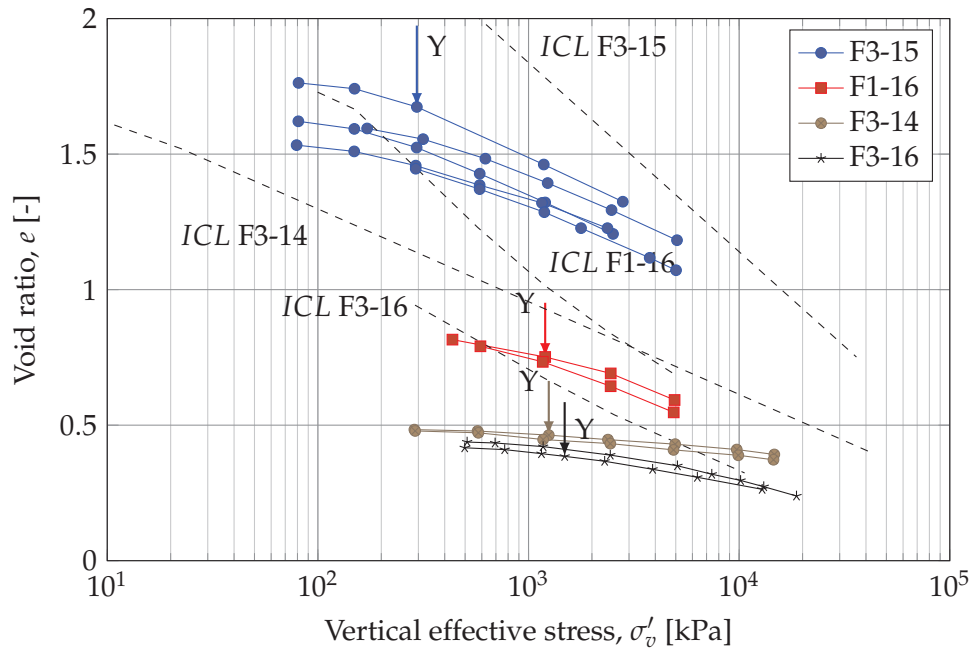
Figure 3.5: *Compression curves for fissured clay specimens with relevant ICL for each clay type. The compression curves are obtained from IL oedometer testing on four clays of very high plasticity. ICL-lines are obtained from testing of reconstituted clay material. After Cotecchia et al. (2011).*

As all the Danish Palaeogene deposits may assumed to be fissured, the conclusions stated above may help explain the low yield stresses observed from tests on natural, intact Palaeogene clays observed by Femern (2014a) for Røsnæs clay, by Krogsbøll et al. (2012) for Little Belt clay and by Mortensen (2012) for clays from a range of Danish sites. Thus, opening of fissures during unloading and closing of fissures during reloading may be assumed to influence the mechanical response, and affect the stiffness and vertical yield stress identified from oedometer tests. It is interesting that the London clay, illustrated in figure 3.4 only to a limited degree show the shift in σ'_{vy} as these clays are also fissured. The smaller influence of the fissures may be caused the by the lower plasticity compared to Danish Palaeogene clays and the Italian specimens presented in figure 3.5.

3.3.5 Effects of swelling

As briefly introduced above, Gasparre et al. (2007a) found that oedometer specimens of London clay swelled to low pressures showed a significant increase in C_S. C_S for the specimens of higher plasticity were found to increase more than less plastic specimens. Krogsbøll et al. (2012) conducted a similar study on a single specimen of Little Belt clay, which was allowed to swell to three different values of σ'_{min}. Hereafter, recompression of the specimen was carried out. Krogsbøll et al. (2012) showed that the yield stress dropped and the compression and swelling index increased with decreasing σ'_{min}-value as an effect of the structural changes. This seems to reflect the de-bonding in the specimen during unloading. Krogsbøll et al. (2012) suggested that for large unloading stresses, the
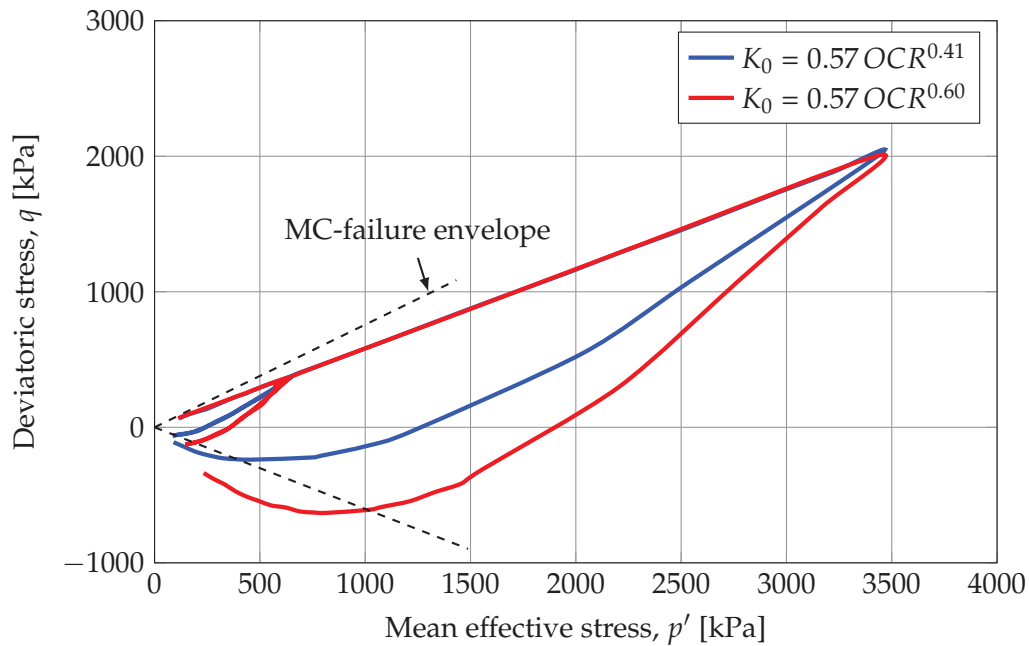
Figure 3.6: *Estimated stress paths for a Little Belt clay specimens based on best fit K_0-relation for folded Røsnæs clay (red) and for destructured clay (blue). After (Krogsbøll et al. 2012).*

K_0 value may reach the coefficient of passive earth pressure, K_p and the soil may be in a state of failure inside the oedometer cell. This is illustrated in the stress paths calculated by Krogsbøll et al. (2012) for the Little Belt clay specimen, tested in the oedometer cell, as presented in figure 3.6.

As the coefficient of passive earth pressure increases with increasing effective strength parameters (Hansen 1953) and effective strength parameters reduce with increasing plasticity, high plasticity specimens tend to have low K_p-values and will hence fail for lower *OCR*-values compared to specimens of low plasticity. The phenomenon illustrated in figure 3.6 may therefore illustrate unloading behaviour for many soils of high plasticity, which may fail during unloading due to low effective strength parameters. This may explain the loss of structure in the specimens when unloaded, and is consistent with the observation, that the large content of smectite minerals in Palaeogene clays may be responsible for the observed loss of stress memory (Mortensen 2012).

Based on the sections above, the observation that $YSR < OCR$ for the Danish Palaeogene clays may be explained by the mineralogical composition of the natural clay. The high smectite content of the natural clays enables the clay to absorb water during unloading and hence to swell significantly. During the swelling process, the internal structure of the clay is (partly) erased, as the distance between clay platelets increase. The higher void ratio and lower degree of internal structure in the specimens is reflected in a low σ'_{vy} compared to the magnitude of the former load sustained by the clay. This effect must be primarily associated with the large smectite content of the Palaeogene clays, as the volume change is directly linked to the adsorption of water, which in turn is a function of the smectite content. In this regard the fissured structure of the clays increases the permeability, but may not alone explain the loss of stress memory during unloading.

3.4 Influence of clay mineralogy on consistency and deformation behaviour

White (1949) carried out a comprehensive study using pure clay minerals to investigate the consistency limits. The testing was carried out with the aim to understand the effect of each mineral on the properties of natural soils containing a mixture of minerals. Later the effect of mixing the clay minerals in different ratios was investigated by Seed et al. (1964), who used kaolinite, illite and bentonite minerals mixed with sand to investigate the effects of varying clay mineral content and type on the Atterberg limits. The results from mixtures without sand showed that the liquid limit of kaolin-bentonite mixtures is essentially a linear function of the bentonite content, whereas the illite seems to suppress and delay the effect of the bentonite in a illite-bentonite mixtures, causing a non-linear relation as illustrated in figure 3.7. The suppression have been explained by inter-particle growth and following reduction of activity of the smectite minerals (Sivapullaiah and Savitha 1999).
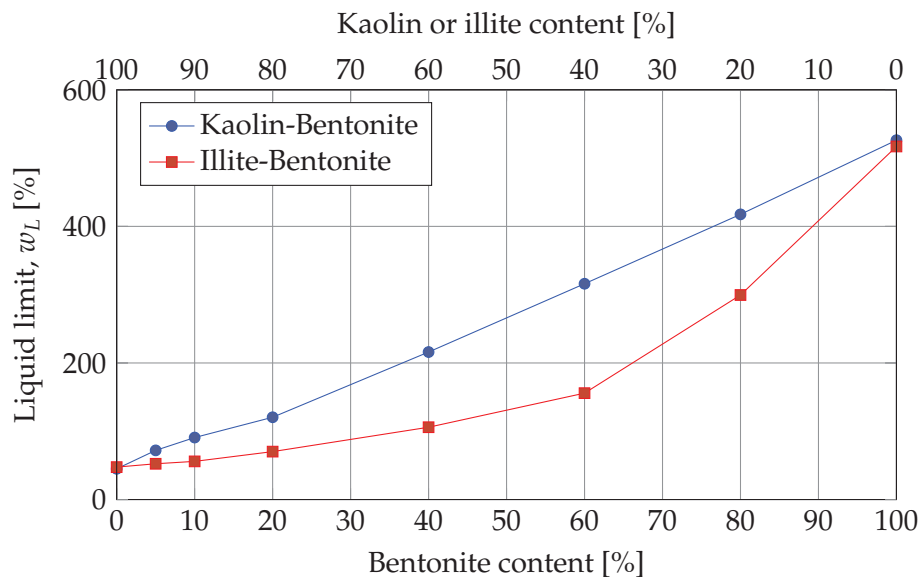
Figure 3.7: *Liquid limits obtained from testing of kaolin-bentonite and illite-bentonite mixtures. After (Seed et al. 1964; Mitchell and Soga 2005). The illite minerals suppress the influence of the smectite minerals in the bentonite, yielding lower w_L-values compared to the kaolin-bentonite mixtures.*

The effect on soil compressibility from the mineralogical composition of soils has been investigated by e.g. Fan et al. (2014), Tiwari and Ajmera (2011), and Spagnoli and Sridharan (2012) for artificial soils containing bentonite mixed with kaolinite. An increase with increasing smectite content is also observed for the compression index (Tiwari and Ajmera 2011) as for the liquid limit (Spagnoli and Sridharan 2012). Thus, comparing the liquid limit and the compression index, an approximately linear relationship has been identified, as may also been inferred from figure 3.8. It should be noted that the relationship proposed by Terzaghi et al. (1996), which is also sketched in figure 3.8, is valid for $w_L \leq 100\%$, where the best fit of that relation to the available data is also observed from the figure.
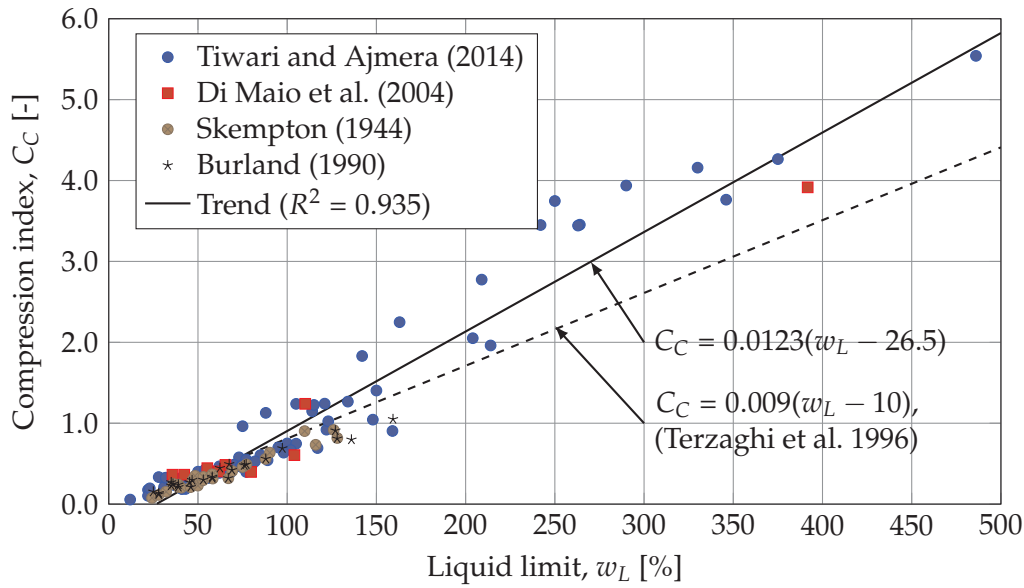
Figure 3.8: Correlation between compression index and liquid limit based on data from literature. The linear trend line (full drawn line) is derived as an overall trend of the soils from all presented literature.

3.5 Effects of pore water chemistry on consistency limits and deformation behaviour

The effect of pore fluid salinity on the consistency limits and the deformation behaviour has been investigated in a number studies for artificial clays, (Tiwari and Ajmera 2014; Yukselen-Aksoy et al. 2008; Cavello et al. 2005) and for natural clays (Grønbech et al. 2010; Di Maio 1996). Generally, a profound effect of the pore fluid salinity is observed for clays with a high clay fraction and where the clay fraction contains a large amount of smectite minerals (Di Maio 1996; Schmitz et al. 2004). A reduction in both w_L and C_C with increasing pore fluid salinity are observed for high plasticity clays, whereas clays of low plasticity (primarily dominated by illite and kaolinite minerals) are relatively insensitive towards pore fluid salinity changes (Tiwari and Ajmera 2014; Yukselen-Aksoy et al. 2008). As an illustration of the effect of pore fluid salinity, the C_C for artificial specimens tested with deionised water ($C_{C,dw}$) and a saline 2.9 % NaCl-solution ($C_{C,s}$) is compared in figure 3.9. As may be observed from the figure the smectite-rich specimens are highly sensitive towards pore fluid salinity, as C_C in the most extreme case drops by a factor of 5.5.

A similar influence of pore fluid salinity is expected for natural clays where the smectite minerals constitute a significant part of the clay mineral content as discussed in section 3.1.4. The results from a number of studies are summarised in figure 3.10, (Di Maio 1996; Di Maio et al. 2004; Grønbech et al. 2010; Geertsema and Torrance 2005). The figure illustrates the decrease of the liquid limit when obtained using pore fluid with increasing salinity, based on a range of tests performed on natural clays. As illustrated in the figure, the liquid limits of high-plasticity clays are very sensitive towards changes in pore fluid salinity. As the natural clays are typically not washed with deionised
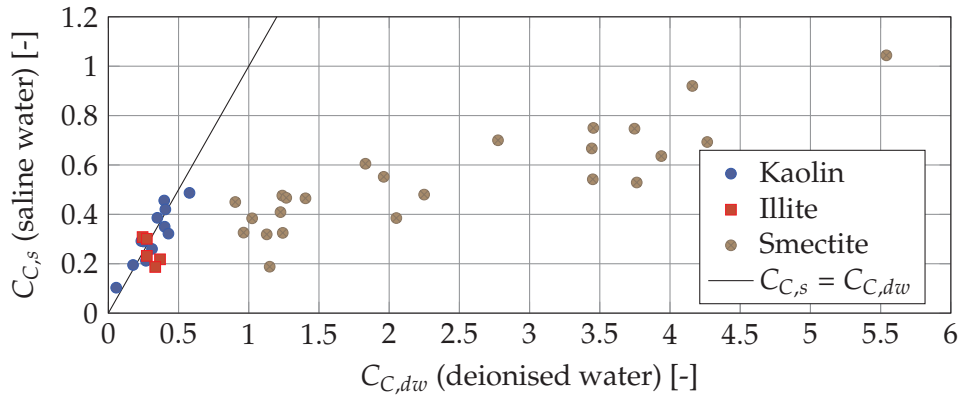
Figure 3.9: *Comparison of compression index for testing of mixtures of different clay minerals with saline (2.9 % NaCl-solution) and deionised water. The dominating clay mineral in each mixture is presented in the legend. After (Tiwari and Ajmera 2014).*

water prior to liquid limit test, the liquid limit at 0 % salinity in figure 3.10 represent a slightly higher, but unknown, salinity. Thus, when performing index testing or advanced laboratory testing, proper attention must be paid to the pore fluid salinity to achieve parameters reflecting the in situ conditions for the clay. As the relationship between w_L and C_C is linear (see figure 3.8), a similar effect of pore fluid salinity on the compression index as found for w_L may be expected for the natural clays.

When testing clays of low plasticity, and in particular clays where illite constitute a significant part of the clay minerals, an increase in the liquid limit is observed with an increase in pore fluid salinity (exemplified by Mink Creek clay in figure 3.10), which may be explained by the increased flocculation of the illite minerals due to the higher pore fluid salinity (Geertsema and Torrance 2005).
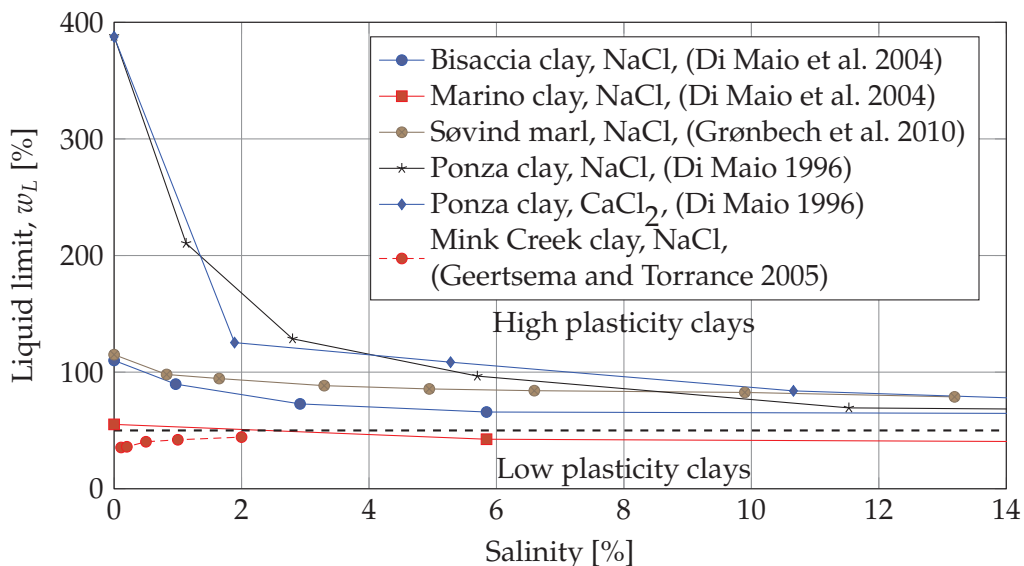
Figure 3.10: *Effect of pore fluid salinity on the liquid limit of a range of natural soils. For each of the soils, the cation of the applied pore fluid is presented.*

3.6 Modelling of clay behaviour

Modelling of clay behaviour is an essential part of geotechnical engineering, be it by simple rules of thumb or by advanced computer models. Historically, consolidation problems have been modelled based on compression curves from oedometer tests, which often are assumed to be linear when strain or void ratio is plotted against $\log(\sigma'_v)$ (Casagrande 1938; Terzaghi et al. 1996). A similar procedure is the core principle for the critical state soil mechanics framework, as used for e.g. the Cam Clay model (Roscoe et al. 1958; Schofield and Wroth 1968). The compression behaviour obtained using the Cam Clay model is illustrated in figure 3.11. As may be observed from the figure, straight lines are applied for virgin compression, unloading and reloading, and the transition between normally consolidated and overconsolidated state is sharp and very well-defined.
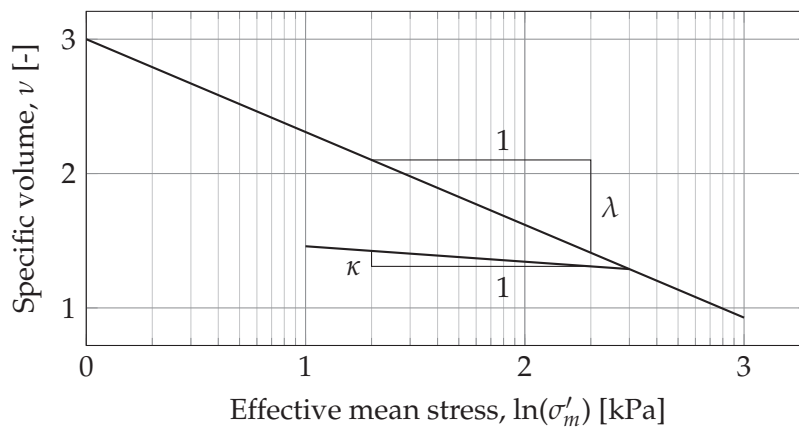
Figure 3.11: *Compression framework for the Cam Clay model. After (Roscoe et al. 1958; Schofield and Wroth 1968). Note that $\ln(x)/\log(x)$ is a constant, which is why the compression curve will move, but remain straight if plotted against $\log(\sigma'_v)$.*

As may be noted when comparing the behaviour of the Cam Clay model with the Danish Palaeogene clay, cf. figures 3.1 and 3.11, the application of straight lines in $\log(\sigma'_v)$ (or $\ln(\sigma'_v)$) is not reasonable for the Palaeogene clay. Both the normally and overconsolidated regions for the natural Danish Palaeogene clays are characterised by curved compression curves, and no clear transition between NC and OC behaviour can be identified. Applications of models relying on straight lines in $\log(\sigma'_v)$, i.e. constant values of C_C and C_S, thus require great care when selecting the input parameters, as they must be selected for the stress intervals relevant for the problem at hand.

3.6.1 Modelling of Palaeogene clays

Femern (2014e) noted that during swelling, the compression curves for the Danish Palaeogene clays, eventually became linear (as may be observed from figure 3.1), and presented a framework for the tangent stiffness during unloading from in situ stress, σ'_{v0}, as the piece-wise function presented in eq. (3.4). The notation has been changed to fit the nomenclature of the present thesis.

$$E_{oed} = \begin{cases} \sigma'_v \dfrac{\ln(10)}{C_{S\varepsilon}} & \text{for } \sigma'_v \leq R\,\sigma'_{\max} \\ A\,\sigma'^{2}_v - B\,\sigma'_v + C & \text{for } R\,\sigma'_{\max} > \sigma'_v > \sigma'_{\max} \end{cases} \tag{3.4}$$

The parameters A, B and C in eq. (3.4) are derived based on the values of R, σ'_{v0} and $C_{S\varepsilon}$ and the parameter $R = 0.95$ was found to yield reasonable results for in situ behaviour (Femern 2014e). The model consists of two parts, below $R\,\sigma'_{\max}$ a linear response is modelled in $(\log(\sigma'_v); \varepsilon_v)$-space whereas the initial part of an unloading (from $\sigma'_{\max}$ to $R\,\sigma'_{\max}$) is modelled using a second degree polynomial. Eq. (3.4) captures the very high initial stiffness during unloading due to the curved swelling curves, and the gradual decrease of E_{oed} to a constant value with sufficient unloading is expressed with the polynomial. For long unloading stress paths the swelling curve grows linear in $\log(\sigma'_v)$-space. It should be noted that the model proposed by Femern (2014e) (eq. (3.4)) is valid only for unloading.

For reloading, based on a stress increase of 200 kPa at foundation of 5 m depth on folded Røsnæs Clay, a relationship between $E_{oed,sec}$ and the q_{net} from CPTu-testing was proposed by Femern (2014e). The relationship is presented in eq. (3.5).

$$E_{oed,sec} = \beta q_{net} \tag{3.5}$$

The model presented in eq. (3.5) was derived by linking values of $E_{oed,sec}$ from IL oedometer tests to the q_{net} values, and fitting the parameter β. A load spread of 1:2 (horisontal:vertical) was used for estimating the required stress for oedometer specimens. Thus, the model enables stiffness assessments based on the CPTu-data, which allows for very detailed stiffness information over depth of a Røsnæs clay deposit.

Hansen and Mise (1964) presented an empirical model for Little Belt clay, which was developed based on oedometer tests performed prior to the construction of the New Little Belt Bridge in the 1960ies. The model successfully captures the non-linearity and hysteresis of the unloading and reloading paths by relying on parabolas in $\log(\sigma'_v)$-space. However, Hansen and Mise (1964) chose to model the geological load history of the natural specimens in the oedometer tests used for deriving the model, and compressed the specimens to 3000–6000 kPa, prior to performing the unloading and reloading loops on which the model was based. Further presentation of the model is given in chapter 7.

As computers have increased in calculation power over the last decades, Finite Element Modelling (FEM) has grown increasingly popular. FEM allows analysis of complex geometries, complex soil models and advanced stress paths to be carried out fairly accurately and fairly quickly. However, FEM-analyses rely heavily on realistic models, which will capture the essentials of the modelled material, and on realistic input-values in these models. The BRICK-model was developed specifically to reproduce the behaviour of the highly plastic London clay, and was proposed by Simpson (1992). The model relies on a kinematic yield surface and has been applied by Femern (2014e) to reproduce the compression curves obtained on natural Danish Røsnæs clay and successfully modelled the curved compression curves obtained from laboratory testing. The analyses presented by Femern (2014e) showed reasonable correspondence between measured and calculated heave, and pore pressure response from unloading, when FEM-analyses are compared with in situ measurements from full-scale testing.

Results from FEM-analyses are no better than the input parameters applied. As the soil models increase in complexity, the number of input parameters also increases. Thus, to provide all needed input parameters for very complex soil models, a range of tests must be applied for proper assessment, which is expensive. If tests are not available e.g. due a small budget on a minor construction project, the input parameters must be estimated based on experience. Thus, the overall model behaviour must be evaluated to assess whether reasonable results are obtained from the FEM-analysis. In this regard, simple models, which may be used to assess the general trend of the outcomes of advanced analyses, are highly valuable.

3.7 Main findings of published literature

The present section briefly sums up the literature study presented in the previous sections to provide the basis for the presentation of the research aims of the present PhD-project in the following section 3.8.

The mechanical response of clays depends heavily on the mineralogical composition, and particular on the content of smectite minerals. Multiple studies show that the liquid limit and compression index are strongly depended on the smectite content for reconstituted specimens. For natural specimens, the smectite content also significantly affects the deformation characteristics, as compressibility generally increases with increasing smectite content. However, effects of structure obtained both during sedimentation and physical and chemical changes after sedimentation, may scatter the picture. Thus, in the works published for the Femern project, a constant $C_{S\varepsilon} \approx 5.1\%$ was found, regardless of specimen plasticity, provided the specimens were unloaded sufficiently. This observation does not imply a link between the smectite content and the deformation behaviour. The large initial stiffness on the unloading and reloading curves observed from testing of natural intact clays have been related to friction between specimen and oedometer ring along with reversal of flow gradients and rotation of principal stresses.

The smectite minerals are highly sensitive towards pore fluid salinity due to the huge specific surface area and a large cation exchange capacity. An increase in pore fluid salinity reduces the settlement potential for high plasticity specimens, which may be modelled using the diffuse double layer theory. As the concentration or valence of the cations in the pore fluid increases, the repulsion between clay platelets reduces, i.e. the diffuse double layer grows thinner, which causes a lower void ratio and a stiffer and stronger response.

Tests from literature on high plasticity clays repeatedly show that the unloading and reloading branches are curved when plotted in $\log(\sigma'_v)$-space. However, the common soil models, e.g. the Cam Clay model, does not allow this feature to be modelled, as these model rely on linear virgin and unloading-reloading curves. A model proposed by Femern (2014e) successfully models the curved unloading paths and the works by Hansen and Mise (1964) show reasonable performance for unloading and reloading paths. Advanced modelling, e.g. FEM-analyses using the BRICK-model proposed by Simpson (1992) allow arbitrary stress paths to be modelled - from recently sedimented clay slurries to highly overconsolidated clays. However, acceptable performance of FEM-model hinges on proper choice of input-parameters, which requires a number of

advanced tests. A relatively simple model to assess the compression behaviour of high plasticity specimens for both virgin loading and unloading-reloading loops has not been identified from the current literature study.

In a range of the published tests on Palaeogene clay discussed in the previous sections, the vertical yield stress, σ'_{vy}, is not in concordance with the previously sustained maximal stress, σ'_{max}, from the same oedometer test. In Danish publications this behaviour of the Palaeogene clay is termed "loss of stress memory". This effect has been attributed to the internal structure of the high plasticity clays, e.g. slickensides and fissures, which influences the deformation behaviour (Cotecchia and Chandler 2000). It has also been proposed that the specimens may be destructured by excessive swelling during unloading (Gasparre and Coop 2008; Krogsbøll et al. 2012), which cause a softening and hence a lower σ'_{vy}.

3.8   Research aims for the present PhD-project

The main focus for the present project is the influence of smectite content on the 1D compression behaviour of clays, documented through incrementally loaded, oedometer testing of artificial, reconstituted specimens. Thus, the test results are related to the intrinsic state of the mixtures and comparison with natural clays may only be carried out if the effects of structure in the natural clay specimens are accounted for. Based on tests of artificial mixtures reflecting a range of plasticities, an empirical model will be proposed, which will cover virgin loading, along with unloading and reloading loops. As the proposed model is based on oedometer tests, it will be valid for conditions similar to the conditions in the oedometer ring. This in turn means that response of the clay specimens for very small strains, as obtained from dynamic testing, will not be covered in the present work.

In the present project testing have been carried out on artificial mixtures of clay minerals (primarily smectite and kaolinite), mixed with tap water. In order to relate the behaviour documented in the tests to in situ behaviour of Danish Palaeogene clay, the effects of pore fluid salinity must be accounted for. As the Danish Palaeogene clays are of marine origin (see section 2.6), the in situ pore fluid will affect the behaviour of the natural clay as the diffuse double layer of the smectite mineral is affected (see also section 2.5).

The overall research aim may be summarized in the following questions:

> How does the content of smectite affect the deformation behaviour of reconstituted specimens?

> How can the unloading and reloading behaviour during IL oedometer testing for high plasticity clays (special focus on shape of curves and the onset of vertical yield) be modelled?

The main research questions presented above are supported by a number of substudies, which have been undertaken as a part of the present PhD-project. These substudies comprise:

> Analysis of the effect of the pore fluid salinity on Atterberg limits and deformation parameters for artificial, high plasticity clays.

> Analysis of the effect of frictional stress loss between clay specimen and oedometer ring, and the influence on the stress memory and the high initial stiffness of high plasticity clays.

> Analysis of the correspondence between previous maximal loading and the vertical yield stress identified during reloading ("loss stress memory").

As the time frame for the present work was finite, a number of studies were not undertaken as a part of the PhD. A brief introduction to some of the major studies not undertaken are presented below.

> Analysis of strength behaviour of high plasticity clays, and correlations with smectite content, pore fluid salinity and stress history.

> Analysis of deformation behaviour of natural clays by performing IL oedometer or CRS tests on natural, intact and/or reconstituted, high plasticity clay specimens to investigate effects of inherent structure, smectite content and specimen plasticity.

> Detailed analysis of the factors affecting the secondary consolidation processes in the high plasticity clays.

> Dynamic testing to assess soil properties (both related to strength and stiffness) for very small strains relevant for dynamic loading conditions.

Materials applied for testing

In the present chapter, the materials used within the present PhD-project are presented. The majority of tests presented within this PhD-dissertation were performed on artificial, reconstituted and preconsolidated specimens. The clay samples were mixed from clay powder and water to form slurries which were preconsolidated prior to trimming and oedometer testing. The present chapter will present the ion content of the water used for slurry mixing along with basic parameters of the used clay powders. Results from index testing, grain size distribution and results from XRD-tests are briefly presented to provide the basic properties of the tested specimens. The methods used for performing the oedometer tests in the project are presented in chapter 5. The application of the materials presented in the current chapter allow accurate knowledge of mineralogical composition and load history to be obtained for the tested specimens.

4.1 Pore water used for testing

The current section presents the different types of water applied during testing, with specific focus on the content of dissolved ions. The dissolved ions in the pore fluids particularly influence the deformation behaviour of the specimens of high plasticity, as discussed in section 3.5.

4.1.1 Tap water

The tests presented in the current PhD-thesis were conducted at Navitas, located at the harbour in Aarhus. A substantial part of the tested slurries were prepared, and later tested in the oedometer apparatus, with tap water as pore fluid. This procedure was selected as it was estimated that the tap water bears close resemblance with natural precipitation, which is why the tests carried out using tap water as pore fluid are assumed to model Danish on-shore conditions.

The laboratory at Navitas is supplied with tap water from the water service company Aarhus Vand. The tap water is pumped from the groundwater magazines near the plant in Beder, south of Aarhus, which is why the composition of dissolved ions in the water is defined by the geology surrounding the groundwater magazine. Aarhus Vand performs an annual evaluation of the quality of the tap water, where the content of dissolved ions and organic compounds along with micro-bacteriological activity are measured. The

composition of dissolved ions is of special interest in the present project. The content of the most common ions is presented in table 4.1, based on ground water quality tests performed by Aarhus Vand A/S (2015, 2017a, 2017b).

Table 4.1: *Contents of dissolved ions in the tap water supply at Navitas, Aarhus. After (Aarhus Vand A/S 2015, 2017a, 2017b).*

	Content [mg/l]			
Ion	2014	2015	2016	2017
Na^+	25	26	23	28
K^+	3.1	3.3	3.3	3.1
Ca^{++}	93	96	91	100
Mg^{++}	11	11	11	11
NH_3, NH_4^+	0.041	0.039	0.006	0.023
F^-	0.26	0.27	0.28	0.29
Cl^-	29	29	27	31
S^{--}	0.02	0.02	0.02	0.02
NO_3^-	0.98	0.94	1.1	0.89
NO_2^-	0.005	0.005	0.001	0.001
HCO_3^-	332	330	316	340
SO_4^{--}	45	48	40	44

Comparing the content of dissolved ions in the tap water with the ion composition of the artificial saline water PC02 (used for testing of Palaeogene clays for the tests carried out for the Femern Fixed Link project, introduced in section 4.1.2), it is seen that in general the same ions are present, but in much smaller concentration in the tap water. Thus, the behaviour documented with the tests performed within the present project using tap water may not be applied to clays in marine conditions, without making proper allowance for the influence of the pore fluid salinity, as previously stressed.

4.1.2 Femern artificial pore water PC02

To allow for reproduction of the marine conditions, where the natural specimens tested in the Femern Fixed Link project were sampled, an analysis of the pore water of the natural clay was conducted (Femern 2014c). Based on the results of this analysis, an artificial pore fluid was developed, based on the measured content of dissolved salts in the pore water of the natural specimens (Femern 2011b). The artificial pore water was named PC02 and is assumed to be representative for in situ pore water conditions for the natural soils tested within the present PhD-project (i.e. Little Belt clay specimens). The ion content in the PC02 pore water is presented in table 4.2a. The PC02 pore water applied in the present project was mixed using deionised water and four commercially available salts, NaCl, $MgCl_2$, $CaCl_2$ and K_2SO_4, following the recipe presented in table 4.2b.

Table 4.2: *Contents of dissolved cations in the PC02 artificial pore water, after (Femern 2011b) and the recipe for mixing the PC02 pore fluid after (Laier 2010). Product # refers to the Sigma Aldrich product numbers.*

(a) Ion content			*(b)* Recipe		
Ion	Content [mg/l]		Salt	Product #	Content [g/l]
Na^+	8030		NaCl	71380-1KG	13.24
K^+	82		$MgCl_2 \cdot 6\,H_2O$	M2670-500G	1.97
Ca^{++}	405		$CaCl_2 \cdot 2\,H_2O$	12022-1KG	1.49
Mg^{++}	235		K_2SO_4	31270-1KG	0.99

4.2 Soils used for testing

The majority of the tests performed within the present project are conducted on artificial specimens, mixed from clay powders and tap water to form slurries. As the constituents of the specimens are two clay powders (kaolin and bentonite), the following section focus on presenting their characteristics.

4.2.1 Naming conventions for slurries, specimens and tests

Throughout the present project, the recipes of tested specimens are named after the convention KXXBYY, where "XX" denotes the percentage of kaolin powder and "YY" the percentage of bentonite powder – determined based on dry mass. Thus, a K40B60-specimen contains 40 % kaolin and 60 % bentonite powder.

After mixing, all slurries were named after the pattern SZZZ, where "ZZZ" is a running number starting at 001 for the first slurry. After preconsolidation, the slurries were trimmed to oedometer specimens, named after the convention OEiiiSZZZ, where "iii" is a consecutive number starting from 001 for the first oedometer test performed. The term SZZZ denotes the name of the slurry the oedometer specimen was trimmed from.

4.2.2 Artificial clays

A significant number of tests were carried out using mixtures of kaolin and bentonite powders. In all artificial mixtures Kaolin 50 and bentonite clay powders were used, which were supplied by Cerama (Kaolin product No. 1450, Bentonite product No. 1410 (Cerama 2017)). The kaolin powder was produced by Sibelco, however it was not possible to obtain information on the origin of the source clay. It was stated by Cerama that the bentonite powder was a Yellowstone bentonite from Wyoming. However, further indication on the producer and the geological origin of the source clay was not attainable.

Grain size analysis for artificial mixtures

Five mixtures of kaolin and bentonite were mixed and a grain size analyses were performed using hydrometer testing. The hydrometer analyses were performed by COWI A/S, Aalborg, Denmark. The obtained grain size distributions are presented in figure

4.1. More details on the test procedures and a comparison of the obtained results with results from laser diffraction analyses are presented in the laboratory report, chapter 4.
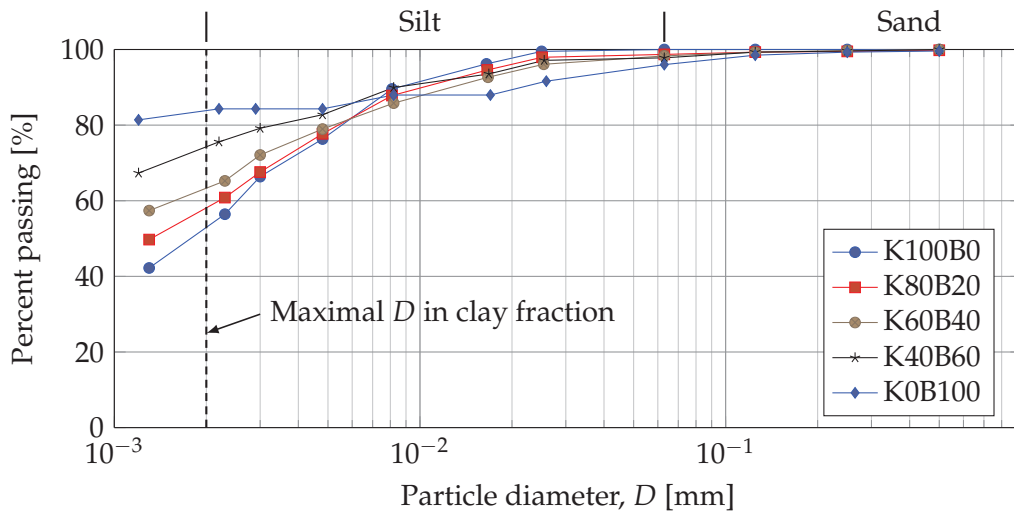
Figure 4.1: Hydrometer analyses of five mixtures from pure kaolin to pure bentonite. The tests were carried out by COWI A/S.

Consistency limits of artificial mixtures

The consistency limits were tested for a range of different mixtures of the kaolin and bentonite used in the present work. The Atterberg limits were determined according to the procedures presented in the laboratory report, chapter 5. A total of 11 different mixtures of kaolin and bentonite were tested, spanning the range from pure kaolin to pure bentonite. Results from the tests are presented in the Casagrande chart in figure 4.2. It should be noted that the chart has been extended far beyond its usual boundaries. As
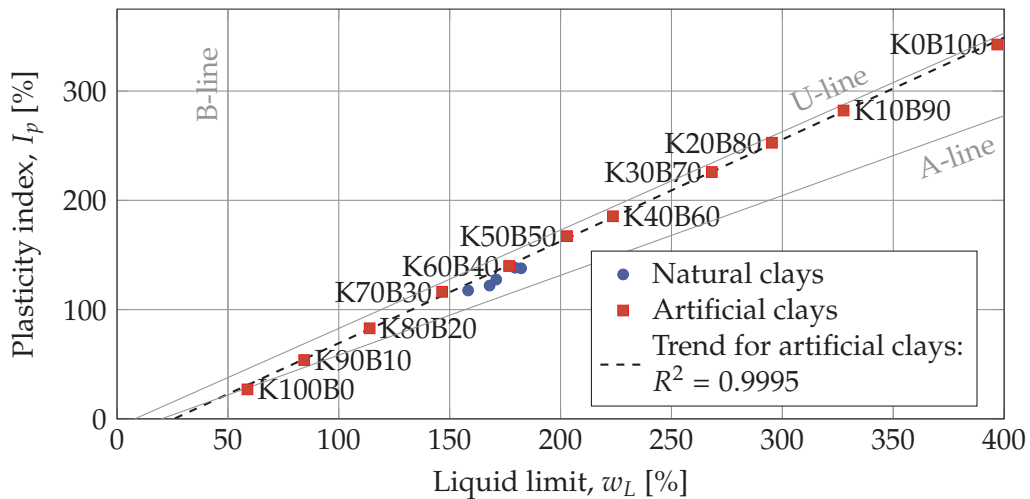
Figure 4.2: Plasticity chart of Casagrande with results plotted from artificial mixtures and natural Little Belt clays tested within the present study. Recipes of the artificial mixtures are presented near the data points.

seen from the figure, all specimens can be designated as highly plastic, inorganic clays based on the Unified Soil Classification System, USCS. Moreover, a very high correlation ($R^2 = 0.9995$ was reached for a best fit obtained using the least squares method) between liquid limit and plasticity index may be identified for kaolin-bentonite mixtures, as also indicated in figure 4.2. The identified correlation is presented in eq. (4.1)

$$I_p = 0.932\,w_L - 23.94 \tag{4.1}$$

Clay mineralogy distribution for artificial clays

For a selected subset of the mixtures tested within the present project (the four mixtures applied during the main laboratory programme were included in the subset), the clay mineralogy was determined using X-Ray Diffraction (XRD) analysis. The XRD-analyses were performed at Department of Geoscience, Aarhus University. A total of seven specimens, comprising two natural and five artificial specimens, were tested as presented in table 2.2 in chapter 2 of the laboratory report.

The mineral distribution in the clay fraction are presented as a function of bentonite and kaolin powder content of the mixtures in figure 4.3 for the artificial specimens and in the ternary plot in figure 4.4 for all tested specimens. As seen from figure 4.3 the content of smectite is fairly proportional with the content of bentonite powder. Moreover, it is seen that the kaolin powder used for testing contains approximately 15 % illite in the clay fraction. Data from four natural Little Belt clay specimens sampled in Little Belt are presented in figure 4.4 for comparison, after (Awadalkarim 2011). As observed from these samples the scatter in clay mineral distribution may be large for natural clays, even
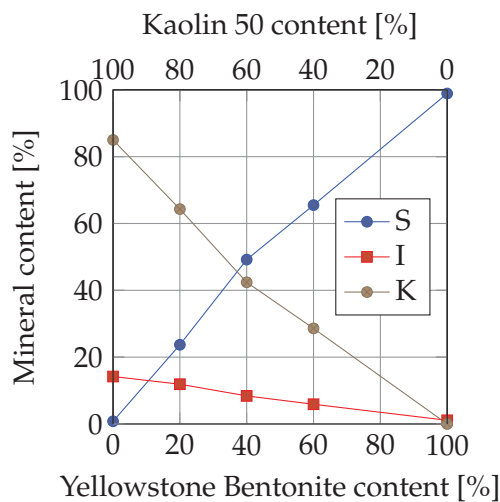
Figure 4.3: *Mineralogical composition of artificial mixtures of kaolin and bentonite (The content of smectite minerals is denoted "S", the content of illite minerals "I" and the content of kaolinite minerals "K").*
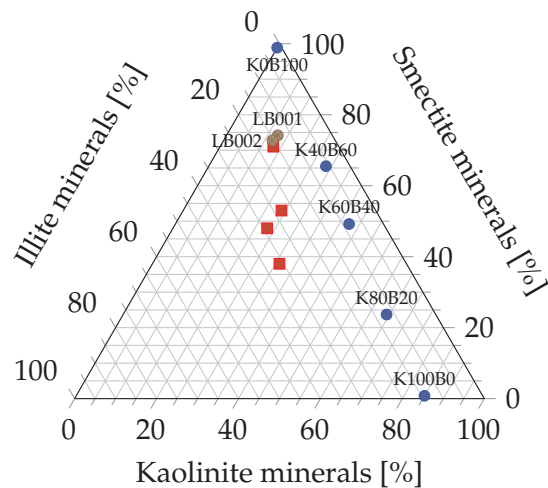
Figure 4.4: *Results from XRD analyses on selected artificial and natural specimens. Red squares designates results from natural Little Belt Clay after (Awadalkarim 2011).*

within the same clay formation. For calculation of mineral content of artificial specimen recipes not directly tested in the XRD test series, a linear interpolation was performed based on the results obtained from the XRD-analyses.

Particle density of artificial mixtures

The particle density, d_s for five mixtures of kaolin 50 and Yellowstone bentonite were tested in the laboratory at Geo, Lyngby, (Geo 2016) by using the small pyknometer method as suggested by BS 1377-2 (1990). The four mixtures used in the main laboratory programme were among the tested mixtures. The obtained results are presented in table 4.3 and figure 4.5.

Table 4.3: Results from particle density analysis on selected artificial specimens. After (Geo 2016).

Specimen mixture	d_s [g/cm^3]
K100B0	2.637
K80B20	2.612
K60B40	2.651
K40B60	2.646
K0B100	2.663
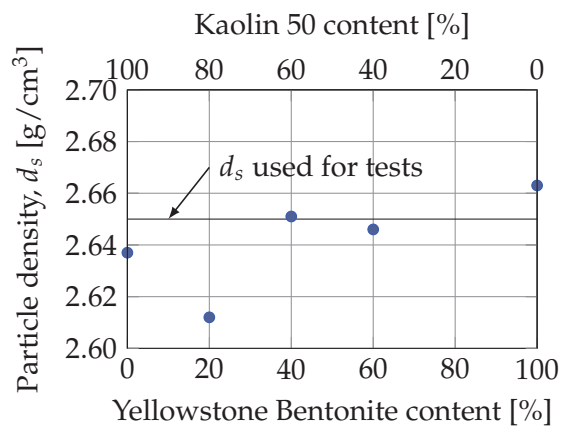
Figure 4.5: Particle densities for selected artificial specimens as a function of clay mineral content. After Geo (2016).

The obtained particle densities of the different mixtures, presented in figure 4.5, were found to be within the expected range. Using the structural formula for kaolinite, Leroy and Revil (2004) calculated the particle density to $d_s = 2.62\,\text{g/cm}^3$. Mitchell and Soga (2005) reports the specific gravity (d_s/d_w, where d_w is the density of water) of kaolinite minerals to be expected in the range of 2.60 to 2.68, whereas the specific gravity of montmorillonite minerals is in the range of 2.35 to 2.7. Data from Cerama, the supplier of the Yellowstone bentonite and Kaolin 50 has not been made available for the project as previously stated.

As presented in figure 4.5, only minor changes in the particle density were observed as the content of bentonite increased. Thus, all calculations presented in the present project were carried out using $d_s = 2.65\,\text{g/cm}^3$ as an average value for all specimen mixed from kaolin and bentonite powders.

4.2.3 Natural Soils

To supplement the tests on artificial clays a limited number of tests on natural Palaeogene clay have been carried out in the present project. The testing programme consisted of tests on natural Little Belt clay sampled in Little Belt, next to the Little Belt railway bridge from 1935 (Femern 2011a). The bore holes with full retrieval of cores were exe-
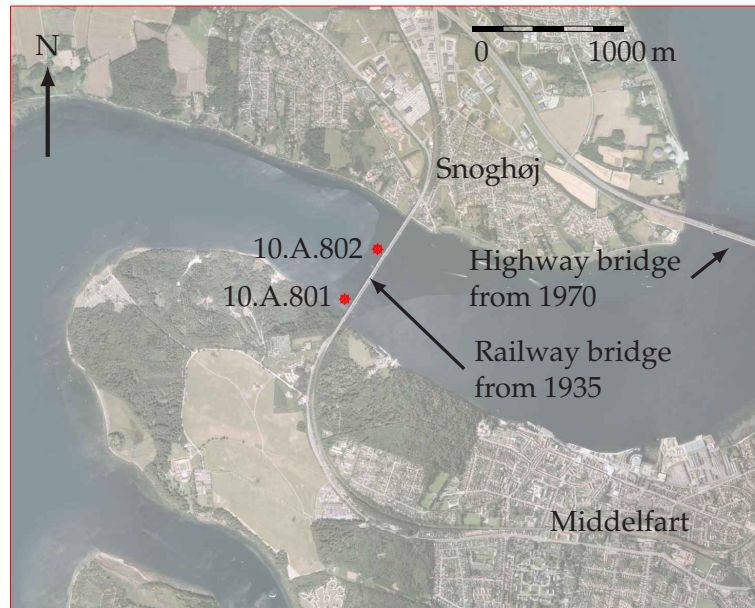
Figure 4.6: *Location of the borings 10.A.801 and 10.A.802 (indicated with the red dots) carried out in Little Belt, Denmark, near the railway bridge from 1935.*

cuted approx. 50 m from the first pier on the Funen side of the Little Belt Bridge, as indicated on figure 4.6, as a part of the ground investigations carried out by Femern (2011a). A Geobor-S system with a triple barrel coring device was employed to retrieve the undisturbed samples, which were then wrapped in cling film and waxed inside a cardboard tube before storage (Femern 2011a). The sampled Little Belt clay is a marine sedimentary Palaeogene clay and is geologically described as a slightly fissured clay of very high plasticity and slightly calcareous (Femern 2011a).

A list of the tested specimens of natural clays are presented in table 4.4. The index parameters for the specimens are presented in the Casagrande plasticity chart in figure 4.2. Two of the natural specimens, LB001 and LB002 (specimens were used in oedometer tests OE016LB001 and OE017LB002) were tested under the XRD-analysis programme as described in section 4.2.2. The two natural specimens consists of a mixture of illite, kaolinite and smectite minerals and plots fairly close to the specimen K40B60 as seen in figure 4.4. However, in terms of consistency limits the K60B40 mixture show similar behaviour to the natural clays as indicated in figure 4.2. Thus, the liquid limit of the

Table 4.4: *List of the intact, natural Little Belt clays tested within the present project.*

Testnumber	Boring	Core	Depth [m]	Type of test
OE016LB001*	10.A.801	10-107904	18.04–18.06	Friction in Oedometer cell
OE017LB002*	10.A.801	10-107904	18.32–18.34	Friction in Oedometer cell
OE025LB003	10.A.801	10-107904	18.38–18.40	Pilot test
OE031LB004	10.A.801	10-107904	18.46–18.47	Pilot test
OE052LB005	10.A.802	10-108051	19.92–19.94	Pilot test

* Oedometer specimen was used for XRD-analysis after test.

natural specimens are lower than what would have been expected from the smectite content and the behaviour of the artificial kaolin-bentonite mixtures. This is most likely due to the content of illite minerals in the natural clay and the inherent content of salt, which partly suppress the effect of the smectite minerals as discussed in sections 3.4 and 3.5.

d_s for the natural Palaeogene clay was tested for the Femern project and was found to lie in the range $2.618\,\text{g/cm}^3$ to $2.894\,\text{g/cm}^3$ with $2.77\,\text{g/cm}^3$ as the mean value (Femern 2014a), which was assumed applicable for the present project. The higher d_s value identified for the natural specimens may be rooted in the specific clay mineral lattice substitutions for the Danish Palaeogene clays. As the bentonite used for creating artificial specimens in the present study origins from Wyoming in the United States, it is very likely that the smectite minerals in the bentonite were formed in a different environment compared to the smectite minerals in the Danish Palaeogene clays. Thus, different lattice structure may be expected due to crystal lattice substitutions, as discussed in section 2.4, which may explain the different d_s-values identified for artificial and natural clays.

General methodology for laboratory testing

Where the materials used for testing were presented in chapter 4, the following chapter briefly outlines the procedures which were followed during the laboratory work presented in this PhD-dissertation. The main goal of the project was to increase the understanding of the deformation behaviour of the high plasticity clays, and specifically to investigate the influence of the smectite content. Another aim of the testing was to develop a deformation model capable of reproducing the features of highly plastic Palaeogene clays observed from oedometer tests.

The procedures are described in more details in the laboratory report, chapter 5 for index testing, in appendix B for the slurry creation and in appendix C for oedometer testing and the following data analysis. Detailed information on the specific laboratory equipment applied during testing is provided in the laboratory report, chapter 1.

5.1   Determination of water content

Water content analysis were carried out by weighing soil samples before and after drying at 110 °C for a minimum of 24 hours.

5.2   Determination of index properties

All testing of the plastic limit, w_p, in the present work was performed by the manual thread rolling method. More details on the procedures are given in section 5.2.2 of the laboratory report.

All testing of the liquid limit, w_L in the present project was performed with the fall cone apparatus. In section 5.2.1 of the laboratory report, the methodology applied during testing is presented. For the tests carried out in the present work, a fixed depth of penetration of 20 mm was used for defining w_L as proposed by the standards (BS 1377-2 1990; DS/CEN ISO/TS 17892-12 2004).

5.3 Preparation of slurry samples

Most of the tested specimens in the present work were trimmed from artificial, reconstituted, preconsolidated samples. These samples were initially prepared as slurries with water content above w_L and preconsolidated to σ'_v = 163 kPa in a floating-ring acrylic consolidometer, to achieve a sufficient firmness for the sample to be handled in the laboratory during trimming. Previously, a significant amount of work has been carried out on reconstituted specimens (Krizek and Sheeran 1970; Burland 1990; Horpibulsuk et al. 2007; Horpibulsuk et al. 2011).

5.3.1 Water content applied for reconstitution

Studies on the intrinsic properties are best carried out on reconstituted slurries with water content of preferably w = 1.25w_L, according to Burland (1990) and Krizek and Sheeran (1970). While this water content is recommended, the intrinsic properties are not sensitive to the water content of the slurry (if between $w = w_L$ and 1.5w_L), duration of load or load increment ratio above unity (Burland 1990).

Initially in the present study, all the slurries were mixed at an initial water content of w = 1.25w_L. However, due to unsatisfactory saturation in the oedometer tests after consolidation of the slurries, some tests were performed to evaluate the obtainable saturation in the consolidometers after installation of the slurry. These tests are presented in appendix B.4. Based on the results from this test series, it was chosen to increase the water content used for reconstitution to w = 1.5w_L. Increasing the initial water content of the slurries allowed easier installation in the acrylic tubes, as the slurries had a more liquid consistency. Slurries produced prior to December 2015 were mixed using w_L = 1.25w_L, whereas all slurries mixed after December 2015 (from slurry S030 and onwards) were mixed using w = 1.5w_L. While 1.5w_L is the upper limit indicated by Burland (1990) the influence of potential unsaturated specimens was considered to be a larger risk compared to the influence of a high initial water content of the slurries. High initial water contents may lead to segregation of the slurry – however, this was not observed in any of the prepared slurries in the present study. It is worth noticing that all sedimentary clays (as the Danish Palaeogene clays) have transitioned from being suspended in water to their current state, with much lower water content.

5.3.2 Homogeneity of preconsolidated slurries

To assess the homogeneity of the preconsolidated, reconstituted slurries, a test was performed based on four slurries of varying smectite content. Due to effects of friction between the sample and the acrylic consolidometers, the stresses applied to the slurry might have decreased with depth, which would cause the mechanical properties of the slurry to vary with height. Thus, the magnitude of variation in water content over height of the slurry was determined from the test by drying 1 cm thick segments of fully consolidated slurries. The investigation is presented in appendix B.8. The water content was indicative of the void ratio achieved during consolidation, which was expected to govern the mechanical behaviour of the artificial oedometer specimens.

The performed test indicated that the reconstituted specimens were sufficiently homogeneous (deviation of $\pm$10 % from the mean value of w_L) to allow multiple simi-

lar specimens to be trimmed from the same preconsolidated slurry sample if possible. Moreover, an excellent concordance of the water content was proven for specimens of same recipe, but from different slurry batches, when subjected to the same preconsolidation stress.

5.4 Trimming procedures for oedometer specimens

After preconsolidation of the prepared slurries, the samples were extruded from the acrylic tubes. The extrusion was performed by placing the consolidometer on a small cylinder on a table, and gently pushing the acrylic tube downwards by hand. This procedure pushed the pressure head up through the tube and gradually allowed removal of the other pressure head and filter, as they emerged from the top of the tube prior to the finished sample. In most cases the samples were used immediately after extrusion, however, a few samples were wrapped in cling-film and stored at $8\,^\circ$C before they were used. The specimens stored in this way were weighed before and after storage, and showed no significant loss of moisture.

During trimming the samples were cut roughly to the proper height (approx. 4–5 cm of sample was used), and placed on a lathe table for trimming. A vacuum-greased cutting ring was used to trim the specimens to the correct diameter. For tests performed using ELE-cells, the cutting ring was also used for trimming the height of the specimens, and ultimately as oedometer ring during testing. For tests performed in the COWI-cells, the radially trimmed specimens were levelled on the top side, transferred to the oedometer ring, and then levelled on the bottom side. The diameter of the specimens tested in the ELE-cells was $d = 63.5$ mm, and the diameter of the specimens tested in the COWI-cells were $d = 60$ mm. The ELE-specimens had a fixed height of $h = 19.5$ mm. The initial height of the COWI-specimens were recorded during trimming and was generally ≈ 20 mm. After trimming some of the trimming material were oven-dried for at least 24 hours at $110\,^\circ$C to determine initial water content, w_0, initial saturation, S_0 and the initial void ratio, e_0 of the oedometer specimen. All measurements for each oedometer specimen are presented in the test reports, which are enclosed in the laboratory report, part IV.

5.4.1 Sample disturbance during trimming

Based on the study introduced in section 5.3.1, all slurries mixed at $w = 1.5w_L$ may be assumed to be fully saturated after preconsolidation in the acrylic consolidometers. Thus, only sample disturbance during the trimming process may explain tests not showing initial saturation $S_0 = 100\,\%$. While the amount of sample disturbance have not been assessed in the present study, all specimens were subjected to loading in the normally consolidated stress regime during the first load steps, which may safely be assumed to eliminate the disturbance, and bring the specimens to a fully saturated state. Thus, all specimens tested in the main laboratory programme may be assumed fully saturated for the parts of the compression curves which were used for calibrating the proposed model.

5.5 Oedometer testing

5.5.1 Testing equipment

The majority of the data presented within the present project, were obtained from incrementally loaded oedometer tests, performed on the artificial specimens, prepared as stated in the sections above. Two types of oedometer apparatuses were used for testing: The conventional, manually operated frame and an automatic load frame. The manually operated frame is based on loading the specimens by adding or removing weights on a lever arm. In the automatic load frame the specimens were loaded by pushing the oedometer cell upwards against a fixed beam with a stepper motor based on real-time readings from a force gauge mounted between the upper pressure head and the beam. In general the same loading programme was obtainable for both types of frames. Additional information concerning transducers, calibration factors etc. are presented in the laboratory report, chapter 1.

The majority of testing was carried out in fixed-ring, double-sided drained oedometer cells, where the oedometer rings were coated with a thin layer of vacuum grease prior to testing. The fixed ring cells were selected for the present project to allow for direct comparison with the tests performed for assessing the effects of internal friction (discussed in section 6.10.1 and appendix H), and to allow comparison with CRS-tests. As a preliminary study indicated that the majority of the compliance originated from the filter papers (see section 1.6.1 of the laboratory report), all tests in the main laboratory programme were carried out without filter paper. A few tests were carried out in special cells. These cells will be introduced, when the data from the tests is presented. During the trimming process the filter discs were kept dry to avoid initiation of swelling before the oedometer cells were placed in the load frames. The loading programmes were initiated with dry filters and without pore fluid in the carriage. After 5 min on the first load step, pore fluid was added to the oedometer carriage. This procedure introduced a risk of trap air in the filter discs upon wetting, however the risk of excessive swelling of the specimens when in contact with wet filter before they were installed in the load frames was considered larger for the present study.

All testing on artificial specimens were performed using tap water in the oedometer carriage, and measures were taken to avoid excessive evaporation. For tests with long durations, i.e. tests on K60B40 and K40B60, the carriage water had to be replenished during testing. Tests performed following the main laboratory programmes were conducted using de-aired tap water in the carriage. All testing performed within the present PhD-study were performed without application of back pressure, and only a few tests in sub-studies (see appendix D) were carried out with measurements of pore water pressure (The tests were performed as single-sided drained tests, with measurements of pore water pressure at the lower pressure head).

5.5.2 Data acquisition from tests

In both the manual and automatic oedometer frames, the displacements of the upper pressure head were logged over time, after initiation of a new load step. A few iterations were made on the intervals between the readings in the displacement log. However,

the main tests were performed using an initial spacing between readings of 0.01 min increasing with time to a maximum reading-interval of 15 min.

The displacement readings were obtained from two types of displacement transducers, namely Novotechnik potentiometric displacement transducers and CDI digital dial indicators. All tests performed in the manually operated frames were logged using Novotechnik transducers, which were calibrated against an analogue micrometer with 0.001 mm resolution. The calibration data is presented in the laboratory report, chapter 1. The automatic load frames were for the first part of the project equipped with Novotechnik transducers. However, due to fluctuations of the readings over time, the Novotechnik transducers were switched with CDI-gauges, which worked better with the automatic system. A short analysis of the fluctuations is presented in section 1.2.1 of the laboratory report.

For tests performed in the automatic oedometer apparatuses, the force gauges were zeroed prior to testing. The force gauges were calibrated when installed on the load frame, and were compared against each other during the project to ensure correct readings. The automatic load frames were able to maintain the vertical load during a load step within an accuracy of ± 0.35 N which was estimated to be negligible.

5.5.3 Oedometer test procedures

All obtained compression curves were corrected for self-deflection of the oedometer frame and cell, by running dummy tests of the loading programmes on a steel disk. As no filter paper was used during the main tests, the filter discs were thoroughly rinsed between individual tests. It was estimated that potential clogging of the filter discs would influence only duration of the tests, and not the final deformations, as only the drainage conditions would be affected. As the flow characteristics of the artificial specimens were not of special focus within the present project, this risk was accepted. Nonetheless, special care was shown when the discs were cleaned in-between tests.

All tests were performed as incrementally loaded tests, where each load step was maintained long enough to allow complete primary consolidation. As the method presented by Casagrande (1938) was the preferred method for analysing the time curves, each load step was maintained until secondary consolidation was clearly identified. Albeit allowing secondary consolidation to be identified, it was sought to keep the load steps as short as possible to minimise the effects of creep on the obtained results. The effects of creep on the deformation response is discussed in section 6.9.

Further details on the applied oedometer equipment, including calibration factors, and presentation of the oedometer cells applied may be found in chapter 1 of the laboratory report.

5.5.4 Interpretation of oedometer tests

All time curves obtained during oedometer testing were interpreted using the Casagrande (1938) method to determine t_{100} and ε_{100} (or e_{100}). The method is presented further in appendix D.1 as a part of a miniature study on four different methods for interpreting the time curves (Appendix D). The miniature study showed that the Casagrande approach yielded similar values of t_{100}, compared to a method based on the strain rate

development on a load step. The values of effective vertical stress, σ'_v, and ε_{100} and e_{100} were used to construct the compression curves. The values of e_{100} were calculated based on initial water content, and verified by comparison between the void ratio determined after testing and the calculated void ratio on the final load step in the oedometer test.

The compression curves were analysed using the methods of Casagrande (1936) and Janbu (1969) as presented in appendix C.3.1 to identify the vertical yield stress, σ'_{vy}. The moduli (C_C, C_S and C_R) of the tested specimens were determined according to the procedures presented in appendix C.3.2. The applied procedures when fitting the proposed model to the observed behaviour of the main laboratory tests are discussed in section 7.3.

## 5.6 Loading programme for main laboratory tests

The main laboratory tests focused on testing four mixtures of artificial specimens, namely K100B0, K80B20, K60B40 and K40B60. The four mixtures were subjected to five different loading programmes; three to provide the basis for the derivation of a deformation model (Load 1–3), and two programmes to assess the behaviour of the proposed model (Load 4–5), when loading scenarios a bit more extreme were undertaken. The three loading programmes used for deriving the model (i.e. the main laboratory programme) were named "Load 1", "Load 2" and "Load 3" and are briefly introduced below and illustrated in figure 5.1, whereas the validation programmes, "Load 4" and "Load 5" are introduced in section 5.6.4 and illustrated in figure 5.2.

5.6.1 Load 1

Load programme 1 comprised three loops of unloading and following reloading. The programme was planned to illustrate the effects of the minimal stress reached during unloading, σ'_{min}, when unloading from a constant maximal stress of $\sigma'_{max} = 475\,\text{kPa}$. During three loops the specimens were unloaded successively to $\sigma'_{min} = 150\,\text{kPa}$, $\sigma'_{min} = 70\,\text{kPa}$ and finally to $\sigma'_{min} = 25\,\text{kPa}$. Between each unloading, the specimens were gradually reloaded to $\sigma'_{max} = 475\,\text{kPa}$. After the final unloading and reloading loop, the specimens were loaded to $\sigma'_v = 3200\,\text{kPa}$ before unloading to $\sigma'_v = 10\,\text{kPa}$, where the specimens were allowed to swell prior to dismantling the oedometer cells and removing the specimens for water content analysis.

5.6.2 Load 2

In loading programme 2, the effect of the maximal stress, σ'_{max} were investigated for the unloading and reloading loops, when the minimal stress was kept constant at $\sigma'_{min} = 100\,\text{kPa}$. For the first unloading and reloading loop, the specimens were loaded to $\sigma'_{max} = 325\,\text{kPa}$, for the second loop to $\sigma'_{max} = 700\,\text{kPa}$ and for the final loop to $\sigma'_{max} = 1800\,\text{kPa}$, reaching $\sigma'_{min} = 100\,\text{kPa}$ during unloading in between each loop. As for Load 1, the specimens were ultimately loaded to $\sigma'_v = 3200\,\text{kPa}$, unloaded to $\sigma'_v = 10\,\text{kPa}$ and extracted from the oedometer cell, prior to oven-drying for determination of the water content.
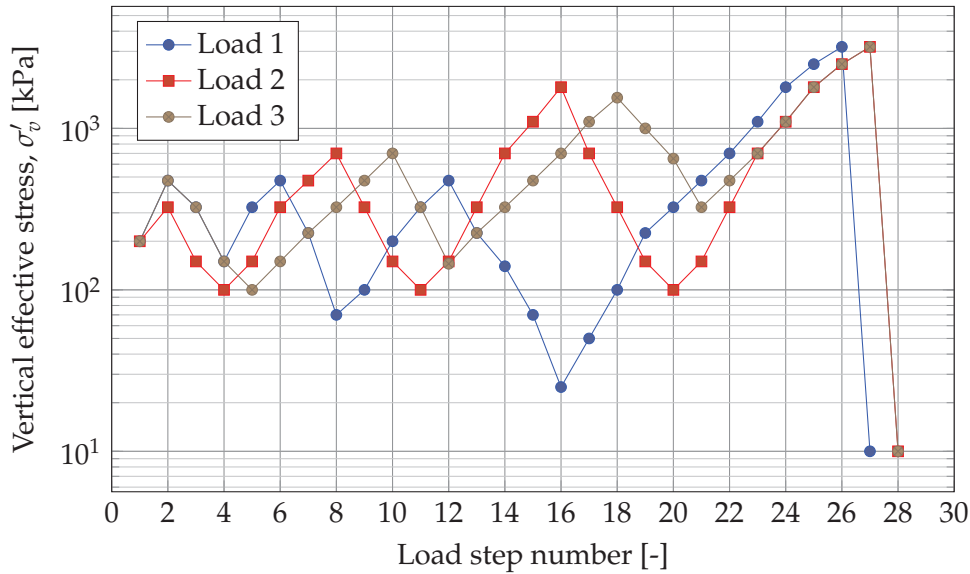
Figure 5.1: Illustration of the loading programmes 1 to 3 of the main laboratory programme.

5.6.3 Load 3

Load 1 and Load 2 focused on the effect of the minimal and maximal stress, respectively, subjecting the specimens to increasing OCR-values as the tests progressed. On the other hand Load 3 was designed with a constant overconsolidation ratio of $OCR = 4.75$, tested at different stress levels. The specimens were initially loaded to $\sigma'_{max} = 475$ kPa and then unloaded to $\sigma'_{min} = 100$ kPa. This loop was followed by a loop with $\sigma'_{max} = 700$ kPa and $\sigma'_{min} = 145$ kPa and the final loop was carried out between $\sigma'_{max} = 1550$ kPa and $\sigma'_{min} = 325$ kPa. Ultimately, the specimens were loaded to $\sigma'_v = 3200$ kPa prior to unloading to $\sigma'_v = 10$ kPa, at which stress the specimens were extracted from the cells, and the water content determined.

5.6.4 Validation programme

After performing the main laboratory tests, the proposed model was fitted to the compression curves for each mixture as presented in section 7.3. To assess the performance of the derived model, eight tests were performed, following two different loading programmes. One of the loading programmes, Load 4, investigated the effect of subjecting the specimen to a high OCR-value at relatively small strains. As the stress paths in loading programme 1 and 2 increased in length during the tests, the largest OCR-values were reached on the third loop. Thus, the specimen may have sustained significant compression and reached a low void ratio. To evaluate the effect of the void ratio, the specimens were loaded to $\sigma'_{max} = 475$ kPa and unloaded to $\sigma'_{min} = 25$ kPa in Load 4. Afterwards the specimens were loaded to $\sigma'_{max} = 700$ kPa, unloaded to $\sigma'_{min} = 225$ kPa and reloaded to $\sigma'_v = 1800$ kPa before unloading and ultimately dismantling the oedometer cell at $\sigma'_v = 10$ kPa.

The other verification programme, Load 5, was a scaled version of Load 1, using the same three σ'_{min}-values, but unloading from $\sigma'_{max} = 1100$ kPa on all three loops. This
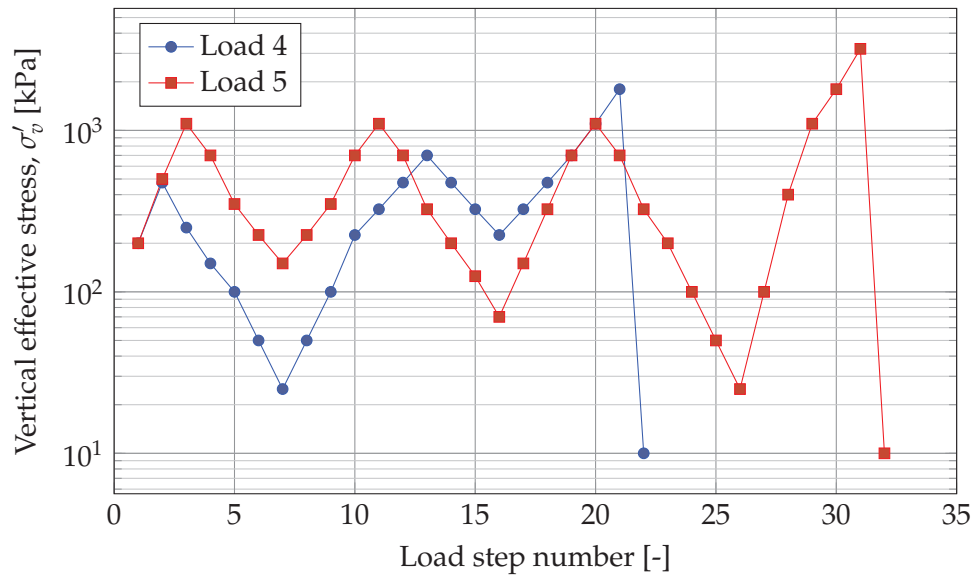
Figure 5.2: *Illustration of the validation loading programmes 4 amd 5.*

programme was planned to investigate the performance of the proposed model at high *OCR*-values, and to assess, whether a linear stress-strain response was obtained with intense unloading as described in section 3.6.1. Moreover, the stress paths modelled from Load 5 were closer to the procedures applied by Hansen and Mise (1964), who initially compressed the specimens to 3000–6000 kPa as discussed in section 3.6.1.

5.6.5 Conducted main tests - an overview

For the K80B20 and K60B40 specimens, each of the main loading programmes were ran twice to investigate the reproducibility between tests of the individual mixtures. An overview over the 18 tests in the main laboratory programme and the 8 tests carried out to assess the performance of the derived model is presented in table 5.1.

Table A.1 in appendix A presents all oedometer tests conducted within the present

Table 5.1: *Distribution of main laboratory tests between the three main laboratory programmes (Load 1–3) and the two validation programmes (Load 4 and 5). Laboratory logs on each test may be found in the laboratory report.*

Specimen	K100B0	K80B20	K60B40	K40B60
Load 1	OE046S035	OE042S034 OE055S046	OE054S040 OE057S041	OE050S039
Load 2	OE047S035	OE043S034 OE056S046	OE059S043 OE058S041	OE051S039
Load 3	OE049S035	OE061S050 OE062S050	OE048S036 OE060S043	OE053S030
Load 4	OE064S052	OE068S051	OE063S044	OE071S047
Load 5	OE065S052	OE069S051	OE073S054	OE072S047

study. The table presents specimen number, recipe of the mixtures, applied pore fluid, initial saturation and initial void ratio of the specimens along with compression index, C_C, swelling index, C_S, and recompression index C_R. Moreover, for each specimen the test purpose is indicated in table A.1.

5.6.6 Conducted sub-studies – an overview

A range of sub-studies were carried out in connection to the present work. An overview of the tests performed under each of these sub-studies are presented in table 5.2. Each of the sub-studies have been related to the observations from the main laboratory tests. The effects of the specific test conditions on the deformation behaviour of artificial, reconstituted clays are discussed in chapter 8.

A list of the oedometer tests performed within each of the sub-studies presented in table 5.2 are presented in appendix A.2. Thus, table A.2 presents the salinity of the pore fluid applied for each test, along with the initial saturation of the specimens, initial void ratio and the compression parameters C_C, C_S and C_R.

Table 5.2: Overview over conducted sub-studies related to the present dissertation.

Study	Area of focus	Tested specimens
(Sigurðardóttir and Dobrescu 2016)	Influence of pore fluid salinity on the consistency limits and deformation response	K100B0, K90B10 and K80B20
(Lodahl et al. 2016)	Influence of frictional stress loss between oedometer ring and specimen	K100B0, K60B40 and natural Little Belt clay
(Ohler 2017)	Influence of pore fluid salinity on the consistency limits and deformation response of illite-rich specimens	K0B0I100*, K40B0I60, K30B10I60, K20B20I60 and K0B40I60
(Dolby 2017)	Influence of frictional stress loss between oedometer ring and specimen based on triaxial and IL oedometer tests	K100B0, and to a limited degree K60B40

* In the mixture recipe KXX denotes kaolin content, BYY denotes bentonite content and IZZ denotes illite content, as discussed in section 8.3.

Observations from the main laboratory tests

The main laboratory tests were carried out based on the loading programmes presented in section 5.6. A total of 18 tests, comprising a total of 54 unloading-reloading loops, were carried out to increase the knowledge on the influence of smectite content on the deformation behaviour of high plasticity clays. Moreover, the tests provide the basis for deriving and calibrating a deformation model, capable of accurately reproducing the features observed for natural Danish Palaeogene clays. Additionally, eight validation tests (a total of 20 unloading-reloading loops) were carried out, which have primarily been used for assessing the behaviour of the derived model, which is presented in chapter 7.

All tested specimens in the main laboratory programmes were prepared as artificial mixtures, with initial water content of $w = 1.5\,w_L$, as discussed in section 5.3. This process have shown to enable creation of high-quality specimens for oedometer testing, compared to the procedures applied for the pilot tests where $w = 1.25\,w_L$ was used, which caused a lower degree of saturation in the specimens prior to testing. The slurries used for the main laboratory programmes were preconsolidated prior to trimming for the oedometer ring and then tested as described in section 5.5.

As previously presented, the objective of the current PhD-study was to investigate the influence of the smectite content on the compression, swelling and recompression behaviour. Thus, the current chapter briefly introduces the outcomes of the main laboratory tests, and highlights the main features, which must be built into the model. Primary focus of the present chapter is the results obtained through the main laboratory tests. A number of pilot tests were carried out to assess the optimal testing procedures and to perform a few supplementary studies. These results are analysed in the appendices for individual sub-studies and more general in appendix E, where the effects of smectite content is discussed more broadly, based on the pilot tests.

6.1   Typical compression curves

Observing the compression curves of the 18 conducted tests in the main laboratory programme (i.e. Load 1, Load 2 and Load 3), introduced in section 5.6, a number of features

may be identified to vary with stress history and smectite content. These features will be discussed in the current section based on representative compression curves. All compression curves are plotted for comparison in the laboratory report, chapter 10. The details of specimen characteristics in terms of state parameters for the main laboratory testing programme are presented in table 6.1.

Table 6.1: State parameters for all tested specimens within the main laboratory programme.

| Mixture	Test number	Loading programme	Clay fraction* [%]	Smectite content*† [%]	w_L* [%]	e_0 [-]	S_0 [%]
K100B0	OE046S035	1				1.16	96.5
K100B0	OE047S035	2	53	0.8	58.8	1.18	98.5
K100B0	OE049S035	3				1.18	97.4
K80B20	OE042S034	1				1.51	100.2
K80B20	OE043S034	2				1.49	102.0
K80B20	OE061S050	3	58	23.7	113.9	1.58	98.5
K80B20	OE055S046	1				1.65	98.4
K80B20	OE056S046	2				1.67	101.1
K80B20	OE062S050	3				1.56	99.5
K60B40	OE054S040	1				2.06	97.6
K60B40	OE059S043	2				2.15	98.7
K60B40	OE048S036	3	64	49.2	176.8	2.06	98.2
K60B40	OE057S041	1				2.26	97.7
K60B40	OE058S041	2				2.23	100.6
K60B40	OE060S043	3				2.29	98.1
K40B60	OE050S039	1				2.76	99.0
K40B60	OE051S039	2	74	65.5	223.6	2.69	99.1
K40B60	OE053S030	3				2.62	97.6

* Result for mixture
† Of clay fraction ($D \leq 2\,\mu m$)

Typical compression curves for the mixtures tested in the main laboratory programme are presented in figures 6.1 to 6.3. Each figure presents the compression curves for each of the four mixtures, compared on a logarithmic stress axis, for tests following the same loading programme. Larger plots are presented in appendix A.1 along with plots on a linear stress axis. As may be observed from figures 6.1 to 6.3 a clear increase in initial void ratio, e_0, compression index, C_C, swelling index, C_S and recompression index, C_R is evident with increasing smectite content of the tested specimens.

As presented in the description of the loading programmes in section 5.6, the interval of stresses covered in the laboratory programmes span the range of 10 kPa to 3200 kPa (10 kPa was reached during the final unloading step in all tests, which is not illustrated in the figures), which is also reflected in the curves illustrated in figures 6.1 to 6.3. Within this stress range, data from a normally consolidated state was obtained for the effective stress interval 200 kPa to 3200 kPa. All stress-void ratio points obtained during virgin compression are illustrated in figure 6.4, where a general trend of increasing compres-
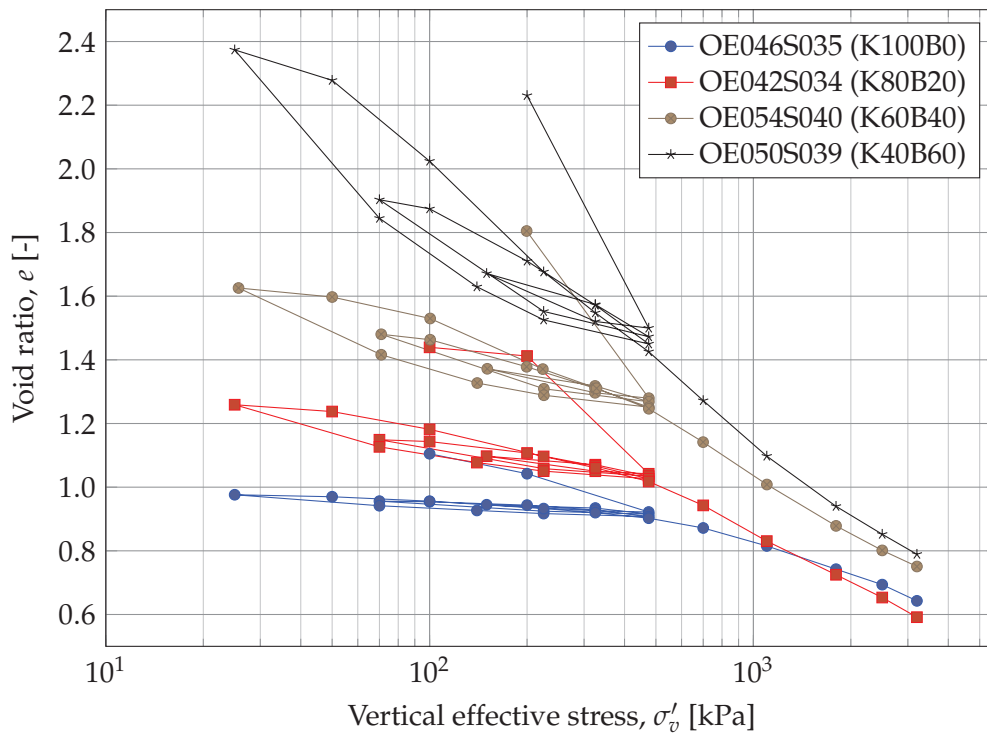
Figure 6.1: *Compression curves for representative tests following loading programme 1 of the main testing programme.*
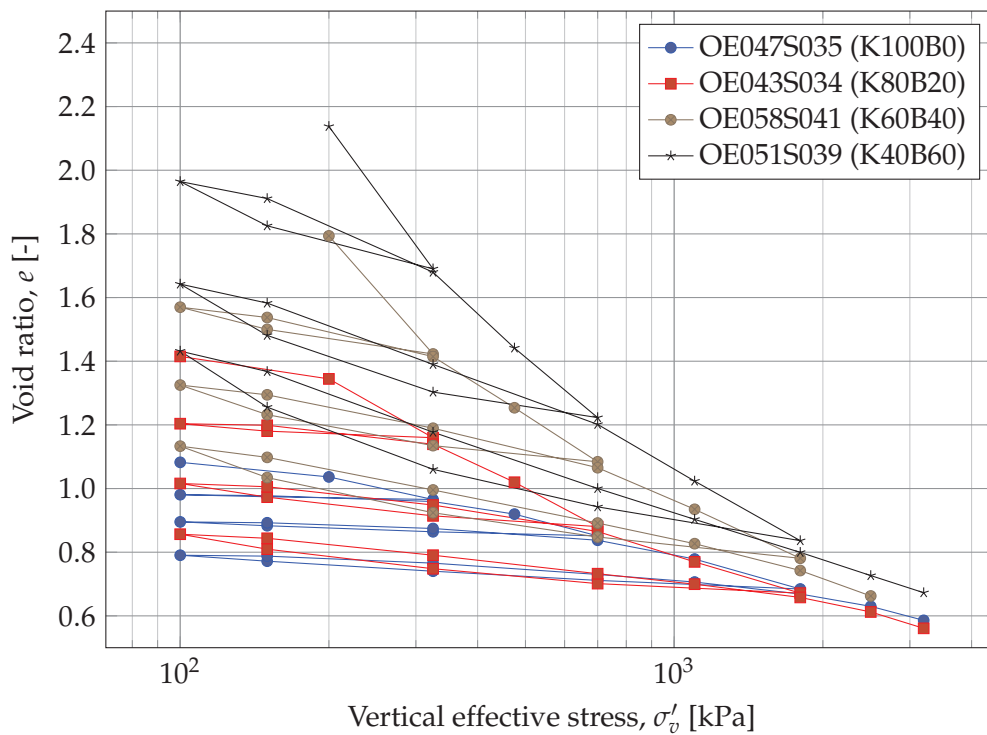
Figure 6.2: *Compression curves for representative tests following loading programme 2 of the main testing programme.*
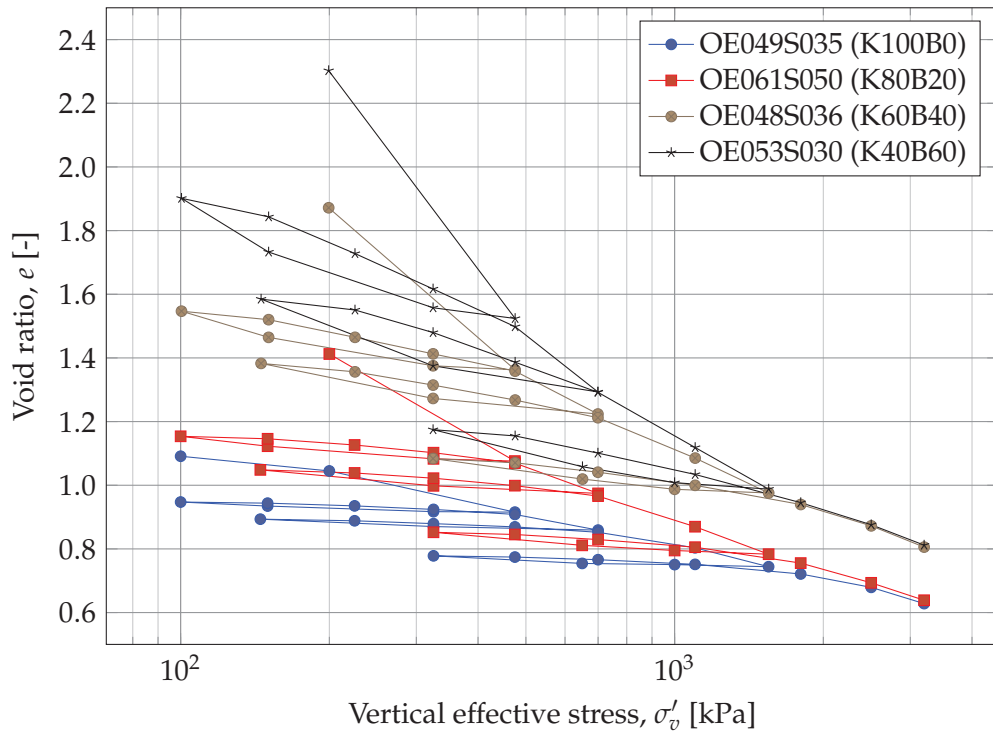
Figure 6.3: *Compression curves for representative tests following loading programme 3 of the main testing programme.*
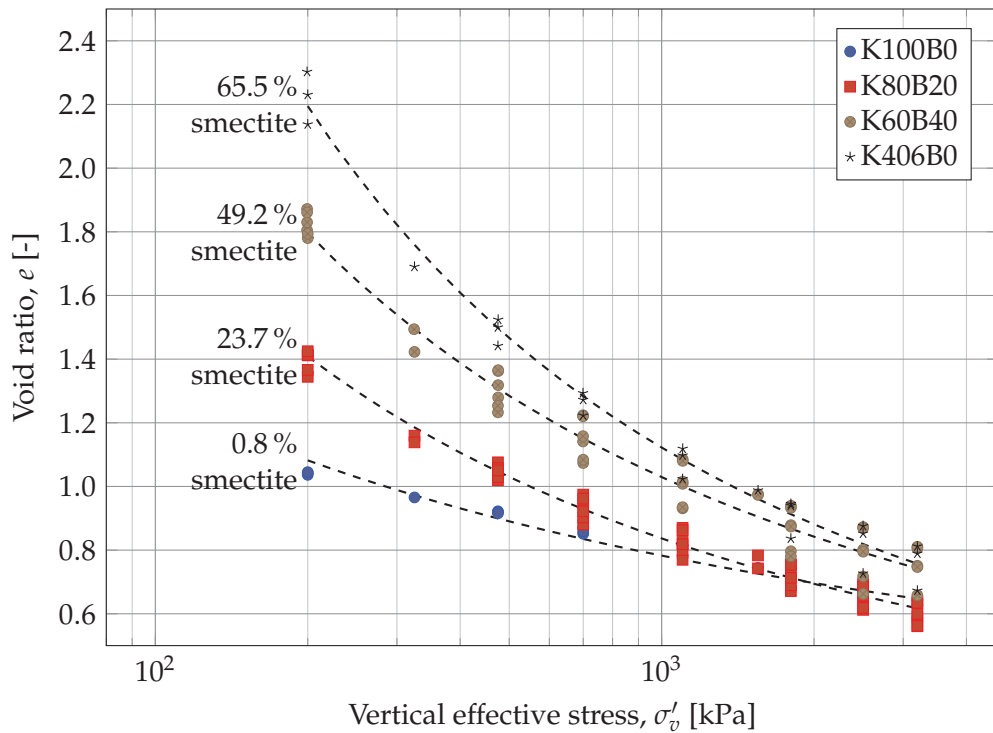
Figure 6.4: *Data points and trend lines from virgin curves of all tests in the main laboratory programme.*

sibility and increasing curvature of the virgin curves may be observed with increasing smectite content of the specimens. Multiple unloading-reloading reversals were carried out in each of the loading programmes, as illustrated in figures 6.1 to 6.3. During these stress reversals *OCR*-values of 3.2 to 19 were reached for all four mixtures, as all four mixtures were tested following the main laboratory programmes.

All tested specimens were preconsolidated to 163 kPa prior to the oedometer testing. Due to the difference in smectite content, the initial void ratio of the tested specimens spanned the range of e_0 = 1.16 (for a K100B0 specimen) to e_0 = 2.76 (for a K40B60 specimen), as also presented in table 6.1. At maximum stress, σ'_v = 3200 kPa, the void ratio of the specimens fell in the range of e = 0.56–0.81. Thus, for the specimens of highest plasticity a decrease in void ratio of approximately Δe = 1.95 was observed when comparing initial void ratio and void ratio at maximum vertical effective stress. This change is large compared to the expected change in void ratio for natural specimens if compressed from σ'_{v0} = 163 kPa to 3200 kPa. Thus, some differences must be expected when tests conducted on artificial specimens are compared to tests on natural Palaeogene clays, as will be briefly touched upon in the following sections.

The large initial void ratios of the tested specimens, caused large vertical strains, ε_v to be developed during testing. Thus, for the final parts of the compression curves, $\varepsilon_v \approx 60\%$ was achieved for the K40B60-specimens, as is illustrated in chapter 10 of the laboratory report. Consequently, the specimens became very thin during testing, which may affect the performed test to a certain degree. The highly curved compression curves may be a result of the large strains. On the other hand, all specimens were prepared as slurries, which is why the zero-reading for the vertical strains in the oedometer tests, corresponds to a state where significant strains have already developed in the acrylic consolidometer. The process applied during testing in the present project resemblance the sedimentation and consolidation processes which natural specimens go through prior to sampling and testing. Thus, no effect of on the mechanical behaviour of the clay was expected. To avoid influence of the definition of the zero-point for the vertical strain, primarily void ratios were used within the present project.

6.2 Effects of smectite content on deformation parameters

One of the primary goals of the present study was to illustrate the effects of smectite content on deformation behaviour of clays. From the XRD-tests, discussed in section 4.2.2, the clay mineralogical composition of the four recipes tested in the main laboratory programme was well-known. Figure 6.5 illustrates the compression indices, C_C, derived for each of the tests in the main laboratory programme and the validation programme, plotted against the smectite content of the specimens. As may be noted from the figure, C_C may be viewed as an essential linear function of the smectite content, however as significant scatter is evident, the presented trends may only be applied for an overall assessment of C_C. The behaviour is in concordance with the diffuse double-layer theory, were an increase in cation exchange capacity, CEC, and specific surface area, SSA, lead to an increase in compressibility. Smectite minerals are characterised by high values of both CEC and SSA, as described in section 2.5. As may be observed from the data points, some scatter is evident within the tests for a particular mixture. The scatter is introduced
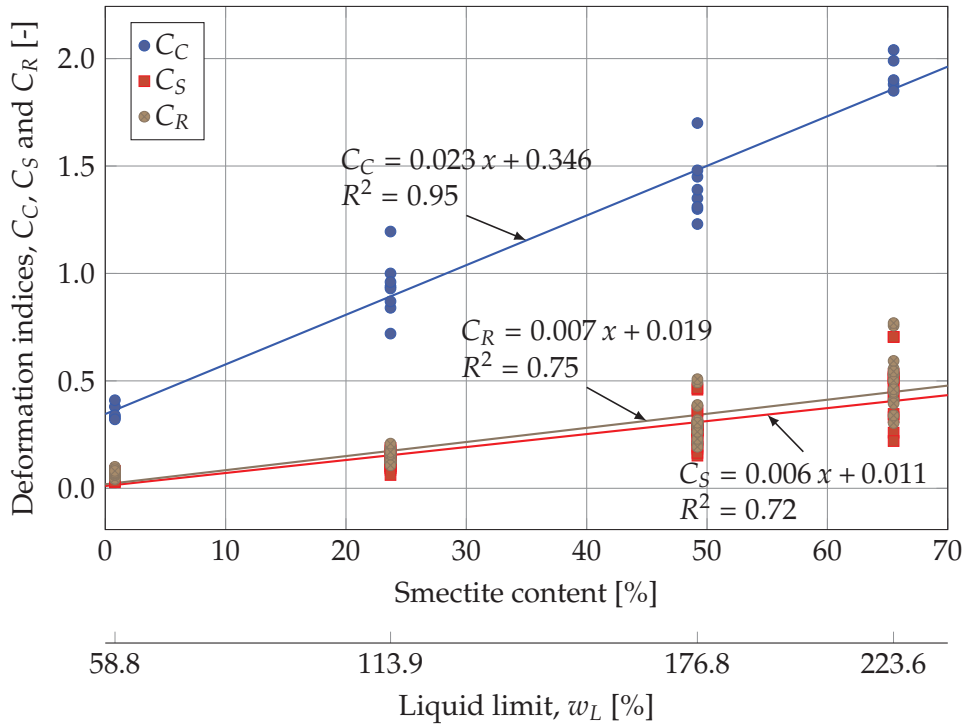
Figure 6.5: *Deformation parameters and their relationship with smectite content of clay fraction. It should be noted that x in the trend line expression denotes the smectite content.*

by use of different stress intervals for extracting C_C-values, as these were extracted on the steepest part of the compression curves, as described in appendix C.3.2.

Figure 6.5 also illustrates the effects of the smectite content on the swelling and re-compression indices. As illustrated in the figure, both indices increase with increasing smectite content, however with large scatter for the specimens of highest plasticity. Thus, the presented relationships should be used with caution. Both parameters, C_S and C_R, were extracted between σ'_{min} and σ'_{max} on the unloading-reloading loops, which explains the relatively small difference between the two relations, as the unloading-reloading loops were almost closed in all the tests. As the smectite content increases, so does the scatter in the calculated parameters C_S an C_R. This is due to the increased curvature of the unloading-reloading loops with increasing smectite content. Thus, for the K40B60-specimens, the parameters C_S and C_R were highly sensitive towards the OCR-value reached during testing, as will be discussed in section 6.6.

6.3 Effects of initial state parameters on compression index

Figure 6.6a presents the correlation between the compression index and the initial void ratio, e_0, from the main laboratory tests. As may be noted, a relatively high degree of correlation is identified, which is not surprising as all specimens were preconsolidated to $\sigma'_v = 163$ kPa prior to the oedometer tests. Thus, the initial state of the specimens reflects a previous normally consolidated state, which is why a close link between the initial void ratio and smectite content is expected, as illustrated in figure 6.5. Figure 6.6b
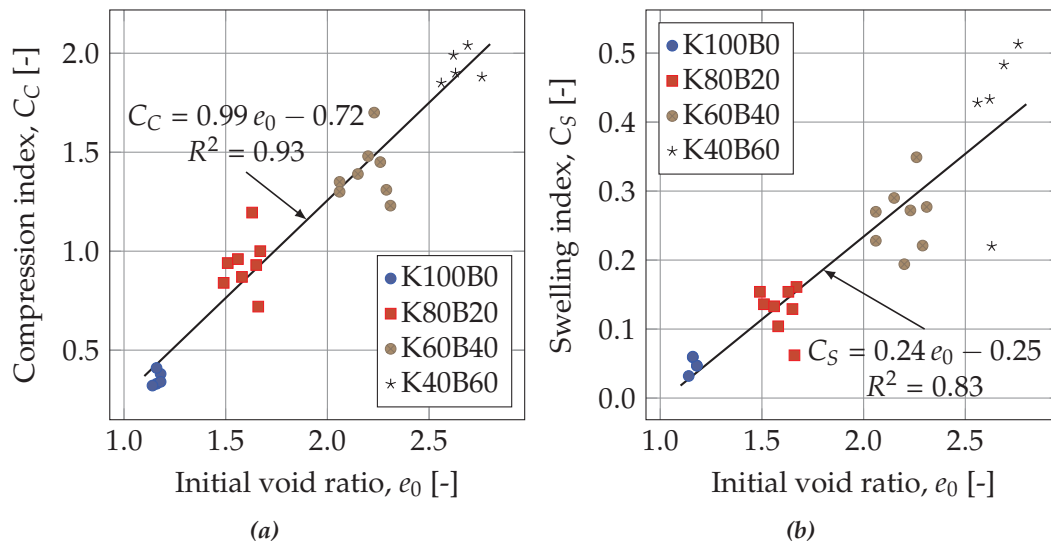
Figure 6.6: *Compression index and swelling index (determined on the second unloading-reloading loop) as functions of initial void ratio for the main laboratory tests. All specimens were preconsolidated to 163 kPa prior to oedometer testing.*

illustrates the swelling index as a function of the initial void ratio of the specimens. Even as the swelling indices illustrated in figure 6.6b were extracted on the second unloading-reloading loop in the tests, a correlation to the initial void ratio was identified, however with larger scatter compared to the correlation for C_C presented in figure 6.6a. The larger scatter indicates that the swelling index is more sensitive towards the stress path followed during the test than the compression index.

6.4 Tangent stiffness on recompression branches

Due to the highly curved unloading-reloading branches observed for specifically the specimens of highest plasticity, the application of the parameters C_S and C_R for assessing settlements for a structure requires extreme care. As the parameters are very sensitive towards the *OCR*-values, the parameters should be extracted for stress conditions similar to the relevant problem. However, formulating a model to yield tangent stiffness along the unloading and reloading curves would enable an approach less sensitive towards the stress conditions during laboratory testing, which would be beneficial. Thus, the development in tangent stiffness during the tests are of interest to the objectives of the present project. Figure 6.7 illustrates the development of the tangent stiffness during reloading in the final unloading-reloading loop and following reloading, for loading programme 1. The figure illustrates the tangent stiffness, calculated for each of the six specimens tested in the loading programme.

As illustrated in figure 6.7 the tangent stiffness in the overconsolidated stress regime, (below $\sigma'_{\max}$) decreases with increasing smectite content. However, the overall shape of the tangent stiffness curves are quite similar. The plot illustrated in figure 6.7 constitutes the basis for deriving the vertical yield stress, σ'_{vy}, by the method suggested by Janbu (1969). The method is described in detail in appendix C.3.1. σ'_{vy} is usually identified to
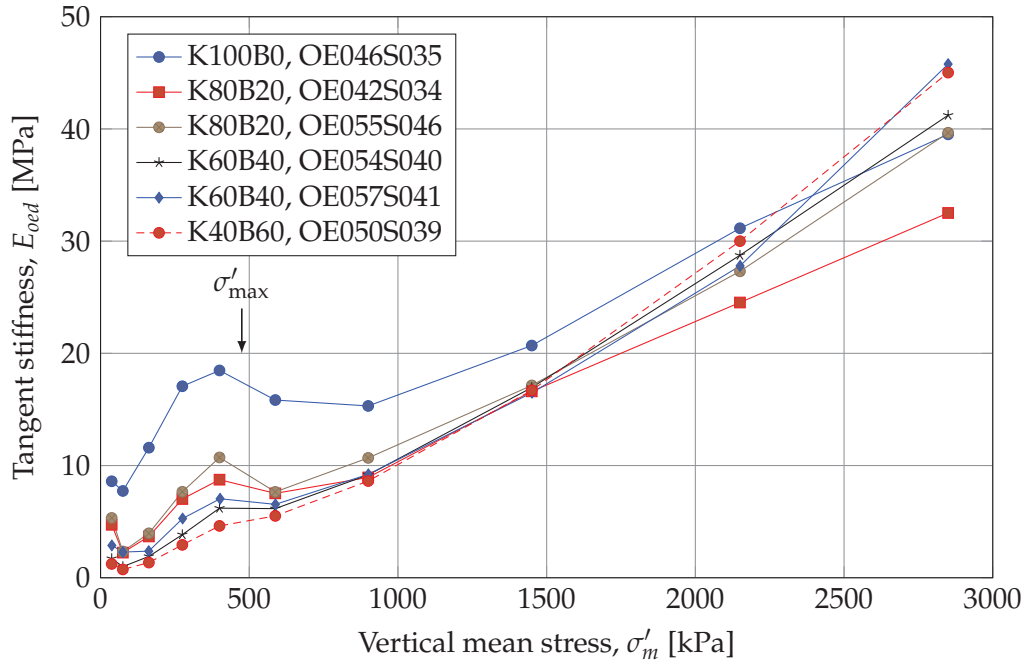
Figure 6.7: *Tangent stiffness calculated for the final part of the compression curve for loading programme 1: Reloading from 25 kPa to σ'_{max} = 475 kPa, and virgin loading from 475 kPa to 3200 kPa.*

the left of the saddle point, which may be clearly identified just above the σ'_{max}-value for the K100B0-specimen in figure 6.7. For increasing smectite content, the bend gradually disappears, which most likely is linked to the gradual loss of stress memory, which is further discussed in section 6.7.

6.5 Observations from normalised curves

Each unloading-reloading loop in the loading programmes 1–3 (a total of nine sets of identical stress paths) were normalised with respect to the void ratio prior to unloading (at σ'_{max}) and at σ'_{min}, using eq. (6.1). Expression (6.1) is a slight modification of the formulation for the void index, I_v, presented by Burland (1990), as discussed in section 3.2. Normalisation of the unloading-reloading curves enabled an evaluation of the fundamental shape of the curves, as all curves were scaled and moved to yield $I_v^* = 0$ prior to unloading (at σ'_{max}) and $I_v^* = 1$ at σ'_{min}. For each of the unloading-reloading loops, the normalised response from the six separate tests (a total of four mixtures) were plotted together. One of these plots are presented in figure 6.8. All normalised plots, one for each of the nine identical stress unloading-reloading loops, may be found in the laboratory report, chapter 10.

$$I_v^* = \frac{e - e_{min}}{e_{max} - e_{min}} \tag{6.1}$$

As may be observed from figure 6.8 and the rest of the normalised plots presented in the laboratory report, the normalised compression curves bear close resemblance to each other, despite being different mixtures. This seems to suggest that the fundamental
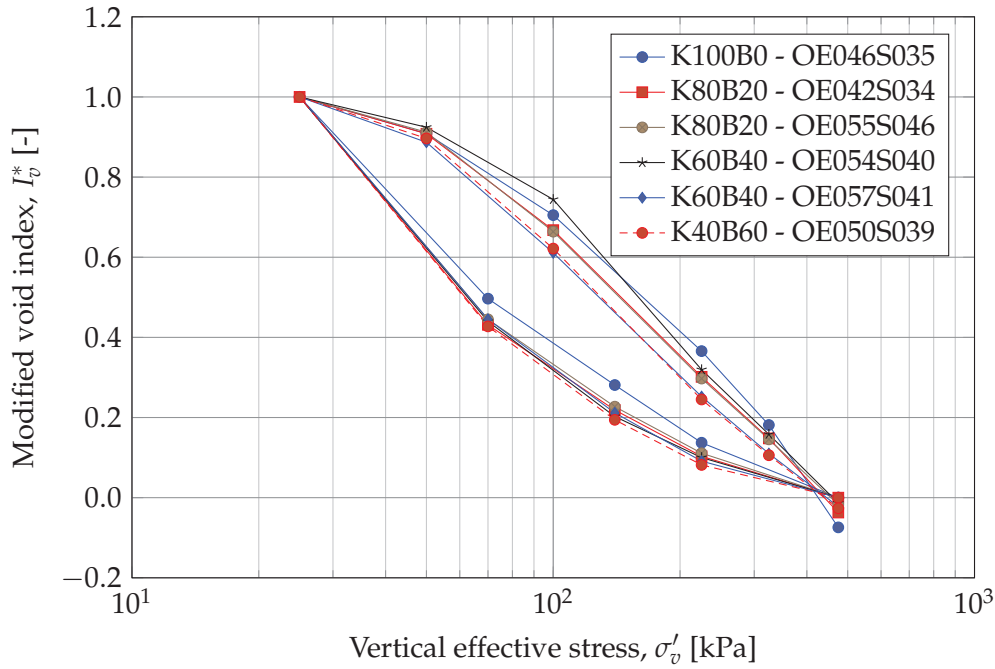
Figure 6.8: *Normalised plot for loop 3 of loading programme 1. $\sigma'_{max} = 475$ kPa and $\sigma'_{min} = 25$ kPa.*

shape of the unloading-reloading curves may be modelled using the same model. The larger compressibility potential of the high-plasticity specimens may be modelled by scaling the fundamental model curve with an appropriate factor to achieve the proper change in void ratio along the stress path of a test.

As previously presented, all unloading and reloading branches were curved in the $\log(\sigma'_v)$-plot. This seems to suggest that the well-known Cam Clay model for 1D compression is inadequate to model the behaviour of very highly plastic specimens, such as the Danish Palaeogene clays. On the other hand the branches did bear some likeness to parabolas, as proposed in the framework presented by Hansen and Mise (1964). The original framework proposed by Hansen and Mise (1964) is introduced in chapter 7 along with the interpretations and modifications applied in the present project.

6.6 Unloading-reloading behaviour of tested specimens

As may be noted from the compression curves (figures 6.1 to 6.3) all unloading-reloading loops were closed, with a hysteresis size varying with smectite content and length of the applied stress path, which is most easily identified for the K40B60-tests. The larger the smectite content of the tested specimens, the larger the hysteresis in the unloading-reloading loops, and the longer the stress path, the larger the hysteresis (cf. the compression curve for K100B0 and K40B60 in figure 6.1). It may also be observed that the unloading branches initiated from the same σ'_{max} followed each other quite close (i.e. in loading programme 1, figure 6.1). This seems to suggest that all unloading loops may be modelled using the same expression, where σ'_{max} is a key parameter. A similar observation can be made for the recompression curves initiated from the same σ'_{min}-value.

Focusing on the unloading branches of the compression curves, presented in e.g. fig-

63

ure 6.1, it is clear that the magnitude of swelling during unloading increased profoundly with increasing content of smectite (the effect is discussed further in the following sections). Moreover, it should be noted that the unloading curves did not turn linear on the logarithmic stress scale, as reported in the Femern project for natural specimens (discussed in section 3.6.1) and for Boom and Ypresian clays presented by Cui et al. (2013) and Deng et al. (2012). It is remarkable that the linear unloading branches were not observed for the specimens tested in the main laboratory programme of the present study. On the contrary, the curvature of the swelling curves (on $\log(\sigma_v')$-scale) continued to decrease with unloading, but did not become linear, during the unloading-reloading loops performed.

It may be that the artificial specimens in the present study were not sufficiently unloaded to develop a linear swelling response in $\log(\sigma_v')$-space. Given the geological history of the natural specimens tested in the Femern project, it is not an unreasonable argument, as the natural specimens were heavily overconsolidated by past glaciations. Albeit, even if the two final points on the unloading branch for the artificial specimens are assumed to be representative of a linear response in $\log(\sigma_v')$-space, it should be noted that a relatively large unloading was required to reach this behaviour. The parameter R, denoting the transition from the curved to the linear part of the unloading branches (introduced in eq. (3.4)) was estimated to $R = 0.95$ for intact Palaeogene clay (Femern 2014e) as discussed in section 3.6.1. However, from the present tests (artificial clays) a much lower value was found in the range of $R = 0.15$–0.3 for final unloading branches of specimens tested after loading programme 1, as presented in figure 6.1. It is worth noticing that even unloading to $OCR = 18$ on the final loop of the test OE051S039 (K40B60 tested using loading programme 2) was insufficient for a linear unloading branch with $\log(\sigma_v')$ to be found. This seems to indicate that a very intensive unloading is necessary for obtaining this linear behaviour, or that the behaviour is triggered by the specific mineralogical composition, inherent structure or in situ conditions of the natural clays.

### 6.6.1 Correlation between compression and swelling index

Kulhawy and Mayne (1990) suggested that a linear relationship exists between the compression and swelling indices. Their observation was based on the linear virgin and unloading-reloading curves suggested by the Cam Clay model. Hence, the link between C_C and C_S may not exist for high plasticity clays as neither the virgin curves nor the unloading-reloading branches were linear in the main laboratory tests, carried out in the current study. Figure 6.9 illustrates the relationship between C_S and C_C for the main laboratory tests and the validation tests. For each test, a single value C_C was determined on the steepest part of the compression curve and three (two for load 4) values of C_S were obtained between $\sigma_{\max}'$ and $\sigma_{\min}'$ – one for each unloading-reloading loop. The values of C_S obtained for each test were each plotted against the value of C_C identified for the same test in figure 6.9.

As illustrated in figure 6.9, the best-fit linear relationship between C_C and C_S may describe the observations for K100B0 and K80B20 sufficiently accurate. However, when specimen plasticity increases, as for specimens K60B40 and K40B60, a single line is not adequate to describe the observations. For the specimens of highest plasticity, the curvature of the unloading-reloading loops significantly influences the C_S-parameters, as
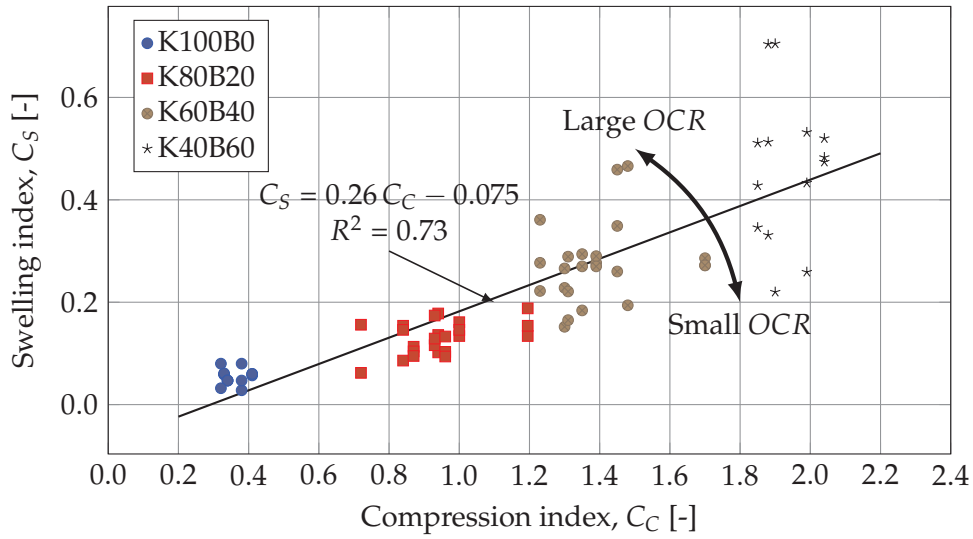
Figure 6.9: *Swelling index plotted against compression index for the four mixtures from the main laboratory programme.*

these were extracted from σ'_{max} to σ'_{min}. Thus, the length of the stress path (i.e. the OCR-value) must be accounted for when assessing secant parameters to be used for practical design. As illustrated in figure 6.9, high OCR-values (long stress paths) yields higher C_S values compared to smaller OCR-values (shorter stress paths).
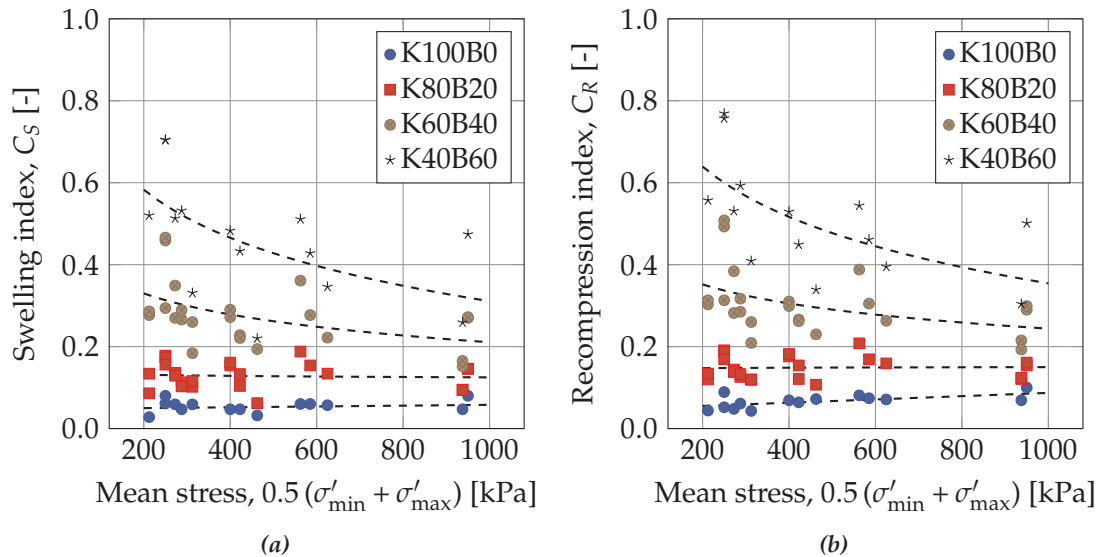
**Figure 6.10:** *Swelling and recompression index as a function of mean stress on the unloading-reloading loops.*

6.6.2 Effects of stress level on swelling and recompression index

As illustrated in figure 6.9, the *OCR*-value, or the length of the unloading-reloading loop, significantly influences the swelling index for the specimens of highest plasticity. As may also be observed from the unloading-reloading loops of loading programme 3, the C_S and C_R parameters decrease with increasing stress level. Figure 6.10 illustrates the parameters C_S and C_R for all unloading-reloading loops, plotted against mean stress for the respective loop. As may be noted from the figure, larger values of the swelling and recompression indices were identified at low stress levels compared to the values at high stress levels.

The data illustrated in figure 6.10 suggests that the unloading-reloading deformation potential is sensitive towards the mean stress level. Thus, for unloading-reloading at large stresses, a stiffer response may be anticipated compared to the response at lower stress levels.

6.6.3 Tangent stiffness for initial part of recompression curves

For each of the unloading-reloading loops, the stiffness on the initial part of the compression curves was calculated. The tangent stiffness, K_t was calculated as a tangent value from the increase in vertical stress and strain over the first load step on the recompression stress path for each unloading-reloading loop. Figure 6.11 illustrates K_t plotted against the void ratio increase, Δe (calculated as illustrated in figure 1 in the nomenclature). Δe was determined from σ'_{max} to σ'_{min} on the unloading stress path prior to the recompression branch, which were used for calculating K_t.


Figure 6.11: Plot of the tangent stiffness for the first reloading step against the void ratio increase in the former unloading.

As illustrated in figure 6.11, the initial tangent stiffness is strongly dependent on
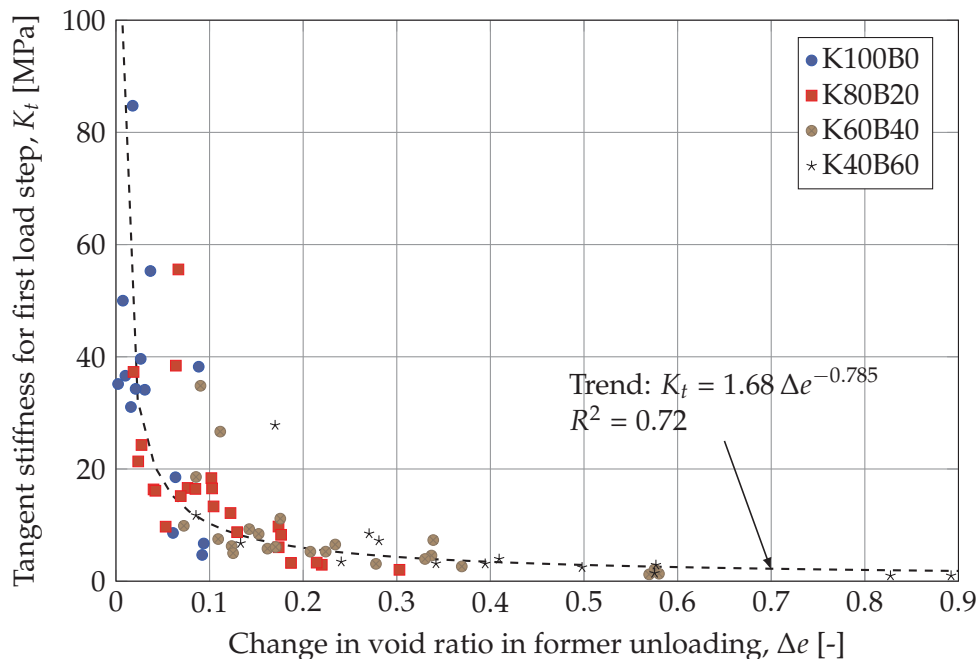
the change in void ratio prior to recompression. Naturally, large OCR-values implies a larger change in void ratio compared to small OCR-values as the stress paths are longer, but as illustrated in figure 6.11, the content of smectite in the K60B40 and K40B60 specimens seems to be the dominating factor. During unloading, the structure built up during former compression is (partly) destroyed, which in turn decreases the tangent stiffness.

6.7 Evaluation of vertical yield stress

As presented in section 3.1.2, the Danish high plasticity clays are prone to exhibit a "loss of stress memory", when tested in the laboratory, i.e. the vertical yield stress identified, using common methods as presented by Casagrande (1936) or Janbu (1969), is lower than the expected (or known) σ'_{max}. For the 18 tests in the main laboratory programme (Load 1–3), each reloading branch was analysed using both methods, and the vertical effective yield stress, σ'_{vy}, was identified, using the procedures outlined in appendix C.3.1. For each of the loops, the yield stress ratio, $YSR = \sigma'_{vy}/\sigma'_{min}$ was calculated and plotted against the overconsolidation ratio $OCR = \sigma'_{max}/\sigma'_{min}$, as presented in figure 6.12.
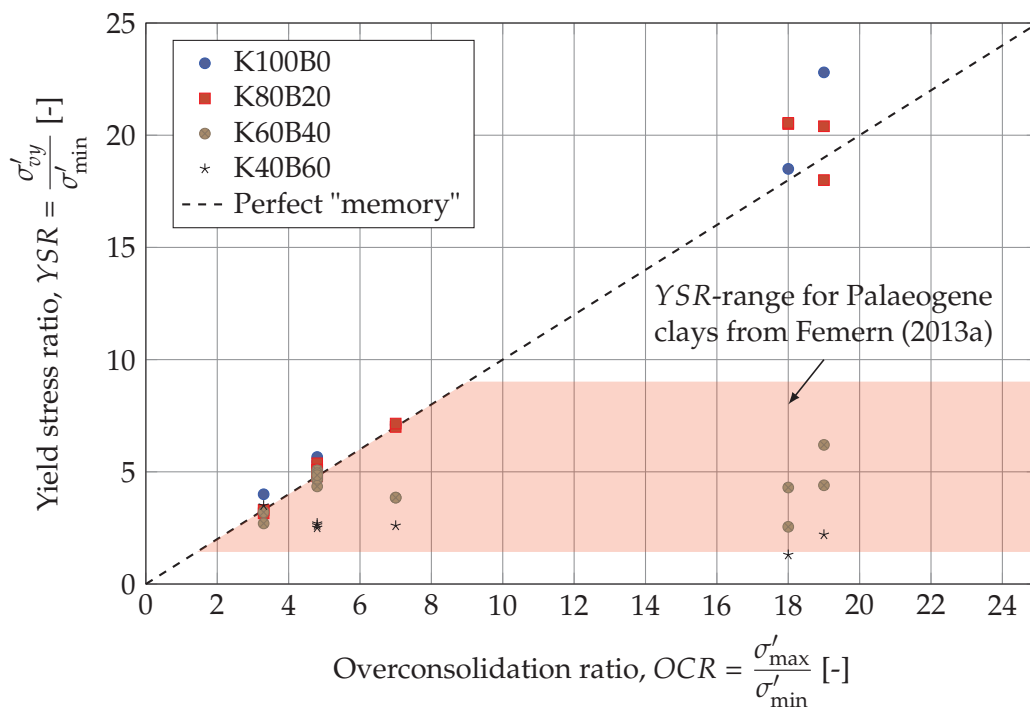

Figure 6.12: *Plot of YSR against OCR from the tests in the main loading programmes. Points that fall below the dashed line indicates specimens showing stress "memory loss" during testing.*

As may be observed from figure 6.12, the YSR-values calculated based on the deduced σ'_{vy}, were in line with the OCR-values, calculated based on the stress path, for all tests on K100B0 and K80B20-specimens, and for small OCR-values ($OCR \leq 5$) for the K60B40 and K40B60-specimens. However, for the longer unloading-reloading loops ($OCR > 5$) for K60B40 and K40B60-specimens, the calculated YSR-values were signi-

ficantly lower than the *OCR*-values. This behaviour was consistent with the observed behaviour in the pilot tests phase on the artificial clays, as described in appendix E.

The same trend is illustrated in figure 6.13. The figure illustrates effect of the void ratio increase during unloading from $\sigma'_{\max}$ to $\sigma'_{\min}$ on the ratio of $\sigma'_{vy}/\sigma'_{\max}$. σ'_{vy} was determined on the recompression curves and following virgin curves after reloading from $\sigma'_{\min}$ to a stress state above the former $\sigma'_{\max}$. Perfect "memory" (and expected behaviour for clays from traditional Danish geotechnical practice from e.g. glacial clay tills) would imply a ratio of unity, as $\sigma'_{vy} \approx \sigma'_{\max}$. As may be noted from figure 6.13 some of the K100B0 and K80B20 specimens was found to reflect a ratio above unity (implies $\sigma'_{vy} \geq \sigma'_{pc}$) which may be achieved due to post-sedimentation structure from secondary consolidation.
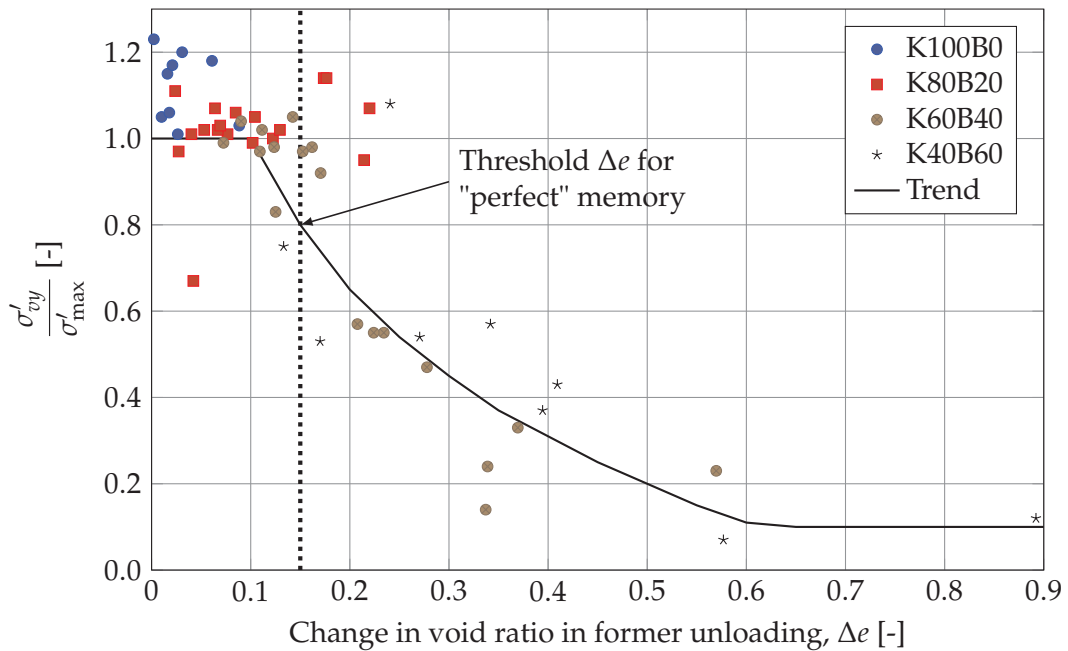
Figure 6.13: *Ratio $\sigma'_{vy}/\sigma'_{\max}$ plotted against the increase in void ratio from former unloading.*

As suggested by figure 6.13, the magnitude of increase in void ratio during unloading significantly affected the σ'_{vy}-value deduced on the following recompression branch, and thus the ratio $\sigma'_{vy}/\sigma'_{\max}$ decreased. This observation suggests that the increase in void ratio during unloading destroyed the structure obtained during former loading, which was reflected in $\sigma'_{vy} < \sigma'_{\max}$, as also discussed by Krogsbøll et al. (2012) and Mortensen (2012). As the increase in void ratio during unloading for a specific stress path is linked to the smectite content of the specimen, the destruction of specimens structure is related to specimen plasticity. This rationale justifies that the loss of stress memory is primarily observed for high plasticity specimens. This observation is similar to the observation for the K_t-values as discussed briefly in section 6.6.3. From the data illustrated in figure 6.13 a threshold value for the void ratio increase prior to onset of the stress memory loss may be identified. The threshold value is approx. $\Delta e \approx 0.15$, as also illustrated in the figure. It should be noted that this value applies for the artificial specimens tested within the present study. Natural specimens may display another (possibly lower) threshold

Δe-value.

The data presented on the figures 6.12 and 6.13, also suggests that a smectite content between 23.7 % (K80B20) and 49.2 % (K60B40) may be regarded as the threshold for the poor memory, cf. figure 6.13 and table 6.1. For K100B0 and K80B20 specimens, the correspondence between the maximal sustained vertical stress, σ'_{max}, and the identified σ'_{vy} was significantly better than for K60B40 and K40B60 specimens. The identified threshold of smectite content corresponds to $I_p = 83\text{--}140\,\%$. The value of $I_p \approx 80\,\%$ corresponds well with the lower end of the interval of plasticity indices encountered for natural Danish Palaeogene clays. On the other hand it is also clear from the tests that the magnitude of swelling of the specimens prior to recompression has a significant influence on the $\sigma'_{vy}/\sigma'_{max}$-ratio, which is not accounted for with a link between memory and I_p.

The loss of "stress memory" in terms of the illustrated reduction of σ'_{vy} may be related to the loss of strength with decreasing effective stress from e.g. excavation, as described from the SHANSEP relationship (Ladd and Foott 1974). As the effective stress decreases, the void ratio increases, which in turn diminishes strength.

6.8 Evaluation of swelling pressure

A series of four tests were carried out to evaluate the swell pressure of the four mixtures, after initial loading to a nominal vertical stress of 163 kPa in the acrylic consolidometers. As all specimens tested within the present project, the four specimens were initially prepared as slurries. The initial water content of the four slurries was $w = 1.5w_L$. After ended preconsolidation to 163 kPa, the samples were extruded and trimmed to the oedometer rings. This procedure represents the standard procedures applied during the present project, which is why the sub-study of swelling pressures verifies the selected level of initial loading in the main laboratory tests (100 kPa for K100B0 and K80B20 specimens and 200 kPa for K60B40 and K40B60 specimens, selected to avoid swelling on the first few load steps).

The initial parameters for the four presented specimens, in terms of void ratio, clay

Table 6.2: *State parameters for the specimens, where the swelling pressure was evaluated through testing.*

Mixture	Test number	Clay fraction* [%]	Smectite content*[†] [%]	w_L* [%]	e_0 [-]	S_0 [%]
K100B0	OE067S052	53	0.8	58.8	1.17	98.4
K80B20	OE066S051	58	23.7	113.9	1.56	99.9
K60B40	OE074S053[‡]	64	49.2	176.8	2.45	96.7
K60B40	OE075S054				2.23	98.1
K40B60	OE070S045	74	65.5	223.6	2.78	98.7

* Result for mixture
[†] Of clay fraction ($D \leq 2\,\mu m$)
[‡] Results not presented in figure 6.14 due to a procedural error during testing

fraction, smectite content and degree of saturation, are presented in table 6.2. In general the state parameters for the specimens tested in the current sub-study were within the limits of the state parameters observed for similar mixtures in the main laboratory programme, cf. tables 6.1 and 6.2.

An initial loading, or seating pressure, of 25 kPa was exerted on the specimens after they were installed in the oedometer load frames. After 5 min, the pressure heads of the automatic LoadTrac III load frame were locked in their current position, water was added to the carriage, and the specimen was allowed to react with the water in the carriage. The pressure exerted by the specimen on the pressure head was logged against time, and the results from the four tests are presented in figure 6.14.
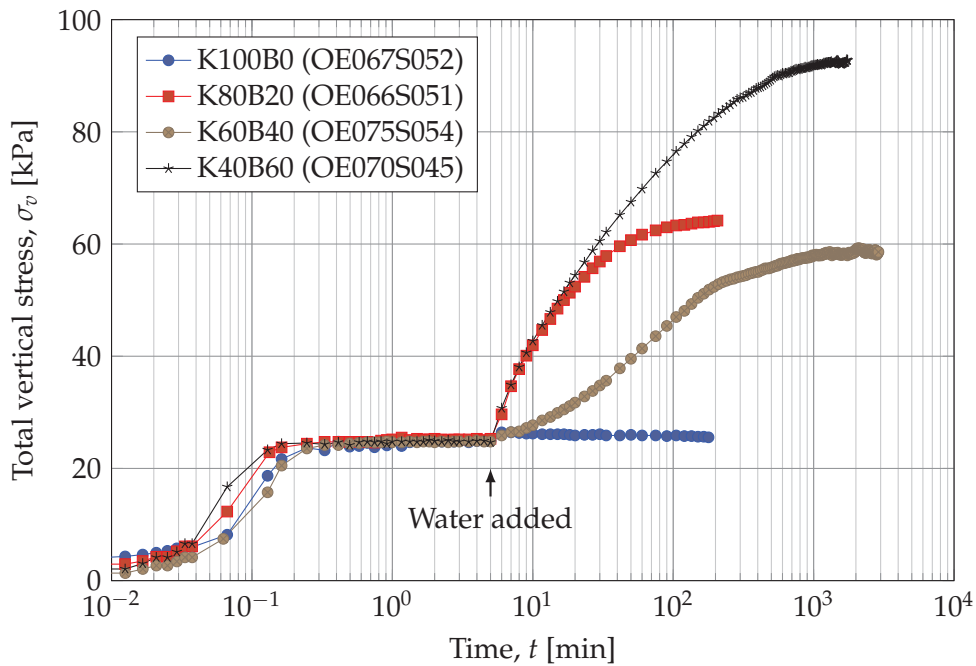

*Figure 6.14: Swelling pressure for the four tested mixtures.*

As may be observed from figure 6.14, the swelling pressure generally increased with increasing smectite content, except for the K60B40-specimen. It is unclear why this specimen did not follow the trend observed for K80B20 and K40B60, but showed a slower build-up of stress. However, the behaviour and magnitude of final vertical stress clearly deviates from the other tests. The results from the test of the K60B40-specimen were obtained in the second attempt of the swell pressure testing on this mixture. During the first attempt (test number OE074S053) the procedures were not strictly followed, as a small change in volume after flooding of the carriages was unintentionally allowed. As may be seen from the laboratory report, the total vertical stress in test OE074S53 developed in a similar way to what is presented in figure 6.14, i.e. a very slow build-up of vertical stress was seen after flooding of the oedometer cell carriage. This behaviour was not seen for the K80B20 and K40B60-specimens, which both showed a very rapid increase in stress after the oedometer carriages were flooded, as illustrated in figure 6.14.

The initial vertical effective stress for all specimens were identical prior to performing the swelling tests, i.e. $\sigma'_v = 163$ kPa. As may be observed from figure 6.14 the iden-

tified swelling pressure ranges σ_{sw} = 25–93 kPa. Thus, it is clear from the tests that the swelling pressures did not conform with the vertical effective stress prior to "sampling" of the slurry (i.e. unloading and extraction of the sample and following trimming of oedometer specimen). As may also be concluded from the tests, the stress applied for initiating oedometer test at σ'_v = 100 kPa for K100B0 and K80B20 specimens, and σ'_v = 200 kPa for K60B40 and K40B60 specimens may safely be assumed to be higher than the swelling pressure of the specimens.

6.9 Secondary consolidation during tests

Though not within the main scope of the present project, a brief discussion on the secondary consolidation observations for the four mixtures is presented in the current section. As the Casagrande (1938) approach was preferred for time curve interpretations, a phase of secondary consolidation was sought on each load step for the tested specimens. The secondary consolidation is expected to induce hardening on the specimens (Bjerrum 1967), which is why excessive secondary consolidation on one load step may affect the primary consolidation phase on the following load step, and hence the deformation parameters derived from the test.

The coefficient of secondary consolidation was derived for tests following loading programme 2, for each of the four mixtures, based on the procedures described in appendix C.3.2. An example of the $C_{\alpha\varepsilon}$-values derived on each of the steps in loading (virgin loading and reloading) is presented in figure 6.15 for test OE051S039 (K40B60-mixture). In figure 6.15 the arrows numbered 1 to 3 indicate the vertical effective yield stresses, σ'_{vy}, derived using the method described by Casagrande (1936) on reloading branch 1 to 3. As may be noted from figure 6.15, the arrows represent σ'_{vy}-values at the stress lev-
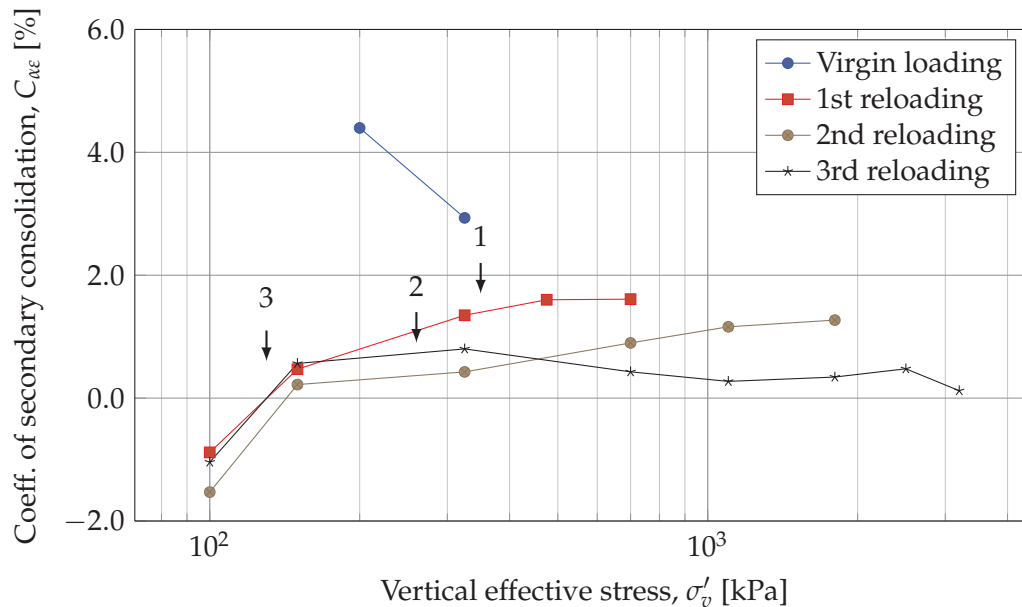
Figure 6.15: *Derived $C_{\alpha\varepsilon}$-values (may represent different intervals of time) for virgin loading and recompression load steps for test OE051S039 (K40B60).*

(a) $C_{\alpha\varepsilon}$ for OE047S035 (K100B0)

(b) $C_{\alpha\varepsilon}$ for OE056S046 (K80B20)

(c) $C_{\alpha\varepsilon}$ for OE058S041 (K60B40)

(d) $C_{\alpha\varepsilon}$ for OE051S039 (K40B60)
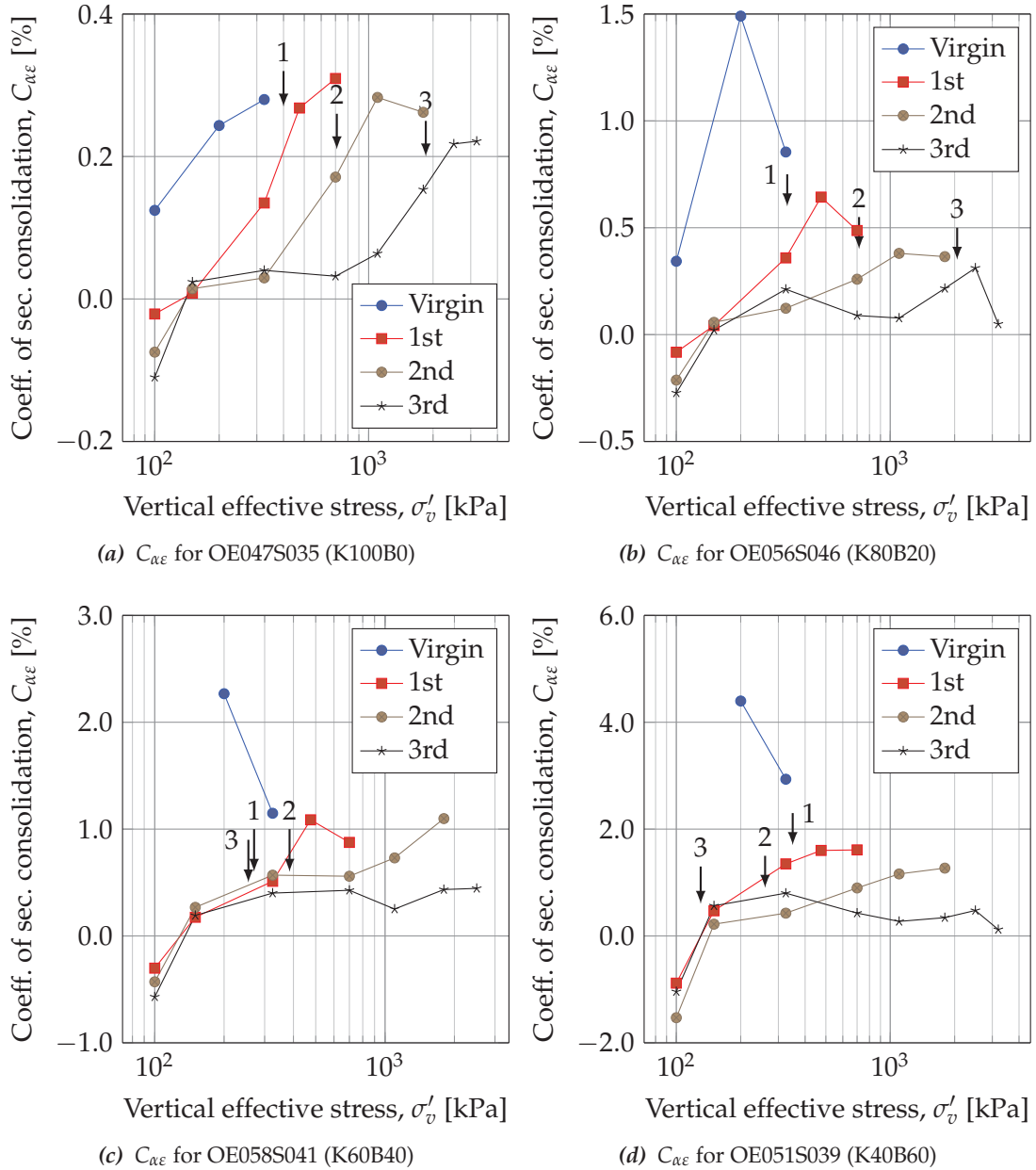
Figure 6.16: *Calculated $C_{\alpha\varepsilon}$-values (may represent different intervals of time) for each load step (during virgin loading and recompression) for selected specimens of the four mixtures. Entries in the legend box have been shortened – full description may be found in the legend box in figure 6.15.*

els where $C_{\alpha\varepsilon}$ turns constant for increasing stress. Thus, the σ'_{vy}-values indicated by the arrows are in concordance with the values indicated by the method proposed by Akai (1960). As may also be noted from the figure, σ'_{vy} does not conform with the previously sustained maximal pressure prior to unloading, except for the initial loop.

In figure 6.16 the $C_{\alpha\varepsilon}$-values for the four tested mixtures are compared. As for figure 6.15, the σ'_{vy}-values interpreted from the compression curves are presented with arrows, where numbers 1, 2 and 3 designate the number of the reloading branch relevant to the respective value of σ'_{vy}.

As may be inferred from figure 6.16 the magnitude of the $C_{\alpha\varepsilon}$-values increased with increasing smectite content of the specimens (the scaling on the y-axes in figure 6.16 should be noted). This may be expected if assuming a constant C_α/C_C-relation for the artificial specimens as for many natural specimens (Kulhawy and Mayne 1990; Mesri and Godlewski 1977). Moreover, the observations regarding the deduced yield stress from the Casagrande and Janbu methods may be repeated for the plots in figure 6.16. Following the procedure presented by Akai (1960), σ'_{vy} may be identified quite early on the recompression branches for the specimens presented in figures 6.16c and 6.16d, especially for unloading to high OCR-values. Thus, the methods of Akai (1960), Casagrande (1936), and Janbu (1969) indicate similar values of σ'_{vy} for the artificial specimens. As may be noted from figure 6.17, $C_{\alpha\varepsilon}$ is not constant for normally consolidated load steps for the specimens of highest plasticity. Instead, $C_{\alpha\varepsilon}$ decreases with increasing stress, which may influence the σ'_{vy}-interpretation by the method of Akai (1960).
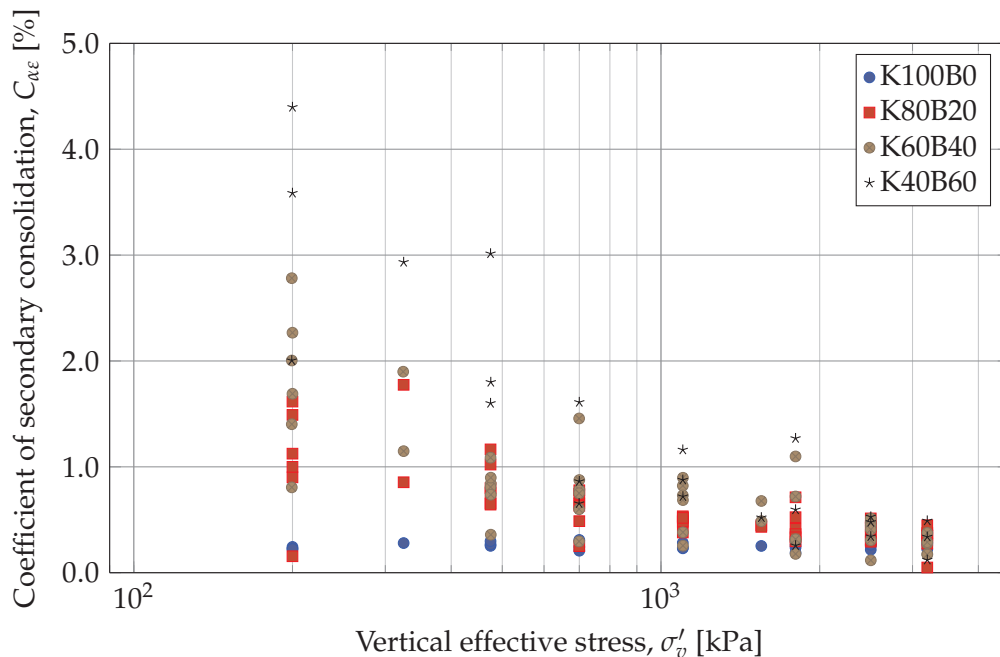
Figure 6.17: *Calculated $C_{\alpha\varepsilon}$-values for normally consolidated load steps (virgin loading) for all tests in the main laboratory programme. The large degree of scatter is introduced by different time intervals used for deriving the parameters.*

The coefficients of secondary consolidation for each load step in virgin loading conditions are presented in figure 6.17 for the four mixtures tested under the main laboratory

programme (Load 1–3). As may be noted from the figure, the $C_{\alpha\varepsilon}$-values were found to depend on the vertical effective stress (or the void ratio) and on the smectite content of the mixtures, as may also be noted from figure 6.16. As may be noted from figure 6.17, a factor of 8 to 18 was observed between the $C_{\alpha\varepsilon}$-values for K100B0 and K40B60-specimens for $\sigma'_v = 200$ kPa under normally consolidated conditions. However, for larger stress levels, the difference between the mixtures was smaller. As may be noted from figure 6.17 a significant deal of scatter is evident – even for mixtures of the same recipe. This is most likely introduced by using different time intervals for assessing $C_{\alpha\varepsilon}$.

6.10 Main results from sub-studies

As introduced previously, a number of sub-studies were carried out alongside the main laboratory tests. The present section briefly presents the main results from the largest of the sub-studies. Other smaller sub-studies, primarily focused on the effects of selected laboratory procedures are presented in appendix A to F. Details on the specimens tested in all sub-studies presented below may be found in tables A.1 and A.2.

6.10.1 Friction in the oedometer cell

A sub-study on the effect of frictional stress loss during the oedometer test on the deformation behaviour was published by Lodahl et al. (2016). The study focused on measurements of the stress loss due to friction between oedometer specimen and oedometer ring, and was based on a total of six tests on natural (two tests) and artificial specimens (four tests). A part of the tests were carried out in the nmGeo-cell, which facilitated measurements of the total stress transferred to the lower pressure head during testing. The cell is presented in more detail in section 1.7 of the laboratory report. The other part of the tests were performed in a steel-reinforced DSS-membrane, which was assumed to represent a friction-free environment.

During the study it was illustrated that a frictional stress loss was approximately constant (percent-wise) in the normally consolidated range, as 10 % to 24 % (interval for all three tested specimens) of the effective stress applied on the upper pressure head was lost. For overconsolidated conditions, the largest stress "loss" amounted $\approx$ −40 % (i.e. the vertical stress on the lower pressure head were larger than the stress on the upper pressure head). The largest stress loss was consistently identified at the $\sigma'_{\min}$-value for all specimens tested in the nmGeo oedometer cell. Thus, it was concluded that the tangent stiffness for the initial part of the recompression branch may be overestimated by 26 % to 28 % for artificial specimens and by $\approx$ 10 % for natural specimen. However, it was also illustrated that high plasticity specimens indeed showed a large initial stiffness when reloaded, even when the frictional stress loss was accounted for. More details on the study are presented in appendix H.

As only a limited set of parameters was investigated in the study presented in appendix H, insufficient data was available to correct all stress paths from the main laboratory tests for frictional stress loss. However, some considerations on the effects of the frictional stress loss is offered in section 8.4.

Dolby (2017) presented observations from testing of artificial K100B0 specimens, tested in a triaxial cell. Two specimens were tested inside a triaxial membrane to avoid

loss of vertical stress due to friction. The study also identified a percent-wise constant stress loss in virgin compression, as discussed above. Moreover, the study by Dolby (2017) showed, that the C_C-values were similar for K100B0 specimens tested in the triaxial cells and in an oedometer cell.

6.10.2 Effects of pore fluid salinity on deformation behaviour

Based on a range of tests performed for various pore fluid salinities and K100B0, K90B10 and K80B20 specimens, Sigurðardóttir and Dobrescu (2016) investigated the effects of pore fluid salinity on the deformation potential of clays. The study comprised tests performed with pore fluids created as solutions of $CaCl_2$ and NaCl salts (2 %, 4 % and 6 %), along with deionised water and the PC02 pore fluid, as presented in section 4.1.2. The study presents results for both Atterberg limits and compression characteristics. The study was submitted for publication by Lodahl and Sørensen (2017) (enclosed as appendix I).

Sigurðardóttir and Dobrescu (2016) concluded that both concentration and valence of the cations in the pore fluids influenced the Atterberg limits for the artificial clays containing smectite minerals. On the other hand, the tested specimens of pure kaolin showed insignificant sensitivity towards the pore fluid salinity. For the K80B20-specimens a reduction of the liquid limit of 40 % was found when comparing tests performed with deionised water and 6 % $CaCl_2$-solutions. Tests performed with lower salinity, or lower cation valence, generally showed smaller reductions of w_L.

The study presented by Sigurðardóttir and Dobrescu (2016) also showed that a significant reduction may be expected for the compression index when comparing IL oedometer test results obtained using deionised water and 6 % $CaCl_2$-solutions ($C_C = 0.77$ for deionised water and $C_C = 0.38$ for 6 % $CaCl_2$ for a K80B02-specimen). Moreover the data provided by Sigurðardóttir and Dobrescu (2016) indicated a linear correlations between w_L and C_C, w_L and C_S, and w_L and c_v, as presented by Lodahl and Sørensen (2017).

6.10.3 Effects of illite minerals on the compression behaviour

Ohler (2017) performed a study on the effects of pore fluid salinity on artificial mixtures containing illite minerals. The study comprised the effects of pore fluid salinity and illite minerals on the Atterberg limits along with the compression characteristics. The illite minerals used in the study were purchased as shales and were ground to powder prior to slurry mixing for testing. However, the ground illite-powder was rather coarse (Ohler 2017), which expectedly influenced the results.

For specimens containing kaolinite and illite minerals, Ohler (2017) found the liquid limits to increase with increasing pore fluid salinity (deionised water and 2 % NaCl-solutions were used for testing). However, all specimens containing smectite minerals showed a decrease in liquid limit when the pore fluid salinity was increased. From the presented tests it may be seen that kaolin-illite specimens reflected higher liquid limit than pure illite specimens, which most likely is related to the coarse illite powder used for testing. The tendencies observed for smectite-containing specimens support the trends presented by Sigurðardóttir and Dobrescu (2016).

For the IL oedometer tests presented by Ohler (2017) similar observations were made as for the Atterberg limit tests. For specimens containing smectite, a reduction of the compression index was observed as the pore fluid salinity increased. The reduction was seen to increase in magnitude with increasing smectite content of the specimens, which is parallel to the conclusions presented by Sigurðardóttir and Dobrescu (2016). The specimens containing illite and kaolinite only, showed a mild increase in compressibility, as the pore fluid salinity increased ($\approx 10\,\%$ increase was found when comparing specimens tested with deionised water and a 2 % NaCl-solution).

6.11 Comparison of test observations with trends from literature

As a number of the observations presented in the sections above dealt with the effects of smectite content, a brief comparison with data presented in literature is presented in the current section.

As observed from the main laboratory tests, the content of smectite affected the magnitude of the compression index, C_C, which increased with increasing smectite content. Similar observations are well-known from literature, both when the smectite content is known (Tiwari and Ajmera 2011) and where only liquid limit of the tested specimens are known (Skempton 1944; Sridharan and Nagaraj 2000; Yukselen-Aksoy et al. 2008). Correlations between w_L and C_C (e.g. (Nagaraj and Murthy 1986)) also verifies the observed trend. As illustrated in table 6.1, the initial void ratio of the specimens was dependent on the smectite content. Gunduz and Arman (2007) showed increasing C_C-values with increasing initial void ratio, which also is in concordance with the trends presented above. As discussed in section 3.4 a linear relationship between smectite content and w_L may be expected for kaolin-bentonite mixtures. Moreover, as a linear relationship have been identified between C_C and w_L, the increasing compressibility with increasing smectite content of the specimens is in line with previous observations.

As also observed from the main laboratory tests, the indices C_S and C_R were also dependent on the smectite content. Tiwari and Ajmera (2011) showed an increasing C_S-value with increasing smectite content and Gunduz and Arman (2007) identified a trend of increasing swelling index, C_S with increasing initial void ratio of test specimens. Both these studies thus confirm the trends observed in the present study as presented in figure 6.6b. The increase in w_L and C_C with increasing pore fluid salinity for illite-rich specimens, as illustrated by Ohler (2017), is also generally observed in literature (Rankka et al. 2004; Torrance 1984; Bjerrum and Rosenqvist 1956).

The virgin curves from the main laboratory testing were upwards concave as discussed in section 6.1. While this is not often observed for natural Danish Palaeogene clays, it is observed for tests on reconstituted clays by e.g. Burland (1990), as discussed in section 3.2. Moreover, the upwards concave shape of the virgin curves are captured by the models built on the diffuse double layer theory as presented in section 2.5. The data presented by Burland (1990) and modelled by the diffuse double layer theory relates to an initial reconstituted state of clays (similar to the specimens tested within the present project). Thus, the void ratio for high plasticity clays at low vertical stresses are very high, compared to the in situ void ratio of natural Danish Palaeogene clays.

Consequently, the absence of upwards concave virgin compression curves for natural intact Danish Palaeogene clays is likely to be caused by the relatively narrow range of void ratios encountered during testing. Considering the IL tests on natural Røsnæs clay presented by Femern (2013a), the initial void ratios were presented to be in the range e_0 = 0.83–1.18. For the specimen with the highest liquid limit (w_L = 183 %) in this set of natural Røsnæs clay, the initial void ratio was e_0 = 1.05 (σ'_{vo} = 225 kPa) and at σ'_v = 4800 kPa the void ratio was e = 0.71. This void ratio reduction of Δe = 0.34 is smaller than the reduction of void ratios observed even for the K100B0 specimens in the present study, which was in the range of Δe = 0.46–0.49 for compression from 100 kPa to 3200 kPa. As the virgin curves for the K100B0-specimens were nearly linear on the $\log(\sigma'_v)$-axis, this observation offers some explanation on the fundamental difference in the shape of the compression curves between natural and artificial specimens.

6.12 Summary of chapter

From the compression curves presented in figures 6.1 to 6.3 (larger versions and plots with linear stress axis are presented in appendix A.1, as stated previously), the following general conclusions be may be drawn, some of which are connected. For each of the conclusions, reference is given to a specific compression curve, which serves to illustrate the validity of the claim.

> All unloading and reloading compression curves were curved in the $\log(\sigma'_v)$-plot. This was especially clear for the largest loop of loading programme 1, presented in figure 6.1. This observation means that constant C_S and C_R-values only adequately describe an unloading-reloading loop, if $\sigma'_{\min}$ and $\sigma'_{\max}$ for the loop are used when the parameters are determined. Moreover, this behaviour causes the C_S and C_R-values (secant values between $\sigma'_{\min}$ and $\sigma'_{\max}$) to increase with increasing change of vertical stress (length of the stress path) during unloading and reloading. This behaviour is illustrated in figure 6.9.

> The virgin curves were increasingly upwards concave with increasing smectite content (cf. the virgin curve for K100B0 and K40B60 in figure 6.1), which was illustrated in figure 6.4. However, this may be an effect of the relatively large change in void ratios for the tested specimens compared to natural Danish Palaeogene clay (where a linear virgin curves are generally observed in the $(\log(\sigma'_v); e)$-space, as discussed above. It should be noted that the virgin compression curves for the K100B0-specimens were close to linear when plotted against $\log(\sigma'_v)$, as illustrated in figure 6.4.

> The secant parameters, C_S and C_R, increased with increasing smectite content for similar OCR-values, as illustrated in figure 6.5. For the largest unloading-reloading loop in loading programme 1 this may also be clearly observed in figure 6.1. For specimens K100B0 and K890B20, a link may be derived between C_C and C_S, but for specimens K60B40 and K40B60, the effect of OCR-value must be accounted for, as illustrated in figure 6.9.

> The C_S and C_R-values decreased with increasing stress level for a constant *OCR*-value, which may be deduced from figure 6.3. This was most clearly illustrated in test OE053S030 (Loading programme 3 on a K40B60-specimen), however the trend was similar for the other mixtures tested after loading programme 3 (and partly for tests following loading programme 2). The effect was discussed in section 6.6.2 based on derived relationships between C_S and C_R and the mean stress for the respective unloading-reloading loops.

> The tangent stiffness along the recompression curves decreased with increasing smectite content as illustrated in figure 6.7. Moreover, the decrease of E_{oed} near σ'_{vy} as known from Janbus framework (denoted the "saddle point" in the present text) is gradually blurred, as the smectite content increases.

> The difference between the preconsolidation pressure and the vertical yield stress increased with increasing smectite content. The magnitude of the difference was related to the void ratio increase during unloading, prior to recompression, as illustrated in figure 6.13.

> The coefficient of secondary consolidation was found to increase with increasing smectite content as illustrated in figure 6.16. Thus, a larger effect of creep on the results obtained for K40B60 specimens compared to the K100B0 specimens may be expected.

The key features identified within the present chapter, and briefly summarised above, constitute the basis for the model derivation, which is presented in the following chapter.

Log-parabolic framework for compression curves

During the design of the highway bridge across Little Belt, Denmark, the Little Belt clay was given much attention (Geoteknisk Institut 1961, 1962, 1964). The present chapter introduces the model developed by Hansen and Mise (1964). The model was based on the laboratory tests conducted on intact specimens of high plasticity Little Belt clay, related to the design of the highway bridge. The model was briefly introduced in section 3.6.1 and was chosen for the analyses presented within the current chapter, as the model reflects the curved unloading and reloading branches, which were observed in section 6.1 for the tests on artificial, reconstituted specimens. Moreover, the model was formulated to provide continuous curves by Hansen and Mise (1964), which is why tangent stiffness values are easily derived for practical use.

Based on observations from the main laboratory tests, conducted within the present study, a number of modifications are proposed to the model, which enables a better fit to the obtained data. Thus, the model proposed by Hansen and Mise (1964) is expanded to consist of five parameters instead of the original four, and these parameters have been formulated and determined to account for the smectite content of the tested artificial specimens. The modifications and some considerations on their physical meaning are presented and the process of fitting the proposed model to the main laboratory tests is outlined. Finally, some analyses of the strengths of the model are presented to evaluate its performance based on the results obtained during the main laboratory tests.

In the following chapter, the updated model, derived within the present PhD-study, is validated, based on the tests following loading programmes 4 and 5. Moreover, some considerations on the effects of pore fluid salinity and internal friction in the oedometer cell on the fundamental shape of the unloading-reloading compression curves are offered in the chapter 8. Chapter 9 presents the application of the model to reproduce the compression curves obtained from tests on natural, intact Palaeogene clays, available from literature. Moreover, some considerations on the practical use of the model are presented, along with three case-studies involving deformation of structures on Danish high-plasticity clays.

7.1 Original framework

Hansen and Mise (1964) suggested to apply parabolas for describing the unloading and reloading curves obtained from oedometer tests, when plotted in the semi-logarithmic stress-strain space $(\log(\sigma'_v), \varepsilon_v)$. This suggestion followed the observation that the unloading and reloading parts of the compression curves contained hysteresis and were fully reversible. The works of Hansen and Mise (1964) only relates to the overconsolidated parts of the compression curves. The model were derived based on IL oedometer tests performed on specimens of intact Little Belt clay, initially compressed to 3 MPa to 6 MPa, prior to unloading to in situ stress and initiation of project specific unloading and reloading loops. As the model presented by Hansen and Mise (1964) is fully empirical, i.e. fitted to test data, the testing procedure may be expected to influence the derived model.

Hansen and Mise (1964) proposed the following expressions for unloading, eq. (7.1a), and reloading, eq. (7.1b), stress-strain curves, respectively:

$$\Delta\varepsilon_v(\sigma'_v) = b \left(\log \frac{\sigma'_{max}}{\sigma'_v} \right)^n \qquad \text{(unloading)} \qquad (7.1a)$$

$$\Delta\varepsilon_v(\sigma'_v) = a \left(\log \frac{\sigma'_v}{\sigma'_{min}} \right)^m \qquad \text{(reloading)} \qquad (7.1b)$$

where the fitting coefficients $m = 2$, $n = 4/3$ and the fitting parameters a and b (termed parabolic indices) were chosen accordingly to the curve to be modelled (Hansen and Mise 1964). The values of σ'_{max} and σ'_{min} were defined within an unloading-reloading loop, as illustrated in figure 1 in the nomenclature. The parameters a and b are interdependent as may be inferred from eq. (7.1), when considering the assumption that all unloading-reloading loops are closed:

$$\frac{b}{a} = \left(\log \frac{\sigma'_{max}}{\sigma'_{min}} \right)^{m-n} \Leftrightarrow a = \frac{b}{\left(\log \dfrac{\sigma'_{max}}{\sigma'_{min}} \right)^{m-n}} \qquad (7.2)$$

b was proposed by Hansen and Mise (1964) to be related to the maximal sustained stress prior to unloading, σ'_{max}:

$$b \approx c \left(\log \frac{\sigma'_{max}}{\sigma'_s} \right)^{m-n} \qquad (7.3)$$

where σ'_s and c were fitting parameters. σ'_s may be viewed as a reference stress and c as a scaling parameter. Hansen and Mise (1964) proposed $\sigma'_s = 270$ kPa and $c = 0.0625$ as being fairly constant values for natural Little Belt clay, both of which must be expected to be influence by the in situ stress of the specimens and the loading programmes applied during testing for the natural specimens.

From eq. (7.1) it may be observed that the parameters n and m governs the curvature of the unloading and reloading curves, respectively, while c and σ'_s is merely scaling parameters on the parameter b (and thus also on a). Thus, c and σ'_s do not influence the
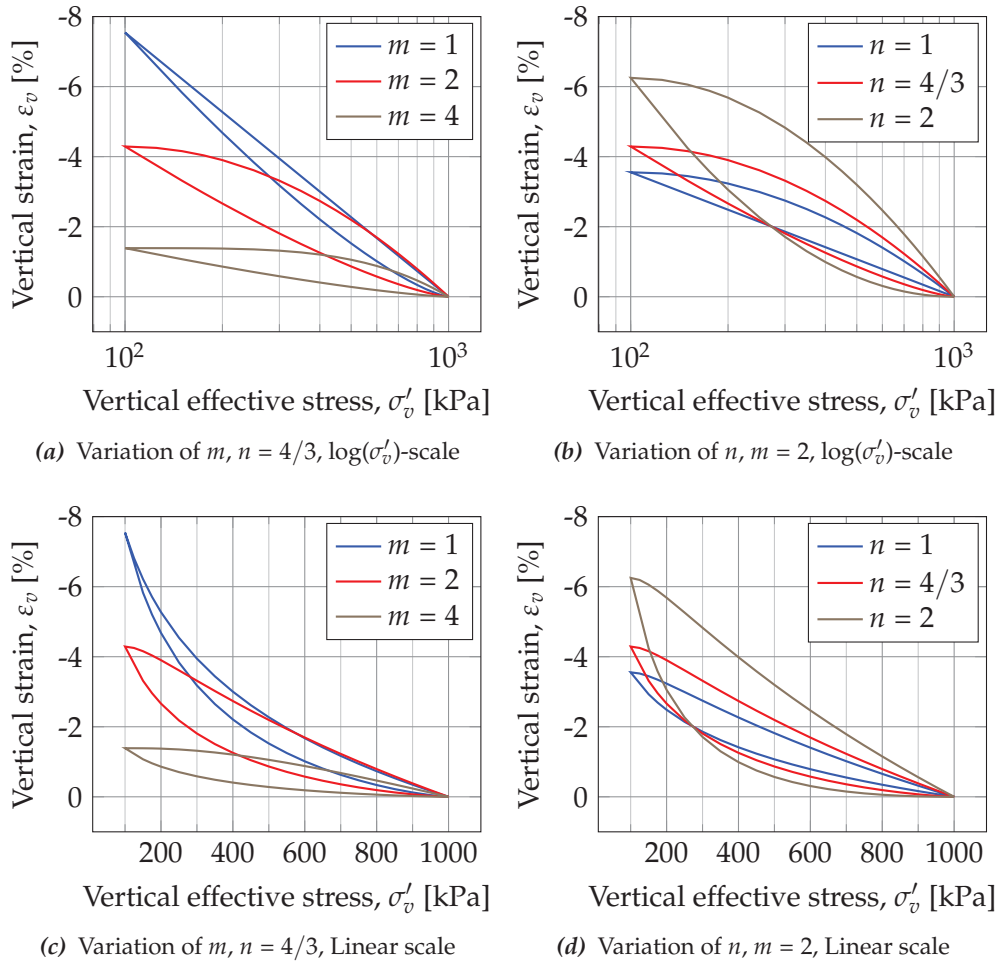
Figure 7.1: *Unloading-reloading loops in $\log(\sigma'_v)$-scale (Figures 7.1a and 7.1b) and linear scale (Figures 7.1c and 7.1d), modelled using parameters, $\sigma'_s = 270$ kPa and $c = 0.0625$ as presented by Hansen and Mise (1964), but varying the exponents m and n, respectively.*

shape of the unloading-reloading curves for a given set of m and n. From figure 7.1 the effect of varying the exponents m and n is plotted for an artificial unloading-reloading loop. As presented in the figure, the higher the exponents m and n, the more curvature on the curves, which may illustrate the versatility of the log-parabolic framework. As may be noted from the figures 7.1c and 7.1d a decrease in the exponent n or an increase in the exponent m, both imply a stiffer response, as the slope of a tangent to the modelled compression curves decrease. Applying values of m or $n = 1$ in eq. (7.1a) and eq. (7.1b) imply linear unloading and reloading curves (in $\log(\sigma'_v)$-space), respectively (as seen from figure 7.1), and use of m or $n < 1$ would imply upwards convex unloading curve and upwards concave reloading curve in $\log(\sigma'_v)$-space.

As may be observed from figure 7.1, the modelled unloading-reloading curves are closed, i.e. fully reversible during unloading and reloading, which is a consequence of the expression for a in eq. (7.2). Thus, the hysteresis observed from the main laboratory tests in the present PhD-project, presented in chapter 6, may be modelled by fitting the parameters m and n, used for calculating the parabolic indices a and b.

7.1.1 Preconsolidation pressure on reloading paths

The curvature of the reloading branches in the log-parabolic framework is reflected in the vertical yield stress, σ'_{vy} determined by e.g. Janbus method (Janbu 1969). In figure 7.2 the tangent stiffness calculated based on the model and parameters proposed by Hansen and Mise (1964) is plotted against mean effective stress. In the figure, the tangent stiffness from three oedometer tests performed by Geoteknisk Institut (1961) are also presented, as these tests were part of the original model derivation. As presented in figure 7.2 a vertical yield stress of approx. 200 kPa may be identified for the reloading curve obtained using the parameters proposed by Hansen and Mise (1964) (the reloading curve was modelled using $n = 4/3$ and $m = 2$ and is plotted in figure 7.1), which corresponds to the behaviour of the natural specimens also presented in the plot. This is noteworthy as all specimens included by Hansen and Mise (1964) were compressed to 3000 kPa to 6000 kPa prior to the unloading and reloading loops that formed the basis for the developed model. Thus, the derived σ'_{vy} is disproportionate to the σ'_{max} achieved during previous loading. In the curves presented in figure 7.2 the maximal stress used in the model was varied without resulting in a shift in the deduced vertical yield stress, σ'_{vy}, which seems to suggest that the value of σ'_{max} applied in the model proposed by Hansen and Mise (1964) is of minor importance on σ'_{vy}.
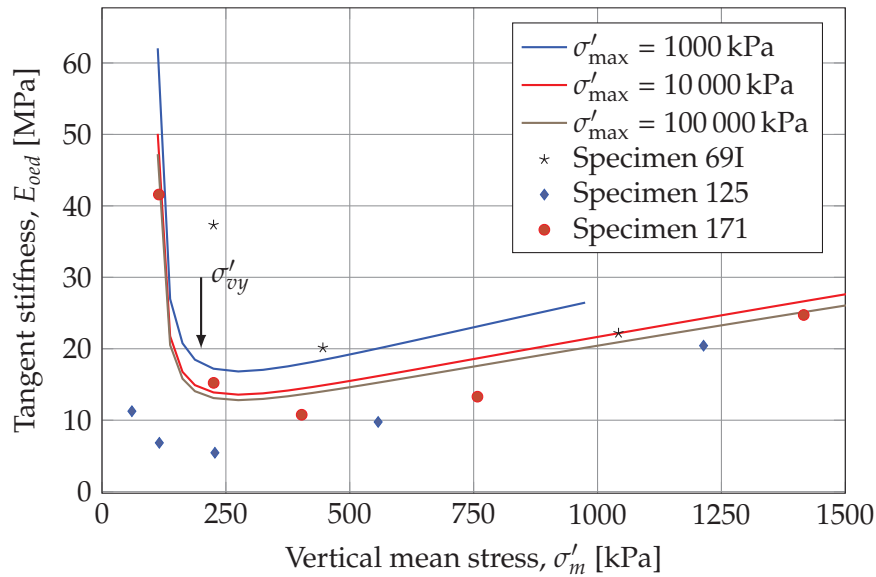

Figure 7.2: *Janbus framework applied to log-parabolic reloading curves proposed by Hansen and Mise (1964). All parameters applied in the modelling was obtained from Hansen and Mise (1964) except for σ'_{max} which was varied to illustrate the effect on the location of the saddle point (σ'_{vy}).*

When modelling a stress path consisting of several loops, the σ'_{max}-value applied during unloading and reloading must correspond to the maximal stress on the loop to be modelled. This is also the case when former unloading and reloading loops were performed with higher σ'_{max}-values. In this regard the model proposed by Hansen and Mise (1964) includes no (poor) "memory" of the clay for the specimens, where large volume changes are observed during unloading and reloading. This effect is in concordance

with the observed features from the main laboratory tests presented in chapter 6. The concept of poor stress memory was introduced in section 3.1.

7.1.2 Modelling of non-closed unloading-reloading loops

A key assumption of the framework proposed by Hansen and Mise (1964) is that all unloading-reloading loops are closed, when performed between the same values of σ'_{min} and σ'_{max}. The works by Hansen and Mise (1964) seems to suggest that unloading from a stress level below the maximal sustained stress in the test, $\sigma'_v < \sigma'_{max}$ requires the value of σ'_{max} to be updated to $\sigma'_{max} = \sigma'_v$.
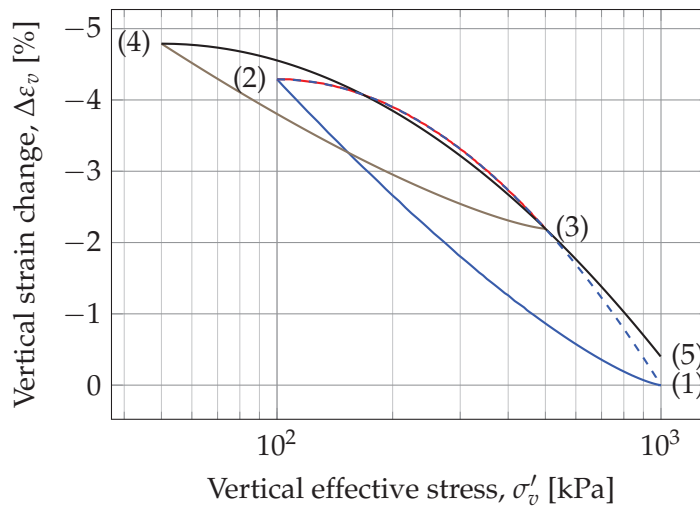
Figure 7.3: *Compression curves modelled using the model and parameters proposed by Hansen and Mise (1964) initiated from $\sigma'_v = 1000\,\text{kPa}$. Stress path $(1) \rightarrow (2) \rightarrow (3) \rightarrow (4) \rightarrow (5)$ is selected to illustrate model performance for non-closed loops.*

The dependency of σ'_{max} in the model for the unloading curves may be observed from figure 7.3. As may be noted from figure 7.3 the unloading paths are very dependent on the value of σ'_{max}, whereas the recompression branches are quite similar, i.e. less dependent on σ'_{max}, cf. stress paths $(1) \rightarrow (2) \rightarrow (3) \rightarrow (4) \rightarrow (5)$ and $(1) \rightarrow (2) \rightarrow (1)$, as also illustrated in figure 7.2. The effect illustrated in the figure is caused by the build-in lack of stress memory in the model, combined with the fixed σ'_s and fixed exponent in eq. (7.3), $m - n$. Modelling unloading-reloading loops with constant σ'_{max}, will cause all modelled unloading branches to follow the stress-strain curve $(1) \rightarrow (2)$ in figure 7.3 and all modelled reloading curves (regardless of σ'_{min}) to return to the initial strain at σ'_{max}, denoted (1) in figure 7.3. It is worth noticing, that the stress path from $(3) \rightarrow (5)$ in figure 7.3 was modelled using $\sigma'_v > \sigma'_{max}$, which is not the intended use of the model proposed by Hansen and Mise (1964).

7.1.3 Limitations of the original model

As presented in eq. (7.1) the model proposed by Hansen and Mise (1964) relies on four parameters, of which m and n were fixed for all clays and σ'_s and c were fitted to test results from a clay unit (through the parameter a, (Geoteknisk Institut 1964)) i.e. they were

constant for e.g. Little Belt clay. As such, all unloading-reloading loops were modelled with same shape of the unloading and reloading curves, regardless of the mineralogical composition of the specimens. This behaviour is in concordance with the observed behaviour from the specimens tested within the present project. However, the values for m and n proposed by Hansen and Mise (1964) does not yield the best fit to the compression curves obtained within the present project.

From the expression for b, eq. (7.3) it is seen, that the exponent was constant for all tested specimens. Moreover, the exponent, $m - n = 2/3$ was positive, which will cause an increase in the parameter b and thus in $\Delta\varepsilon$ (eq. (7.1a)), with increasing stress level. This behaviour suggests that the specimens would soften with increasing stress level, as σ'_s was a constant. Thus, when unloading to $OCR = 10$ (i.e. one logarithmic decade of stress) from a high stress the model will suggest larger swelling strains than when unloading to $OCR = 10$ from a lower stress level. The behaviour is illustrated in figure 7.3. This is in direct contrast to what was observed from the tested artificial specimens, where unloading from a larger stress caused a stiffer behaviour of the specimens, as presented in section 6.1. However, this effect may be amplified by the large change in void ratio observed during testing. As the specimens were compressed, the void ratio decreased significantly, and a stiffer response was thus expected. For natural clays, where the change in void ratio is expectedly smaller (for the stress range applied in the tests in the present project), the application of a constant exponent on parameter b will not influence results as gravely as if applied for the artificial specimens.

In the following, some minor modifications to the model presented by Hansen and Mise (1964) are proposed, which have proven to provide a better fit to the compression curves obtained within the present project. Moreover, where possible, the parameters are related to physical quantities.

7.2 Modified log-parabolic framework

In order to generalise the framework proposed by Hansen and Mise (1964), some modifications are proposed to the definition of the parameter b, cf. eq. (7.3) and eq. (7.4). Originally the framework was proposed based on strains. However, for the present project it is convenient to express the model in terms of void ratio. It should be noted that conversion from void ratio to strains is trivial.

In the original framework, the exponent in the expression for b was the difference $m - n$. In the present work, this exponent is selected independently from the m and n parameters. Thus, the parameter b^* is modelled using eq. (7.4), which also introduces the additional parameter k. The model proposed in the present project thus consists of five parameters opposed to the four parameters suggested by Hansen and Mise (1964).

$$b^* = C_b \left(\log \frac{\sigma'_{max}}{\sigma'_s} \right)^k \tag{7.4}$$

In eq. (7.4) the parameters k and C_b are fitted parameters which vary with the mineralogical composition of the soil specimen. The unloading-reloading curves are thus to be modelled by eq. (7.5), using eq. (7.5a) for unloading and eq. (7.5b) for reloading (equivalent to eq. (7.1) related to void ratio rather than strains), and the parameter a is to be

calculated from eq. (7.2), using b^* calculated with eq. (7.4). Eq. (7.2) (slightly modified) is repeated below to provide the complete framework:

$$\Delta e(\sigma_v') = b^* \left(\log \frac{\sigma_{max}'}{\sigma_v'} \right)^n \quad \text{(unloading)} \tag{7.5a}$$

$$\Delta e(\sigma_v') = a \left(\log \frac{\sigma_v'}{\sigma_{min}'} \right)^m \quad \text{(reloading)} \tag{7.5b}$$

$$a = \frac{b^*}{\left(\log \dfrac{\sigma_{max}'}{\sigma_{min}'} \right)^{m-n}} \tag{7.2 revisited}$$

In the following sections a more detailed explanation is offered on the individual parameters in the proposed modified framework. Where appropriate, the parameters have been related to physical quantities and the effect of varying their magnitude is outlined. The influence of the additional parameter k, proposed in the present project, is also discussed in detail in the following sections.

7.2.1 Influence of n and m

The model framework is illustrated in figure 7.4, where the effects of varying m and n are illustrated when plotting void ratio change against $\log(\sigma_v')$ and σ_v'. As illustrated in the figure, the new formulation presented in eq. (7.5) fully separates the expressions for unloading and reloading, as the unloading curves are identical for all choices of m (figures 7.4a and 7.4c), and the reloading curves are identical for all n-values (figures 7.4b and 7.4d). The behaviour is rooted in the less restrictive choice of the exponent k on the factor b^* (eq. (7.4)) in the proposed model formulation opposed to the fixed exponent $m - n$ on the factor b proposed by Hansen and Mise (1964) (eq. (7.3)).

The fitting of m and n may be carried out on normalised curves, which greatly increases the number of available points for the fitting procedure, as may be observed from figure 6.8. This approach highlights that m and n only govern the shape of the curves and not the magnitude of Δe during unloading and reloading. Performing unloading or reloading over one logarithmic decade of stress reduces eq. (7.5a) and eq. (7.5b) to $(\log 10)^n = (\log 10)^m = 1$, which is why the swelling index over one stress decade, $C_{S,lcs}$ is not affected by the choice of m and n. However, if the stress path is shorter or longer than one logarithmic decade, the C_S-value will be affected as it is defined as a secant value.

7.2.2 Influence of C_b

As may be deduced from eq. (7.4), the parameter C_b is a scaling parameter. When unloading exactly one logarithmic decade of stress, the ratios $\sigma_{max}'/\sigma_v' = \sigma_{max}'/\sigma_{min}' = 10$. Thus, the parameters $a = b^* = C_b$, cf. eq. (7.1) and eq. (7.2). Based on this observation, the value of C_b may be interpreted as the $C_{S,lcs}$-value when unloading from $\sigma_{max}' = 10$ kPa to $\sigma_{min}' = 1$ kPa. This is illustrated in figure 7.5 where the modelled stress path for this

(a) Variation of m, $n = 4/3$, $\log(\sigma'_v)$-scale

(b) Variation of n, $m = 2$, $\log(\sigma'_v)$-scale

(c) Variation of m, $n = 4/3$, Linear scale

*(d)* Variation of n, $m = 2$, Linear scale
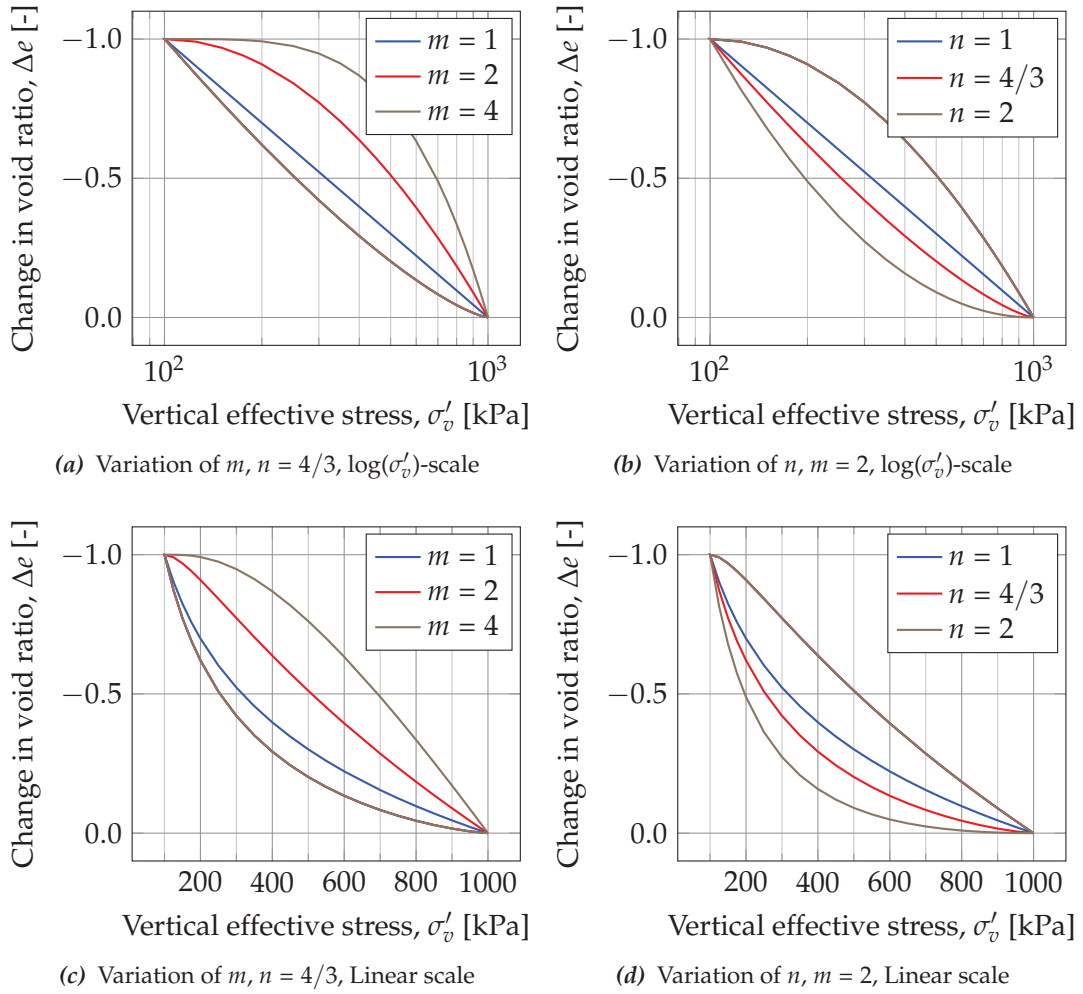
Figure 7.4: *Unloading-reloading loops in $\log(\sigma'_v)$-scale (Figures 7.4a and 7.4b) and linear scale (Figures 7.4c and 7.4d), modelled using parameters, $\sigma'_s = 1\,\mathrm{kPa}$, $k = 0$ and $C_b = 1$ for the modified framework, but varying the exponents m and n, respectively.*

unloading and reloading loop is presented. Though C_b may be physical related to the swelling properties of a soil specimen, unloaded from $10\,\mathrm{kPa}$ to $1\,\mathrm{kPa}$, development of tests to allow easy determination of this property for practical purposes may pose a challenge due to the very low stress level.

7.2.3 Influence of k

The parameter k accounts for the change in secant slope on the unloading-reloading branches at different stress levels (i.e. the change in the C_S-parameter with stress level, determined as a secant value from $\sigma'_{\max}$ to $\sigma'_{\min}$). As described in chapter 6, the secant value of C_S for the main laboratory tests decreases with increasing stress level. Thus, the parameter k is negative for the artificial specimens. The absolute value of k is seen to increase with increasing smectite content from the observations presented in section 6. Thus, k governs the size of a unloading-reloading loop at a given stress level, relative

to the size of the loop from 10 kPa to 1 kPa, which is defined by C_b. Based on the choice of the parameter k, different magnitudes of reduction of b^* with increasing stress levels may be modelled, as illustrated in figure 7.5.
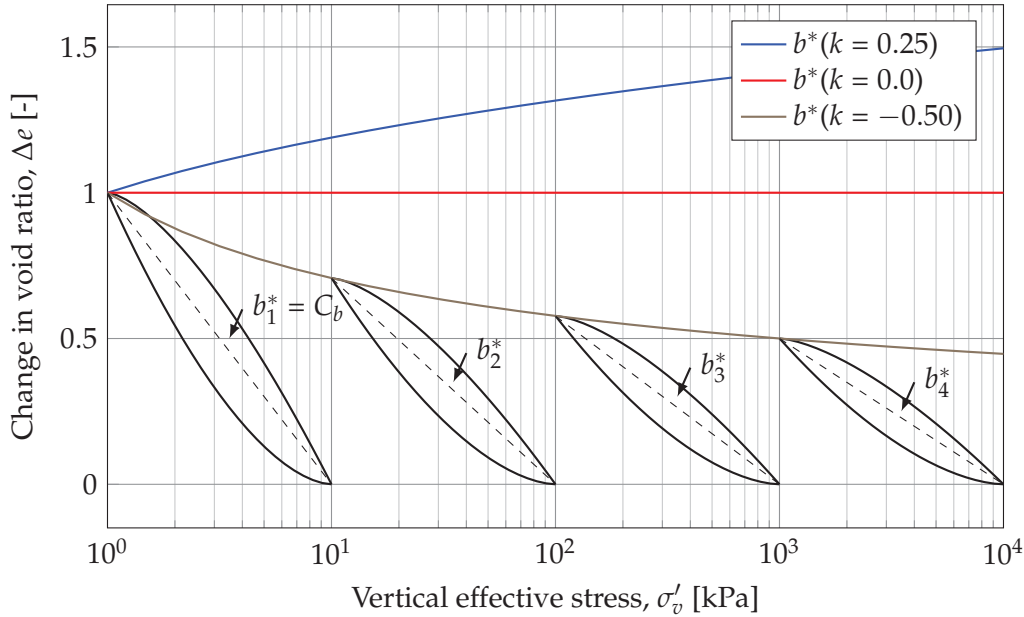
Figure 7.5: *A range of unloading-reloading loops illustrating the effect of the k-parameter on b^*. The curves for $b^*(k)$ denotes the effect of k on the decline in the secant C_b of the curves (secant is indicated with a thin dashed line), $C_b = b_1^* > b_2^* > b_3^* > b_4^*$ for $k = -0.5$.*

As may be inferred from figure 7.5 a choice of $k = 0$ enables modelling of a material where the secant swelling index (and recompression index) is not affected by the stress level. This behaviour is comparable with the Cam Clay model, where all unloading and reloading paths are modelled using a constant slope κ (Roscoe et al. 1958). It should however be noted, that the Cam Clay model defines κ (and λ as discussed for the virgin curve later) based the natural logarithm to mean stress, $\ln(\sigma'_m)$, which does not allow for direct comparison between the parameters in the two frameworks.

7.2.4 Influence of σ'_s

The value of σ'_s = 270 kPa proposed by Hansen and Mise (1964) may be viewed as a reference stress state. This stress state was originally chosen somewhat arbitrary during fitting to the performed oedometer tests and was connected to the sample disturbance (Hansen and Mise 1964) and possibly also to the effects of the applied loading programme and the relatively small natural variation of the tested natural Little Belt clay specimens, compared to the variation in consistency of the specimens tested within the present project.

In the present PhD-project all modelling is performed using σ'_s = 1 kPa. With this choice, the reference state for the unloading and reloading models is the void ratio at 1 kPa after unloading from 10 kPa, which is somewhat parallel to the reference state of the Cam Clay model (The Cam Clay model relates the virgin curve to the void ratio 1 kPa) (Roscoe et al. 1958). As an interesting note, the unloading and reloading models
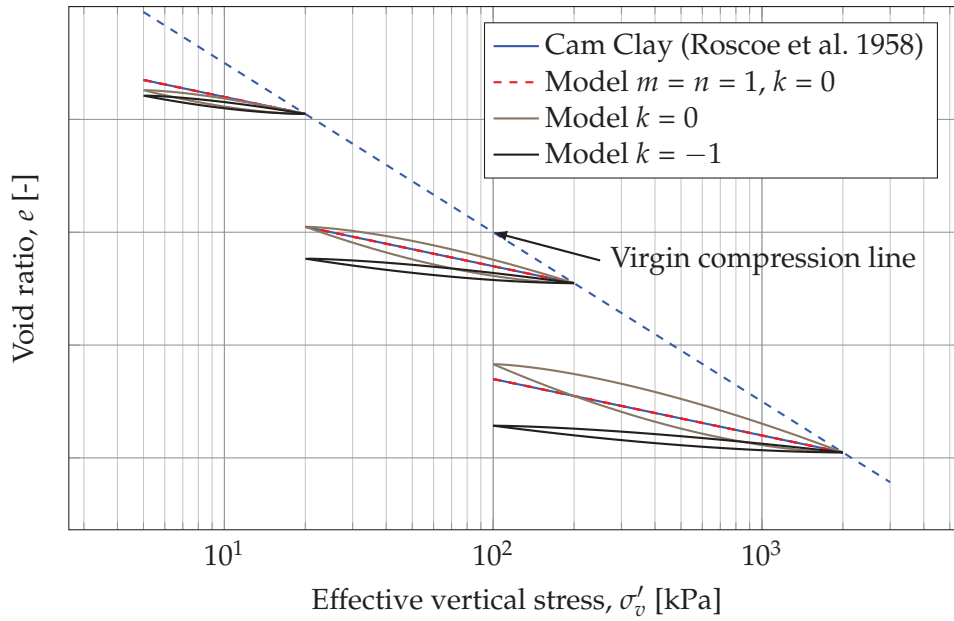
Figure 7.6: Models describing unloading and reloading curves. Note how the proposed model reduces to the Cam Clay model dependent on selected parameters. The Cam Clay model is expressed in terms of mean stress, which may be transferred to effective vertical stress using K_0. The k-parameter in the model was introduced in the present PhD-project.

proposed in eq. (7.5), reduce to the Cam Clay model for an overconsolidated stress state by choosing $m = n = 1$ and $k = 0$ as illustrated in figure 7.6.

For loading over exactly one logarithmic decade of stress, the parameters a and b^* reduces to $C_S = C_R$, which denote the secant parameters between σ'_{max} and σ'_{min} for the selected formulation of the model. For loading on a stress path shorter than one logarithmic decade, the proposed model will yield a stiff response compared to e.g. the Cam Clay model, whereas stress paths longer than one decade of stress yields softer response (for $k = 0$). An illustration of the three lengths of stress paths is given in figure 7.6.

7.2.5 Yield stress along reloading path

The effects of the curved recompression curves (discussed in section 7.1.1) are maintained in the proposed model, as the basal shape of the recompression curve is governed by the choice of the parameter m. Thus, based on the values of C_b and k, the recompression curves will be scaled. A more pronounced scaling of the recompression curves will thus lead to a stronger visual impression of a curvature on the recompression path, which may influence the determination of the yield stress (discussed in section 7.6) as the slope of the tangent at low stresses is relatively small for high plasticity specimens as illustrated in figure 6.11. Moreover, as illustrated in section 6.1, the virgin curves are upwards concave. Thus, the transition from the convex recompression branch and the concave virgin curve may be very difficult to visually identify for high plasticity specimens.

7.3 Procedure for fitting model to main tests

7.3.1 Parameters n and m

The parameters n and m may be fitted to the normalised unloading-reloading loops. As all normalised loops have the same fundamental shape, as presented in chapter 6, it seems that the parameters m and n are constant for all the tested mixtures within the present project. A spreadsheet-based routine was set up to minimise the sum of the squared residuals during fitting. The normalised unloading and reloading branches were analysed separately. However, all stress paths for all mixtures were included in the fits for the unloading and reloading branches, respectively. The fitting was performed by minimising the square of the error, F, between test observations e_i and the value predicted by the model, $\hat{e}_i$ according to eq. (7.6). The test observation for the minimum stress on an unloading-reloading curve (i.e. the void ratio at σ'_{min}) was included in fits for both branches.

$$F = \min \sum_{i=1}^{n} (\hat{e}_i - e_i)^2 \tag{7.6}$$

By minimising the sum of the squared errors on each stress path, the parameters $n = 1.67$ and $m = 1.42$ were reached for the unloading and reloading branches, respectively. The coefficient of correlation was calculated after eq. (7.7) to $R^2 = 0.997$ and $R^2 = 0.974$ for the unloading and reloading branch, respectively. In eq. (7.7) F is calculated using eq. (7.6) and $\bar{e}$ denotes the mean value of the data set for the fitted curve.

$$R^2 = 1 - \frac{F}{\sum\limits_{i=1}^{n} (e_i - \bar{e})^2} \tag{7.7}$$

The normalised modelled curves obtained using the fitted values of n and m are illustrated for each loop in chapter 11 of the laboratory report. As may be noted, when comparing the fitted model and the compression curves obtained from testing, a discrepancy was present for some of the points on the recompression branches. The largest discrepancies were found on loop 2 and loop 3 of loading programme 2 (normalised loops from testing are compared with normalised loops from modelling in figure 11.5 and 11.6 in the laboratory report, for loop 2 and loop 3 respectively). For these two loops, the normalised recompression curves seems to flatten with an increase in smectite content (i.e. a decrease in the parameter m), with is not captured in the proposed model. However, it is believed that the observed difference between the model and the tests for the specimens of higher plasticities may be caused by secondary consolidation during testing. As the curves are normalised based on $e(\sigma'_{max})$ prior to unloading and $e(\sigma'_{min})$, see eq. (6.1), the effects of secondary consolidation were accumulated during the tests, and would thus have affected the final points heavier than the first points on the unloading-reloading loops. As discussed in section 6.9 the magnitude of secondary consolidation was found to be up to a factor of approx. 20 larger for the K40B60 specimens compared to the K100B0 specimens at low stresses (NC conditions). At larger stresses the difference in the $C_{\alpha\varepsilon}$-values was smaller. From figure 6.16 a value of approx. five may be deduced for a stress level of approx. 500 kPa to 1000 kPa.

7.3.2 Parameters k and C_b

The parameters k and C_b were fitted based on results from the tests on each mixture individually, as the two parameters are related to the smectite content of the specimens.

As may be inferred from eq. (7.4) and eq. (7.5) the parameters k and C_b relate to the coefficient b^*, which does not vary with the effective vertical stress during an unloading-reloading loop (as σ'_{max} is constant). To obtain a fit of C_b and k, the parameter b^* was fitted to minimise the square of the errors on the unloading-reloading loops, using the values of n and m previously found based on the normalised curves. Due to the link between parameters a and b^* in eq. (7.2), the parameter a change with the fitting of b^*, which enables the recompression branches to be included to determine the optimal b^*-values. For each loop on the stress paths of the main laboratory tests, the square of the residuals was minimised to obtain the best fit of the b^*-parameter. Figure 7.7 illustrates the power function fitted to the obtained optimal b^*-parameters from each test on the K40B60-mixtures, and the values of $z = \log(\sigma'_{max})$ for each loop.
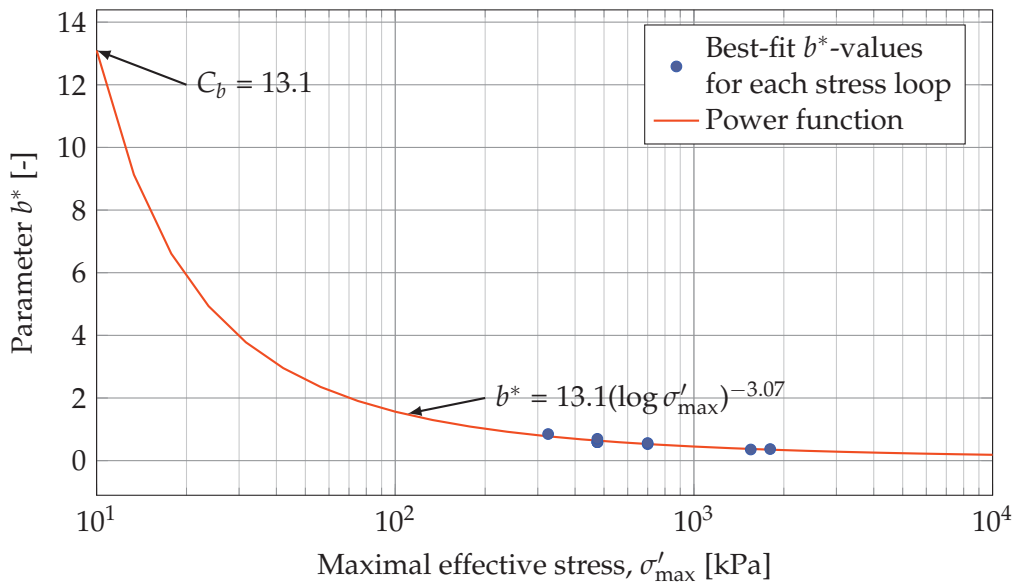
Figure 7.7: *Fitting of power function to b^* against $z = \log(\sigma'_{max})$ for the K40B60-mixtures tested in the main laboratory tests (3 oedometer specimens with at total of 9 unloading-reloading loops).*

As may be noted from figure 7.7 the intersection with the y-axis at $\sigma'_{max} = 10\,\text{kPa}$ corresponds to the definition of C_b from subsection 7.2.2, as the value corresponds to unloading from $\sigma'_{max} = 10\,\text{kPa}$ to $1\,\text{kPa}$. Moreover, the exponent on the fitted expression in figure 7.7 was defined as k in subsection 7.2.3, as may be seen in eq. (7.4).

The fitting procedure was carried out on each of the four mixtures, yielding four sets of values of C_b and k. For the K100B0 mixtures, the fitting procedure suggested $k = 1.60$, which would suggest an increase in compressibility when unloading one logarithmic decade of stress from an increasing σ'_{max}. This is not in concordance with the observations from the tests, where generally a decrease in compressibility, with increasing σ'_{max} was observed, as presented in chapter 6. Focusing only on the tests performed on the K100B0-mixtures the variation in the derived C_S is minor, which is why these
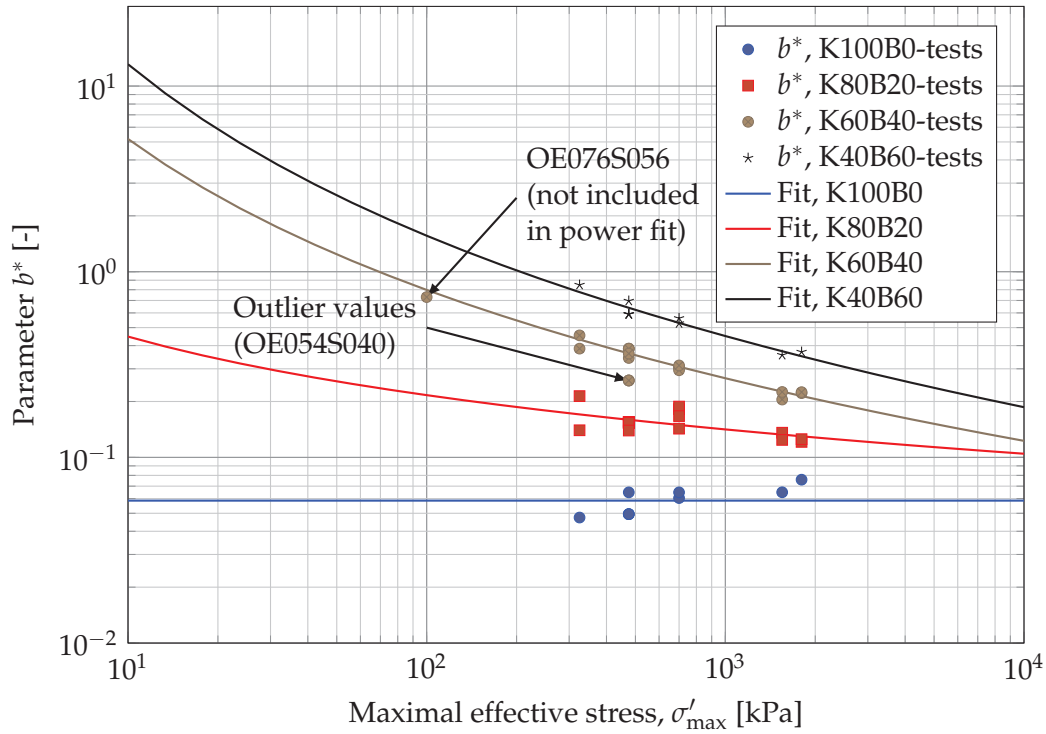
Figure 7.8: *Fitting of power function to the fitted values of b* against z = log(σ'_{max}) for the main laboratory tests (3 oedometer specimens with at total of 9 unloading-reloading loops for K100B0 and K40B60, and 6 oedometer specimens with at total of 18 unloading-reloading loops for the K80B20 and K60B40 mixtures). The marked outlier values for OE054S040 were not included in the fitting of k and C_b for K60B40-mixtures.*

tests were modelled using $k = 0$ and $C_b = \bar{b}^* = 0.059$, where $\bar{b}^*$ is the mean value of the fitted b^*-values. Figure 7.8 presents the b^*-values fitted to the laboratory tests and the corresponding power fits to identify C_b and k for each of the tested mixtures.

As illustrated in figure 7.8, the data points acquired from the main laboratory programme are all situated from $\sigma'_{max} = 325$ kPa–1800 kPa, which is quite far from the fitted value of C_b at $\sigma'_{max} = 10$ kPa. Thus, to strengthen the reliability of the obtained fits, a series of tests carried out with lower σ'_{max}-values may be performed, which would reduce the gap between data points and the obtained C_b-values for the different mixtures, and hence strengthen the outcome of the procedure. The optimal test for determining k and C_b could be to load a slurry specimen to 10 kPa, unload to 1 kPa, then load to 100 kPa and unload to 10 kPa and so on. The loops at the largest stress levels may be performed on a preconsolidated slurry specimen, parallel to the procedures applied within the present project.

Due to constraints of time, the type of testing proposed above was not extensively performed within the present PhD-project. However, a single test was carried out, namely OE076S056, which were installed in the oedometer cell as a slurry, loaded to 100 kPa, unloaded to 10 kPa and then reloaded past 100 kPa. Thus, a complete unloading-reloading loop between 10 kPa and 100 kPa was undertaken in the test. The best b^* parameter identified for test OE076S056 is plotted in figure 7.8. Even as this point was not included in the power function fit for K60B40-mixtures, a very nice fit between the trend

91

for the K60B40-mixtures and the data point for test OE076S056 may be observed from the figure.

From figure 7.8 a general trend of increasing curvature (increasing absolute size of k) and increasing intersection with the y-axis, i.e. increasing C_b-values, of the fitted power functions may be noted with increasing smectite content of the specimens. This is consequently also observed from the fitting constants for each mixture. Figure 7.9 presents the fitting parameters, k and C_b as a function of the smectite content of the tested mixtures. As may be noted from the figure, a linear trend line may be proposed for the relationship between smectite content of the clay fraction and the parameter k, whereas the proposed relationship between smectite content and C_b is a power function. It should be stressed that only a very limited number of points were available for curve fitting, which is why no firm conclusions may be drawn from the available data.

(a) Parameter k
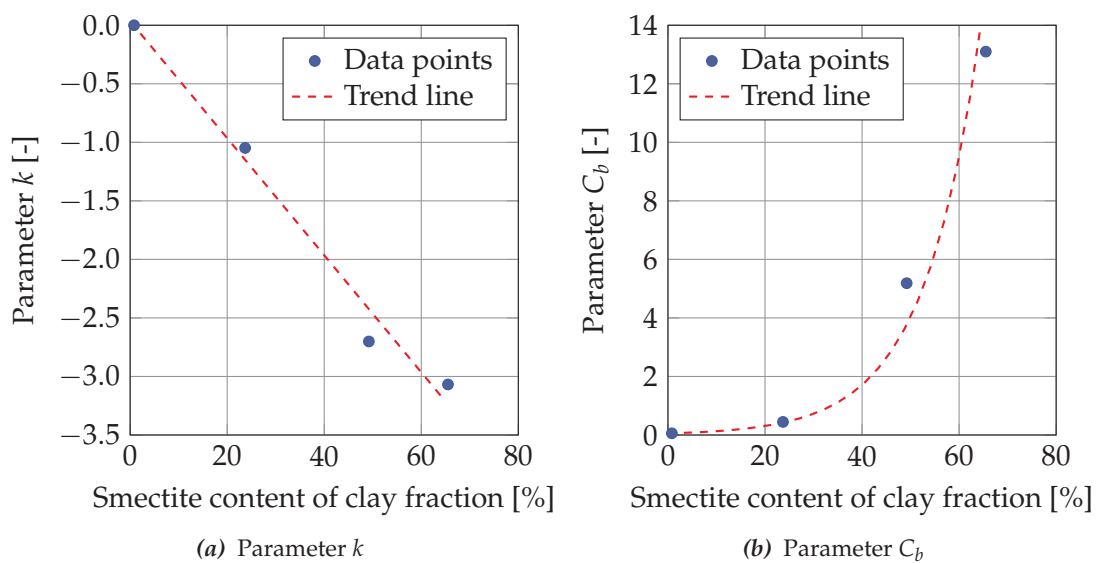
(b) Parameter C_b

Figure 7.9: *Trend lines for parameters k and C_b as a function of smectite content of the clay fraction of the tested mixtures.*

7.4 Modelling of virgin curves from main tests

As may be observed from the plots of the main laboratory tests in chapter 10 of the laboratory report, the compression curves for normally consolidated load steps are up-wards concave when plotted against $\log(\sigma'_v)$. Traditionally, the virgin curves are assumed to be linear when plotted on a logarithmic stress axis (Terzaghi et al. 1996; Holtz et al. 2011), which are also reflected in e.g. the Cam Clay model (Schofield and Wroth 1968), though using the $\ln(\sigma'_m)$-axis. The difference between expected behaviour for natural clays and the behaviour observed for natural specimens is expected to be grounded in the high initial void ratios for the artificial specimens. The initial void ratio for the oedometer tests performed for the Femern project (used for estimating σ'_{vy}) spanned the range of 0.825 to 1.82 with a mean value of 1.02, which was considerately lower than the initial void ratios for oedometer tests within the present project (where the range is 1.16 to 2.76

with a mean value of 1.89), see table 6.1 for details. Thus, the artificial specimens may be expected to yield a larger change in stiffness during virgin compression, compared to the natural specimens, which may cause the concave virgin compression curves.

Based on a least-square approach, a model was fitted to all available points on the virgin curves for each mixture. The model is presented in eq. (7.8). Parallel to the proposed models for the overconsolidated regions of the compression curves, presented in section 7.2, the proposed model for the virgin curve may be reduced to the well-known linear expression by choosing the exponent $i = 1$. In this case h_C will reduce to C_C, which may be related to the λ-parameters applied in the Cam Clay model. Figure 7.10 illustrates the void ratios in the normally consolidated stress regime as a function of effective stress. Both data from tests and modelled data are presented in the figure.

$$e(\sigma_v') = h_C \log \left(\frac{\sigma_v'}{1\,\text{kPa}} \right)^i \tag{7.8}$$
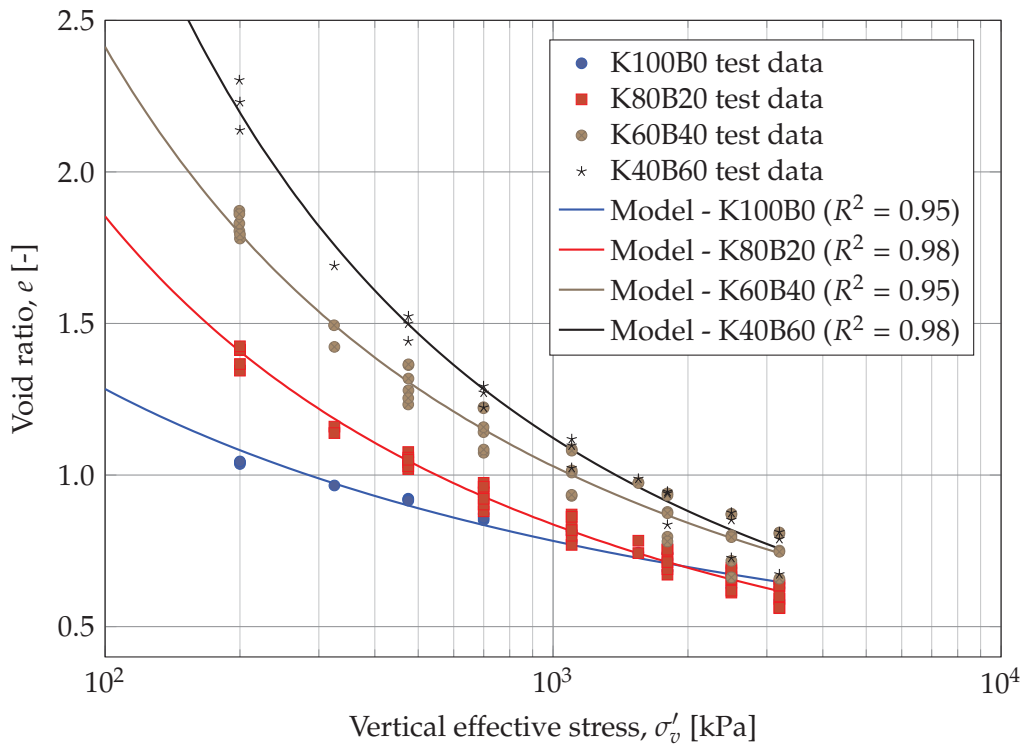
Figure 7.10: Data points from virgin curves and the fitted model for each of the four mixtures.

As may be seen from figure 7.10 the correlation coefficients of the fitted models were found in the range of 0.95 to 0.98, which suggest a quite close fit within the range where data was available from testing. It should however be noted, that the proposed model for the virgin curves does not adequately describe the compression of the specimens at very low stresses as $\lim_{\sigma_v' \to 1\,\text{kPa}} e(\sigma_v') \to \infty$. Thus, within the present project the model will only be applied for $\sigma_v' \geq 100\,\text{kPa}$. This choice is substantiated by the fact that all tested specimens were consolidated to $\sigma_v' = 163\,\text{kPa}$ in the acrylic tubes, prior to performing the oedometer tests. Thus, extrapolating of the curves to stress levels lower than 100 kPa

will be associated with significant uncertainty. On the other hand, it seems that the virgin curve at low stress levels for test number OE076S056 (tested as a slurry build directly in the oedometer cell) did follow the illustrated trend for stress levels above approx. 50 kPa, which is comparable with observations from literature, as will be presented below. The same behaviour was observed when comparing specimens from the pilot testing, as presented in appendix B.9.

It may be worth noticing that the upwards concave virgin compression curves are expected if evaluation of the (e, σ_v')-relationships are performed using the diffuse double layer theory (Sridharan and Jayadeva 1982; Bharat and Sridharan 2015), as discussed in section 6.11. Data from compression tests on pure Na-Wyoming bentonite (Bolt 1956) also display an upwards concave compression curve for vertical stresses above $\sigma_v' \geq 50\,\text{kPa}$ as illustrated in figure 2.6b. For very low stresses, $\sigma_v' \leq 10\,\text{kPa}$, the compression curves seem to drop below the void ratio suggested by the diffuse double layer theory, becoming upwards convex (Bharat and Sridharan 2015; Sridharan 2014). This may suggest that the clay platelets at such low stress levels are separated too far by absorbed water for the diffuse double layer repulsion to counteract gravity and external stress on the clay particles.

7.5 Summary of model calibration

Table 7.1 contains the fitted parameters for the models for virgin loading, unloading and reloading, which were presented in the previously sections, along with the original parameters presented by Hansen and Mise (1964). In the table the parameter $k = m - n$ is presented for the original framework. Thus, the total number of fitting constants for the original framework was four as opposed to the modified framework proposed in the present thesis, which consists of five parameters for the overconsolidated stress regime. It should be noted that the framework presented by Hansen and Mise (1964) applied for natural, intact Little Belt clay, whereas the framework presented in the present work is derived for reconstituted, artificial specimens.

Figure 7.11 illustrates the output of the proposed model for a stress path equivalent

Table 7.1: *Fitted parameters for the proposed model for each of the four tested mixtures and the original parameters from Hansen and Mise (1964).*

Model	Mixture	OC state					NC state	
		m	n	C_b	k	σ_s'	h_C	i
Current PhD-project	K100B0	1.42	1.67	0.06	0	1 kPa	2.99	−1.22
	K80B20	1.42	1.67	0.45	−1.05	1 kPa	7.21	−1.96
	K60B40	1.42	1.67	5.19	−2.70	1 kPa	10.34	−2.10
	K40B60	1.42	1.67	13.10	−3.07	1 kPa	18.08	−2.53
Hansen and Mise (1964)	Little Belt clay	2	1.33	0.0625*	$m - n$	270 kPa	N/A[†]	N/A[†]

* Related to strain in original formulation
[†] Model only applicable for unloading-reloading curves
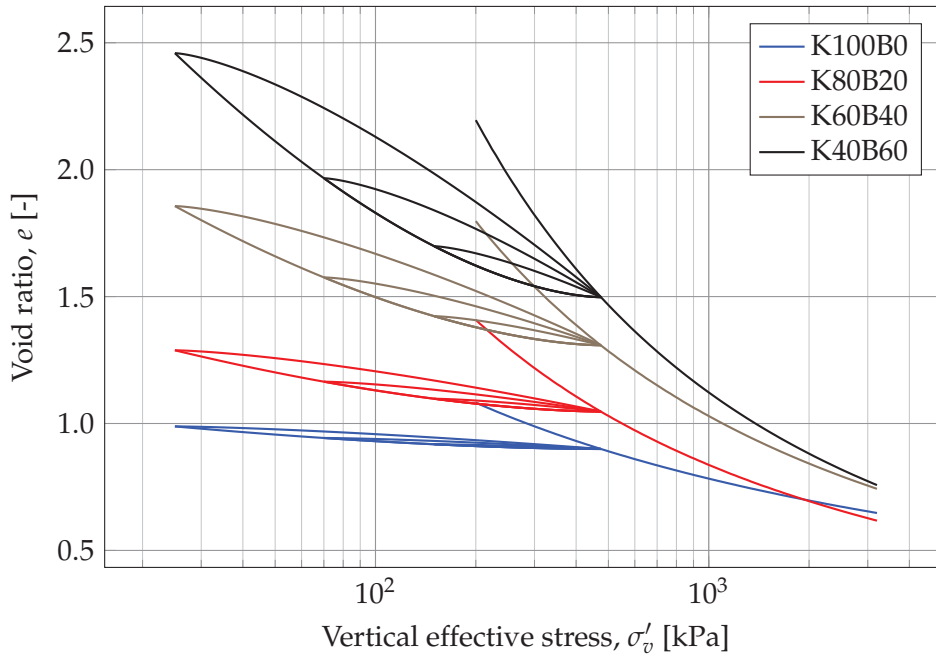
Figure 7.11: *Modelling of loading programme 1 for the four tested mixtures using the model presented in eq. (7.5) and eq. (7.8).*

to loading programme 1, for each of the individual mixtures tested within the main laboratory programme. As illustrated in the figure, the proposed framework reproduces the observations from the main laboratory tests, as presented in section 6.1. Specifically, the closed unloading-reloading loops, the curved unloading and reloading branches and the upwards concave virgin curves should be noted. Unloading-reloading curves, computed for all tests in the main laboratory programme (Load 1–3), are presented and compared with test data in chapter 12 of the laboratory report.

7.6   Analysis of fitted model

From the fitting process a set of parameters was found for each of the tested mixtures, as described in the previous sections. A comparison between the obtained compression curves from the laboratory testing and the modelled compression curves have been presented in the laboratory report, chapter 12, based on the $(\log(\sigma'_v), e)$-space.

   As observed for the original model proposed by Hansen and Mise (1964) the modelling of non-closed loops is not well explained, as illustrated in figure 7.3. The present section visualise the performance of the proposed model with regards to deformation response in non-closed stress loops.

   An observed feature from the main laboratory tests was the gradual shift of the yield stress, σ'_{vy} towards lower stresses with increasing content of smectite, as indicated by both Casagrandes and Janbus methods. The shift seemed to be related to the increase in void ratio during the former unloading, which in turn is related to the smectite content, as illustrated in figure 6.13. In the following sections, two approaches have been followed to illustrate and explain this behaviour, based on the proposed model.

7.6.1 Modelling of non-closed loops

A limitation of the model proposed by Hansen and Mise (1964) was presented in section 7.1.2 concerning the model behaviour when modelling non-closed stress paths. The same stress path was applied in the proposed model, (eq. (7.5)), to illustrate the effect of the proposed modifications. The modelled compression curves are presented in figure 7.12 along with the applied parameters.
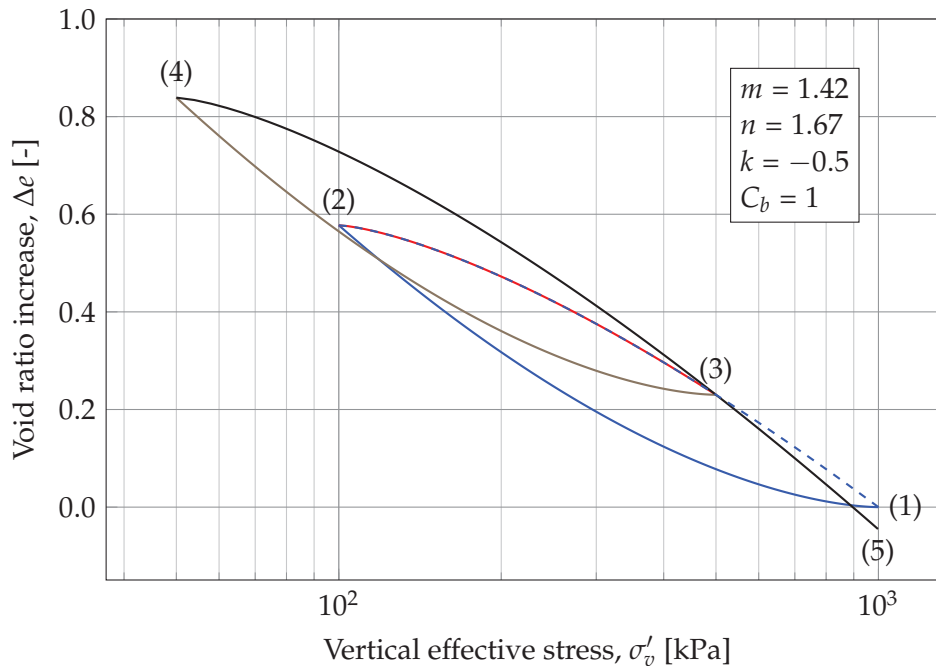

Figure 7.12: *Compression curves modelled using the model and parameters proposed in the present project. The stress path is initiated from $\sigma'_v = 1000$ kPa: (1) → (2) → (3) → (4) → (5) and is selected to illustrate effect of non-closed loops. The part of the recompression loop (4) → (5) is modelled using σ'_{max} from (3), i.e. a situation of $\sigma'_{max} < \sigma'_v$.*

As may be noted from the figure, the unloading branches are quite close, and fall back to a common "back-bone" curve, i.e. a better correspondence is observed between the unloading curves (1) → (2) and (3) → (4), which seems closer to the expected behaviour, compared to the behaviour described in section 7.1.2. The same tendency may be observed for the reloading paths, where the recompression path (4) → (5) are quite similar to a path from (2) → (1). This is thus a significant improvement from the model proposed by Hansen and Mise (1964) to the model proposed in the present PhD-project.

7.6.2 Yield stress from Janbu-approach

To illustrate the effect of the smectite content on the tangent stiffness along a recompression curve, the final reloading loop and following primary loading from loading programme 1 was modelled. Prior to the reloading, the specimens were unloaded from $\sigma'_{max} = 475$ kPa to $\sigma'_{min} = 25$ kPa, and the reloading was carried out from σ'_{min} to $\sigma'_v = 3200$ kPa. The void ratio for each of the load steps applied during testing was calculated using eq. (7.5) and eq. (7.8) for the recompression curve and the virgin curve, respec-
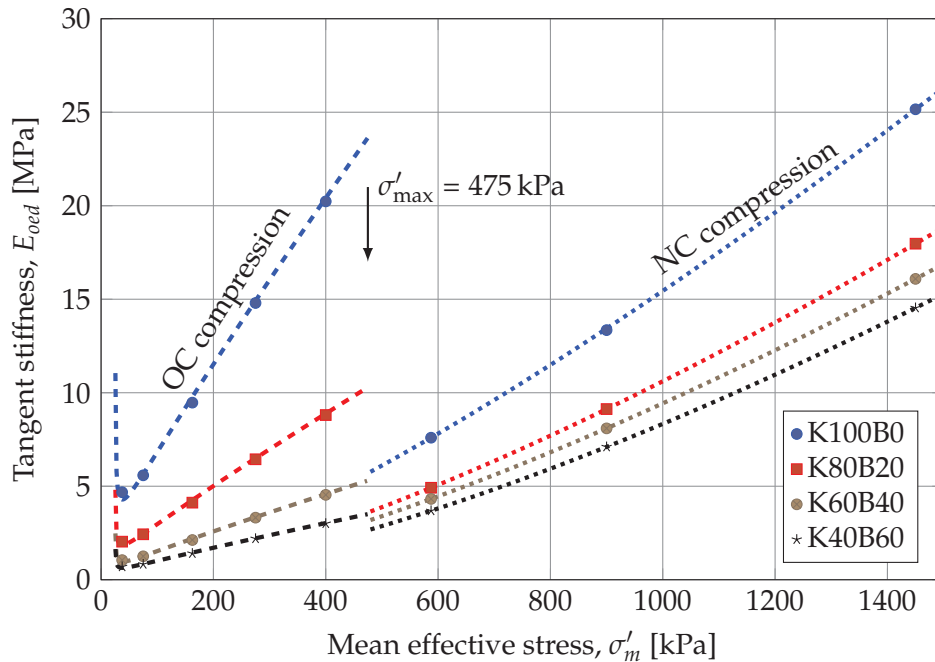
Figure 7.13: *Janbu approach to final reloading loop for loading programme 1 (25 kPa to 3200 kPa) modelled using fitted parameters for the four tested mixtures. Points presented for each mixture were modelled based on actual load steps in loading programme 1.*

tively. The calculated void ratios were converted to strain and the tangent stiffness were calculated after $E_{oed} = \Delta\sigma'_v/\Delta\varepsilon$. The tangent stiffness for each mixture was then plotted against the mean effective stress, $\sigma'_m = (\sigma'_{v,i} + \sigma'_{v,i+1})/2$, as illustrated in figure 7.13. Please note that the plot only include a part of the modelled virgin curve, which continues to curve upwards with increasing stresses. The indicated points in figure 7.13 corresponds to the load steps from the loading programme, the dashed lines indicate the tangent stiffness calculated based on the reloading curve and the dotted line the tangent stiffness for the virgin curve modelled using the proposed model. For IL oedometer tests, only the points indicated in the figure are available, which is why the transition between OC and NC conditions, when σ'_{max} is exceeded, is not clearly distinguishable for the high plasticity specimens.

As may be noted from figure 7.13, the Janbu-curve for the K100B0-mixture shows a very distinctive decrease in tangent stiffness when the previous σ'_{max} is surpassed (σ'_{max} = 475 kPa for the curves in figure 7.13). However, as the smectite content increases, the drop grows less distinct. Ultimately, for the K40B60 specimen the change in E_{oed} near the previous σ'_{max} is so small, that it might be attributed to uncertainties from testing and thus will not identified as the vertical yield stress, σ'_{vy}.

As discussed in section 7.2.5, the framework of the proposed model implies that the slope of the tangent to the recompression curve at small stresses is relatively small. Thus, the saddle point implied by the model (at approx. 75 kPa) may – for specimens of high plasticity – be interpreted as the yield stress, σ'_{vy}, as indicated in figure 7.14. At the same time, the effects of friction between specimen and oedometer ring will tend to cause an increase of the calculated stiffness at the first load step(s) during reloading. Thus, the

(a) Janbus original framework

(b) Tangent stiffness from model and test
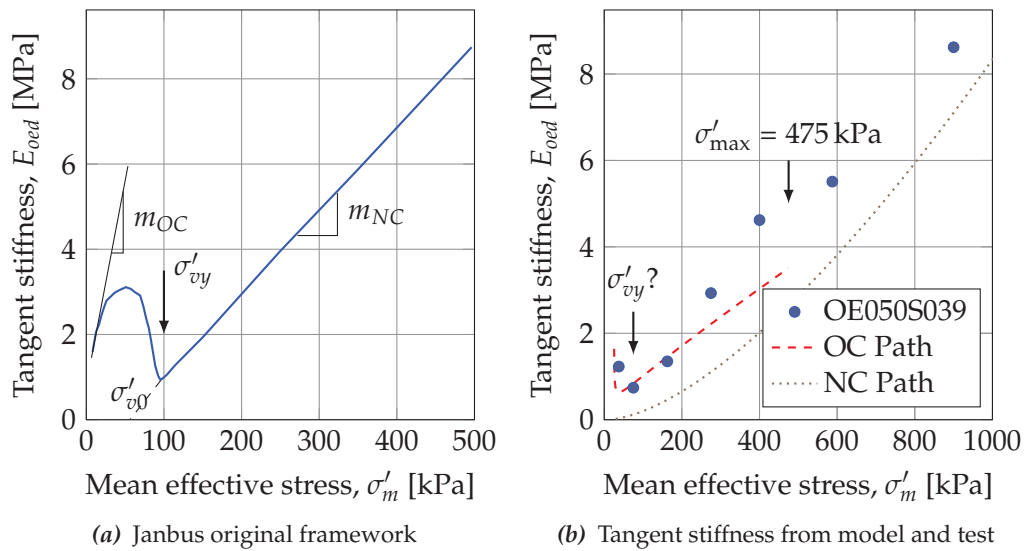
Figure 7.14: *Comparison of Janbus original framework for OC clay (Janbu 1969), and the Janbu framework applied to the proposed model, modelling load 1 and test data for a K40B60 specimen.*

yield stress identified are very likely to be small compared to the previously sustained maximal pressure. As may be noted from figure 7.14, the saddle point at approx. 75 kPa (designated by σ'_{vy}? for the test data in the figure) bears closer resemblance to the visual appearance of the yield stress in the Janbu method than the slight bend in the curve at σ'_{max}, cf. figure 7.14a and 7.14b.

It should be noted that modelling a reloading path for a smaller *OCR*-value would increase the size of the jump in stiffness when reaching NC conditions for the K40B60 specimen. Thus, it would be more likely that σ'_{vy} approaches σ'_{max}, as the tangent stiffness curve becomes more similar to the classical Janbu framework, as presented in figure 7.14a. Thus, this is in concordance with what was observed from testing, that the "stress memory" is better for low *OCR*-values than for high values, as the increase in void ratio during unloading to a low *OCR* naturally is lower than during unloading to a high *OCR*. This behaviour is illustrated in figure 6.13.

Figure 7.15 compared the calculated E_{oed} based on test data from Load 1 and output from the calibrated model for each of the tested recipes, modelling the same stress path as tested. As may be noted from the figure, the output of the model and the data from the tests show reasonable agreement – especially for the specimens of highest plasticity. As may also be noted from the figure, the saddle point used for derivation of σ'_{vy} in Janbus method grows increasingly vague with increasing smectite content. Thus, the larger content of smectite minerals, the larger the possibility of identifying a low σ'_{vy}-value. It should be noted that all tests presented were subjected to a similar stress history, which is why the only variable that differs between tests, is the smectite content.
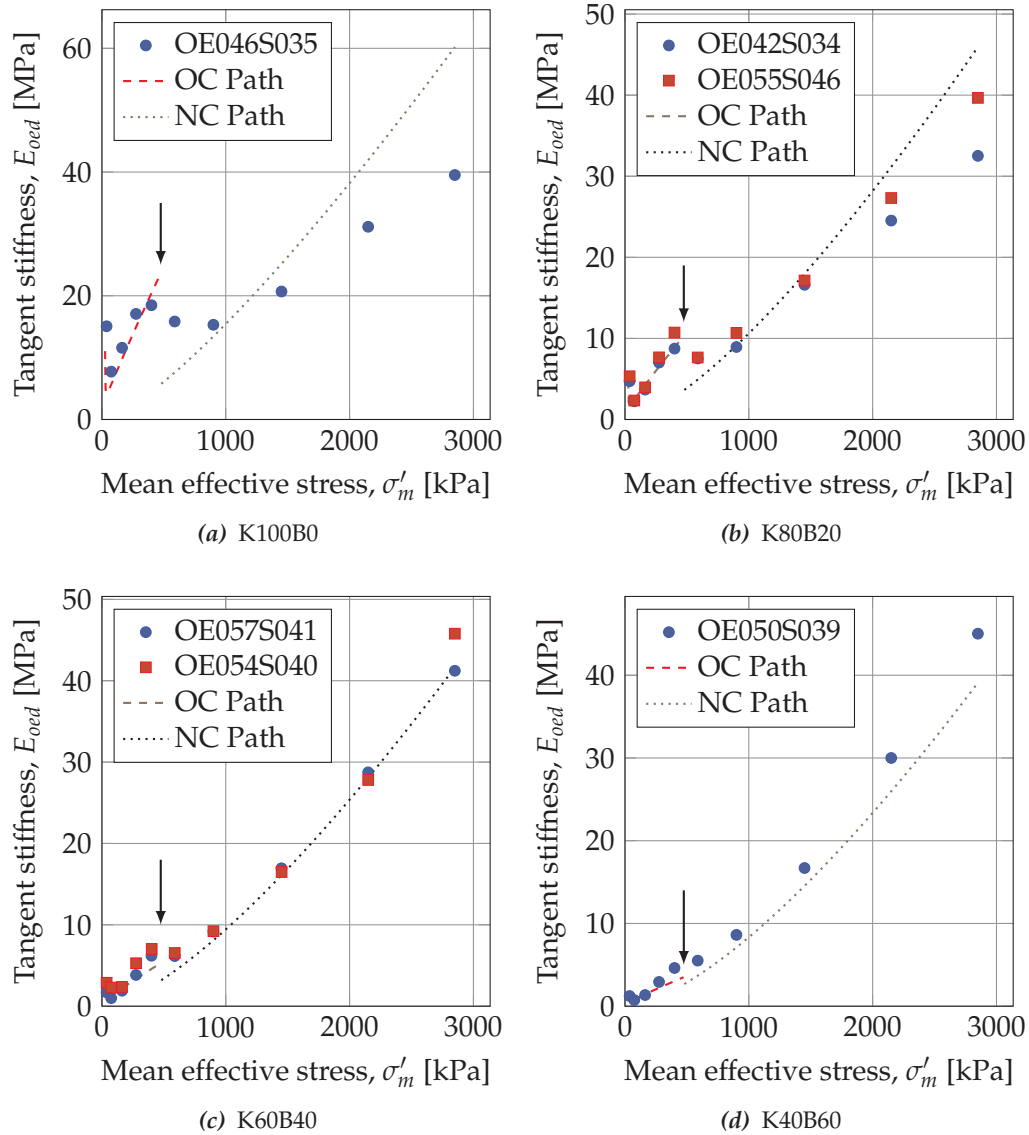
Figure 7.15: *Comparison of tangent stiffness calculated from test data and modelled based on eq. (7.5) and eq. (7.8). The arrows indicate the value $\sigma'_{\max} = 475$ kPa.*

7.6.3 Yield stress from Casagrande approach

The identification of yield stress proposed by Casagrande (1936) is based on identifying the maximal curvature of the compression curve using a visual approach. Mathematically the curvature of the compression curve, κ_R may be found based on the differentiation and double-differentiation of the piece-wise function presented in eq. (7.9), as applied in eq. (7.10),

$$
e(\sigma_v') = \begin{cases} e(\sigma_{min}') - a\left(\log \dfrac{\sigma_v'}{\sigma_{min}'}\right)^m & \text{for } \sigma_v' \leq \sigma_{max}' \\[3mm] h\left(\log \dfrac{\sigma_v'}{1\,\text{kPa}}\right)^i & \text{for } \sigma_v' > \sigma_{max}' \end{cases}
\tag{7.9}
$$

$$
\kappa_R = \frac{\dfrac{d^2\,e(\sigma_v')}{d\,\sigma_v'^{\,2}}}{\left(1 + \left(\dfrac{d\,e(\sigma_v')}{d\,\sigma_v'}\right)^2\right)^{3/2}}
\tag{7.10}
$$

where $e(\sigma_{min}')$ is the (constant) void ratio at σ_{min}', calculated based on virgin loading to σ_{max}' (from eq. (7.8)) and the void ratio increase during unloading from σ_{max}' to σ_{min}' (from eq. (7.5)). A graphical representation of eq. (7.10) based on the derivatives of eq. (7.9) is presented in figure 7.16.
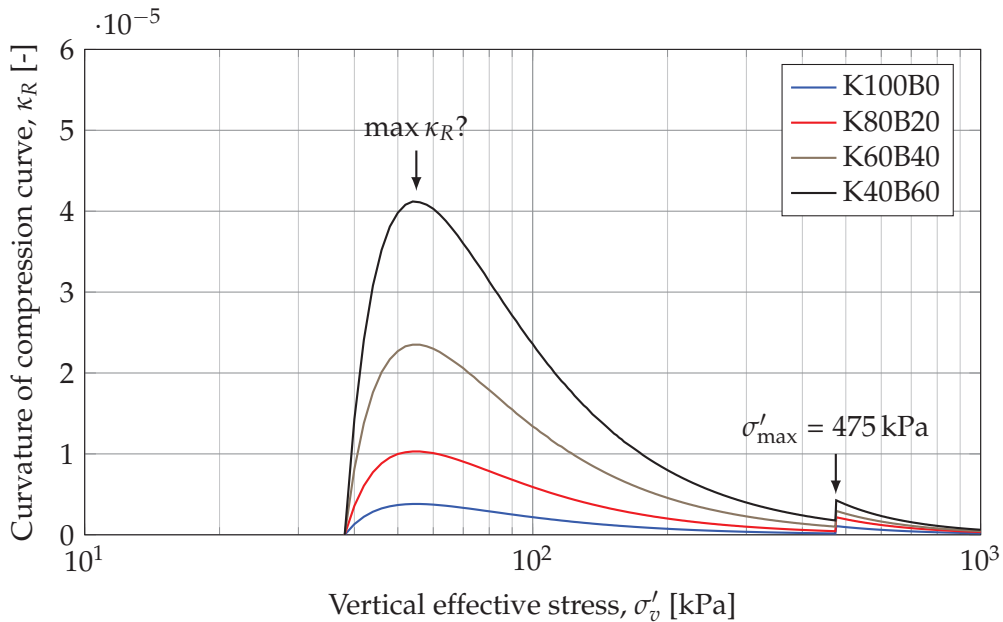
Figure 7.16: *Curvature of stress path modelled for final reloading loop for loading programme 1 (25 kPa to 475 kPa) using fitted parameters for the four tested mixtures. As may be noted from the figure, the location of the maximum curvature along the modelled stress paths shifts with increasing bentonite content.*

As may be observed from the figure, the K40B60-model suggest a much larger curvature (a factor of approx. eight may be deduced from the figure) at approx. $55\,\mathrm{kPa}$ compared to the K100B0 specimens, which is a consequence of the larger C_b-value. For all specimens a sharp increase in curvature is observed when overrunning σ'_{max}. For the K100B0-specimen, the jump when exceeding σ'_{max} and the relatively small curvature on the reloading branch enables visual identification of the maximal curvature near σ'_{max}. However, for the K60B40 and K40B60-specimens, the much larger curvature at low stress levels leads to a visual identification of the maximum curvature at a low stress level.

When the position of maximum curvature along the compression curve is identified at a low stress level, the tangent and bisector lines will be constructed at low stresses during the application of Casagrandes method. Thus, the tangent line from the final part of the compression curve and the bisector line will intersect at lower stresses, which leads to an identified σ'_{vy} lower than σ'_{max}. This may to a certain degree explain the decrease of the deduced σ'_{vy} with increasing smectite content. However, it should be noted that the curved recompression curves is a phenomenon observed from testing, which is why the proposed model eq. (7.5) is in concordance with physical behaviour. The specimens of high plasticity is thus expected to behave according to the identified σ'_{vy}-value, even as the value is lower than the known σ'_{max}. As found by Femern (2014a) none of the tested specimens of Palaeogene origin displayed an $OCR > 5$, despite being previously compressed by ice caps, which corresponds well with the discrepancy between σ'_{max} and σ'_{vy} identified in the tests on the artificial clays of highest plasticity (K60B40 and K40B60-specimens in figure 6.13).

As illustrated in figure 7.10 the proposed model for the virgin curve is upwards concave when plotted against $\log(\sigma'_v)$. This feature introduces further uncertainties in the Casagrande approach, which relies on determination of the tangent to the final, linear part of the compression curve. Thus, an inherent assumption for the Casagrande method is linear virgin compression curves. In the present project this issue was tackled by identifying the tangent to the steepest part of the compression curve to be used for intersection with the bisector line.

It should be noted that modelling a reloading path for a smaller OCR-value would increase the difference in curvature between the reloading branch and the virgin curve (the stiffness jump at σ'_{max}). Thus, it is more likely that σ'_{vy} would be identified in concordance with σ'_{max}. As for the Janbu approach, discussed in section 7.6.2, this is in concordance with the observation from the main laboratory tests.

7.7 Summation of chapter

Based on an empirical model proposed by Hansen and Mise (1964) a set of models were presented and fitted to the data obtained during laboratory testing. The essential features observed from the main laboratory testing programme were modelled successfully by the proposed framework. Thus, the effects of increasing compressibility with increasing smectite content, the curved unloading and reloading curves and the loss of stress memory were all included in the proposed model framework.

The model proved also to provide a more satisfying behaviour when performing non-closed stress loops compared to the original model proposed by Hansen and Mise

(1964). Moreover, some considerations on the behaviour of the proposed model when identifying the yield stress, σ'_{vy} based on Casagrande and Janbus methods were presented. It was found that the model satisfactory describes the observed trends from laboratory testing, namely a gradual decrease in σ'_{vy} with increasing bentonite content and achieved *OCR*-value prior to reloading.

Effects of test conditions on model validity

The following chapter details the effects of various test conditions on the validity of the proposed model framework. The model proposed in section 7.2 was derived based on the main laboratory tests (Load 1–3), which is why the performance of the model, when applied for modelling stress paths not used for calibration (Load 4 and 5), is investigated in the current chapter.

The present chapter comprises an evaluation of the significance of the test conditions on the validity of the model framework. The discussion of the test conditions entails a brief assessment of the influence of pore fluid salinity, clay mineralogical composition and of the internal friction in the oedometer cell. In each of the following sections the effect of a specific condition on the shape of the unloading and reloading curves is assessed, and the validity of the model proposed in the present PhD-work is discussed based on the presented results.

In the following sections a number of MSc-studies related to the present PhD-work are introduced. In general, only parts of the studies are extracted and discussed in the following. An overview over the conducted sub-studies is presented in appendix A.2. For more detailed introduction to test procedures and a more comprehensive overview of the results obtained from the individual studies, references to the original project reports are given in the following. Thus, detailed descriptions of test equipment and methods for each of the studies are outside the scope of the discussion in the present chapter. The author of the present PhD-dissertation acted as co-supervisor on all related MSc-projects presented in the current chapter.

8.1 Modelling of tests from loading programme 4 and 5

As introduced in section 5.6.4, two loading programmes were laid out to evaluate the performance of the proposed deformation model. The model was calibrated for each of the tested mixtures based on the compression curves from loading programmes 1 to 3. In the present section the calibrated model was applied on stress paths not included in the calibration process. Thus, any potential weak traits of the model would be exposed, and not masked under the fitting process. Loading programme 4 and 5 were in general a

Table 8.1: State parameters for the specimens tested in the validation laboratory programme, consisting of loading programme 4 and 5.

Mixture	Test number	Loading Programme	Clay fraction* [%]	Smectite content*† [%]	w_L* [%]	e_0 [-]	S_0 [%]
K100B0	OE064S052	4	53	0.8	58.8	1.14	99.7
K100B0	OE065S052	5				1.16	97.9
K80B20	OE068S051	4	58	23.7	113.9	1.66	99.2
K80B20	OE069S051	5				1.63	100.1
K60B40	OE063S044	4	64	49.2	176.8	2.20	96.7
K60B40	OE073S054	5				2.31	98.6
K40B60	OE071S047	4	74	65.5	223.6	2.63	99.2
K40B60	OE072S047	5				2.56	99.7

* Result for mixture
† Of clay fraction ($D \leq 2\,\mu m$)

bit more extreme than loading programme 1 to 3 in terms of larger OCR-values, different loading sequence etc.

The eight tests in the validation laboratory programme are presented in table 8.1. As may be noted from the table, the state parameters of the specimens were comparable with the specimens in the main laboratory programme, cf. tables 6.1 and 8.1.

Figure 8.1 presents the unloading and reloading branches of the compression curves obtained from testing K40B60-specimens by loading programme 4 and 5. Moreover, the figure illustrates the unloading-reloading response generated by the proposed model, using the parameters identified for the relevant mixture (K40B60) based on the main laboratory tests (Load 1–3). As may be noted from the figure, a discrepancy can be identified for loading programme 5, where the unloading reloading loops were rather long, i.e. high OCR-values were reached during unloading. For these curves, the model seems to overestimate the void ratio increase during unloading. This suggests an overestimation of the settlements or heave predicted by the model.

The overestimation of the increase in void ratio during unloading for loading programme 5, as indicated in figure 8.1, seems not to be a general trend, when considering the other tests performed on mixture K40B60. Specifically, the test OE051S039, performed following loading programme 2, displays a larger increase in void ratio when unloading to $OCR = 18$ ($\sigma'_{max} = 1800$ kPa, $\sigma'_{min} = 100$ kPa) than predicted by the proposed model, even as the test data was included in the calibration procedure. Thus, the data from the model calibration constitute the best fit to all available curves, which in the present case have put more emphasis on unloading-reloading loops reaching $OCR = 3 - 7$, where a better fit was obtained. This illustrates that a significant amount of data is required to calibrate the model to yield accurate results for arbitrary stress paths.

For the tests in loading programme 4 and 5, the normalised unloading-reloading curves generally confirm the trend observed for compression curves from loading programmes 1 to 3: For similar stress paths, the unloading-reloading loops may be adequately described using the same fundamental shape, when normalised according to eq. (6.1).

(a) Loading programme 4

(b) Loading programme 5
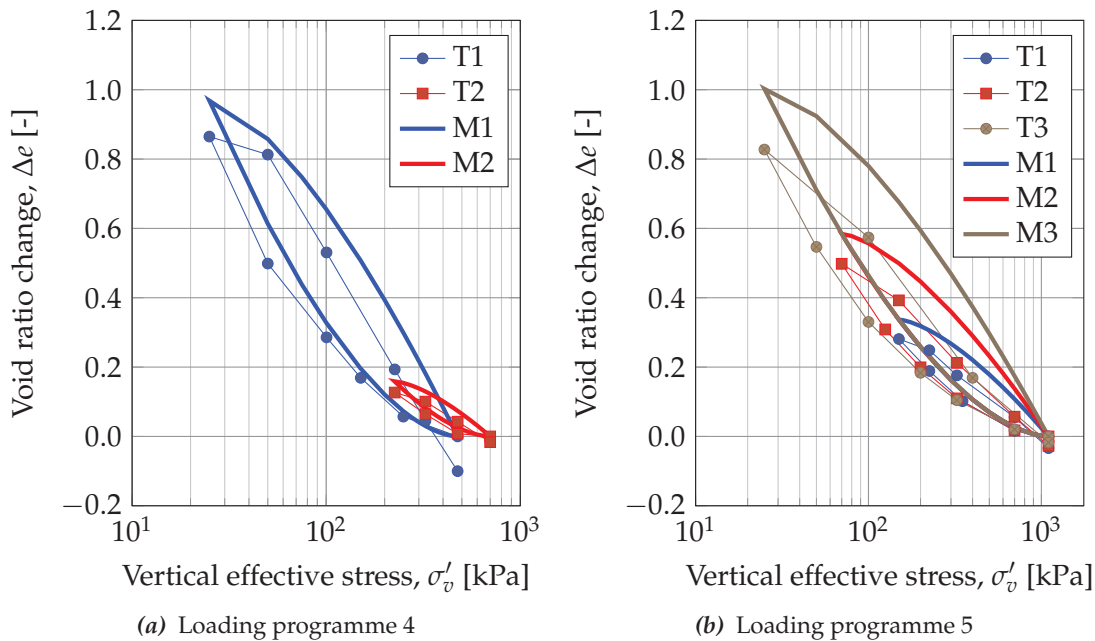
Figure 8.1: *Performance of the proposed model when applied to tests, which were not included in the model calibration. It should be noted that only the change in void ratio on the unloading-reloading curves are presented in the figure, which is why the loops were normalised using $e(\sigma'_{\max}) = 0$. In the legend "T" denotes values from the Test, whereas "M" denotes values obtained from the Model. The numbers following "T" or "M" refers to the number of the unloading-reloading loop.*

Thus, it is estimated that mainly the parameters C_b and k need to be calibrated in order to achieve a better fit for arbitrary stress paths. As only one data point is obtained from an unloading-reloading loop, significantly fewer data points were available for fitting C_b and k, compared to the available data for fitting n and m. Thus, it makes sense that the uncertainty was introduced through C_b and k. Additional tests to provide a larger database for fitting C_b and k were not performed with in the present project due to time constraints. However, it is recommended to perform additional tests to strengthen the model calibration process.

8.2 Pore fluid salinity

Sigurðardóttir and Dobrescu (2016) performed a study on the effect of pore fluid salinities on the deformation behaviour of high to extremely high plasticity clays (mixtures K100B0, K90B10 and K80B20). In the study a range of NaCl and $CaCl_2$ solutions were applied for slurry mixing and following for flooding the oedometer carriages during IL oedometer testing. The effects of pore fluid salinities on the deformation characteristics (Compression and swelling indices) are presented by Lodahl and Sørensen (2017) (enclosed as appendix I). In the present subsection, the effects of pore fluid salinity on the fundamental shape of the unloading-reloading curves are discussed, and the fitting constants presented in section 7.5 are evaluated based on the results obtained by Sigurðardóttir and Dobrescu (2016).
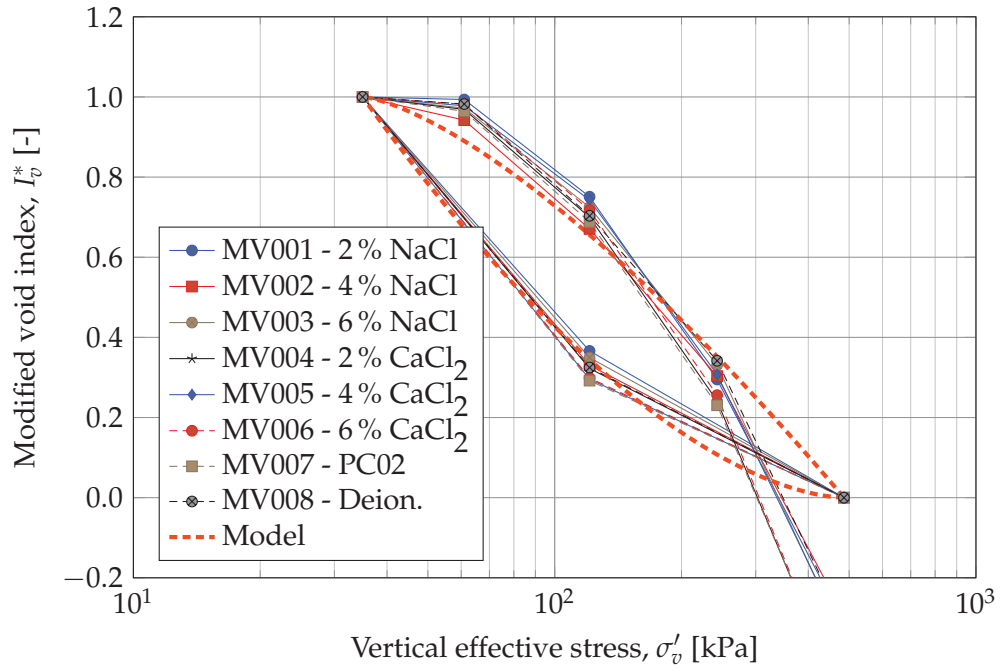
Figure 8.2: *Normalised plot for K100B0 specimens tested with various pore fluid salinities and different cations by Sigurðardóttir and Dobrescu (2016). σ'_{max} = 486 kPa and σ'_{min} = 35 kPa.*

Figure 8.2 illustrates the normalised compression curves for the K100B0 mixtures tested by Sigurðardóttir and Dobrescu (2016). As may be noted from the figure, all curves collapse to a common curve when normalised using eq. (6.1) for the modified void index, I_v^*. Similar behaviour was observed for the specimens K90B10 and K80B20, regardless of the pore fluid composition for the specimens. This observation is in line with the observations from the normalised curves as presented in section 6.5, for the main laboratory tests performed with tap water. As may also be noted from the figure, the normalised compression curves were not closed, which is likely to be a consequence of the low plasticity of the specimens. This is seen from the fact, that for tests performed with deionised water, the gap between the void ratio prior to unloading (at σ'_v = 486 kPa) and the void ratio after the unloading-reloading loop (when σ'_v = 486 kPa is reached again) is smaller, compared to the other tests. The liquid limits is highest for low pore fluid salinity (Lodahl and Sørensen 2017), which is why the liquid limit of the specimens created and tested with deionised water was higher than for the other specimens. It should be noted that similar observations occasionally were made for the K100B0 and K80B20 specimens tested in the main laboratory programme.

In figure 8.2 the model proposed in section 7.2 is also plotted for the stress path tested during unloading and reloading. As may be noted from the figure, the normalised unloading curves from the model and from the tests align quite well, i.e. the values of n and m seems to apply regardless of pore fluid salinity. For the reloading curves however, a larger initial stiffness may be identified from the test results obtained by Sigurðardóttir and Dobrescu (2016) compared to the general trends observed from the main laboratory testing. This is consistent across all tests performed by Sigurðardóttir and Dobrescu (2016). As noted above, the salinity of the pore fluid reduces the liquid limits but not the

plastic limits of the specimens, which is why the plasticity indices are lower for saline specimens. Thus, all tests performed with saline pore fluids are in the lower end of the interval of plasticity indices tested within the present project. As may be observed from e.g. the unloading-reloading loops of loading programme 1 (figure 11.1 to 11.3 of the laboratory report), the pure kaolin specimens showed similar behaviour. Thus, it may be concluded that the proposed model performs less satisfactory for specimens of relatively low plasticity, (e.g. K100B0-specimens) than for high plasticity specimens.

As concluded by Sigurðardóttir and Dobrescu (2016), the deformation parameters C_C, C_S and C_R were found to reduce with increasing pore fluid salinity. As such, the scaling parameters C_b and k are expected to also reduce with increasing pore fluid salinity. However, it was not possible to verify this hypothesis as all unloading-reloading loops performed by Sigurðardóttir and Dobrescu (2016) were carried out following identical stress paths, i.e. from identical values of σ'_{max}.

8.3 Effects of clay mineralogical composition on model framework

A study of the effects of illite minerals on the deformation characteristics of artificial mixtures was carried out by Ohler (2017). During the study, specimens with a varying mix of kaolin, bentonite and illite were tested for saline and freshwater conditions in IL oedometer tests. Figure 8.3 presents the normalised compression curves (normalised after eq. (6.1)) during unloading and reloading for eight specimens. The specimens were named after the convention KXXBYYIZZ, where XX, YY and ZZ denotes the content of kaolin, bentonite and illite, respectively, as percent of dry mass.

As may be observed from the figure some scatter is evident, when the normalised compression curves and the normalised model curves are compared. The scatter was most likely introduced by the illite minerals in the tested mixtures. The illite minerals were purchased as shales in form of course gravel (lumps of approx. Ø50 mm). The shale gravel was ground to powder prior to preparing mixtures applied for testing. However, the clay fraction of the grounded illite powder was not very high: $CF \approx 20\%$ (Ohler 2017). Thus, it is unclear whether the illite behaved as clay minerals or as relatively inert silt-sized particles during testing, which may add to the uncertainty.

The comparison between the normalised compression curves modelled using eq. (7.5) and the normalised compression curves obtained by Ohler (2017) illustrates that the same fundamental shape may be identified for all curves, despite the scatter between the individual curves. As illustrated in section 8.2, a better correspondence between the model and the test results was found for unloading stress paths, compared to the reloading branches. As for the analysis of the effects of pore fluid salinities discussed in section 8.2, the specimens tested by Ohler (2017) are of fairly low plasticity, compared to the specimens tested within the main laboratory programme of the present work. As such, the deformations on the unloading and reloading branches are relatively small, which will cause a small deviation on non-normalised scales to appear larger in the normalised plots. Thus, the effect of the mineral composition of the specimens may be concluded to be of smaller importance than the plasticity of the specimens.

The loading programme applied in the study by Ohler (2017) does not allow for
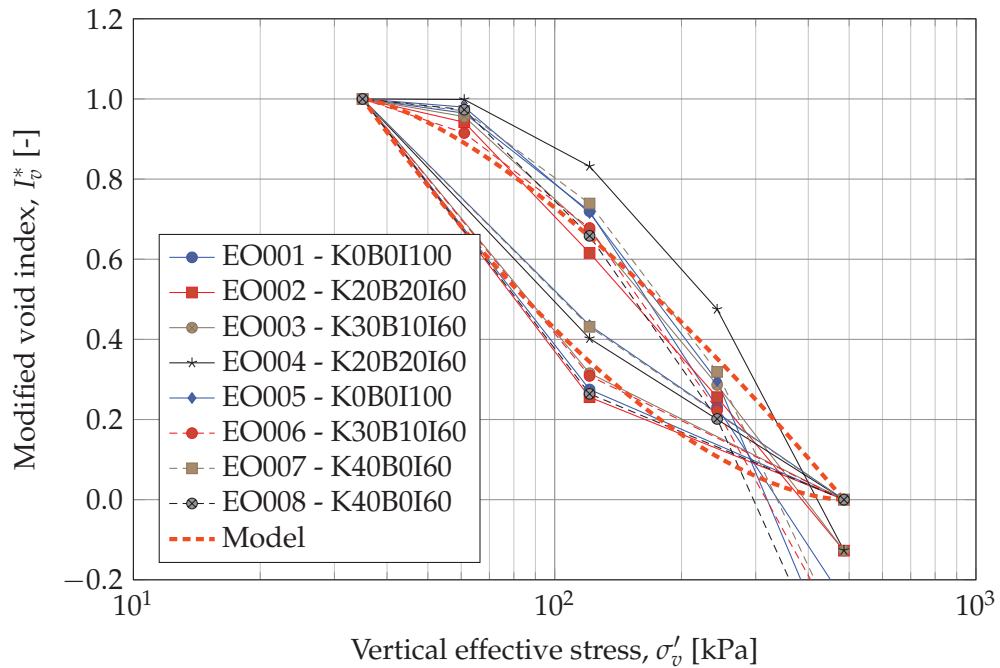
Figure 8.3: *Normalised plot for specimens with varying content of illite, tested with deionised water (test no. EO001–EO003+EO008) and 2 % NaCl (tests no. EO004-EO007) by Ohler (2017). σ'_{max} = 486 kPa and σ'_{min} = 35 kPa.*

evaluating the C_b and k parameters for the specimens containing illite as unloading-reloading loops were only performed from one σ'_{max}-value. However, the data presented by Ohler (2017) suggests an approximately linear relationship between w_L and C_S and w_L and C_R. This may suggest that the parameters C_b and k would increase with increasing liquid limit of the specimen. This observation is similar to the tendency illustrated for the specimens tested in the main laboratory programme of the present PhD-study, as discussed in section 6.5.

8.4   Effect of internal friction on model framework

The following section discusses the effects of internal friction in the oedometer apparatus, which was evaluated as a part of the present PhD project, based on tests in the nmGeo-oedometer cell. The nmGeo-cell is presented in section 1.7 of the laboratory report. A (small) study on the significance of internal friction on the tangent stiffness, E_{oed}, derived from oedometer testing was published by Lodahl et al. (2016) (enclosed as appendix H). The following section focuses on the effects of the internal friction on the shape of the compression curves, and does also entail a discussion of the results obtained by Dolby (2017), based on tests performed in triaxial cells.

8.4.1   Shape of unloading and reloading curves

Dolby (2017) conducted two tests on K100B0 specimens (mixed and tested with tap water) in triaxial cells. The two tests were conducted to mimic an oedometer test, but the

use of triaxial membranes to contain the specimens ensured, that no vertical stress was lost due to friction between specimen and a confining ring. One of the triaxial tests applied an isotropic stress state during consolidation, and is named ISO TX in the figure, and the other TX-test employed a K_0 stress state (i.e. maintaining $\varepsilon_v = \varepsilon_{vol}$ during testing), and is named K_0 TX. For each test, a series of load steps were employed to model the loading programme in the oedometer cell.

Figure 8.4 illustrates the compression curves obtained from the two triaxial tests and an IL oedometer test performed in the nmGeo-cell on a similar specimen. Due to the varying effective stress conditions on the specimens between the tests, the compression curves are presented on the basis of mean effective stress. As the test conditions differ between the tests, the effective mean stress calculated for the same vertical effective stress also differ between tests. The mean effective stress for the test performed in the nmGeo-cell was calculated based on the nominal effective vertical stress (on the upper pressure head) and the K_0-value for the respective load step, determined from the K_0-TX test. It should be noted that the mean effective stress for the tests presented in the current subsection is calculated based on eq. (8.1).

$$p' = \frac{\sigma_v' + 2\,\sigma_h'}{3} \tag{8.1}$$

Even as the effective mean stress paths differ between the tests conducted in the different apparatuses, the same tendencies from the compression curves may be observed in figure 8.4. Thus, all three unloading-reloading curves are curved when plotted against $\log(p')$. Moreover, the unloading-reloading curves for all three tests are nearly closed. Thus, the majority of the discrepancy between the three curves presented in figure 8.4 may be attributed to different initial void ratios of the three tested specimens. Based
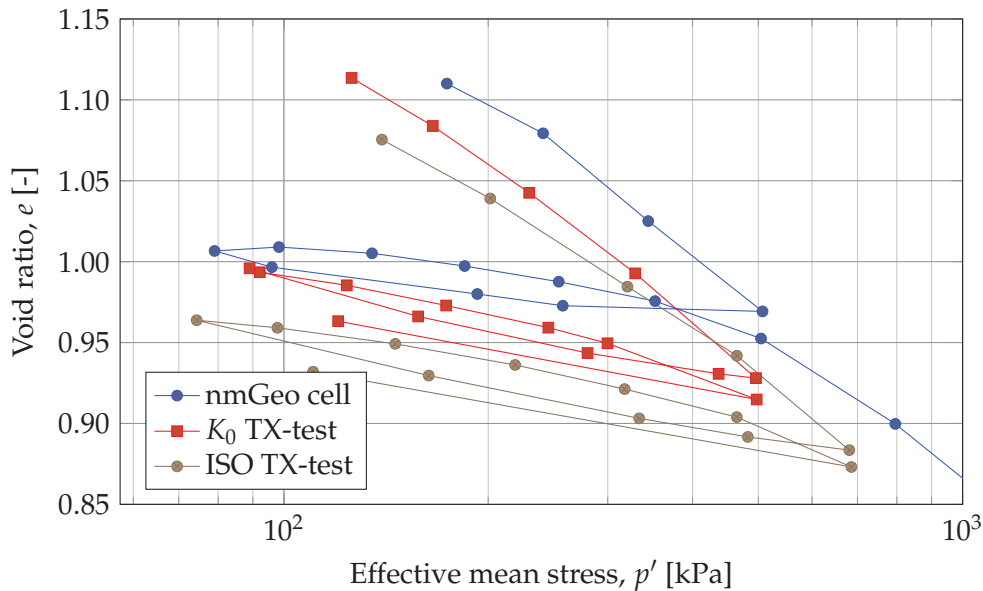
Figure 8.4: *Comparison of compression curves (in terms of mean stress from eq. (8.1)) obtained for K100B0-specimens by Dolby (2017).*

on the curves, it cannot be concluded that the internal friction between oedometer ring and specimen had a significantly influence the fundamental shape of the unloading-reloading curves.

8.4.2 Modelling of corrected stress paths

Two artificial specimens, namely a K100B0 and a K60B40 specimen, were tested in the nmGeo-cell as presented by Lodahl et al. (2016). Based on the readings of stress below the lower pressure head during testing, corrected compression curves were constructed. Figure 8.5 illustrates the two corrected compression curves obtained from testing.

(a) K100B0 (OE020S018) *(b)* K60B40 (OE018S017)
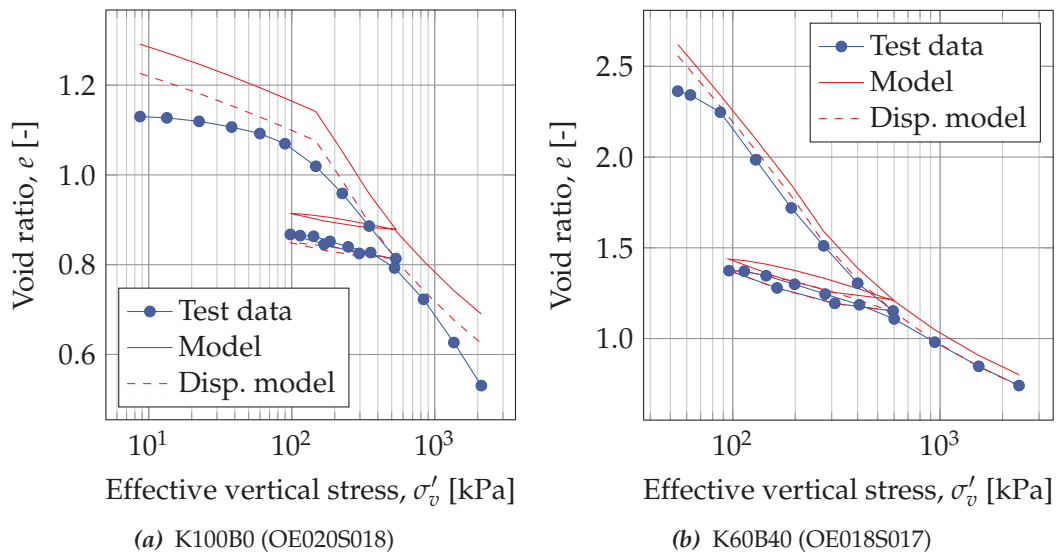
Figure 8.5: *Comparison of model and compression curves obtained from testing. The values of effective vertical stress were corrected for frictional stress loss. The curves labelled "Disp. model" have been parallel-displaced to achieve a better fit to the compression curves obtained from testing.*

Based on the model calibration factors obtained for similar mixtures, as presented in section 7.5, the corrected stress path followed during the two tests were modelled with the proposed framework. The modelled compression curves for each of the two mixtures are presented in figure 8.5. As illustrated in figure 8.5 nice fit was obtained if a parallel-displacement of the modelled curves was introduced. The parallel-displacement accounts for a discrepancy in the initial void ratio between the tests and the model. However, as no change was introduced in the shape of the curves, the modelled stiffness remains unaffected by the parallel-displacement. This in turn means than the tangent stiffness derived from the modelled compression curve constitute a nice fit to the values obtained from testing.

Based on the two studies presented in the current section, it cannot be concluded that internal friction in the oedometer cell did affect the model parameters m, n, C_b or k. As the effects of internal friction were not corrected for in the main laboratory tests, this makes sense. However, as seen from the comparison of the output of the proposed model and stress paths corrected for loss of vertical stress during testing, the model is

capable of reproducing an accurate response, also for the corrected stress path. This is a result of the differences between the $\sigma'_{\max}$ and $\sigma'_{\min}$ values on the nominal stress path and the corrected stress path. Thus, the corrected stress path are modelled equally well as any other stress path, based on the proposed framework and model parameters calibrated for the relevant specimen mixture.

8.5 Summation of chapter

The current chapter investigates the performance of the proposed model, when compared to laboratory tests which were not included in the model calibration procedure. Thus, the results from the eight oedometer tests in the validation programme have been compared to the model output for the tested stress paths. It was concluded that the model performed best for $OCR \leq$ 3–7, as minor deviations arose for long unloading loops.

In the sections above, a number of studies related to the present PhD-project have been revisited to investigate the effects of specific test conditions on the validity of the proposed model. None of the related studies included tests performed with multiple unloading-reloading loops, which is why the considerations presented above is based on comparing behaviour qualitatively between the main laboratory test and the related studies.

It was concluded that the pore fluid salinity of the specimens did not affect the fundamental shape of the unloading-reloading curve. However, an effect on the magnitude of the secant swelling and reloading parameters was observed, which in turn means that the C_b and k values in the model must be affected by pore fluid salinity.

In the series of tests where illite minerals were included in the mixtures for the artificial specimens, some scatter was observed. This was believed to origin from the illite minerals, which may interact with the smectite minerals and reduce specimen plasticity, see figure 3.7. However, it was concluded that the n and m values may be used for modelling of the compression loops with satisfying accuracy due to the similar fundamental shape between the illite-rich specimens and the specimens tested in the main laboratory programme.

Finally, the current chapter concludes that the effects of internal friction seem negligible when deriving the model parameters for the proposed framework. Two tests performed in friction-free environments (TX-membranes) did also show curved unloading-reloading loops, and the proposed deformation model performed well when applied on stress paths which were corrected for frictional stress loss. Thus, no influence of the internal friction is expected on any of the model parameters.

Modelling of natural Palaeogene clays

Based on the observations from the oedometer tests on artificial, reconstituted clays presented in section 6, a deformation model was proposed in section 7. The proposed model was calibrated based on the smectite content for each of the tested specimens. Overall, the model proved able to reproduce the compression curves obtained from the main laboratory programme on four different mixtures of artificial clays. Moreover, the model proved satisfactory capable of reproducing the compression curves obtained during the validation test programme (Chapter 8) along with other tests focused on effects of pore fluid salinity, specimen mineralogy and effects of internal friction in the oedometer cell – even as these compression curves were not included in the model calibration process.

Natural Danish high plasticity clays often are fissured, slickensided and of marine origin, i.e. the in situ pore fluid is saline. Moreover, the geological models indicate that they are overconsolidated. In total, the in situ state of Danish high plasticity Palaeogene clays deviate significantly from the state of the artificial specimens that provides the experimental basis for the proposed model. In the present chapter, a range of oedometer tests performed for the Femern Fixed Link project and the Little Belt bridge project from the 1960ies were analysed, along with other studies presented in literature. These tests comprised specimens of a range of plasticities and were all performed following stress paths, which consisted of at least one unloading-reloading loop. The five parameters for the model formulation in the overconsolidated stress regime were fitted to the compression curves for the natural clays, and the results are presented in the present chapter.

Moreover, the chapter includes case studies on two structures situated on high plasticity Palaeogene clays, namely the pier 3 of the Little Belt Bridge from 1935 and a breakwater in Puttgarden harbour, constructed in the early 1960ies. For both structures the settlements since construction has been logged – more or less consistently – to present day, which enables an analysis based on full scale behaviour of the high plasticity clay. Finally, to evaluate the model performance for unloading conditions, the expected heave in the trial excavation, performed as a part of the full-scale testing for the Femern project, was investigated using the proposed model. Data on the trial excavation is presented by Femern (2014d).

The current chapter also comprises some recommendations on procedures for se-
lection of model parameters and outlines testing programmes to be followed if the pro-
posed framework is to be calibrated to reflect the in situ behaviour of a natural high
plasticity clay.

9.1 Relation of smectite content and liquid limit

In the main laboratory tests, which were applied for calibrating the proposed model,
the content of smectite was well-known for each specimen, as presented in section 4.2.
Moreover, as may be observed from figure 6.1 in the laboratory report, an approximately
linear relationship was proven to exist between the content of smectite and the liquid
limit for the artificial specimens, which is why the model parameters expectedly may be
expressed as a function of the Atterberg limits.

For natural specimens, due to the very small deposition rates during sedimenta-
tion (see section 2.6) the content of smectite may vary greatly, even for small changes
in depth. Thus, as the clay mineralogical composition was not routinely obtained for
each of the specimens tested for the Femern Fixed Link project, a certain scatter in the
relationship between smectite content and liquid limit must be expected. Awadalkarim
(2011) performed a range of XRD tests on natural Palaeogene clay specimens obtained
during the geotechnical boring programmes for the Femern Fixed Link. For each of the
XRD-tests, the Atterberg limits (determined on materials obtained from depths as close
as possible to the depths of the XRD material) were extracted from the tests presented
by Femern (2013a, 2011c). Figure 9.1 illustrates the liquid limit plotted against the smec-
tite content of the clay fraction of the specimens ($D \leq 2\,\mu m$) for the tests. The data was
divided into the main Palaeogene units. As illustrated in the figure no overall trend of
increasing liquid limit with increasing smectite content may be identified, as results are
very scattered.
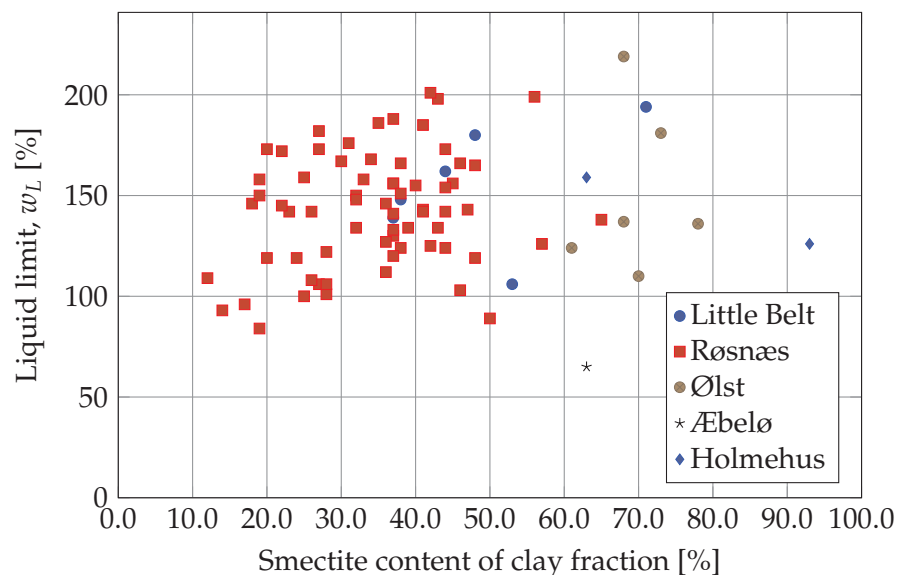
*Figure 9.1: Relation between smectite content in clay fraction and liquid limit. Compiled from data
from Awadalkarim (2011) and Femern (2013a, 2011c).*

Part of the scatter illustrated in figure 9.1 was possibly introduced by the fact that XRD-tests and liquid limit tests were not performed on the exact same clay sample. Thus, it is likely, that a deviation in the clay mineralogical composition was introduced between the two tests. Moreover, it is possible that a part of the scatter illustrated in figure 9.1 is rooted in the content of illite minerals in the natural clays, which constitutes approx. 10 % to 50 % of the clay fraction. As illustrated in figure 3.7 illite minerals suppress the liquid limit of illite-smectite mixtures. Thus, for specimens with varying content of illite, the magnitude of the suppression will also vary. Finally, the in situ salinity of the tested specimens varied, which was shown to influence the Atterberg limits (as discussed in section 3.5 and (Lodahl and Sørensen 2017)). The concentration of the cations in the pore fluid generally were highest for the intact Røsnæs clay, lower for folded Ølst clay and folded Røsnæs clay and lowest for floes of Røsnæs clay/Little Belt clay (Femern 2013a). Thus, a sample obtained from a floe of Røsnæs clay and a sample obtained from intact Røsnæs clay may show different w_L-values, despite having a similar clay mineralogical composition, due to the different salinity at w_L as also presented in section 3.5, section 6.10 and by Lodahl and Sørensen (2017). This is a consequence of applying deionised water for all Atterberg limit testing performed for the Femern Fixed Link project (Femern 2011b). In conclusion a relationship built on the consistency parameters cannot be expected to yield accurate parameters to be used in the proposed model, based on the data available for the present project. Thus, in the following the natural clays were treated in groups, based on their geological unit. That is, the Røsnæs clay specimens were analysed separately from the specimens of Little Belt clay.

9.2 Calibration of model for natural clays

A survey of the Femern database revealed 19 IL oedometer tests on intact specimens, where an unloading-reloading stress loop was performed. The tests were primarily carried out on Røsnæs clay specimens. Moreover, (Geoteknisk Institut 1964, 1962, 1961; Krogsbøll et al. 2012) represent a total of 12 tests performed on intact Little Belt Clay, which were all tested following stress paths with at least one unloading-reloading loop. The preliminary work on natural clays performed within the present PhD-project additionally provides five tests with unloading-reloading loops on natural intact Little Belt clay. 15 tests on Belgian Boom and Ypresian clays (Deng et al. 2012; Cui et al. 2013; Nguyen et al. 2013; Nguyen et al. 2014) were included in the analysis along with 12 tests performed on Søvind marl from Aarhus Harbour (Geo 2010a, 2015).

Table A.3 presents the range of identified tests from literature, all containing at least one unloading-reloading stress loop. The table presents specimen laboratory number along with depth below seabed, in situ vertical stress, σ'_{v0}, plasticity index, I_p, initial void ratio, e_0 and information on the origin of the specimens in terms of main clay unit. The tests on natural intact Røsnæs clay, Little Belt clay, Boom and Ypresian clays and Søvind Marl were used as separate datasets and were treated individually when fitting the model parameters. The fitting process is explained in more details in the following sections.

An example of a compression curve for Little Belt Clay and Røsnæs clay is presented in figure 9.2. It should be noted that the compression curves were converted to void ratio
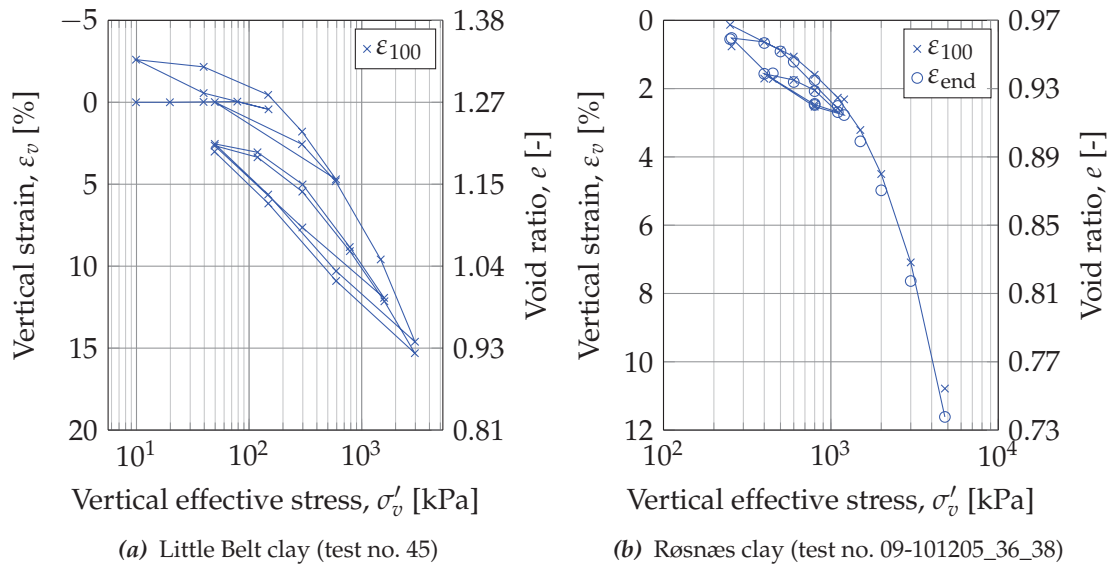
Figure 9.2: *Illustration of compression curve for Little Belt Clay, after (Geoteknisk Institut 1961) and Røsnæs clay after (Femern 2014a).*

for use in the present context, if originally formulated based on strains. As may be observed from the compression curves for the intact clays in figure 9.2, the virgin part of the compression curves are upwards convex or linear when plotted against $\log(\sigma'_v)$, which is representative for all the natural clays analysed in the present chapter. Thus, this behaviour contradicts the observed behaviour of the artificial specimens tested within the present PhD-project, as illustrated in figure 7.10. The behaviour implies that the exponent i of eq. (7.8) would be positive for the natural Palaeogene clays. As discussed in section 7.4 the high initial void ratios for the artificial specimens were the likely cause for the upwards concave virgin curves. In the following, no attempt has been made to model the virgin curves obtained from testing of natural specimens, as the focus is solely on the unloading-reloading behaviour of the natural, intact, highly plastic clays.

9.2.1 Fitting of n and m

The tests presented in table A.3 were carried out for specific projects, which is why the stress paths were selected based on project-specific conditions. Thus, as the values of σ'_{min} and σ'_{max} generally differ between the tests, it was not possible to verify whether identical unloading-reloading stress paths yielded normalised compression loops of the same fundamental shape, even when specimens of varying plasticity were tested. However, due to the convincing data obtained for the artificial specimens, this behaviour was assumed for the natural intact specimens. Thus, for each of the four data sets, the values of m and n were obtained based on a least-square fit to all unloading and reloading curves within the set, following the procedures outlined in section 7.3.

Table 9.1 presents the values of m and n obtained based on the fits for the four datasets. As may be noted from the table, m is larger than n for all data sets. This contradicts the behaviour observed for the artificial specimens, but confirms the tendencies described by Hansen and Mise (1964), who proposed $m = 2$ and $n = 4/3$. The condi-

Table 9.1: *Fitted parameters for the proposed model for each of the three data sets of natural clays. The mean I_p and mean e_0 presented constitute average values for all test included in the fitting procedure. N denotes the number of unloading-reloading loops included in the fit for each data set. $\sigma'_s = 1\,\mathrm{kPa}$ was applied for all loops.*

Data set	N	Mean I_p [%]	Mean e_0 [-]	m [-]	n [-]	C_b [-]	k [-]
Ypresian and Boom clay[*]	22	70	0.85	1.84	1.28	0.029	0.640
Røsnæs clay[†]	29	125	1.03	1.73	1.44	0.021	1.366
Little Belt Clay[‡]	27	105	1.13	1.92	1.23	0.041	0.862
Søvind Marl[§]	24	127	1.16	1.89	1.14	0.232	−0.831
All clays	102	110	1.04	—[¶]	—[¶]	0.124	−0.261

[*] Data from (Deng et al. 2012; Cui et al. 2013; Nguyen et al. 2013; Nguyen et al. 2014).
[†] Data from (Femern 2014a).
[‡] Data from (Geoteknisk Institut 1964, 1962, 1961; Krogsbøll et al. 2012) and OE016LB001, OE017LB002, OE025LB003, OE031LB004 and OE052LB005.
[§] Data from (Geo 2010a, 2015).
[¶] Values of n and m differ between clay units.

tion $m > n$ for the natural specimens describe, that the recompression curves holds a higher degree of curvature compared to the swelling curves. As discussed in section 3.6.1 it was noted that swelling curves (in a $(\log(\sigma'_v); e)$-plot) all became linear for the Røsnæs clay when unloaded sufficiently in the testing programme for the Femern fixed link (Femern 2014e). This observation seems consistent with the other tests included in the fitting procedure, which explains the lower degree of curvature for the swelling curves compared to the recompression curves. Thus, the m-value being larger than the n-value may have basis in the observed behaviour from the IL oedometer tests, as the unloading branches tended to become linear during unloading as opposed to the recompression branches. For the artificial clays a linear part of swelling curves was not identified within the present project which is why, for these clays, $n > m$.

For each of the data sets the fitted parameters n and m have been applied during the fitting process of C_b and k, which is described in the following subsection.

9.2.2 Fitting of C_b and k

For each of the unloading-reloading loops of the tests presented in table A.3, the methodology introduced in section 7.3.2 was applied. The unloading and reloading loops were modelled using eqs. (7.5a) and (7.5b), respectively, using the fitted values of n and m for each data set. By minimising the square of the errors between the void ratios during the unloading-reloading loops obtained from testing and the model, the optimal value of b^* was found for each unloading-reloading loop. The fitted b^* values were plotted against the appropriate $\sigma'_{\max}$-values in figure 9.3. In the figure, data from Røsnæs Clay is presented after (Femern 2013a), data for Little Belt clay is from (Geoteknisk Institut 1964, 1962, 1961; Krogsbøll et al. 2012), data for Boom clay is from (Nguyen et al. 2013; Deng et al. 2012), data for Ypresian clay is from (Nguyen et al. 2014; Deng et al. 2012) and data from Søvind Marl is presented after (Geo 2010a, 2015).

The curves describing the expressions for $b^*(\sigma'_{\max})$ for Røsnæs clay and Little Belt
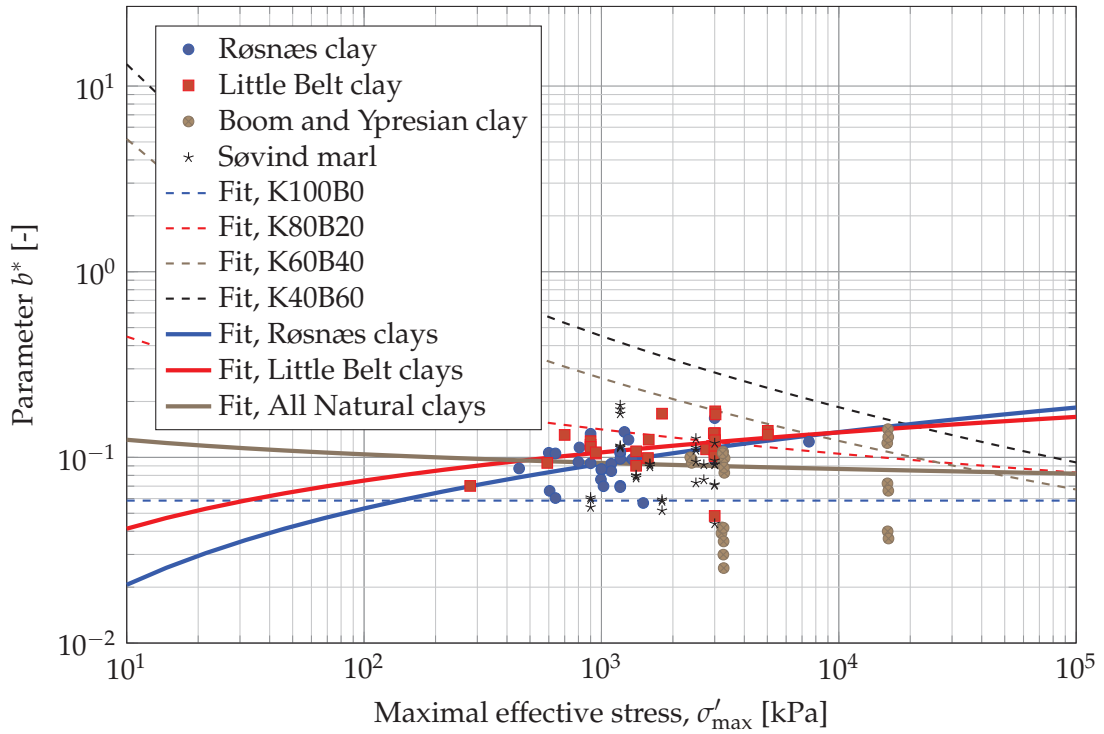
Figure 9.3: *Fitting of power function to the optimal values of b^* against $z = \log(\sigma'_{max})$ for the natural specimens.*

clay both imply a positive k-parameter, as indicated in figure 9.3. Again this behaviour contradicts the behaviour observed for the artificial specimens (indicated with dashed lines in figure 9.3). However, as may also be noted from figure 9.3, a fit to the data points for all natural, intact clays indicates a negative k-parameter as expected from the tests on the artificial clays (the difference in parameters n and m between the data sets should be acknowledged though). The tests on Ypresian and Boom clays compressed to 16 MPa are expected to cause this change in behaviour. The shift in parameter k, when including tests compressed to large stresses prior to unloading, seems to imply that the internal structure of the specimens affects the observed deformation behaviour. As all natural clays used for the current model calibration were overconsolidated by glaciations and following erosions, a more complex structure may be expected, compared to the artificial specimens. Loading to large stresses and following unloading caused a destructuring of the specimens (as discussed in section 3.3), which in turn increased deformation potential during unloading and reloading. Hence, if tests on specimens prepared from reconstituted, natural clays were carried out, expectedly larger optimal b^*-values would be found at low stress levels, which would cause the curves to shift towards a negative k-parameter as seen for the artificial specimens.

During the fitting process it was observed on several occasions that an unloading-reloading loop initiated at a low stress level yielded a smaller b^*-value compared to the value for a loop initiated from a larger stress level within the same test. This observation further strengthen the argument that the inherent structure of the specimens influenced the observed deformation behaviour, which caused the trends to appear as presented

in figure 9.3. It should be noted that a positive k-parameter implies a softer response when unloading from a high stress than from low stress, which is why a change in the internal structure with increasing stress may offer the explanation needed for $k \leq 0$ to make physical sense.

In case the proposed model is to be used for estimating the settlements for structures situated on high plasticity clays, the value of C_b and k matters less, provided test data is available within the stress levels relevant for the specific structure. However, when a model is sought which is able to predict deformation response within a wide range of stresses (i.e. predict deformation behaviour in a stress level where no data is available, e.g. for unloading from 10 kPa to 1 kPa), it is imperative that the values of C_b and k are representative for a wider stress range. Thus, it is strongly recommended to carry out tests on reconstituted natural specimens, where unloading and reloading loops are planned from a range of $\sigma'_{\max}$-values, to account for the effects of the inherent structure in the natural clays.

For all tests on natural, intact, Palaeogene clay included in the present chapter, the model is capable of reproducing the unloading-reloading compression curves, provided the use of the proper parameters m, n, C_b and k. Thus, the model seems to be a able to model the essential feature of the natural clays, and the lack of a convincing correlations between the some of the parameters and the model formulation may be explained by the difference in structure, salinity and smectite content from specimen to specimen.

9.3 Derivation of model parameters for natural clays

The procedures presented above have been successfully employed to derive the model parameters m, n, C_b and k for a range of unloading-reloading loops from tests on natural, intact Palaeogene clays, presented in literature. As the test results were obtained from literature, they may not provide the best basis for assessing the parameters. Thus, the present section seeks to outline the optimal testing programme to enable a good fit of the model parameters for a specific unit of high plasticity clays.

As presented above, each of the unloading-reloading loops was normalised to enable a fit of n and m to the unloading and reloading branch, respectively. Thus, an obvious requirement for tests to assess the model parameters is a minimum of one unloading-reloading loop in each tests. The loop(s) should consist of a number of steps to allow multiple fitting points to be obtained. A natural consequence of this is, that the CRS-test may be preferred for obtaining the n and m, due to the very high number of $(\sigma'_v; e)$-points on both unloading and reloading branches. The testing programme may include a few tests, performed with identical stress paths during unloading and reloading, to enable comparison of the shape of the normalised curves, as discussed in section 6.5.

To calibrate the parameters C_b and k, unloading-reloading loops initiated from different stress levels must be performed. As briefly discussed in section 7.3.2, the test programme should include an unloading-reloading loop performed at a relatively low stress level, to reduce the magnitude of the required extrapolation to reach the value of C_b. For normally consolidated specimens, loops from $\sigma'_{\max} \approx 100$ kPa, $\sigma'_{\max} \approx 750$ kPa and $\sigma'_{\max} \approx 3000$ kPa would ensure that a range of b^*-parameters were available for fitting. For normally consolidated specimens, b^*-points at stress levels below in situ

stress may be obtained by testing reconstituted specimens, which are installed in the oedometer cell as slurries. For each of the $\sigma'_{\max}$-values, the specimens should be loaded to varying *OCR*-values, to ensure that the calibrated model is capable of modelling a broad range of *OCR*-values. Naturally, test series consisting of multiple tests are preferred over single tests due to the larger number of available data points for fitting C_b and k.

9.3.1 Overconsolidated natural specimens

The considerations presented above are valid for normally consolidated specimens. However, the Danish Palaeogene clays are overconsolidated. Thus, unloading-reloading loops performed at low stress levels will expectedly be influenced by the internal structure achieved during the overconsolidation process. The unloading-reloading response at low stress levels for these specimens will be smaller than for a reconstituted state, as the internal structure of the high plasticity clays governs deformation behaviour. To account for the effects of the previous overconsolidation of the clays, one of two ways may be followed, which is briefly outlined below.

> The calibration of the proposed model is carried out on specimens tested for the expected stress change, going from in situ conditions to final, fully consolidated state after e.g. construction of a structure. However, this approach results in model parameters somewhat limited to the specific site and structure, due the dependency of the model parameters on the stress path applied during testing, as discussed in section 9.2.

> The calibration of the model is performed based on reconstituted specimens, tested as described above. Thus, both slurry specimens and reconstituted, preconsolidated specimens should be tested to allow a broad range of $\sigma'_{\max}$-values to be included in the fit. After the model have been calibrated, the actual stress path of the in situ clay, from deposition over in situ conditions to final, fully consolidated state is modelled using the model. This approach further more allows for transfer of the model parameters for the reconstituted clay, which may then be applied using a different stress path for another structure situated on the same clay unit. This approach requires knowledge on the $\sigma'_{\max}$-value previously sustained by the clay deposit.

As relatively few tests on natural, intact, Palaeogene clays have been included in the model calibration, a number of tests will be required to ensure that the model performs adequately for a given high plasticity clay deposit. Thus, the fitting processes for both m and n as well as for C_b and k should include an appropriate number of points. If the model is eventually proven to be able to model the in situ behaviour of the high plasticity clays, the calibration process for a construction site may be performed based on a single oedometer test, which comprise the three unloading-reloading loops discussed above. From one such test, a number of points for m and n-calibration will be available, along with three points for the C_b and k evaluation.

9.3.2 Selection of $\sigma'_{\max}$

As mentioned in section 2.6, the Danish Palaeogene clays are overconsolidated by previous glaciations and following ice retreats. Thus, the in situ state, in terms of internal structure and current void ratio, is a result of at least one previous loading to a relatively large (but unknown) stress, followed by unloading to the current in situ stress. This loading sequence imply, that the $\sigma'_{\max}$ value that should go into eq. (7.5) is large, but unknown. For reloading, the unknown $\sigma'_{\max}$ pose a problem, whereas for further unloading from the in situ stress, the current in situ stress may be used as $\sigma'_{\max}$-value without introducing a large error, as the unloading branches eventually collapses onto each other, as illustrated in figure 7.12.

As discussed in section 7.6, the methods for identifying the yield stress proposed by Casagrande (1936) and Janbu (1985) both indicate that $\sigma'_{vy} < \sigma'_{\max}$ when modelling specimens of very high plasticity. A similar trait was identified for the natural Danish clays, as illustrated in figure 3.1. Thus, the value of $\sigma'_{\max}$ to be used for natural clays must be higher than the yield stress identified by the two methods on the reloading branches for the high plasticity clays.
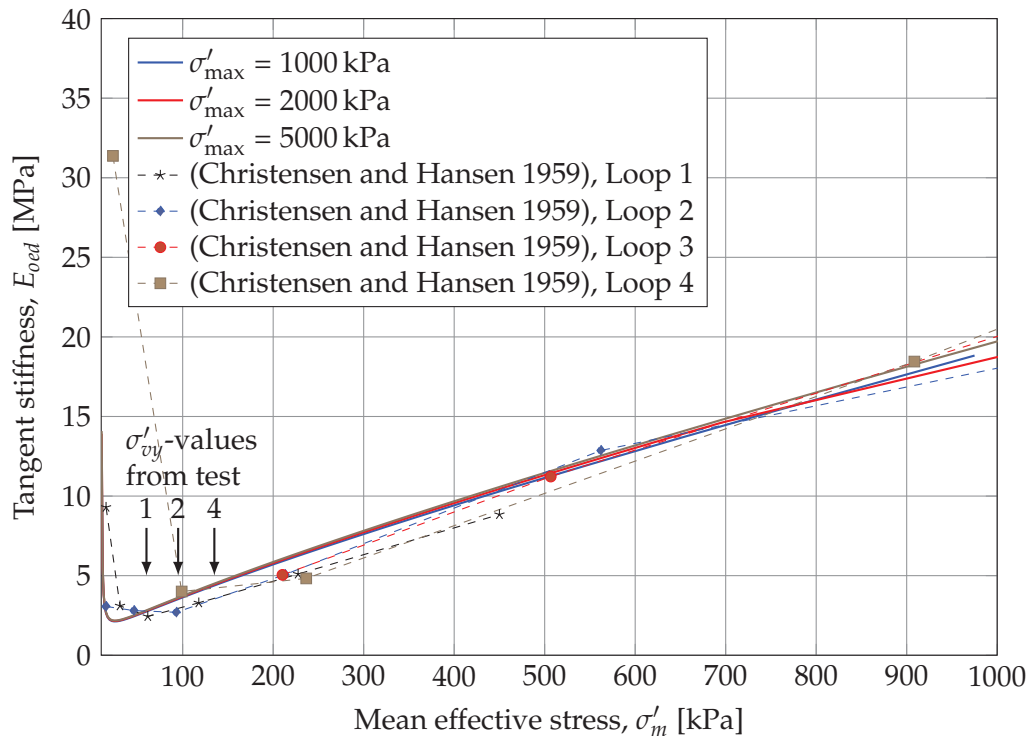
Figure 9.4: *Tangent stiffness calculated along a reloading path modelled by the proposed model using three different $\sigma'_{\max}$ values. Test data for Skive Septarian clay are included for comparison.*

Skive Septarian clay (Christensen and Hansen 1959) was selected to assess the significance of $\sigma'_{\max}$, when analysing the stiffness response during reloading. As the clay was not included in the fitting procedures, it have been assumed, that the parameters for Little Belt clay, as presented in table 9.1 was appropriate for Skive Septarian clay. A reloading branch from $(\sigma'_{\min}; e) = (10\,\text{kPa}; 1.0)$ was modelled, parallel to the unloading-

reloading loops presented by Christensen and Hansen (1959). However, the σ'_{max}-value was unknown. Based on a range of σ'_{max}-values, the tangent stiffness along the recompression curves was calculated using the proposed model formulation and compared to evaluate the sensitivity towards the σ'_{max}-value. The tangent stiffness along the recompression curve, calculated for three different values of σ'_{max}, is presented in figure 9.4. In the figure arrows indicate the σ'_{vy}-values calculated for the recompression branches 1, 2 and 4 (not enough points were available on loop 3 for σ'_{vy}-evaluation).

As may be noted from figure 9.4 no significant effect of σ'_{max} is observed on the derived tangent stiffness. In figure 9.4 the tangent stiffness values derived along the four reloading paths from a test on Skive Septarian clay are also illustrated to visualise the validity of the proposed model, when comparing with actual IL oedometer tests, which were not included in the fitting process. As may be seen from the figure, very satisfying fits have been obtained. Thus, it does not seem far-fetched to assume that the Palaeogene clays reflect a σ'_{max}-value corresponding to an unloading (due to ice retreats and erosion) of 3000 kPa. Thus, $\sigma'_{\mathrm{max}} = \sigma'_{v0} + \sigma'_{\mathrm{unload}}$ where $\sigma'_{\mathrm{unload}}$ = 3000 kPa was applied for the Danish natural clays analysed in the present chapter. This value is in concordance with the value suggested by Hansen and Mise (1964), yet lower than values presented by Grønbech (2015).

Based on the discussion above, it is worth to notice that neither the tests carried out on natural clays presented in the current chapter, nor the tests on artificial clays presented in chapter 6 were carried out using stress paths, which allow for a proper analysis of which σ'_{max}-values to be used in settlement calculations. A test series to analyse σ'_{max} could be planned using the following loading programme.

1. Loading to a given stress level in the normally consolidated regime, i.e. to a known value of σ'_{max}

2. Unloading to an arbitrary σ'_{min}-value

3. Reloading to $x\,\sigma'_{\mathrm{max}}$, where the factor $x < 1$

4. Unloading from $x\,\sigma'_{\mathrm{max}}$ and subsequent reloading

A number of tests performed following the stress path laid out above would clarify, which σ'_{max}-value to be used when reloading in natural clays, where the true value of the historical maximal load is unknown. From the indicated stress path, it should be possible to identify whether the initial (highest) σ'_{max}-value or the second (lower) value should be used for modelling the final stress loop. Moreover, it would be possible to evaluate the necessary stress change required, in unloading or reloading, for a clay specimen to reflect an updated value of σ'_{max}.

9.4 Case study I: Little Belt Bridge, Pier 3

The combined railway and highway bridge between Funen and Jutland was opened in 1935 after approx. a decade of construction works. The bridge consists of a riveted steel cantilever superstructure, carried by four concrete piers. Each of the bridge piers is

Figure 9.5: *Photo of the Little Belt Bridge from 1935. The settlements of the piers have been monitored closely since construction. Photo after (Colourbox 2017).*

founded on a caisson, which is installed directly in the highly plastic Little Belt clay. A photo of the Little Belt Bridge is presented in figure 9.5.

Each of the four piers have settled significantly since the opening of the bridge due the deformation characteristics of the high plasticity clay. Pier no. 3 has settled the most and has accumulated a settlement of approx. 65 cm since the 1930ies. Of the 65 cm, approx. 11 cm has been estimated to origin from volumetric secondary settlements (Femern 2014e). Due to the large settlements of the four piers, a strengthening project was initiated in 2013 and carried out in 2014 (Banedanmark 2013; COWI 2015).

As the bridge piers have been monitored since the bridge was opened in 1935, a unique set of data is available, containing the settlements of each of the piers over time. The settlement observations were analysed by Hansen and Mise (1964) to assess the accuracy of their model. Moreover, in the Femern Fixed link project, the settlement data for the Little Belt Bridge, and data from geotechnical investigations carried out near the bridge in 2010, was used to assess the validity of the proposed models (Femern 2014b). In the present section, the correspondence between the observed settlements of pier 3 of the Little Belt bridge and the settlements calculated from the proposed model framework (see section 7.2) was investigated based on the fitted parameters for the Little Belt clay. The applied parameters are presented in table 9.1.

9.4.1 Geometry of the piers and ground conditions

The caisson below pier 3 is approx. 45 m long and approx. 24 m wide and the vertical load applied by the self-weight of the concrete pier and traffic loading is approx. 364 MN (Rambøll 2014), corresponding to a stress of approx. 380 kPa just below the tip of the skirt. The tip of the skirt for the caisson below pier 3 is situated approx. 13.7 m below the seabed. The foundation has been modelled as a rectangle, with width of 24 m and an equivalent length to match the actual area of the foundation (approx. 40 m have been applied) in the present work. In the following calculations a 3D load spread of 1:2 (horizontal:vertical) was applied below the tip of the skirt of the caisson for stress distribution with depth.

The initial void ratio of the Little Belt clay over depth was estimated based on the approach presented by Femern (2014e), where void ratios determined during the boring campaign were plotted against the respective depths, and a logarithmic function was
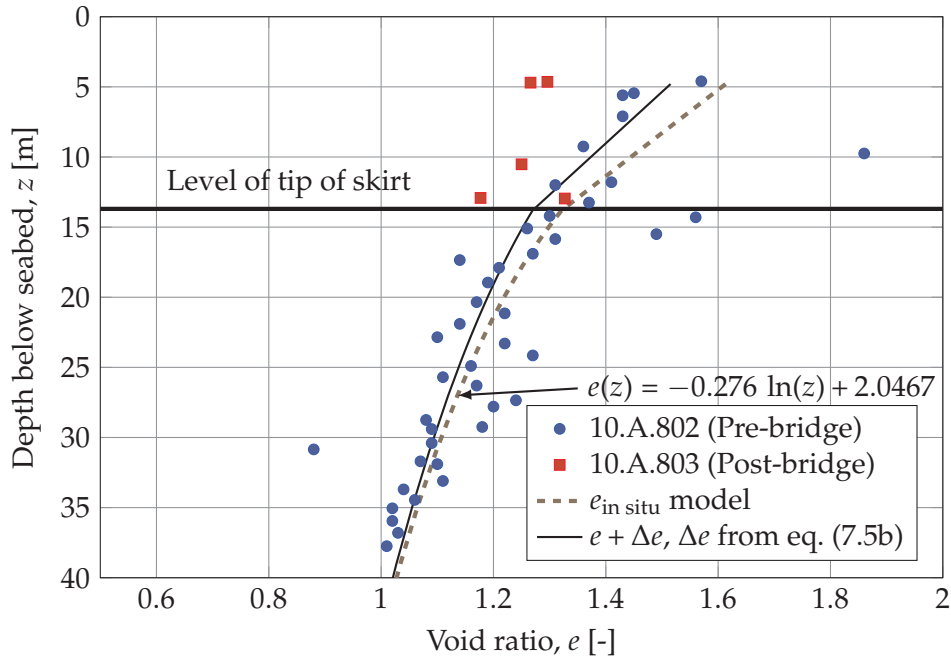
Figure 9.6: *Void ratio over depth for the Little Belt bridge. Values from boring 10.A.802 (pre-bridge situation) were estimated during the boring programme, whereas values from boring 10.A.803 (post-bridge situation) were extracted from laboratory testing.*

fitted to the values. Based on the boring 10.A.802, (which were situated approx. 50 m from pier 3, as illustrated in figure 4.6) an expression for the in situ void ratios with depth were obtained as illustrated in figure 9.6. The model proposed in eq. (7.5b) was applied, using the model parameters calibrated for Little Belt clay and $\sigma'_{max} = \sigma'_{v0} + 3000\,\mathrm{kPa}$. The soil column below the bridge pier was divided in increments, and for each increment the change in void ratio was calculated. The vertical displacement for each increment, $\delta_{v,i}$, was calculated from eq. (9.1), based on the void ratio change for the increment Δe_i calculated from eq. (7.5b) and the height of the increment h_i:

$$\delta_{v,i} = \frac{\Delta e_i}{1 + e_0}\, h_i \tag{9.1}$$

Ultimately, the settlements for each depth increments were summed. The summation was carried out to a depth of 200 m. The total settlement of pier 3 was calculated to 34 cm, which is a little lower compared to the estimations from Hansen and Mise (1964) and Femern (2014a), as also illustrated in table 9.2.

Table 9.2: *Comparison of settlement evaluations for pier 3 of the Little Belt bridge.*

Eq. (7.5)	Hansen and Mise (1964)	Femern (2014c)	Observed[*]
34 cm	37 cm	41 cm	65 cm

[*] The observed settlements also include secondary settlements. The secondary settlements have been estimated to constitute approx. 11 cm (Femern 2014b).

The calculated void ratios as a function of depth after full consolidation for the load induced by the bridge pier are illustrated in figure 9.6. The figure moreover illus-

trates void ratios obtained from laboratory testing on specimens extracted from boring 10.A.803, which was performed through the bottom slab of pier 3 (Geo 2010b). As seen from the figure, the void ratios obtained from testing of 10.A.803-specimens are lower compared to the calculated void ratio profile, which also illustrates that the void ratio decrease estimated by the proposed model is too small. This deviation is most likely rooted in the fitted parameters C_b and k (no tests were identified with unloading from small $\sigma'_{\max}$-values), as discussed above. Thus, it would be interesting to re-evaluate the settlement calculations based on a new set of model parameters, obtained from fitting data from oedometer tests on natural specimens including unloading-reloading loops performed at low stress levels.

It should be noted that the seabed, where pier 3 of the Little Belt Bridge is situated, is inclined approx. 15° compared to the horizontal plane. The sloping seabed caused shear stresses to develop under the pier, which has been illustrated to yield significant settlements of the bridge piers due the shear strains developed during primary and secondary consolidation (nmGeo 2013). Thus, it is natural that all settlement estimations presented in table 9.2 are smaller than the observed values for the bridge pier, even when accounting for secondary volumetric consolidation settlements.

Pier 1 of the Little Belt bridge have settled 27 cm between 1932 and 2012 (Banedanmark 2013). The bridge pier is similar to bridge pier 3 in terms of footing area and stress at foundation level. As this pier is situated on a flat seabed, no shear strains have developed, which is why the model output should be valid for the in situ conditions. Comparing the calculated settlements (settlement of 34 cm as presented in table 9.2) with the observed settlements, the model seems to over-predict the settlements. However, it has been noted that the soil seems stronger below pier 1 (Femern 2014b). Moreover, pier 1 was emptied of water in 1990, which initiated a consolidation process, which seems to be still on-going, as discussed by Vosgerau (2012).

9.5 Case study II: Puttgarden Breakwater

A second case study analysed by Femern (2014b) was the eastern breakwater at Puttgarden harbour. A photo of the breakwater and the pier head is presented in figure 9.7. The pier head was built in elevation −9 m on a 1.5 m thick gravel bed, placed directly on top of the Palaeogene Røsnæs clay. The original seabed is located 3 m above the foundation level of the pier in level −6 m. The vertical stress directly below the gravel bed was estimated to $\sigma'_v = 171$ kPa by Femern (2014b).

The present analysis follows the procedures set out in section 9.4. The initial void ratio with depth were assessed using the void ratio model presented by Femern (2014e), which is based on a logarithmic fit to the measured in situ void ratios, plotted against depth.

Due to the geometry of the breakwater, a plane strain analysis was carried out, focusing on a 1 m segment of the structure. Thus, load spread was only included in one direction, perpendicular to the alignment of the breakwater. The model parameters obtained from fitting of the tests performed on Røsnæs clay, presented in table 9.1, were applied in the analysis.

The total settlement was calculating by summing up the settlement increments over

Figure 9.7: *Photo of the Puttgarden Breakwater. After (Femern 2014c).*

the depth increments to a total depth of 200 m, using eq. (9.1) for assessing the settlement in each depth increment. The calculated void ratio profile after full consolidation under the load from the pier head is illustrated in figure 9.8. The described procedure lead to a total calculated settlement of 20 cm, which is slightly below the values predicted by Femern (2014e) and the observed value of 24 cm (primary consolidation settlements), as indicated in table 9.3.

As may be noted from table 9.3, the settlement predicted by the model, is slightly lower than the observed value. Again, the lack of tests performed with unloading-reloading loops, initiated from small stress levels may be blamed for the discrepancy.
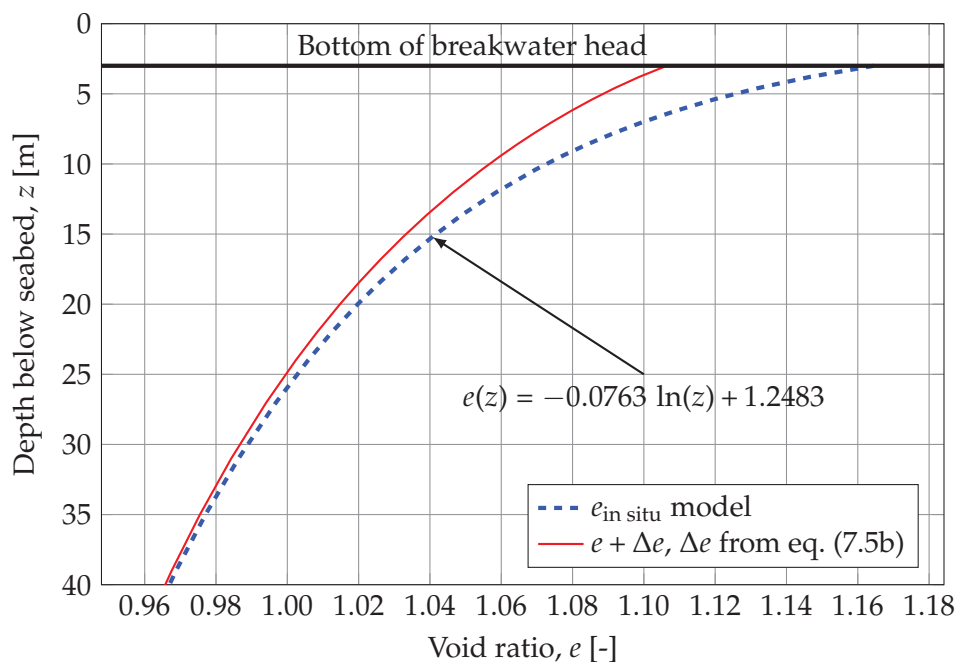
Figure 9.8: *Void ratio over depth for the Puttgarden breakwater. The initial void ratio is calculated based on the void ratio model presented by Femern (2014e) and the final void ratio was calculated based on the void ratio decrease modelled by eq. (7.5).*

Table 9.3: Comparison of settlement evaluations for the pier head of Puttgarden breakwater.

Eq. (7.5)	Femern (2014c)	Observed[*]
20 cm	26 cm	34 cm (24 cm)

[*] The observed settlements include approx. 10 cm of
secondary settlements.

Thus, the parameters applied in the present analysis reflects a more structured state, compared to the expected in situ state of the upper few meters of the clay deposit. Here, the unlimited access to water will have caused for large void ratios, which in turn would have erased a significant part of the inherent structure, achieved during the geological preconsolidation.

9.6 Case study III: Femern trial excavation

To assess the model performance during unloading, the trial excavation performed as a part of the Femern-investigations was modelled. The trial excavation is located on a water depth of 10 m and is situated approx. 1 km east of the Puttgarden harbour entrance, where folded Røsnæs clay is found from the seabed level (Femern 2014d). 10 m of Røsnæs clay was excavated, corresponding to an unloading of $\Delta\sigma'_v = 85$ kPa. In phase II of the excavation, which will be considered in the following, the bottom of the trial excavation measured 30 m by 30 m. The sides were sloping from seabed to the bottom of the excavation with a 2:1 slope (horizontal:vertical). The effect of shear stresses due to the slopes have been disregarded in the present analysis. A rendering of the excavation is illustrated in figure 9.9.
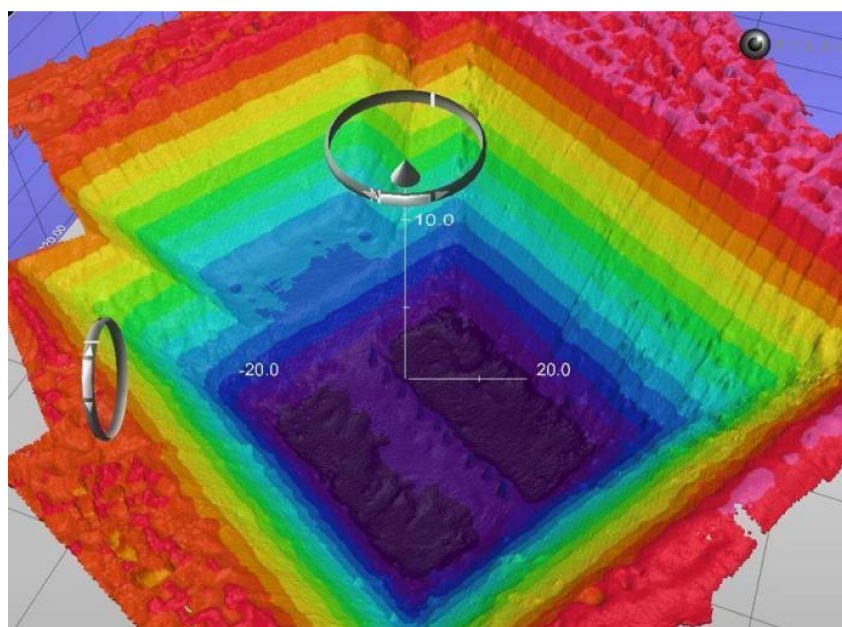
Figure 9.9: Rendering of the trial excavation performed on the German side of the Femern belt. After (Femern 2013b).

The in situ void ratio prior to excavation was modelled using the void ratio model (Femern 2014e) and eq. (7.5a) was applied for calculating the increase in void ratio in each increment over depth, as a consequence of the unloading. A load spread of 1:2 (horizontal:vertical) was applied for assessing the stress decrease with depth. Finally, the total expected heave was calculated by integrating over depth. A total expected heave of 20 cm was calculated based on the proposed framework and the parameters fitted for the Røsnæs clay, which is lower than the estimations presented by Femern (2014b). A comparison between the three methods applied by Femern (2014b) and the proposed model is presented in table 9.4. The three models applied by Femern (2014b) to assess the magnitude of heave of the bottom of the trial excavation may be briefly introduced as:

NUMHEAVE
> A 1D model based on the stiffness model presented in eq. (3.4). The model is based on a finite-difference modelling of the dissipation of excess pore pressure using classical consolidation theory, as presented in (Femern 2014e).

BRICK-model
> An advanced FEM model (formulated by Simpson (1992)) capable of modelling soil behaviour over a wide range of strains. A non-linear, 2D analysis is referenced in the current section, as presented in (Femern 2014e).

Void ratio model
> The heave were evaluated as difference between the best-fit curve expressing the current void ratio and the similar curve, translated 10 m downwards, which was assumed to model the void ratio after full dissipation of excess pore pressure, i.e. by use of the void ratio model illustrated in figure 9.8.

The calculated heave from the three Femern models and the model proposed in the present work is compared in table 9.4.

As for the settlement evaluation for the pier head of the Puttgarden breakwater, the calculated value of heave is small for the proposed model, compared to the other estimations of heave. Again it should be noted that the relevant stress range for the upper approx. 25 m of the trial excavation evaluations are lower than the σ'_{max}-values from the tests used for calibrating the model parameters, which introduce significant uncertainty in the present model. The smallest σ'_{max}-value for the tests included in the fitting procedure is approx. 450 kPa as indicated in figure 9.3. As expected, the proposed model predicts the largest part of the settlement to origin from the upper few meters. Thus, the need for testing natural specimens unloaded from small values of σ'_{max} is illustrated.

Table 9.4: *Comparison of heave evaluations for the trial excavation off the coast of Puttgarden harbour.*

| | Femern (2014c) | | |
Eq. (7.5)	NUMHEAVE model	BRICK-model	Void ratio model
20 cm	28.5 cm	36.5 cm	55 cm[*]

[*] The estimated settlements include secondary settlements.

9.7 Gains from proposed model

As illustrated in chapter 7, 8 and the current chapter, the model proposed in eq. (7.5) provides a framework, which is flexible enough to model clays of a wide range of plasticities, for arbitrary stress paths in an overconsolidated state. The proposed model was inspired by the model for Little Belt clay presented by Hansen and Mise (1964), yet the additional parameter k was introduced in the present work. Thus, the proposed model consists of five model parameters as opposed to the four parameters presented by Hansen and Mise (1964).

In the current model formulation, the expressions for modelling unloading and reloading curves are separated, which enables a fitting process for n and m, separately, for the unloading and reloading curves, respectively. Parallel with the model proposed by Hansen and Mise (1964), the proposed framework predicts closed unloading-reloading loops, provided the stress path returns to the original value of σ'_{max}.

The introduction of the parameter k in the present framework allows for modelling of clays with varying hardening behaviour, with unloading from increasing σ'_{max}-values. As illustrated in figure 9.3, even softening with unloading from increasing stresses may be modelled with the proposed framework, provided that a positive k-value is used. As previously discussed, the softening of natural clays may be introduced when internal structure is destroyed during intensive loading, which causes a less structured and softer response during following unloading and reloading.

As briefly outlined in section 9.3.1, the model may be applied in two different ways for overconsolidated specimens. The work presented by Hansen and Mise (1964) relied on approach 1, where the model was calibrated based on compression curves obtained for realistic stress paths considering the load imposed by the Little Belt bridge structure. As no unloading-reloading loops was found on natural, reconstituted, Danish Little Belt or Røsnæs clay, the case studies presented in sections 9.4 to 9.6 were carried out based on a similar approach for the model calibration.

As briefly touched upon previously, the data obtained from testing of reconstituted, natural specimens may be used on a different site for the same clay deposit as opposed to calibration factors obtained for project-specific stress paths. Eventually, the data obtained from different sites may be compiled to a database, which may provide the parameters necessary to fully calibrate a general model for Danish Palaeogene clay. Test data from reconstituted natural clays are also expected to correlate better with smectite content and thus with consistency parameters, due to the completely destructured state.

9.8 Summary of chapter

The current chapter deals with modelling behaviour of natural clays, using the model framework derived for artificial, reconstituted clays. The natural clays generally differs in terms of clay mineral distribution in the clay fraction (which is not uniquely reflected in the liquid limit) and internal structure, yet it was concluded that the same slope of the swelling curves were found regardless of specimen plasticity (Femern 2014a). Thus, based on the very scattered relationship between smectite content and consistency parameters (see figure 9.1), and the differences in internal structure of the specimens, a

certain degree of scatter was expected, when calibrating the derived model to tests performed on natural, intact Palaeogene clays.

The analysis presented in the current chapter generally showed, that the unloading-reloading loops could be simulated by the proposed deformation model, provided that proper model parameters were selected. This goes to illustrate the versatility of the proposed model as being capable of reproducing compression curves for both artificial, reconstituted clays as well as natural, intact clays. However, the model parameters fitted to the tests on natural intact Palaeogene clays presented in literature, did show unexpected features, as the data sets for Røsnæs clay and Little Belt clay both showed positive k-values. As discussed in the current chapter, the positive k-values for the two data sets are probably rooted in the fact that no reconstituted specimens were tested, which is why the inherent structure of the specimens differ between the tests on natural and artificial clays. Including clays compressed to very high stress levels, when assessing the parameters C_b and k for all the natural clays included in the present study, yielded behaviour similar to what was observed for the artificial clays. This seems to be caused by destructuring of the specimens when loaded to large stress levels, as was also observed by Gasparre et al. (2007a) for natural London clay. Thus, inclusion of tests carried out on reconstituted specimens are very important for a successful calibration of the proposed model for general stress paths.

As the natural Danish Palaeogene clays are overconsolidated, the model-parameter σ'_{max} must be assessed to be able to apply the proposed model for settlement calculations in reloading conditions. A small sensitivity analysis was presented in the current chapter, which illustrates, that if σ'_{max} is high enough, the effect on the calculated settlement is not excessive. Thus, a fixed value of $\Delta\sigma'_v = 3000\,\mathrm{kPa}$ was proposed as unloading stress to be applied for natural Danish Palaeogene clays.

Three case studies were analysed to assess the performance of the model. In all three cases, the model under-predict the magnitude of settlements or heave, which is linked to the fitted values of C_b and k, which in turn hinges on the stress paths followed for the IL oedometer tests included in the model calibration. It is believed that tests on reconstituted specimens would result in a better set of C_b and k, which in turn would increase the magnitude of calculated settlements or heave, provided that the full stress path from deposition of the clay to full consolidation under the imposed load is modelled. Thus, the model may show better concordance with the observed settlements (or heave) in the three considered case studies, as a realistic stress path for the in situ state of the clay may be modelled.

Conclusions

The present dissertation summarises the PhD-project: "Influence of smectite content on the deformation behaviour of clays" which was carried out as an industrial PhD-project in collaboration between COWI and Aarhus University. The project focused on testing of artificial specimens, mixed from kaolin and bentonite in varying ratios. During the project a range of index tests were performed on artificial mixtures of varying ratios of kaolin and bentonite and natural clays. Moreover, a total of 76 incrementally loaded oedometer tests were conducted, primarily on reconstituted, artificial clays, which were mixed as slurries, and preconsolidated prior to oedometer testing. Of the 76 tests, a total of five tests were conducted on natural specimens. 18 of the oedometer tests, comprising a total of 54 unloading-reloading loops, were conducted as the main laboratory programme and additional eight tests, with a total of 20 unloading-reloading loops, were conducted as validation tests. The following sections briefly draws attention to the main conclusions drawn, prior to recommending a few topics for further studies.

10.1 Pilot tests

A range of pilot tests were carried out to identify the most suitable laboratory procedures, and to assess the overall effects of the smectite content on the deformation behaviour. The pilot tests showed that high-quality specimens could be created by reaching an initial water content of $w = 1.5w_L$ of the clay slurries prior to preconsolidation. Specimens prepared with this procedure proved to be reproducible and to reach a consistent state after preconsolidation when different slurries of the same recipe were compared.

One of the aims of the pilot testing was to assess the effect of the internal friction in the oedometer cell on the deformation response. A pilot study was carried out, which indicated than the stress lost due to friction between specimen and oedometer ring amounted a percent-wise constant fraction of the vertical load in the normally consolidated stress regime. Thus, the compression index seemed unaffected by the frictional stress loss. The maximal effects of friction was observed for the final unloading step in an unloading-reloading loop. Here the friction increased the vertical effective stress at the bottom of the specimens, which yielded a stiffer response. However, the tangent stiffness values calculated based on corrected stress paths were high for the first few points during reloading across all tests.

10.2 Artificial specimens

Based on the performed oedometer tests in the main laboratory programme, a number of key observations were presented for reconstituted, artificial clays. Of these comprised, among others, the following:

> All unloading and reloading branches were curved when plotting the compression curves in $\log(\sigma'_v)$-space.

> Unloading-reloading loops performed by following the same stress paths may be normalised to the same fundamental shape, regardless of the content of smectite in the tested mixture.

> The compression indices (C_C, C_S and C_R) all increased with increasing smectite content, when derived for similar stress paths.

> For specimens K60B40 and K40B60 (smectite content 49.2 % and 65.5 %, respectively) the vertical yield stress identified on reloading branches was significantly lower than the previously sustained maximal stress. I.e. the "loss of stress memory" was identified to depend on the smectite content of the specimen. This was observed when estimating σ'_{vy} by the methods of Casagrande (1936), Janbu (1969), and Akai (1960).

> The large increase in void ratio during unloading for specimens of high plasticity manipulated the vertical yield stress during the following reloading. The effect was strongest for large smectite contents and high OCR-values.

> Specimens unloaded from a high stress level showed stiffer response compared to similar specimens, unloaded from low stress levels.

> All tests performed on artificial, reconstituted clay specimens produced upwards concave virgin curves. It was concluded that the concave shape was a result of the large changes in void ratio during compression.

Based on the 54 unloading-reloading loops within the main laboratory programme, an empirical deformation model was derived based on a previously published framework for natural Danish Little Belt clay. The model was validated against the 20 unloading-reloading loops in the validation programme, along with a range of special tests conducted in MSc-studies connected to the present PhD-project (35 tests, where main focus was effects of pore fluid salinity, clay mineralogical composition and internal friction on the deformation behaviour). For the artificial, reconstituted specimens, satisfactory concordance between the model framework and the test results was obtained. Moreover, it was proven that the "loss of stress memory" observed from testing was also included in the proposed model.

The calibration performed based on the tests in the main laboratory programme illustrated that the model parameters m and n, which govern the fundamental shape of the unloading-reloading loops, were not dependent on the smectite content of the specimens. On the other hand the scaling parameters C_b and k proved to rely heavily on the smectite content of the specimens. As a linear relation was found between the liquid

limits of the specimen and smectite content, the parameters C_b and k also showed good concordance with specimen plasticity. It was found that the proposed model performed the best for moderate overconsolidation ratios, i.e. OCR = 3–7 and for specimens with plasticity index above approx. 80 %.

10.3 Natural clays

The deformation model was calibrated based on analysis of a total of 102 unloading-reloading loops obtained from literature, based on tests of natural, primarily Danish, high plasticity clays. The main conclusions from the present study are presented below:

> As opposed to what was found for the artificial clays, no trend was identified between liquid limit and smectite content for natural clays. This observation may be explained by the fact that different specimens were used for XRD-testing and Atterberg limit testing, by varying content of illite minerals in the natural specimens and by varying in situ pore fluid salinity of the natural specimens.

> Contrary to the behaviour of the artificial specimens, the calibration of the model to the natural specimens yielded $m > n$. This is consistent with observation from literature, that the unloading branches turned linear for sufficient unloading.

> The calibration of the deformation model to the oedometer tests on natural clay indicated, that the compression curves obtained from literature were significantly influenced by the internal structure in the specimens – especially at low stresses. Thus, the natural specimens showed a tendency to soften when unloaded from large stresses, where the artificial specimens showed hardening behaviour.

> The output of the model calibration process, in terms of the optimal b^*-values, which were to be used for calibration the scaling parameters C_b and k, showed a very scattered behaviour. A likely cause of this is the combination of the effects of inherent structure in the specimens, and the applied stress paths.

The proposed model, calibrated based on site specific clays, were applied for settlement estimations of Pier 3 of the Little Belt Bridge from 1935, the eastern breakwater of Puttgarden harbour and the expected heave of the bottom of the trial excavation, performed as a part of the large scale testing under the Femern Fixed Link project. In all three cases the model predicted smaller deformations than observed. It was concluded that this outcome most likely was caused by the lack of tests unloaded from small values of σ'_{max}.

10.4 Further works

The experimental data provided by the present PhD-project have provided a significant insight to the deformation behaviour of artificial clays during unloading and reloading. Specifically, the effects of clay mineralogical composition on the deformation behaviour has been illustrated. Based on the discussion in the preceding chapters, a few recommendations for further research on the unloading-reloading deformation behaviour of both artificial and natural clays are presented below:

> Testing of natural, reconstituted, Palaeogene clays to assess the deformation behaviour at very low stresses, without influence of structure in the specimens. Especially, the development of parameters C_b and k when unloading from increasing stress levels are of interest, along with any correlation between the parameters C_b and k and the consistency parameters.

> As discussed for each of the case studies presented in chapter 9, the lack of tests performed at low stress levels expectedly influenced the settlement evaluations. Thus, it is recommended to perform tests on natural, intact clays, to enable an evaluation of the influence of the inherent structure on deformation response at low stress levels.

> Testing of artificial, reconstituted clays with unloading-reloading loops at low stress levels (similar stress paths as in test OE076S056). Additional data points at low values of $\sigma'_{\max}$ will provide data closer to the y-axis when plotting the calibrated b^*-values against $\sigma'_{\max}$. Thus, the power fit to identify C_b and k can be made on a larger range of data, which will increase the reliability of the calibration.

> Tests including non-closed unloading-reloading loops to assess the governing $\sigma'_{\max}$-value are also recommended, as discussed in section 9.3. Based on a series of tests with non-closed loops of varying length, it will be possible to identify the necessary amount of unloading to update the $\sigma'_{\max}$-value. Thus, a better estimation of the $\sigma'_{\max}$-value to be applied for analysis of structures situated on natural, intact Palaeogene clays may be obtained.

> Additional tests on artificial specimens, unloaded to large OCR-values are also recommended. As identified in section 8.1 the model proved less capable of reproducing unloading-reloading curves for large OCR-values. Hence, a larger database of test results could be applied to further analyse this matter.

> A range of CRS-tests, performed on both natural and artificial specimens, would greatly increase the number of available data-points for the calibration of n and m. Alternatively, IL oedometer tests with measurements of excess pore pressure in the specimens during testing, may also be used for achieving more points during unloading and reloading. However, both alternatives may imply significantly different strain rates during tests, compared to the tests contained in the present project.

Bibliography

Aarhus Stiftstidende. 2016. "To investorer vil bygge 110 meter højt fyrtrån på Aarhus Ø." September 21. Accessed March 3, 2017. `http://stiften.dk/aarhus/To-investorer-vil-bygge-110-meter-hoejt-fyrtaarn-paa-Aarhus-Oe/artikel/370326`.

Aarhus Vand A/S. 2015. *Bederværket Udvidet Kontrol.* Personal correspondance. Accessed September 17, 2015. `www.aarhusvand.dk`.

Aarhus Vand A/S. 2017a. *Udvidet kontrol 2016 Bederværket.* Personal correspondance. Accessed February 3, 2017. `www.aarhusvand.dk`.

Aarhus Vand A/S. 2017b. *Udvidet kontrol 2017 Bederværket.* Personal correspondance. Accessed March 31, 2017. `www.aarhusvand.dk`.

Akai, K. 1960. *Die strukturellen Eigenschaften von Schluff.* Heft 22. Institut für Verkehrwasserbau, Grundbau und Bodenmechanik der Technischen Hochschule Aachen.

ASTM D4318. 2000. *Standard Test Methods for Liquid Limit, Plastic Limit, and Plasticity Index of Soils.* ASTM. doi:`10.1520/D4318`.

Awadalkarim, A. 2011. *XRD analysis, Fehmarnbelt Fixed Link.* Technical report. DTU.

Banedanmark. 2013. *Stability of the Bridge Piers of the Little Belt Bridge - Cover Report on the Work of the Geotechnical Expert Panel.* Technical report 87-20414. Teknisk Drift, Lumbyesvej 34, 7000 Fredericia, Denmark: Banedanmark.

Bharat, T. V., and A. Sridharan. 2015. "Prediction of Compressibility Data for Highly Plastic Clays Using Diffuse Double-Layer Theory." *Clays and Clay Minerals* 63 (1): 30–42. doi:`10.1346/ccmn.2015.0630103`.

Bjerrum, L., and I. T. Rosenqvist. 1956. "Some experiments with artificially sedimented clays." *Géotechnique* 6 (3): 124–136. doi:`10.1680/geot.1956.6.3.124`.

Bjerrum, L. 1967. "Engineering Geology of Norwegian Normally-Consolidated Marine Clays as Related to Settlements of Buildings." *Géotechnique* 17 (2): 83–118. doi:`10.1680/geot.1967.17.2.83`.

Bolt, G. H. 1956. "Physico-Chemical Analysis of the Compressibility of Pure Clays." *Géotechnique* 6 (2): 86–93. ISSN: 1751-7656. doi:`10.1680/geot.1956.6.2.86`.

BS 1377-2. 1990. *Methods of test for soils for civil engineering purposes - Part 2: Classification tests.* ISBN: 0 580 17867 6. BSI British Standards. doi:`10.3403/00793481`.

BS 1377-5. 1990. *Methods of test for Soils for civil engineering purposes - Part 5. Compressibility, permeability and durability tests.* ISBN: 0 580 18030 1. BSI British Standards.

Burland, J. B. 1990. "On the compressibility and shear strength of natural Clays." *Géotechnique* 40 (3): 329–378. doi:`10.1680/geot.1990.40.3.329`.

Casagrande, A. 1936. "The determination of the pre-consolidation load and its practical significance." *Proceedings of the First International Conference on Soil Mechanics and Foundation Engineering* 3 (D-34): 60–64.

Casagrande, A. 1938. ""Notes on Soil Mechanics - First Semester" Harvard University, Cambridge MA." ISBN: 9780137011322.

Cavello, M., M. Lasco, R. Vasallo, and C. D. Maio. 2005. "Compressibility and residual shear strength of smectitic clays: influence of pore aqueous solutions and organic solvents." *Italian Geotechnical Journal* 1:34–46.

Cerama. 2017. "Cerama catalog." `http://kortlink.dk/cerama/qk7t`.

Christensen, N. H., and B. Hansen. 1959. *Shear strength properties of Skive Septarian clay.* Danish Geotechnical Institute.

Colourbox. 2017. "Foto: Colourbox.dk/Knud Erik Christensen." `www.colourbox.dk`.

Conte, O., S. Rust, L. Ge, and R. Stephenson. 2011. "Evaluation of Pre-Consolidation Stress Determination Methods." In *Instrumentation, Testing, and Modeling of Soil and Rock Behavior.* American Society of Civil Engineers (ASCE). doi:`10.1061/47633 (412)20`.

Coop, M. R., J. H. Atkinson, and R. N. Taylor. 1995. "Strength and stiffness of structured and unstructured soils." In *Proceedings of the 11th European Conference on Soil Mechanics and Foundation Engineering, Copenhagen,* edited by D. G. Society, 1:55–62.

Cotecchia, F., and R. J. Chandler. 2000. "A general framework for the mechanical behaviour of clays." *Géotechnique* 50 (4): 431–447. ISSN: 1751-7656. doi:`10.1680/geot.2000.50.4.431`.

Cotecchia, F., G. Mitaritonna, and C. Vitone. 2011. "Investigating the influence of microstructure, loading history and fissuring on the clay response." In *Deformation Characteristics of Geomaterials,* 53–83. ISBN: 978-1-60750-822-9. doi:`10.3233/978-1-60750-822-9-53`.

COWI. 2015. *Forstærkning af Lillebæltsbroen af 1935 — et overblik.* Technical report.

Cui, Y., X. Nguyen, A. Tang, and X. Li. 2013. "An insight into the unloading/reloading loops on the compression curve of natural stiff clays." *Applied Clay Science* 83-84:343–348. doi:`10.1016/j.clay.2013.08.003`.

Dantonit A/S. 2014. "Naturprodukt med uanede muligheder." `http://dantonit.dk/da/Produkter-og-anvdendelse/Om-rastoffet-Bentonit/`.

Darcy, H. 1856. *Les fontaines publiques de la ville de Dijon.*

Deng, Y., Y. Cui, A. Tang, X. Li, and X. Sillen. 2012. "An experimental study on the secondary deformation of Boom clay." *Applied Clay Science* 59-60:19–25. doi:`10.1016/j.clay.2012.02.001`.

Di Maio, C. 1996. "Exposure of bentonite to salt solution: osmotic and mechanical effects." *Géotechnique* 46 (4): 695–707. doi:`10.1680/geot.1996.46.4.695`.

Di Maio, C., L. Santoli, and P. Schiavone. 2004. "Volume change behaviour of clays: the influence of mineral composition, pore fluid composition and stress state." *Mechanics of materials* 36 (5): 435–451. doi:`10.1016/S0167-6636(03)00070-X`.

Dolby, J. 2017. "Triaxial and oedometer tests of reconstituted preconsolidated kaolin specimens." Research report, Aarhus University, Department of Engineering.

DS/CEN ISO/TS 17892-12. 2004. *CEN ISO/TS 17892-12, Geotechnical investigation and testing - Laboratory testing of soil - Part 12: Atterberg limits.* Danish Standards Association.

Dueck, A., and U. Nilsson. 2010. *Thermo-Hydro-Mechanical properties of MX-80. Results from advanced laboratory tests.* Technical report SKB TR-10-55. ISSN 1404-0344. Swedish Nuclear Fuel and Waste Management Co. `http://www.skb.se/upload/publications/pdf/TR-10-55.pdf`.

Fan, R. D., Y. J. Du, K. R. Reddy, S. Y. Liu, and Y. L. Yang. 2014. "Compressibility and hydraulic conductivity of clayey soil mixed with calcium bentonite for slurry wall backfill: Initial assessment." *Applied Clay Science* 101:119–127. doi:`10.1016/j.clay.2014.07.026`.

Femern. 2011a. *GDR 17.0-005 Boring campaign Lillebælt.* Technical report. Femern A/S.

Femern. 2011b. *GDR 18.0-002 Advanced Laboratory Testing, Laboratory Procedures.* Technical report. Femern A/S.

Femern. 2011c. *GDR 18.0-007 Advanced Laboratory Testing, Fehmarnsund and Lillebælt.* Technical report. Femern A/S.

Femern. 2013a. *GDR 18.0-005 Advanced Laboratory Testing, Clays of Palaeogene origin.* Technical report. Femern A/S.

Femern. 2013b. *GDR 19.0-101 Large Scale Testing, Trial Excavation, instrumentation & Surveys.* Technical report. Femern A/S.

Femern. 2014a. *Appendix GDR 00.1-001-D Geotechnical Properties for Clays of Palaeogene Origin.* Technical report. Femern A/S.

Femern. 2014b. *Appendix GDR 00.1-001-F Geotechnical Properties for Clays of Palaeogene Origin at Lillebælt, Fehmarnsund and Puttgarden Harbour.* Technical report. Femern A/S.

Femern. 2014c. *GDR 00.1-001 Ground Investigation Report.* Technical report. Femern A/S.

Femern. 2014d. *GDR 09.0-101 Large Scale Testing - Trial Excavation and Monitoring.* Technical report. Femern A/S.

Femern. 2014e. *GDR 09.0-701 Soil Models - Palaeogene Clay.* Technical report. Femern A/S.

Femern A/S. 2016. "A New Fixed Link — The tunnel across Fehmarnbelt." `http://femern.com/en`.

Foged, N., and J. Baumann. 1999. "Clay membrane made of natural high plasticity clay: leachate migration due to advection and diffusion." *Engineering Geology* 54 (1-2): 129–137. doi:`10.1016/S0013-7952(99)00068-X`.

Gasparre, A., S. Nishimura, M. R. Coop, and R. J. Jardine. 2007a. "The influence of structure on the behaviour of London Clay." *Géotechnique* 57 (1): 19–31. ISSN: 1751-7656. doi:`10.1680/geot.2007.57.1.19`.

Gasparre, A., S. Nishimura, N. A. Minh, M. R. Coop, and R. J. Jardine. 2007b. "The stiffness of natural London Clay." *Géotechnique* 57 (1): 33–47. doi:`10.1680/geot.2007.57.1.33`.

Gasparre, A. 2005. "Advanced Laboratory Characterisation of London Clay." PhD diss., Imperial College London.

Gasparre, A., and M. R. Coop. 2008. "Quantification of the effects of structure on the compression of a stiff clay." *Canadian geotechnical journal* 45 (9): 1324–1334. ISSN: 1208-6010. doi:`10.1139/t08-052`.

Geertsema, M., and J. K. Torrance. 2005. "Quick clay from the Mink Creek landslide near Terrace, British Columbia: Geotechnical properties, mineralogy, and geochemistry." *Canadian Geotechnical Journal* 42 (3): 907–918. doi:`10.1139/t05-028`. `http://dx.doi.org/10.1139/T05-028`.

Geo. 2010a. *Århus, Navitas Park, Geoteknisk undersøgelse.* Technical report. Geo.

Geo. 2010b. *Femarnbelt Fixed Link. The old Little Bridge. Geotechnical boring from inside the base of bridge pier 3.* Technical report 33132. Geo.

Geo. 2015. *Aarhus Havn. Pier 4, Byggefelt X2, Geotechnical soil Investigation - Data report.* Technical report. Geo.

Geo. 2016. *Kornrumvægte.*

Geoteknisk Institut. 1961. *Ny Lillebæltsbro ved Lyngs odde: Geoteknisk rapport no. 1 med bilag: A1-A4, A7-A10, B1-B11, C1-C4, D1-D17, E1-E5, F1, G1-G10, H1-H57.* Technical report. Geoteknisk institut.

Geoteknisk Institut. 1962. *Ny Lillebæltsbro ved Lyngs odde: Geoteknisk rapport no. 2 med bilag: A1a, A5, A11, A12, B12-B19, D18-D28, E6, E7, F2, G11-G20, H58-H74.* Technical report. Geoteknisk institut.

Geoteknisk Institut. 1964. *Ny Lillebæltsbro ved Lyngs odde: Geoteknisk rapport no. 5 med bilag A 87 - 91 og A 125 - 146.* Deformationsegenskaber. Technical report. Geoteknisk institut.

Giasi, C. I., C. Cherubini, and F. Paccapelo. 2003. "Evaluation of compression index of remoulded clays by means of Atterberg limits." *Bulletin of Engineering Geology and the Environment* 62 (4): 333–340. doi:`10.1007/s10064-003-0196-3`.

Graff-Petersen, P. 1955. "Lillebæltsler. En lermineralogisk undersøgelse." *Bulletin of the Geological Society of Denmark* 13 (1): 1–14. `http://2dgf.dk/xpdf/bull-1955-13-1-1-14.pdf`.

Grim, R. E. 1962. *Applied Clay Mineralogy.* McGraw-Hill.

Grønbech, G. L., L. B. Ibsen, and B. N. Nielsen. 2015. "Preconsolidation of Søvind Marl - A Highly Fissured Eocene Clay." *Geotechnical Testing Journal* 38 (4): 1–11. ISSN: 0149-6115. doi:`10.1520/gtj20140246`.

Grønbech, G. L. 2015. "Søvind Marl - Behaviour of a plastic fissured Eocene clay." ISBN: 978-87-7112-227-5. PhD diss., Aalborg University.

Grønbech, G. L., B. N. Nielsen, and L. B. Ibsen. 2010. *Comparison of Plasticity Index of Søvind Marl found by use of Casagrande Cup, Fall Cone apparatus and Loss on Ignition.* Technical report. Aalborg University. Department of Civil Engineering.

Grønbech, G. L., B. N. Nielsen, L. B. Ibsen, and P. Stockmarr. 2015. "Geotechnical properties of Søvind Marl - a plastic Eocene clay." *Canadian Geotechnical Journal* 52 (4): 469–478. doi:`10.1139/cgj-2014-0066`.

Gunduz, Z., and H. Arman. 2007. "Compression and recompression of a high plasticity clay consolidated under isotropic stresses." *Kuwait Journal of Science and Engineering* 34 (1B): 19–34. ISSN: 2307-4108.

Hansen, J. B. 1953. "Earth Pressure Calculation." PhD diss., Danish Technical University.

Hansen, J. B. 1961. *A model law for simultaneous primary and secondary consolidation.* Danish Geotechnical Institute Bulletin No. 13.

Hansen, J. B., and T. Mise. 1964. *An empirical evaluation of consolidation tests with Little Belt Clay.* Danish Geotechnical Institute Bulletin No. 17.

Heilmann-Clausen, C. 1995. "Palæogene aflejringer over danskekalken." Chap. 5 in *Danmarks geologi fra Kridt til i dag*, 70–111. Geologisk Institut, Aarhus Universitet.

Hight, D. W., A. Gasparre, S. Nishimura, N. A. Minh, R. J. Jardine, and M. R. Coop. 2007. "Characteristics of the London Clay from the Terminal 5 site at Heathrow Airport." *Géotechnique* 57 (1): 3–18. doi:`10.1680/geot.2007.57.1.3`.

Hight, D. W., F. McMillan, J. J. M. Powell, R. J. Jardine, and C. P. Allenou. 2003. "Some characteristics of London Clay." In *Characterisation and Engineering Properties of Natural Soils: Proceedings of the International Workshop, Singapore, 2-4 December 2002*, edited by T. S. Tan, K. K. Phoon, D. W. Hight, and S. Leroueil, 2:851–908. Swets & Zeitlinger BV. ISBN: 978-90-5809-537-4.

Himenz, P. C., and R. Rajagopalan. 1997. *Principles of Colloid and Surface Chemistry.* 3rd ed. CRC Press. ISBN: 978-0-8247-9397-5.

Holmboe, T. 2001. *Teglværksler i Danmark.* Technical report 92. GEUS, Geological Survey of Denmark and Greenland.

Holtz, R. D., W. D. Kovacs, and T. C. Sheahan. 2011. *Introduction to Geotechnical Engineering.* 2nd. ISBN: 9780137011322. Pearson.

Horpibulsuk, S., S. Shibuya, K. Fuenkajorn, and W. Katkan. 2007. "Assessment of engineering properties of Bangkok clay." *Canadian geotechnical journal* 44 (2): 173–187. doi:`10.1139/t06-101`.

Horpibulsuk, S., N. Yangsukkaseam, A. Chinkulkijniwat, and Y. J. Du. 2011. "Compressibility and permeability of Bangkok clay compared with kaolinite and bentonite." *Applied Clay Science* 52 (1–2): 150–159. doi:`10.1016/j.clay.2011.02.014`.

Hueckel, T. 2002. "Reactive plasticity for clays during dehydration and rehydration. Part 1: concepts and options." *International Journal of Plasticity* 18 (3): 281–312. doi:`10.1016/S0749-6419(00)00099-1`.

Janbu, N. 1985. "Soil models in offshore engineering." *Géotechnique* 35 (3): 241–281. doi:`10.1680/geot.1985.35.3.241`.

Janbu, N. 1969. "The resistance concept applied to deformations of soils." In *Proceedings for the 7th international conference on Soil Mechanics and Foundation Engineering*, 1:191–196.

Krizek, R. J., and D. E. Sheeran. 1970. *Slurry Preparation and Characteristics of Samples Consolidated in the Slurry Consolidometer.* Technical report. Northwestern university, Evanston Illonois, Dept. of Civil Engineering. `http://oai.dtic.mil/oai/oai?verb=getRecord&metadataPrefix=html&identifier=ADA040188`.

Krogsbøll, A., O. Hededal, and N. Foged. 2012. "Deformation properties of highly plastic fissured Palaeogene clay - lack of stress memory?" In *NGM 2012 - Proceedings of the Nordic Geotechnical Meeting*, 133–140.

Kulhawy, F. H., and P. W. Mayne. 1990. *Manual on estimating soil properties for foundation design.* Technical report EPRI-EL-6800. Cornell University, Ithaca, NY. `http://www.epri.com/abstracts/Pages/ProductAbstract.aspx?ProductId=EL-6800`.

Ladd, C. C., and R. Foott. 1974. "New Design Procedure for Stability of Soft Clays." *Journal of the Geotechnical Engineering Division* 100 (7): 763–786.

Laier, T. 2010. *Fehmarnbelt Synthetic pore water.* Technical report. GEUS.

Leroy, P., and A. Revil. 2004. "A triple-layer model of the surface electrochemical properties of clay minerals." *Journal of Colloid and Interface Science* 270 (2): 371–380. doi:`10.1016/j.jcis.2003.08.007`.

Lighthouse*. 2017. "Pressebilleder." `http://lighthouse-aarhus.dk/presse/pressebilleder/`.

Lodahl, M. R., and K. K. Sørensen. 2015. "Influence of Smectite Content on the One-Dimensional Deformation Behavior of Reconstituted High Plasticity Clay." In *Deformation Characteristics of Geomaterials - Proceedings of the 6th International Symposium on Deformation Characteristics of Geomaterials, IS-Burnos Aires 2015.* Edited by V. A. Rinaldi, M. E. Zeballos, and J. J. Clariá. doi:`10.3233/978-1-61499-601-9-1057`.

Lodahl, M. R., and K. K. Sørensen. 2017. "Effects of pore water chemistry on the unloading-reloading behaviour of reconstituted clays." *European Journal of Environmental and Civil Engineering.* Submitted. ISSN: 2116-7214.

Lodahl, M. R., K. K. Sørensen, N. Mortensen, and H. Trankjær. 2016. "Oedometer tests with measurements of internal friction between oedometer ring and clay specimen." In *NGM 2016 Reykjavik - Proceedings of the 17th Nordic Geotechnical Meeting - Challenges in Nordic Geotechnics 25th - 28th of May*, 289–298. ISBN: 978-9935-24-002-6. `http://www.ngm2016.com/papers.html`.

Lunne, T., T. Berre, and S. Strandvik. 1997. "Sample disturbance effects in soft low plastic norwegian Clay." In *Recent Developments in Soil and Pavement Mechanics: Proceedings of the International Symposium, Rio De Janeiro, Brazil, 25-27 June 1997*, 81–102. ISBN: 9054108851. CRC Press.

Mesri, G., and P. M. Godlewski. 1977. "Time and stress - compressibility interrelationships." *Journal of the Geotechnical Division, ASCE* 103 (GT5): 417–430.

Mesri, G., and R. E. Olson. 1971. "Consolidation Characteristics of Montmorillonite." *Géotechnique* 21 (4): 341–352. doi:`10.1680/geot.1971.21.4.341`.

Mitchell, J. K., and K. Soga. 2005. *Fundamentals of Soil Behavior.* 3rd. ISBN: 9780471463023. John Wiley & Sons.

Morris, G. E., and M. S. Żbik. 2009. "Smectite suspension structural behaviour." *International Journal of Mineral Processing* 93 (1): 20–25. doi:`10.1016/j.minpro.2009.05.003`.

Mortensen, N. 2011. "Reflections on primary and secondary consolidation." In *Proceedings of the 15th European Conference on Soil Mechanics and Geotechnical Engineering*, edited by A. Anagnostopoulos, M. Pachakis, and C. Tsatsanifos, 229–234. doi:`10.3233/978-1-60750-801-4-229`.

Mortensen, N. 2012. "High plasticity Palaeogene clay; A soil type with a very moderate long-term memory." In *NGM 2012 - Proceedings of the Nordic Geotechnical Meeting*, 413–420.

Nagaraj, T. S., and B. R. S. Murthy. 1986. "A critical reappraisal of compression index equations." *Géotechnique* 36 (1): 27–32. doi:`10.1680/geot.1986.36.1.27`.

Nguyen, X., Y. Cui, A. Tang, Y. Deng, X. Li, and L. Wouters. 2013. "Effects of pore water chemical composition on the hydro-mechanical behavior of natural stiff clays." *Engineering Geology* 166:52–64. doi:`10.1016/j.enggeo.2013.08.009`.

Nguyen, X., Y. Cui, A. Tang, X. Li, and L. Wouters. 2014. "Physical and microstructural impacts on the hydro-mechanical behaviour of Ypresian clays." *Applied Clay Science* 102:172–185. doi:`10.1016/j.clay.2014.09.038`.

Nielsen, O. B. 1974. "Sedimentation and diagenesis of lower eocene sediments at Ölst, Denmark." *Sedimentary Geology* 12 (1): 25–44. doi:`10.1016/0037-0738(74)90014-1`.

Nielsen, O. B. 2014. "RE: Erhvervs-PhD ang. fedt, palæogent ler." Personal correspondance.

Nielsen, O. B., and C. Heilmann-Clausen. 1988. "Palaeogene volcanism: the sedimentary record in Denmark." *Geological Society, London, Special Publications* 39 (1): 395–405. doi:`10.1144/gsl.sp.1988.039.01.35`.

Nielsen, O. B., E. S. Rasmussen, and B. I. Thyberg. 2015. "Distribution of Clay Minerals In the Northern North Sea Basin During the Paleogene and Neogene: A Result of Source-Area Geology and Sorting Processes." *Journal of Sedimentary Research* 85 (6): 562–581. ISSN: 1527-1404. doi:`10.2110/jsr.2015.40`.

nmGeo. 2013. *Lillebælt Bridge, Laboratory Test Results and Their Implications.* Technical report nmGeo-2013-02. nmGeo.

Ohler, E.-E. 2017. "The influence of mineralogy and pore water chemistry on the deformation behaviour illite rich of clays." Master's thesis, Aarhus University, Department of Technical Geology.

Olphen, H. van. 1977. *An Introduction to Clay Colloid Chemistry.* Second Edition. ISBN: 978-0471014638. John Wiley & Sons.

Popescu, M. E. 1986. "A comparison between the behaviour of swelling and of collapsing soils." *Engineering Geology* 23 (2): 145–163. doi:`10.1016/0013-7952(86)90036-0`.

Porrenga, D. H. 1966. "Clay minerals in recent sediments of the Niger Delta." *Clays and Clay Minerals* 14 (1): 221–233. doi:`10.1346/CCMN.1966.0140119`.

Pusch, R., A. Drawrite, R. N. Yong, and M. Nakano. 2010. "Stiffening of smectite buffer clay by hydrothermal effects." *Engineering Geology* 116 (1-2): 21–31. doi:`10.1016/j.enggeo.2010.07.002`.

Pusch, R., J. Kashohm, T. Hoang-Minh, S. Knutsson, and L. Nguyen-Thanh. 2015. "Holmehus clay - A Tertiary smectitic clay of potential use for isolation of hazardous waste." *Engineering Geology* 188:38–47. doi:`10.1016/j.enggeo.2015.01.005`.

Pusch, R., and R. N. Yong. 2005. *Microstructure of Smectite Clays and Engineering Performance.* ISBN 9-78-0-415-36863-6. Taylor & Francis.

Rambøll. 2014. *The Little Belt Bridge of 1935 - Load on piers.* Technical report. Rambøll.

Rankka, K., Y. Andersen-Sköld, C. Hultén, R. Larsson, V. Leroux, and T. Dahlin. 2004. *Quick clay in Sweden.* Technical report 1-03003-0129. Swedish Geotechnical Institute. ISRN: SGI-R–04/65–SE.

Rhoades, J. D. 1982. "Cation Exchange Capacity." *Methods of soil analysis. Part 2. Chemical and microbiological properties:* 149–157.

Roscoe, K. H., A. N. Schofield, and C. P. Wroth. 1958. "On the yielding of soils." *Géotechnique* 8 (1): 22–53. doi:`10.1680/geot.1958.8.1.22`.

Schmitz, R. M., C. Schroeder, and R. Charlier. 2004. "Chemo–mechanical interactions in clay: a correlation between clay mineralogy and Atterberg limits." *Applied Clay Science* 26 (1-4): 351–358. doi:`10.1016/j.clay.2003.12.015`.

Schofield, A., and P. Wroth. 1968. *Critical State Soil Mechanics.* McGraw Hill. ISBN: 978-0-07-094048-2.

Seed, H. B., R. J. Woodward, and R. Lundgren. 1964. "Clay Mineralogical Aspects of the Atterberg Limits." *Journal of the Soil Mechanics and Foundations Division* 90 (4): 107–134.

Sigurðardóttir, M. E., and V.-A. Dobrescu. 2016. "The influence of pore water chemistry on the deformation behaviour of Clays." Master's thesis, Aarhus University, Department of Engineering.

Simpson, B. 1992. "Retaining structures: displacement and design." *Géotechnique* 42 (4): 541–576. doi:`10.1680/geot.1992.42.4.541`.

Sivapullaiah, P., and S. Savitha. 1999. "Index Properties of Illite-Bentonite Mixtures in Electrolyte Solutions." *Geotechnical Testing Journal* 22 (3): 257–265. ISSN: 0149-6115. doi:`10.1520/gtj11116j`.

Skempton, A. W. 1944. "Notes on the compressibility of clays." *Quarterly Journal of the Geological Society* 100 (1-4): 119–135. doi:`10.1144/gsl.jgs.1944.100.01-04.08`.

Sørensen, K. K. 2015. "Slurries_mætningsgrader" [in Danish]. E-mail.

Sørensen, K. K., B. A. Baudet, and B. Simpson. 2007. "Influence of structure on the time-dependent behaviour of a stiff sedimentary clay." *Géotechnique* 57 (1): 113–124. ISSN: 1751-7656. doi:`10.1680/geot.2007.57.1.113`.

Sørensen, K. K., and N. Okkels. 2013. "Correlations between drained shear strength and plasticity index of undisturbed overconsolidated clays." In *Proceedings of the 18th International Conference on Soil Mechanics and Geotechnical Engineering, Paris,* 423–428.

Sørensen, K. K., and N. Okkels. 2015. "Correlations between compression index and index parameters for high plasticity Palaeogene clays." In *Proceedings of the XVI ECSMGE,* 3371–3376. doi:`10.1680/ecsmge.60678.vol6.528`.

Spagnoli, G., T. Fernandez-Steeger, M. Feinendegen, H. Stanjek, and R. Azzam. 2010. "The influence of the dielectric constant and electrolyte concentration of the pore fluids on the undrained shear strength of smectite." *Soils and Foundations* 50 (5): 757–763. doi:`10.3208/sandf.50.757`.

Spagnoli, G., and A. Sridharan. 2012. "Liquid limit of mixtures of smectite, kaolinite and quartz powder with water and NaCl solution." *International Journal of Geotechnical Engineering* 6 (1): 117–123. doi:`10.3328/ijge.2012.06.01.117-123`.

Sridharan, A. 2014. "Fourth IGS-Ferroco Terzaghi Oration: 2014." *Indian Geotechnical Journal* 44 (4): 371–399. doi:`10.1007/s40098-014-0136-0`.

Sridharan, A., and G. Venkatappa Rao. 1975. "Mechanisms controlling the liquid limit of clays." In *Proceeding of the Istanbul conference on soil mechanics and foundation engineering,* 75–84. 1.

Sridharan, A., and M. S. Jayadeva. 1982. "Double layer theory and compressibility of clays." *Géotechnique* 32 (2): 133–144. doi:`10.1680/geot.1982.32.2.133`.

Sridharan, A., N. S. Murthy, and K. Prakash. 1987. "Rectangular hyperbola method of consolidation analysis." *Géotechnique* 37 (3): 355–368. doi:`10.1680/geot.1987.37.3.355`.

Sridharan, A., and H. B. Nagaraj. 2000. "Compressibility behaviour of remoulded, fine-grained soils and correlation with index properties." *Canadian geotechnical journal* 37 (3): 712–722. doi:`10.1139/t99-128`.

Sridharan, A., S. M. Rao, and N. S. Murthy. 1986. "Compressibility behavior of homoionized bentonites." *Géotechnique* 36 (4): 551–564. doi:`10.1680/geot.1986.36.4.551`.

Sridharan, A., S. M. Rao, and N. S. Murthy. 1988. "Liquid limit of kaolinitic soils." *Géotechnique* 38 (2): 191–198. doi:`10.1680/geot.1988.38.2.191`.

Sridharan, A., and G. Venkatappa Rao. 1973. "Mechanisms controlling volume change of saturated clays and the role of the effective stess concept." *Géotechnique* 23 (3): 359–382. doi:`10.1680/geot.1973.23.3.359`.

Taylor, D. W. 1948. *Fundamentals of Soil Mechanics.* John Wiley & Sons.

Taylor, R. K., and T. J. Smith. 1986. "The Engineering Geology of Clay Minerals: Swelling, Shrinking and Mudrock Breakdown." *Clay Minerals* 21 (3): 235–260. doi:`10.1180/claymin.1986.021.3.01`.

Terzaghi, K., R. B. Peck, and G. Mesri. 1996. *Soil mechanics in engineering practice.* 3rd edition. Wiley-Interscience. ISBN: 978-0-471-08658-1.

Thøgersen, L. 2001. "Effect of Experimental Techniques and Osmotic Pressure on the Measured Behaviour of Tertiary Expansive Clay." ISSN 1398-6465 R2035. PhD diss., Aalborg University, Soil Mechanics Laboratory.

Tiwari, B., and B. Ajmera. 2011. "Consolidation and swelling behavior of major clay minerals and their mixtures." *Applied Clay Science* 54 (3–4): 264–273. doi:`10.1016/j.clay.2011.10.001`.

Tiwari, B., and B. Ajmera. 2014. "Effects of saline fluid on compressibility of clay minerals." *Environmental Geotechnics* 1 (2): 108–120. ISSN: 2051-803X. doi:`10.1680/envgeo.13.00053`.

Torrance, J. K. 1984. "A comparison of marine clays from Ariake Bay, Japan and the South Nation River landslide site, Canada." *Soils and Foundations* 24 (2): 75–81. doi:`10.3208/sandf1972.24.2_75`.

Trankjær, H., and L. Christensen. 2012. "Har lermineralsammensætningen i fede, danske lerarter betydning for funderingen." In *NGM 2012 - Proceedings of the Nordic Geotechnical Meeting*, 251–259.

Varv. 1992. *Kort over Prækvartær - overfladen.* `http://data.geus.dk/geusmap/ ?mapname=denmark&lang=da#zoom=2&lat=6313666.5564372&lon= 498432.39389209&visiblelayers=Topografisk&filter=&layers=unde rgrundskort_varv&mapname=denmark&filter=&epsg=25832&mode=map& map_imagetype=png&wkt=.`

Vitone, C., and F. Cotecchia. 2011. "The influence of intense fissuring on the mechanical behaviour of clays." *Géotechnique* 61 (12): 1003–1018. ISSN: 1751-7656. doi:`10.1680/ geot.9.p.005`.

Vosgerau, A. S. 2012. "Scale Effects Relevant for Palaeogene Clays - Main Report." Master's thesis, Technical University of Denmark.

White, W. A. 1949. "Atterberg Plastic limits of clay minerals." *American Mineralogist* 34 (7-8): 508–512. `https://www.ideals.illinois.edu/bitstream/handle/ 2142/35091/atterbergplastic144whit.pdf?sequence=2`.

White, W. A. 1955. *Water sorption properties of homoionic clay minerals.* Technical report 208. Illinois State Geolocial Survey.

Yukselen-Aksoy, Y., A. Kaya, and A. H. Ören. 2008. "Seawater effect on consistency limits and compressibility characteristics of clays." *Engineering Geology* 102 (1-2): 54–61. ISSN: 0013-7952. doi:`10.1016/j.enggeo.2008.07.005`.

Part I

Side studies

Overview over tests

An overview of all tests conducted within the present PhD-project is given in table A.1. In the table the names of the oedometer tests and the clay mineral mixtures for each test are presented, along with initial saturation, S_0 and initial void ratio e_0. Moreover, the compression index, swelling index and recompression index are presented for each test. It should be noted that the presented indices were calculated based different stress intervals, which is why the values are highly dependent on the loading programme. Details on the relevant stress levels may be found in the laboratory reports for the respective tests.

Table A.1: *Overview over oedometer tests performed by the author on artificial and natural specimens. Moreover, selected results from the tests are presented. For each test, a test report may be found in the laboratory report, part IV.*

Name	Recipe	Test Programme	Pore fluid	S_0 [%]	e_0 [-]	C_C [-]	C_S [-]	C_R [-]
OE001S001	K100B0	Pilot test	Tap	98.7	1.23	0.40	0.05	0.09
OE002S001*	K100B0	Pilot test	Tap	97.9	1.25	0.29	0.05	0.09
OE003S002	K100B0	Pilot test	Deion.	98.9	1.25	0.40	0.05	0.09
OE004S003	K100B0	Pilot test	Tap	—†	—†	—†	—†	—†
OE005S003	K100B0	Pilot test	Tap	—†	—†	—†	—†	—†
OE006S004	K100B0	Pilot test	Tap	97.6	1.31	0.35	0.06	0.08
OE007S005	K90B10	Pilot test	Tap	95.7	1.34	0.47	0.09	0.13
OE008S006	K80B20	Pilot test	Tap	92.9	1.61	0.91	0.14	0.20
OE009S007	K50B50	Pilot test	Tap	100.3	5.92	3.57	0.66	0.83
OE010S008	K0B100	Pilot test	Tap	97.2	13.67	7.29	3.15	3.96
OE011S008	K0B100	Pilot test	Tap	98.6	4.75	3.47	1.42	1.63
OE012S008	K0B100	Pilot test	Tap	99.2	5.05	3.63	1.09	1.31
OE013S010	K80B20	Pilot test	Tap	89.8	2.14	1.00	0.18	0.22
OE014S011	K80B20	Pilot test	Tap	94.4	1.87	0.90	0.19	0.23
OE015S012	K80B20	Pilot test	Tap	77.9	1.59	0.50	0.10	0.15
OE016LB001	Natural	Friction test	PC02	95.5	1.20	0.25	0.15	0.18

Table A.1 – continued from previous page

Name	Recipe	Test Programme	Pore fluid	S_0 [%]	e_0 [-]	C_C [-]	C_S [-]	C_R [-]
OE017LB002	Natural	Friction test	PC02	101.5	1.11	0.26	0.14	0.16
OE018S017	K60B40	Friction test	Tap	95.8	2.39	1.30	0.25	0.29
OE019S017	K60B40	Friction test	Tap	99.2	2.23	1.35	0.33	0.47
OE020S018	K100B0	Friction test	Tap	95.4	1.16	0.45	0.08	0.09
OE021S018	K100B0	Friction test	Tap	96.7	1.14	0.32	0.05	0.07
OE022S019	K40B60	Pilot test	Tap	100.6	4.02	3.72	0.47	0.65
OE023S020	K50B50	Pilot test	Tap	97.4	3.45	2.34	0.44	0.53
OE024S024	K60B40	Pilot test	Tap	100.3	6.01	2.69	—	—
OE025LB003	Natural	Pilot test	Tap	95.4	1.10	9.67	0.11	0.14
OE026S025	K70B30	Pilot test	Tap	99.1	5.07	2.18	—	—
OE027S026	K80B20	Pilot test	Tap	99.4	3.91	1.14	—	—
OE028S027	K90B10	Pilot test	Tap	98.8	2.88	0.70	—	—
OE029S028	K100B0	Pilot test	Tap	99.7	2.13	0.34	—	—
OE030S029	K70B30	Pilot test	Tap	99.0	1.85	1.02	0.26	0.34
OE031LB004	Natural	Pilot test	PC02	100.1	1.14	0.24	0.09	—
OE034S038	K90B10	Procedure test	Tap	97.2	1.39	0.48	0.12	—
OE035S037	K90B10	Procedure test	Tap	98.0	1.37	0.54	0.11	—
OE036S032	K60B40	Procedure test	Tap	97.1	2.07	1.29	0.49	—
OE037S032	K60B40	Procedure test	Tap	96.7	2.07	1.5	0.53	—
OE038S033	K60B40	Procedure test	Tap	97.8	2.08	—	0.47	—
OE039S042	K90B10	Procedure test	Tap	98.2	1.34	0.50	0.12	—
OE040S042	K90B10	Procedure test	Tap	100.3	1.31	—	0.10	—
OE041S042	K90B10	Procedure test	Tap	100.8	1.35	0.49	0.12	—
OE042S034	K80B20	Main test	Tap	100.2	1.51	0.98	0.14	0.14
OE043S034	K80B20	Main test	Tap	102.0	1.49	0.83	0.15	0.18
OE044S033	K60B40	Procedure test	Tap	95.7	2.06	1.26	0.49	—
OE045S036	K60B40	Procedure test	Tap	97.8	2.07	1.26	0.43	—
OE046S035	K100B0	Main test	Tap	96.5	1.16	0.33	0.06	0.05
OE047S035	K100B0	Main test	Tap	98.5	1.18	0.39	0.05	0.07
OE048S036	K60B40	Main test	Tap	98.2	2.06	1.30	0.23	0.27
OE049S035	K100B0	Main test	Tap	97.4	1.18	0.34	0.05	0.06
OE050S039	K40B60	Main test	Tap	99.0	2.76	1.88	0.51	0.53
OE051S039	K40B60	Main test	Tap	99.1	2.69	2.04	0.48	0.53
OE052LB005	Natural	Pilot test	Tap	100.6	1.12	0.46	0.18	—
OE053S030	K40B60	Main test	Tap	97.6	2.62	1.99	0.43	0.45
OE054S040	K60B40	Main test	Tap	97.6	2.06	1.35	0.27	0.28
OE055S046	K80B20	Main test	Tap	98.4	1.65	0.93	0.13	0.14
OE056S046	K80B20	Main test	Tap	101.1	1.67	1.01	0.16	0.18
OE057S041	K60B40	Main test	Tap	97.7	2.26	1.45	0.35	0.38
OE058S041	K60B40	Main test	Tap	100.6	2.23	1.70	0.27	0.30

Continued on next page

Table A.1 – continued from previous page

Name	Recipe	Test Programme	Pore fluid	S_0 [%]	e_0 [-]	C_C [-]	C_S [-]	C_R [-]
OE059S043	K60B40	Main test	Tap	98.7	2.15	1.39	0.29	0.31
OE060S043	K60B40	Main test	Tap	98.1	2.29	1.31	0.22	0.26
OE061S050	K80B20	Main test	Tap	98.5	1.58	0.86	0.10	0.12
OE062S050	K80B20	Main test	Tap	99.5	1.56	0.96	0.13	0.15
OE063S044	K60B40	Validation test	Tap	96.7	2.20	1.48	0.47	0.51
OE064S052	K100B0	Validation test	Tap	99.7	1.14	0.32	0.08	0.09
OE065S052	K100B0	Validation test	Tap	97.9	1.16	0.41	0.06	0.07
OE066S051	K80B20	Swell test	Tap	99.9	1.56	—	—	—
OE067S052	K100B0	Swell test	Tap	98.4	1.17	—	—	—
OE068S051	K80B20	Validation test	Tap	99.2	1.66	0.72	0.16	0.17
OE069S051	K80B20	Validation test	Tap	100.1	1.63	1.20	0.15	0.17
OE070S045	K40B60	Swell test	Tap	98.7	2.78	—	—	—
OE071S047	K40B60	Validation test	Tap	99.2	2.63	1.90	0.71	0.77
OE072S047	K40B60	Validation test	Tap	99.7	2.56	1.85	0.43	0.46
OE073S054	K60B40	Validation test	Tap	98.6	2.31	1.23	0.28	0.31
OE074S053	K60B40	Swell test	Tap	98.2	2.45	—	—	—
OE075S054	K60B40	Swell test	Tap	96.7	2.23	—	—	—
OE076S056	K60B40	Validation test	Tap	100.0	7.28	2.62	0.78	0.89

[*] Specimen stored wrapped in cling-film at room temperature for 27 days prior to testing (i.e. the specimen was dried out).

[‡] Mass of specimen not recorded prior to testing.

A.1 Compression curves for main tests

Compression curves from the main laboratory tests (Load 1–3) and the validation tests are presented in the current section. The compression curves are presented on both the $\log(\sigma_v')$-axis and on a linear stress axis.
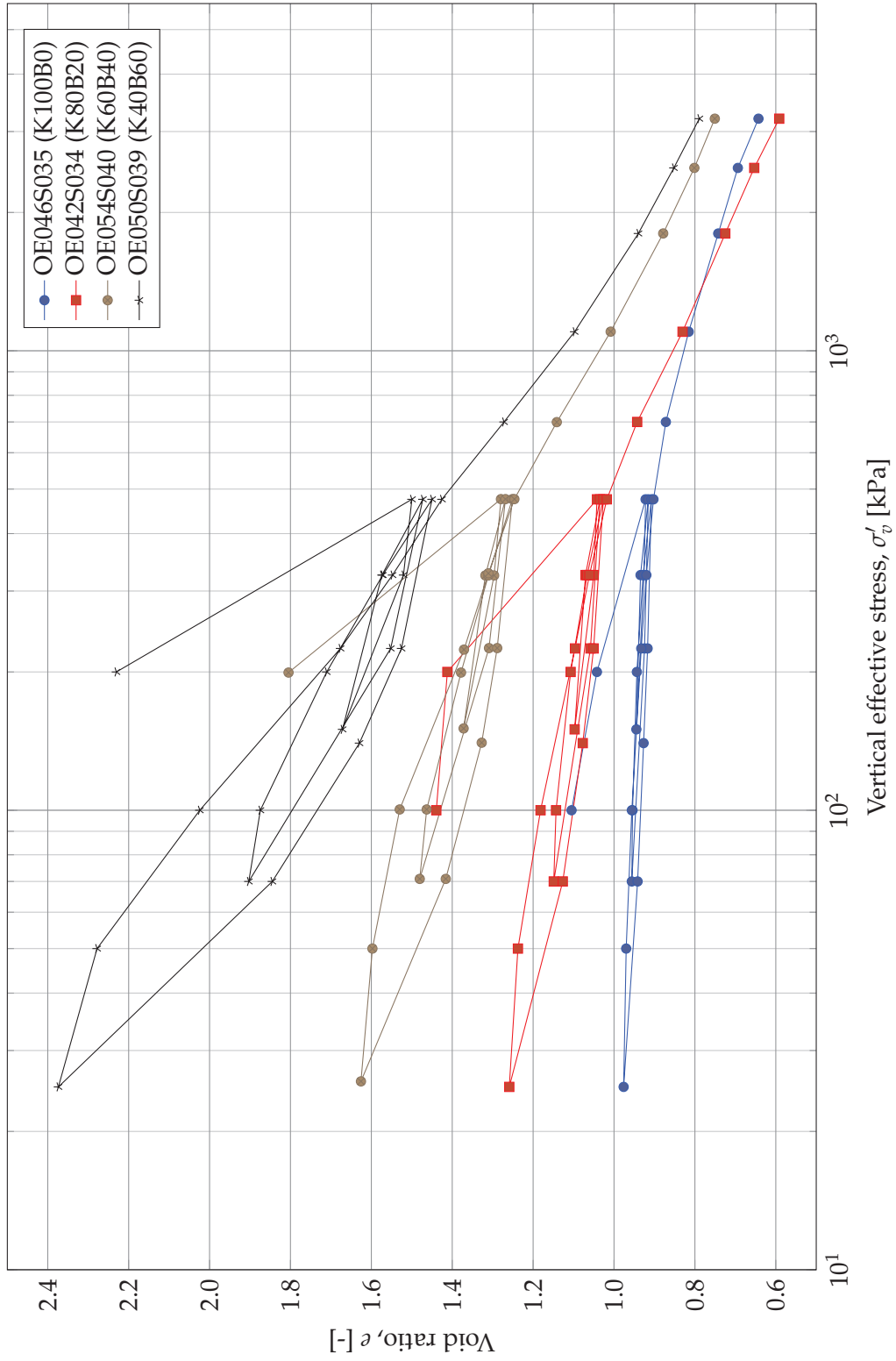
Figure A.1: *Compression curves for tests following loading programme 1 of the main laboratory programme.*
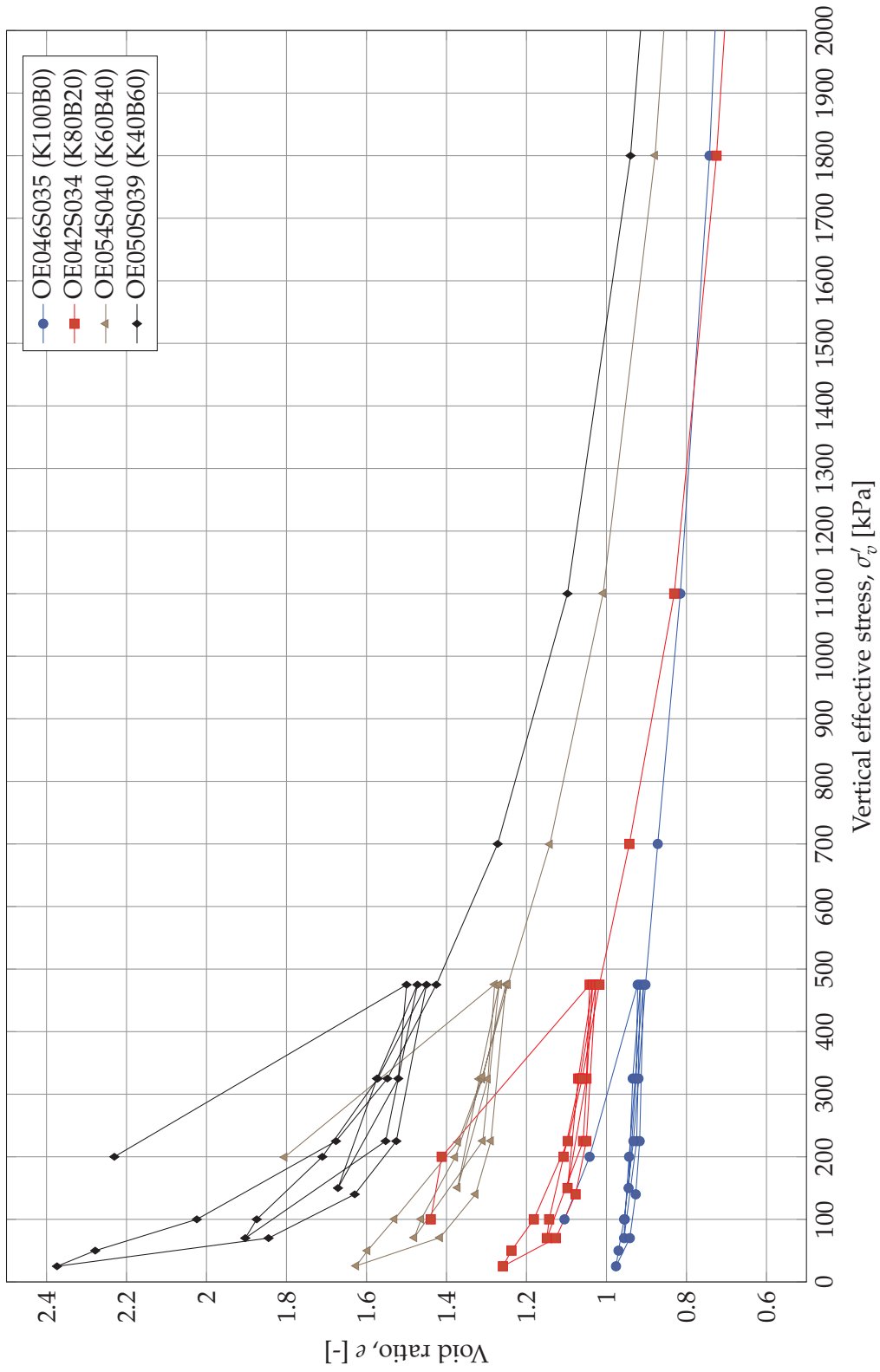
Figure A.2: *Compression curves for tests following loading programme 1 of the main laboratory programme. The part of the virgin curve above 2000 kPa is not shown in the figure.*
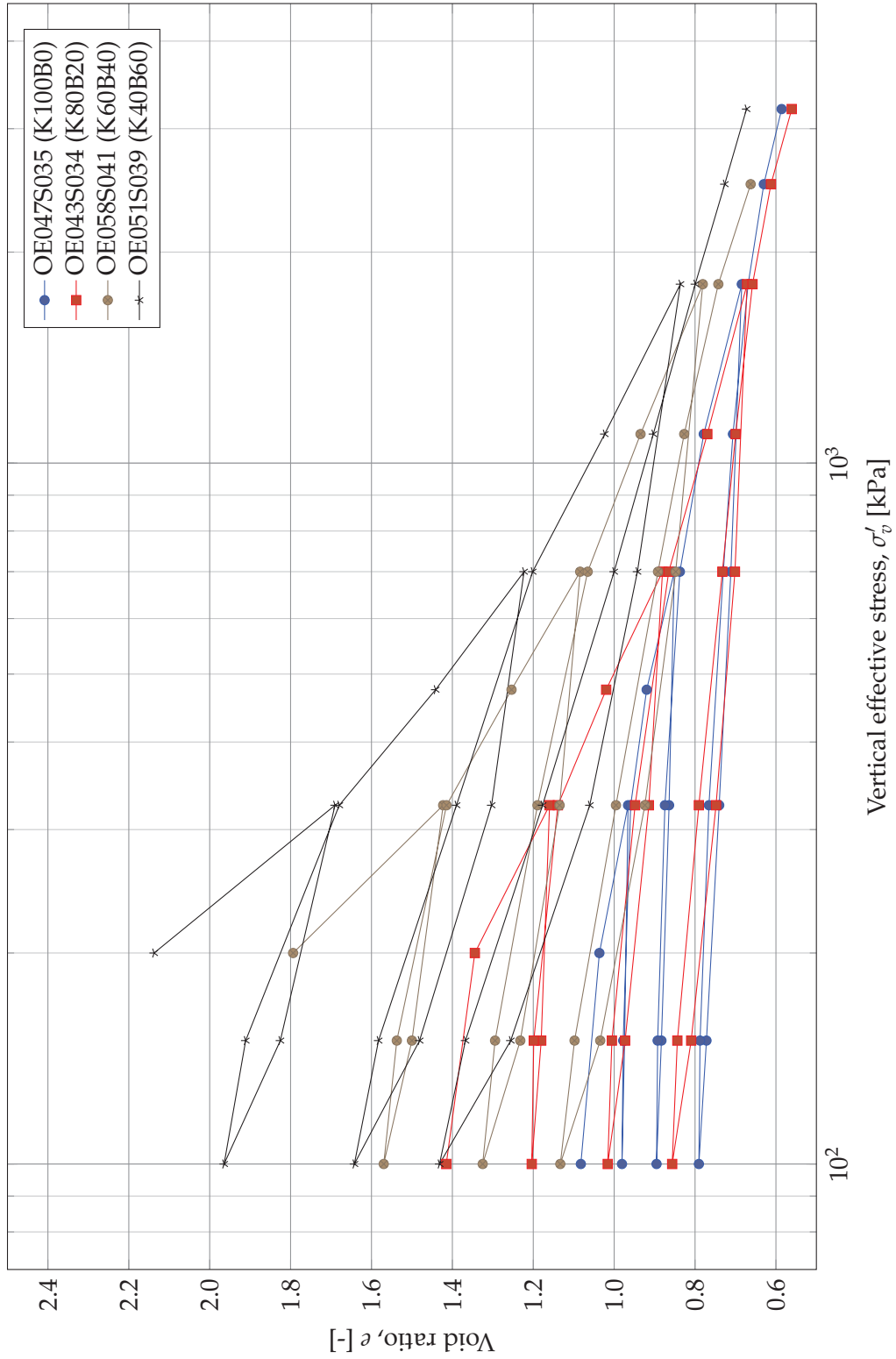
Figure A.3: *Compression curves for tests following loading programme 2 of the main laboratory programme.*

154
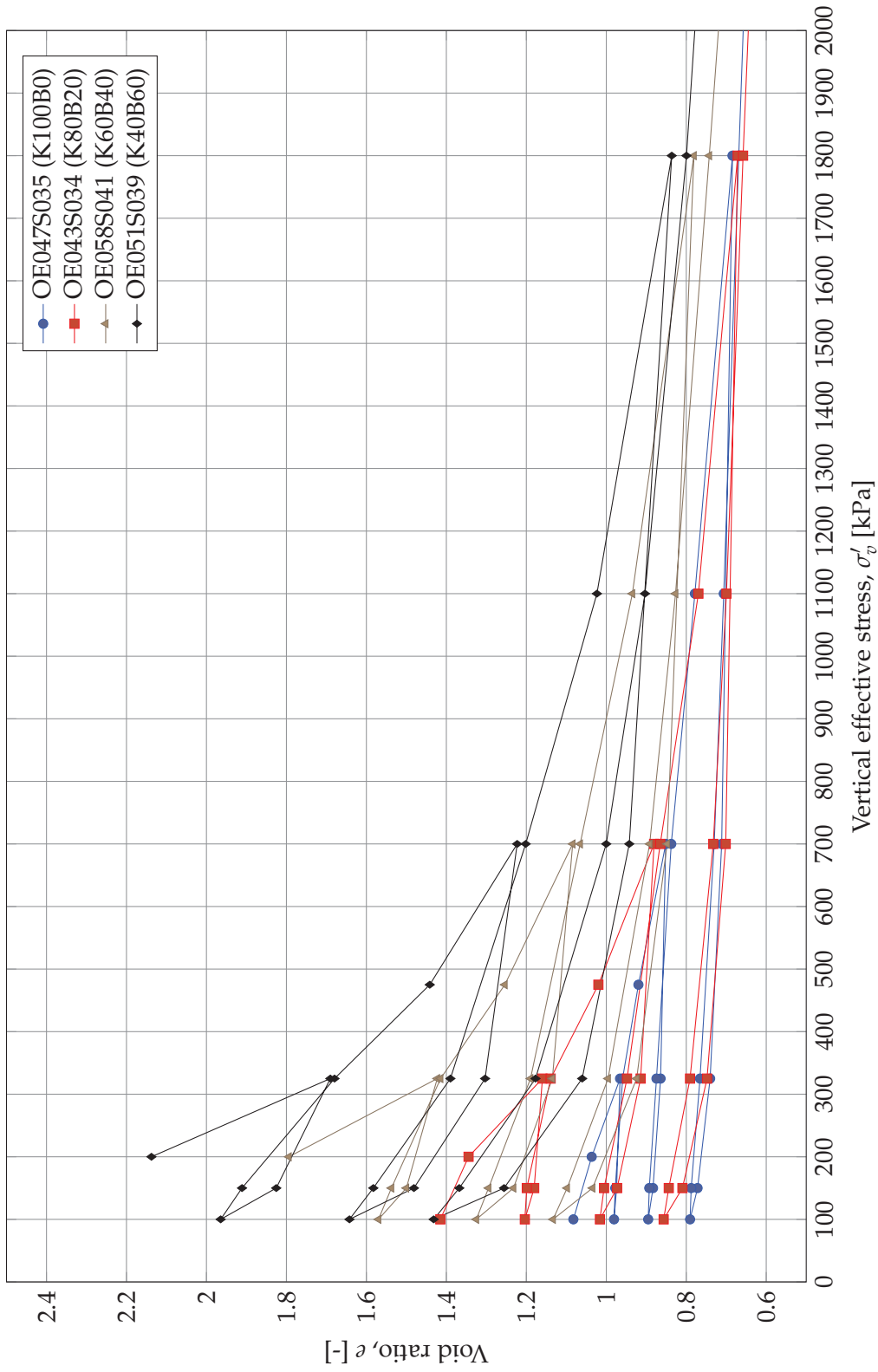
Figure A.4: *Compression curves for tests following loading programme 2 of the main laboratory programme. The part of the virgin curve above 2000 kPa is not shown in the figure.*
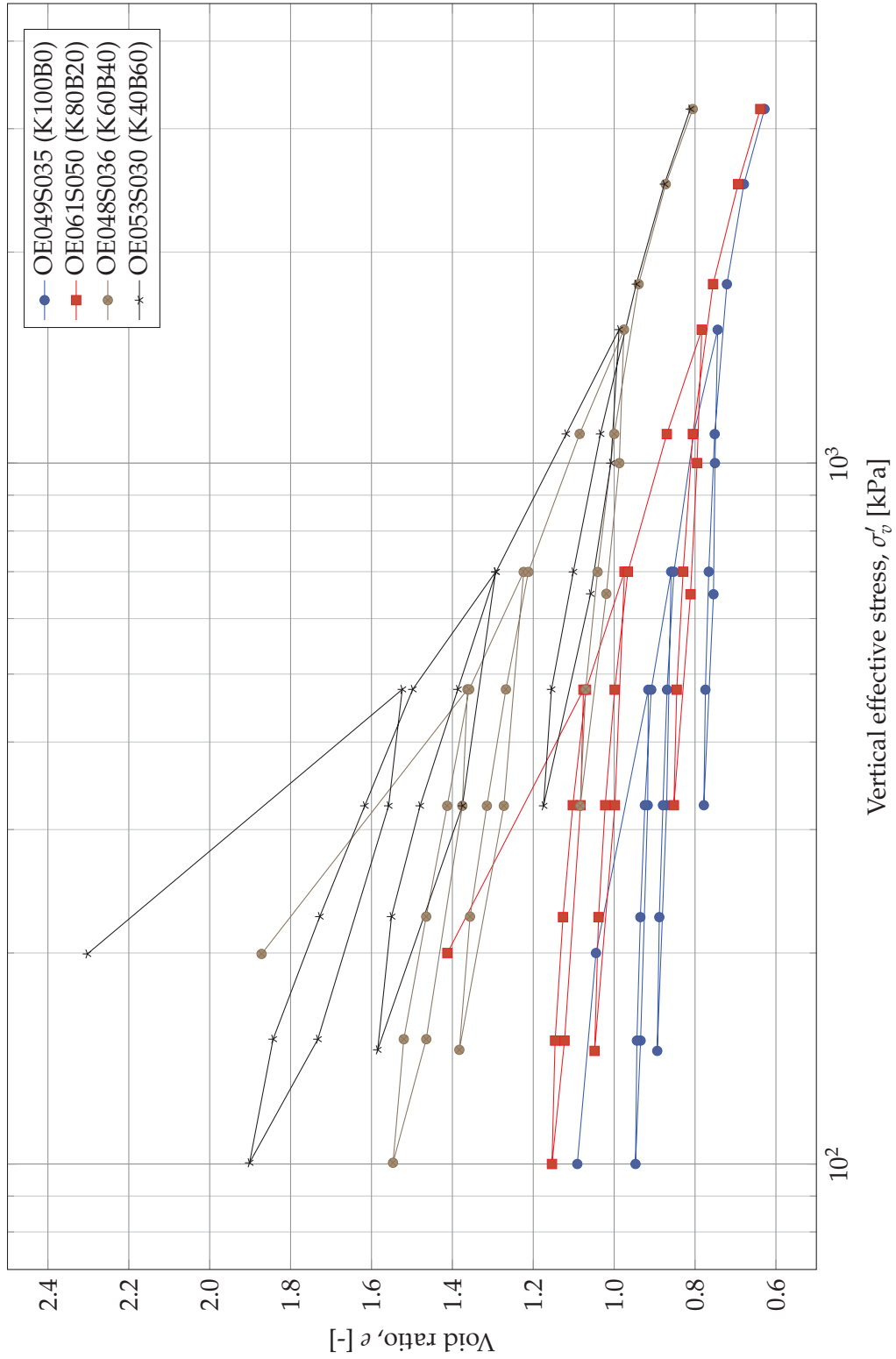
Figure A.5: *Compression curves for tests following loading programme 3 of the main laboratory programme.*
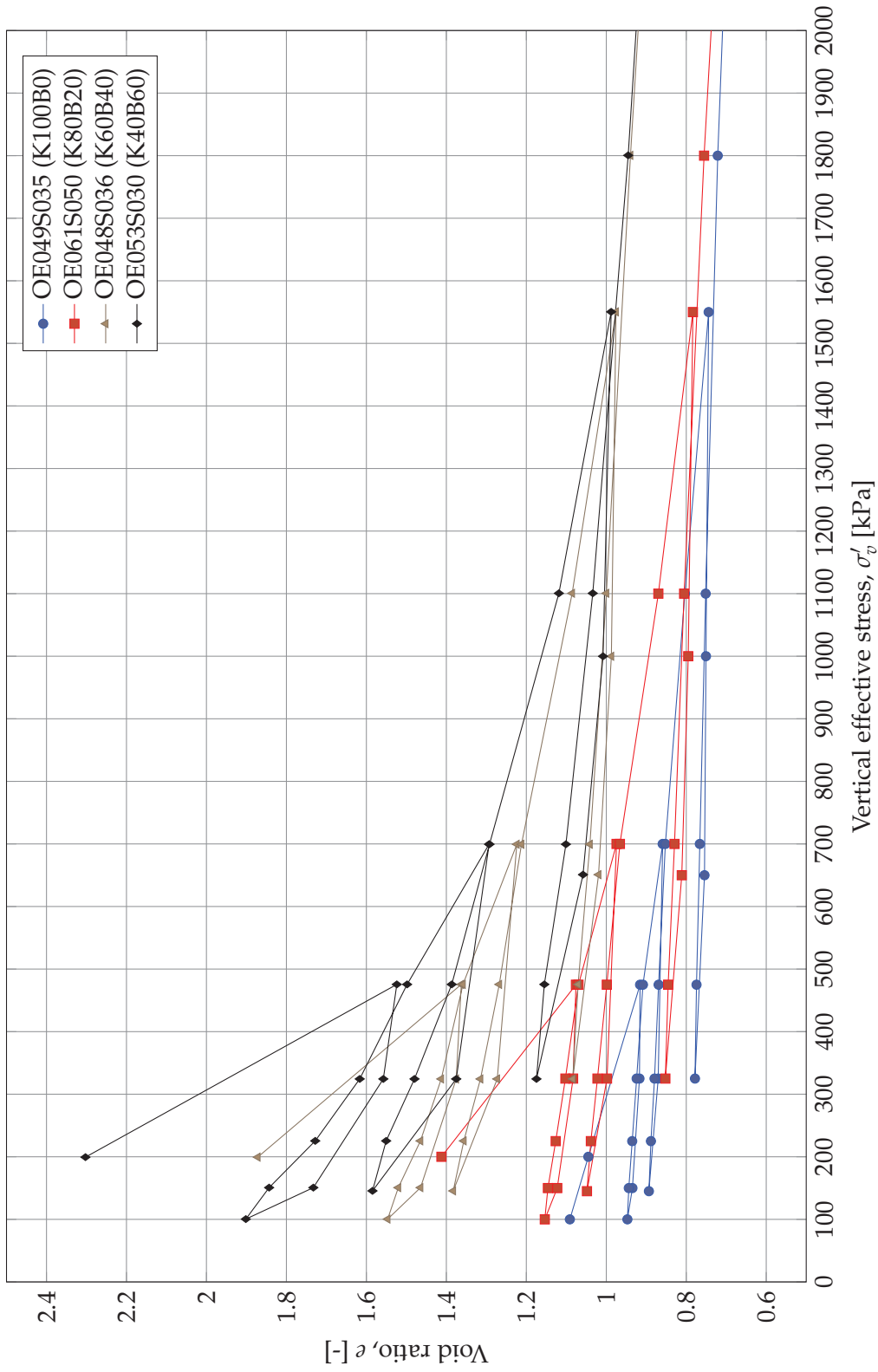
Figure A.6: *Compression curves for tests following loading programme 3 of the main laboratory programme. The part of the virgin curve above 2000 kPa is not shown in the figure.*
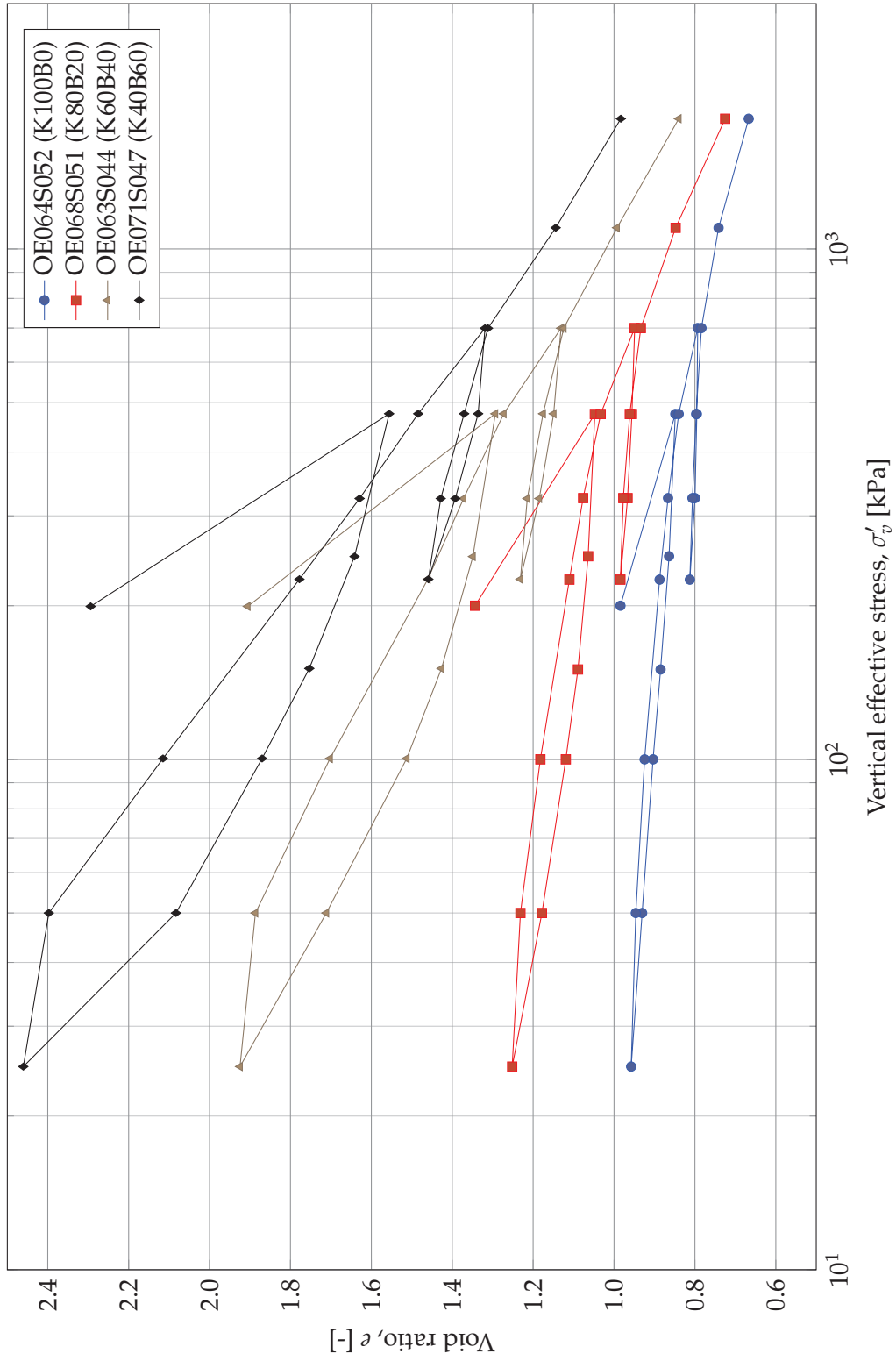
Figure A.7: *Compression curves for tests following loading programme 4 of the validation laboratory programme.*
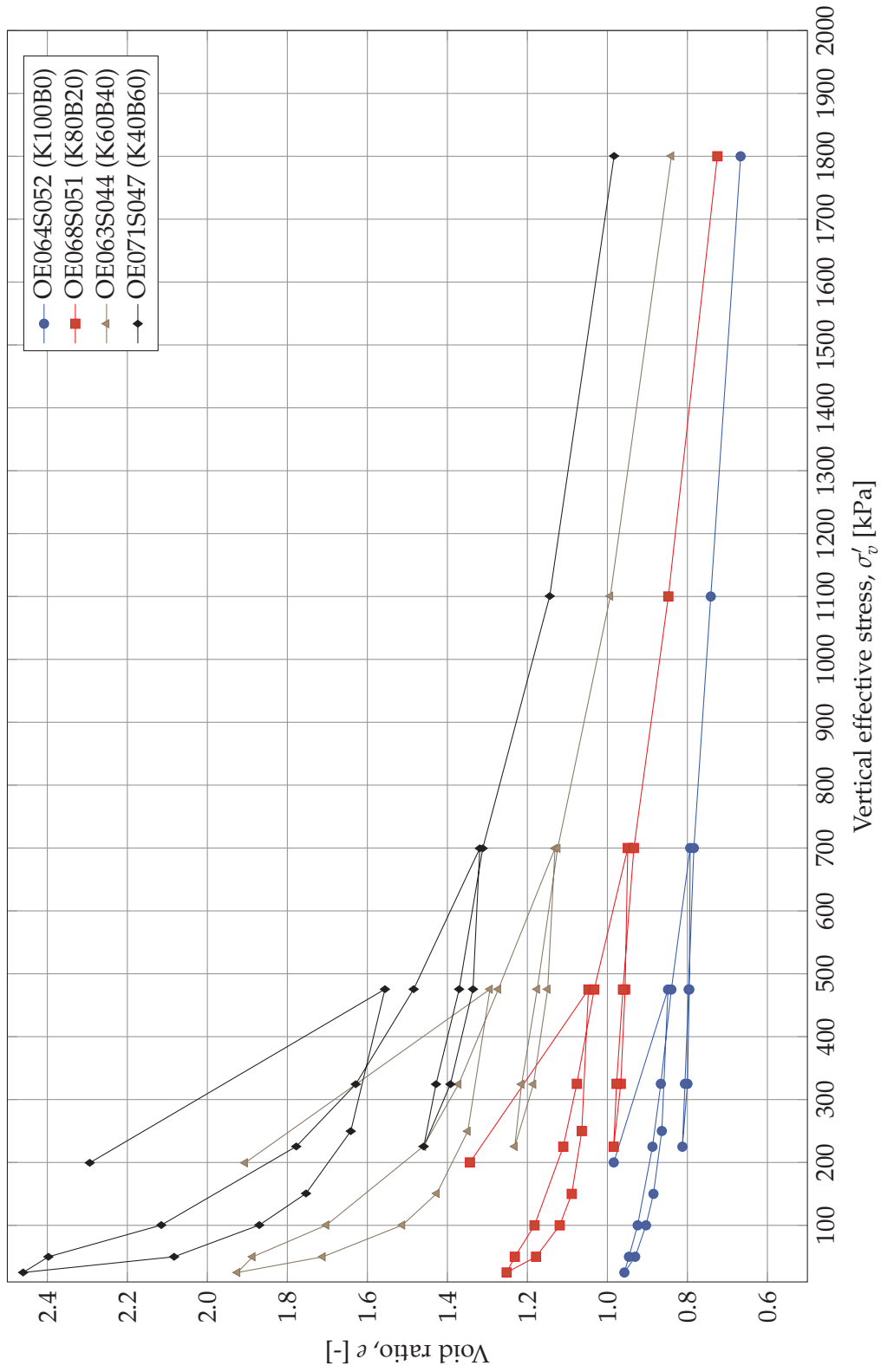
Figure A.8: Compression curves for tests following loading programme 4 of the validation laboratory programme.
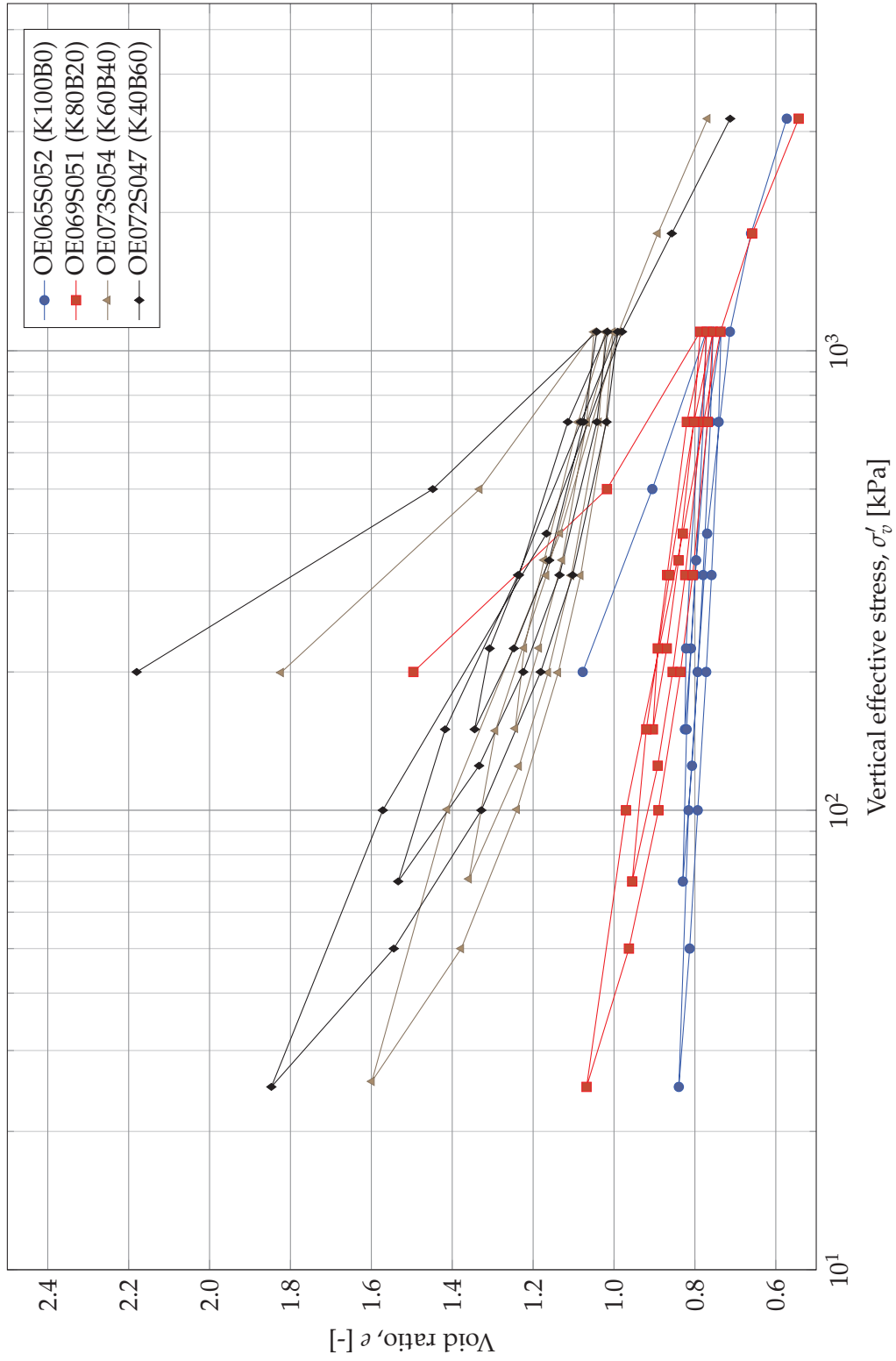
Figure A.9: *Compression curves for tests following loading programme 5 of the validation laboratory programme.*
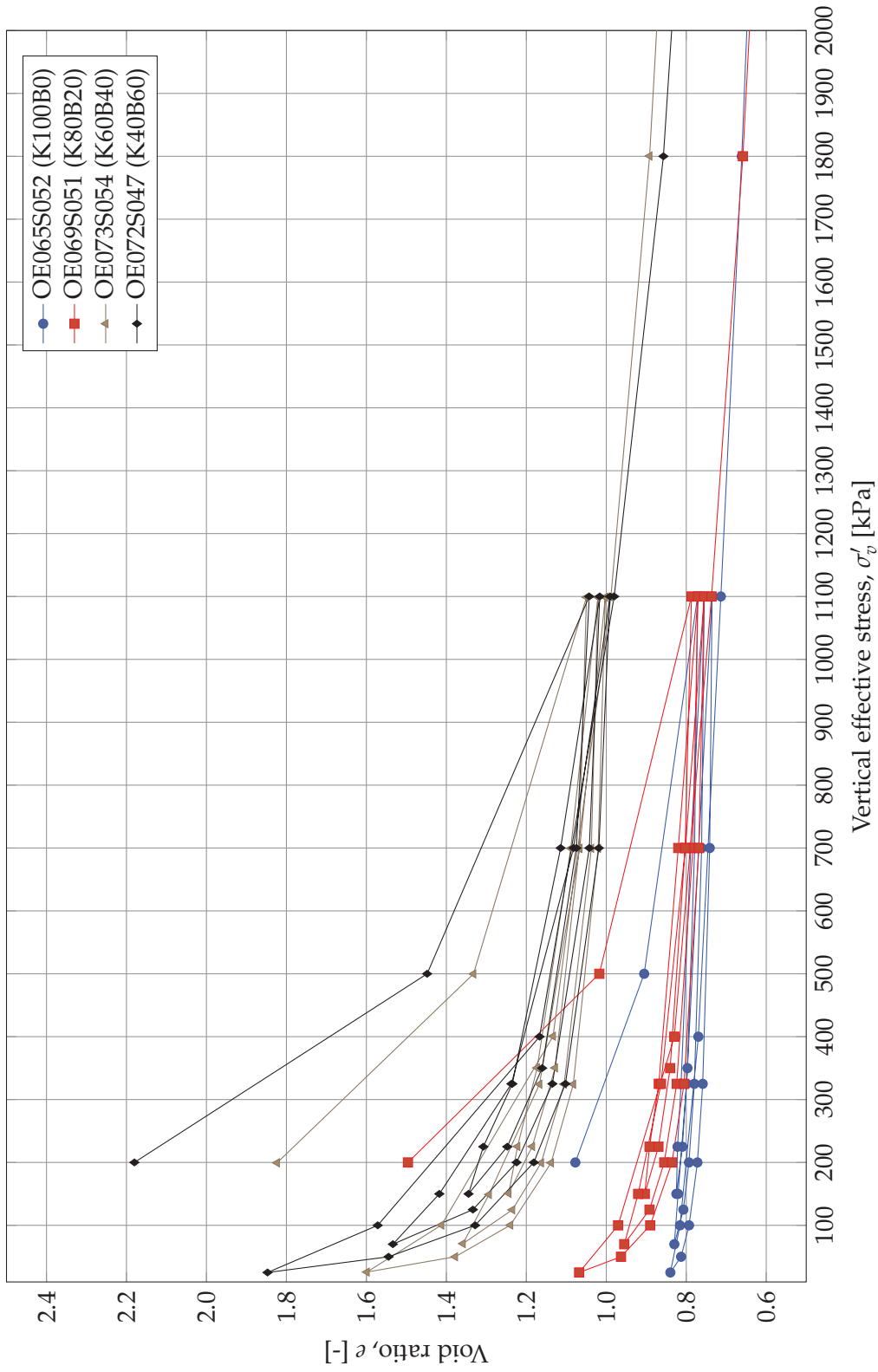
Figure A.10: *Compression curves for tests following loading programme 5 of the validation laboratory programme. The part of the virgin curve above 2000 kPa is not shown in the figure.*

A.2 Tests performed by students

A number of tests were carried out during MSc-projects, where the author of the present dissertation was co-supervisor. The MSc-projects were related to the subject of the present thesis, and an overview over the conducted tests are presented in table A.2.

Table A.2: Overview over tests performed by MSc-students on artificial specimens. For each test, a test report may be found in the laboratory report, part V. Tests named MV were carried out by Sigurðardóttir and Dobrescu (2016), tests named JD were carried out by Dolby (2017), tests labelled ExpGeo were carried out by the class of experimental geotechnics 2016 and tests labelled EO were carried out by Ohler (2017).

Name	Recipe	Pore fluid	S_0 [%]	e_0 [-]	C_C [-]	C_S [-]	C_R [-]
MV001	K100B0	2 % NaCl	97.0	1.22	0.29	0.04	0.04
MV002	K100B0	4 % NaCl	95.6	1.26	0.31	0.05	0.05
MV003	K100B0	6 % NaCl	102.6	1.28	0.30	0.04	0.04
MV004	K100B0	2 % $CaCl_2$	97.0	1.22	0.29	0.04	0.04
MV005	K100B0	4 % $CaCl_2$	96.1	1.23	0.28	0.04	0.04
MV006	K100B0	6 % $CaCl_2$	97.0	1.27	0.29	0.05	0.05
MV007	K100B0	PC02	95.3	1.31	0.31	0.05	0.05
MV008	K100B0	Deion.	95.8	1.23	0.28	0.04	0.04
MV009	K90B10	2 % NaCl	93.7	1.44	0.40	0.07	0.07
MV010	K90B10	4 % NaCl	98.9	1.31	0.37	0.05	0.05
MV011	K90B10	6 % NaCl	97.9	1.32	0.35	0.06	0.06
MV012	K90B10	2 % $CaCl_2$	97.4	1.25	0.32	0.05	0.05
MV013	K90B10	4 % $CaCl_2$	96.1	1.24	0.31	0.04	0.04
MV014	K90B10	6 % $CaCl_2$	96.9	1.29	0.34	0.04	0.04
MV015	K90B10	PC02	99.7	1.29	0.37	0.06	0.06
MV016	K90B10	Deion.	98.5	1.43	0.52	0.10	0.10
MV017	K80B20	2 % NaCl	94.9	1.42	0.47	0.07	0.07
MV018	K80B20	4 % NaCl	106.1	1.35	0.43	0.06	0.06
MV019	K80B20	6 % NaCl	94.3	1.40	0.41	0.06	0.06
MV020	K80B20	2 % $CaCl_2$	98.8	1.36	0.38	0.07	0.07
MV021	K80B20	4 % $CaCl_2$	98.1	1.29	0.36	0.06	0.06
MV022	K80B20	6 % $CaCl_2$	101.3	1.37	0.38	0.06	0.06
MV023	K80B20	PC02	101.2	1.45	0.45	0.08	0.08
MV024	K80B20	Deion.	90.6	1.90	0.77	0.15	0.15
EO001	K0B0I100	Deion.	108.3	0.68	0.21	0.03	0.03
EO002	K20B20I60	Deion.	57.3*	1.61	0.92	0.27	0.31
EO003	K30B10I60	Deion.	100.1	1.18	0.49	0.09	0.10
EO004	K20B20I60	2 % NaCl	102.7	1.20	0.40	0.07	0.08
EO005	K0B0I100	2 % NaCl	101.9	0.85	0.23	0.04	0.05
EO006	K30B10I60	2 % NaCl	102.8	1.08	0.35	0.05	0.07

Continued on next page

Table A.2 – continued from previous page

Name	Recipe	Pore fluid	S_0 [%]	e_0 [-]	C_C [-]	C_S [-]	C_R [-]
EO007	K40B0I60	2 % NaCl	106.2	0.94	0.22	0.04	0.05
EO008	K40B0I60	Deion.	102.0	0.94	0.20	0.04	0.04
ExpGeo001	K0B10I90	Deion.	103.7	2.15	0.74	0.10	—
ExpGeo002	K0B10I90	2 % NaCl	97.1	1.78	0.38	0.04	—
JD002[†]	K1000B0	Tap	97.1	1.18	—	—	—
JD003[‡]	K1000B0	Tap	104.4	1.12	—	—	—
JD005	K1000B0	Tap	90.3	1.27	0.34	0.04	0.06
JD007[§]	K1000B0	Tap	103.8	1.12	—	—	—

[*] Measurements seem to be wrong.
[†] Isotropic CID triaxial test.
[‡] K_0 CAD triaxial test.
[§] CID triaxial test.

A.3 Tests from literature

A number of tests performed for Danish construction projects or published in literature was included in the present project. The tests were applied to assess the performance of the proposed deformation model, when dealing with natural, intact clays. The included tests are presented in table A.3. All the tests include at least one unloading-reloading loop. Compression curves not available in literature have been enclosed in the laboratory report, part VI.

Table A.3: *Natural clay specimens included in the present study. Data from Røsnæs Clay after (Femern 2013a), data for Little Belt clay from (Geoteknisk Institut 1964, 1962, 1961; Krogsbøll et al. 2012), data for Boom clay from (Nguyen et al. 2013; Deng et al. 2012) and data for Ypresian clays (Orchies and Roubaix) from (Nguyen et al. 2014; Deng et al. 2012). Data from Søvind marl after (Geo 2015, 2010a).*

Boring	Lab no.	Depth[*] [m]	σ'_{v0} [kPa]	I_p [%]	e_0 [-]	Clay unit
09.A.003	09-101847_04_06	41.85	385	71.5	1.151	Røsnæs
10.A.051	10-105072_54_56	16.34	140	72.5	0.939	Røsnæs
09.A.002	09-101462_01_03	90.21	809	90.6	0.940	Røsnæs
09.A.003	09-101850_56_58	46.41	420	100.0	1.123	Røsnæs
09.A.002	09-101439_31_33	11.81	105	110.8	1.141	Røsnæs
09.A.002	09-101477_44_46	22.64	200	116.3	1.040	Røsnæs
10.A.051	09-105043_05_07	24.90	215	121.6	1.026	Røsnæs
09.A.002	09-101435_45_47	33.40	295	122.1	0.933	Røsnæs
09.A.001	09-101205_36_38	32.36	255	129.3	0.966	Røsnæs
09.A.003	09-101858_07_09	34.32	320	135.1	1.074	Røsnæs
09.A.003	09-101858_04_06	34.29	320	135.1	0.967	Røsnæs

Continued on next page

Table A.3 – continued from previous page

Boring	Lab no.	Depth* [m]	σ'_{v0} [kPa]	I_p [%]	e_0 [-]	Clay unit
09.A.002	09-101437_34_36	29.89	265	136.7	1.043	Røsnæs
09.A.002	09-101472_41_43	45.16	400	140.2	1.022	Røsnæs
09.A.001	09-101232_08_10	45.18	360	143.9	0.952	Røsnæs
10.A.055	10-105204_06_08	27.31	250	147.8	1.136	Røsnæs
10.A.055	10-105272_10_12	43.10	380	152.1	1.042	Røsnæs
09.A.001	09-101199_48_50	26.33	206	153.2	1.074	Røsnæs
09.A.003	09-101856_07_09	23.42	225	168.3	0.967	Røsnæs
09.A.003	09-101856_04_06	23.39	225	168.3	1.058	Røsnæs
	Ess75Oedo2	219.41	2200	45.0	0.79	Boom, Putte
	Ess75Oedo1	219.41	2200	45.0	0.79	Boom, Putte
	B04	227.15	2400	32.5	0.72	Boom
	YK43O2	330.44	3200	41.6	0.81	Roubaix
	YK43O1	330.44	3200	41.6	0.78	Roubaix
	YK64O2	351.17	3200	80.1	0.79	Roubaix
	YK64O1	351.17	3200	80.1	0.80	Roubaix
	YK73O2	362.21	3200	100.5	0.94	Roubaix
	YK73O1	362.21	3200	100.5	0.93	Roubaix
	YK95O2	381.94	3200	88.5	0.94	Orchies
	YK95O1	381.94	3200	88.5	0.94	Orchies
	YPClay43	330.19	3200	41.6	0.81	Roubaix
	YPClay64	351.25	3200	80.1	0.79	Roubaix
	YPClay73	361.32	3200	100.5	0.94	Roubaix
	YPClay95	382.40	3200	88.5	0.95	Orchies
LB4	16	5.6	44	61.3	0.88	Little Belt
LB4	24	7.4	60	54.4	1.12	Little Belt
LB4	40	12.1	99	67.2	1.26	Little Belt
LB4	45	14	115	67.2	1.17	Little Belt
LB4	45II	14	115	67.2	1.27	Little Belt
LB3	60	2.9	26	68.1	1.06	Little Belt
LB1	112	18.2	192	54.4	1.05	Little Belt
LB1	119	24.4	236	94.2	1.19	Little Belt
LB3	143	16.1	138		1.22	Little Belt
LB1	181I	26.4	254	124.8	1.14	Little Belt
LB7	312	3	175	73.1	1.08	Little Belt
10.A.801	LB#1	21.5	170	183.0	1.22	Little Belt
BH103	13	31.6	158	95	1.16	Søvind
BH103	21	43.8	251	152	1.34	Søvind
BH103	27	51.9	312	151	1.17	Søvind
BH103	33	61.3	384	123	0.93	Søvind
TR103	64	29.9	145	141	1.16	Søvind

Table A.3 – continued from previous page

Boring	Lab no.	Depth* [m]	σ'_{v0} [kPa]	I_p [%]	e_0 [-]	Clay unit
TR103	80	39.9	221	170	1.35	Søvind
13	N14	16	60	67	1.04	Søvind
11	N34	16	175	48	0.89	Søvind
13	N40	15.7	130	124	1.26	Søvind
11	N43	20.5	180	89	1.12	Søvind
13	N50	19.8	166	202	1.42	Søvind
11	N61	25.8	244	157	1.07	Søvind

* Depth below seabed or surface.

Procedures for sample reconstitution

B.1   Introduction

The present chapter introduces the methods applied for creating preconsolidated, reconstituted, artificial clay samples for oedometer testing. The artificial specimens were created as slurries which were incrementally consolidated in a consolidometer to enable handling and to trimming to the oedometer ring.

In the following sections a number of minor tests are also introduced, which were carried out to validate the applied procedures.

B.2   Preparation of slurry

The required content of clay powders were weighed and mixed thoroughly in dry state to match the recipe of the desired slurry. Based on the total mass of clay powder and the target water content, the mass of tap water to be added was weighed and added to the mixing bowl. The mixture was mixed in a Bjørn Teddy mixer for 5 min, then any clay material sticking to the sides of the mixing bowl was scraped down using a rubber spatula and the slurry was mixed for another 5 min. In case the slurry by visual inspection looked inhomogeneous, the sides of the bowl were scraped again and the slurry mixed for another 5 min. This procedure was repeated until slurry appeared uniform and homogeneous by visual inspection.

B.3   Installation of slurry in consolidometer

The filter stones were boiled in the selected pore fluid (most often tap-water) to remove air bubbles and were allowed to cool before use. One of the loading caps with a drainage channel was placed in the bottom of the acrylic tube with the radial drainage channel facing downwards. One of the filter stones was placed on the bottom loading cap. A wetted Ø70 mm filter paper was placed on the filter stone (figure B.1).

The slurry was installed in the tube with a teaspoon, while carefully avoiding to trap air by tapping the spoon against the side of the acrylic tube. The slurries were usually quite liquid and could be installed by vibrating a small amount of the slurry in

(a)   *(b)*   *(c)*
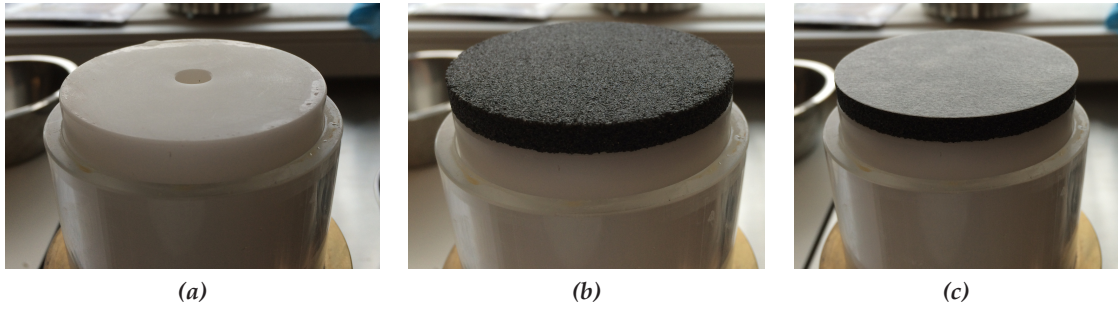
Figure B.1: *Preparation of consolidometer for preloading of slurry. (a) The loading cap with drainage channel was inserted in the acrylic tube, (b) the filter stone was installed and (c) the filter paper was installed on top of the filter stone.*

the tube. Care was taken not to lift the filter paper and trap slurry below it during slurry installation. The process is depicted in figure B.2.

(a)   *(b)*   *(c)*
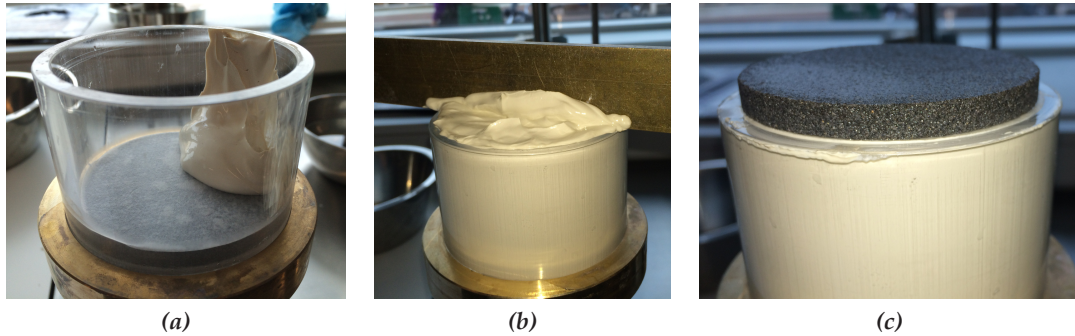
**Figure B.2:** *Finishing the installation of the slurry into the acrylic tube. (a) Installation of the slurry by tapping the spoon against the tube wall, (b) levelling of the slurry to make a flat surface for the filter stone and (c) installation of the filter paper and filter stone.*

After all the slurry was installed, the surface of the slurry was levelled as shown in figure B.2b and the filter paper and filter stone were installed (figure B.2c). The upper acrylic plug was installed and the acrylic tube was gently lifted to guide the upper plug. The initial height of the slurry and the total mass of slurry installed in the tube was noted to allow the initial void ratio and the initial degree of saturation of the slurries to be calculated.

The entire tube with plugs and slurry was placed in a bowl with the selected pore fluid covering the drainage channel in the lower plug. Small spacers were placed under the acrylic tube to keep the drainage channel open during the first stages of consolidation if necessary. The sample was loaded with weights as shown in figure B.3.

B.4   Degree of saturation in artificial samples and specimens

During the pilot testing phase it was observed that some of the tested oedometer specimens (slurries were created with $w = 1.25w_L$) had a low initial degree of saturation, despite being prepared according to the procedures presented by Burland (1990). It was
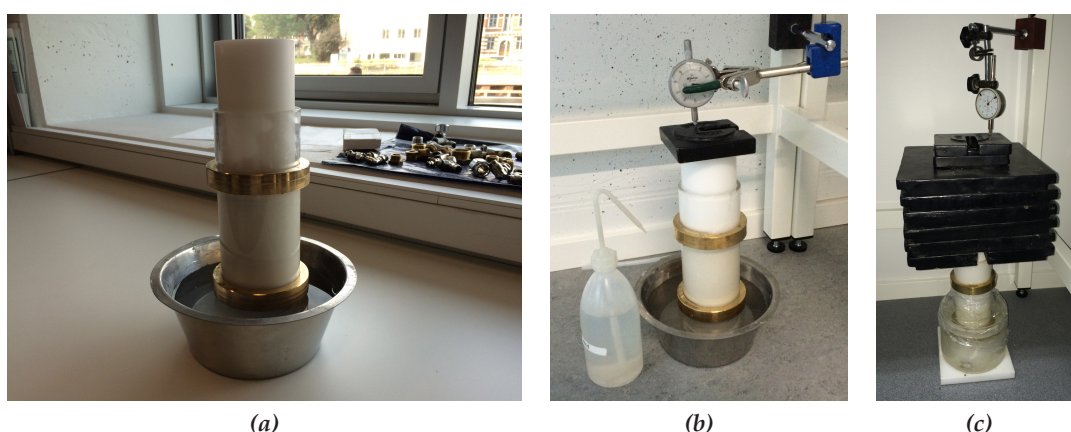
Figure B.3: *Preloading process of the slurries. (a) The tube with slurry is ready for loading with weights, (b) the first load step of 1 kg applied on the slurry, (c) final load step of 64 kg applied on the slurry.*

noted that the degree of saturation was lower for specimens of high plasticity. Thus, a small test was setup to investigate the obtainable saturation of the slurries, when they were installed in the acrylic consolidometers.

B.4.1 Aim of test

With the test series it was sought to document the achievable degree of saturation of the slurries prior to installation in the acrylic consolidometers. The tests were performed with three different mixtures of kaolin and bentonite, closely resembling the mixtures applied in the main laboratory programme.

B.4.2 Test procedures and analysis

A series of tests on the obtainable saturation during slurry installation in a Ø50 mm by 100 mm steel tube was carried out (Sørensen 2015). The slurry was installed in the tube using similar procedures as described in section B.3. After the tube was filled, it was weighed and the water content of the slurry inside the tube was tested, to allow calculation of e and S.

This study proved that it was possible to obtain S_0 in the 97.7 % to 99.5 %-range, as presented in table B.1 and figure B.4. As may be observed from the table, the degree of saturation S is depended on the water content applied when mixing the slurry. Hence, it may be expected that increasing the water content of the slurry will increase the saturation of the oedometer specimens. As may moreover be noted from the table, the saturation decreased slightly when the slurry was left in the fridge. For the K40B60 specimen an insignificant effect of resting time was noted, whereas a possible effect of storage time was observed for the K80B20 specimen. However, as only one test have been performed insufficient data is available for further analysis.

169

Table B.1: *Degrees of saturation, obtained for three selected slurries, calculated using the grain density for the mixtures (d_s = 2.65). Modified after Sørensen (2015).*

Recipe	w_L [%]	w [%]	w/w_L [%]	Rest [days]	S [%]
K80B20	114	149	1.3	0	97.7
K80B20	114	176	1.5	0	99.0
K80B20	114	199	1.7	0	99.4
K80B20	114	199	1.7	1	98.7
K60B40	177	277	1.6	0	99.1
K40B60	224	300	1.3	0	98.0
K40B60	224	357	1.6	0	98.7
K40B60	224	415	1.9	0	99.3
K40B60	224	465	2.1	0	99.5
K40B60	224	457	2.0	3	99.4
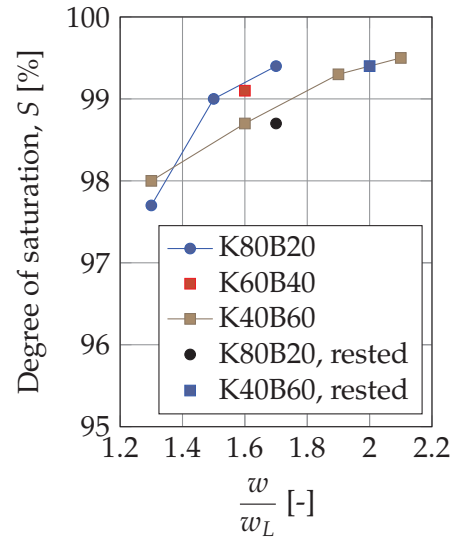
Figure B.4: *Graphical representation of the data in table B.1.*

B.4.3 Conclusion

Based on the results presented in table B.1 and figure B.4 it was decided to increase the water content applied during reconstitution of the slurries in the present PhD-project from $w = 1.25w_L$ to $w = 1.5w_L$, which improved the degree of saturation prior to oedometer testing. Thus, all slurries from S030 and onwards are prepared using $w \geq 1.5w_L$, which is why it may be assumed that all slurries from S030 are fully saturated after the preconsolidation process. All slurries prior to S030 were prepared using $w = 1.25w_L$, which is why the initial load steps may be influenced by insufficient saturation. However, as large strains generally developed in the tests, the specimens is expected to be saturated after only a few load steps. In case the initial saturation for an oedometer specimen was significantly below $S_0 = 100\,\%$, it was assumed to originate from small errors during the trimming procedure.

B.5 Preconsolidation of the slurries

The loading program for preconsolidation was initiated with a weight low enough to ensure that the slurry was not squeezed up between the filter stone and the acrylic tube. In many cases an initial load of 1 kg to 10 kg were found to be adequate. After an appropriate number of load steps the spacers under the acrylic tube were removed, and the acrylic tube was moved upwards to minimise friction under preconsolidation (ensuring use of a floating ring). The tube was moved regularly during the preconsolidation process to avoid build-up of friction between the acrylic plugs and the tube, which would influence the load on the slurry sample. For the slurries of highest plasticity a new load step was initiated prior to achieving full consolidation for intermediate load steps to save time.

The final load of 64 kg corresponds to a nominal pressure of approximately 163 kPa.

However, it should be noted that the friction in the consolidometer may cause the actual load on the slurry to be less than the applied load on the loading cap. The maximal load of 64 kg was shown to compress the slurries sufficiently to enable handling and trimming for further testing. The first and the last load step for a slurry in an acrylic tube consolidometer is illustrated in figure B.3.

After application of the first load on the slurry sample, the upper drainage channel was filled with the selected pore fluid to avoid stress increase due to evaporation. Measures were taken to minimise evaporation during the preconsolidation phase.

B.6 Evaluation of required time for complete consolidation

A number of oedometer tests have been carried out on slurries, to assess compressibility and consolidation behaviour. For each these tests, the average c_v value has been calculated, and used to assess the required time for complete consolidation. For each slurry, the average from c_v-values for load steps from 5.1 kPa to 163 kPa are calculated, and the time for achieving $T = 2$ is calculated based on a set of mean heights of the consolidating slurry. The curves for the expected consolidation times are presented in figure B.5.
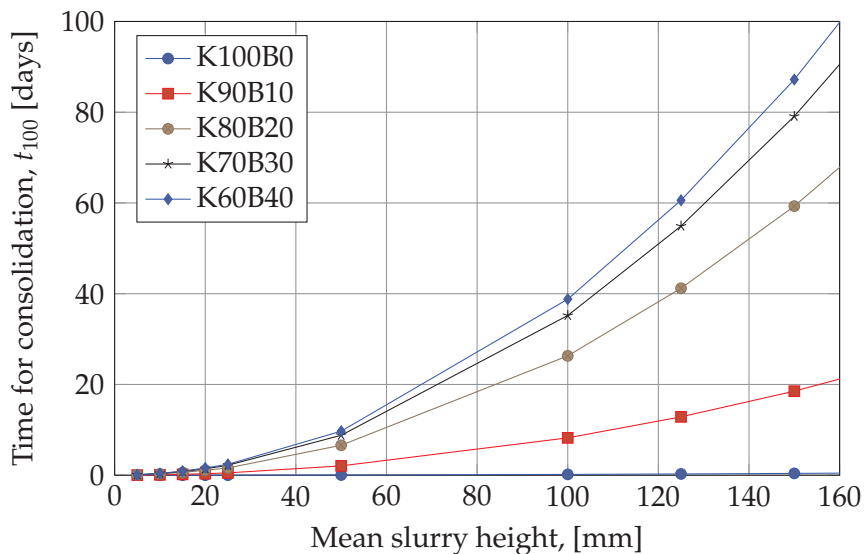
Figure B.5: *Estimation of t_{100} for slurry consolidation.*

As seen from the figure, a change of height significantly influences the time for complete consolidation, t_{100} as expected. Moreover, a significant increase is seen in the consolidation times with increasing content of smectite, the relative change being largest going from pure kaolin to approximately 20 % bentonite.

The curves in figure B.5 served as a guide for estimating when the slurries were fully consolidated on the final load step (64 kg corresponding to 163 kPa). Two tests were logged on the final load step to verify the tendencies illustrated in the figure. These tests were generally reflected t_{100}-values in line with the curves in figure B.5.

B.7 Extraction of the samples

The final height and mass of the samples were recorded after removing of the applied loads. The sample was pressed out of the tube and placed in the sample lathe adapter and pressed into a cutting ring for 1D consolidation testing. The material that was removed above and below the sample during the trimming process was collected and quickly tested for water content. In case the samples were not to be tested instantly after the preconsolidation phase, they were stored in an upright position at 8 °C, wrapped in cling film. The samples stored in the refrigerator were weighed before and after storage to assess the loss of moisture due to evaporation.

B.8 Homogeneity of prepared slurry samples

To investigate the homogeneity of the prepared slurries, prior to testing in the oedometer apparatus, a testing programme was carried out to assess the variation of water content with depth of samples with varying content of smectite.

B.8.1 Aim of test

With these tests it was investigated whether the procedures for making reconstituted samples were adequate for the achieving oedometer specimens of the same state prior to testing, even when the specimens were trimmed from different samples. Thus, it was tested whether oedometer specimens trimmed from different depths of the samples had a similar water content.

B.8.2 Test procedures and analysis

Four slurries with varying bentonite content were reconstituted following the procedure of Burland (1990) ($w = 1.25w_L - 1.75w_L$) and were preconsolidated to $\sigma'_v = 163$ kPa. After the preconsolidation phase, the slurries were cut in approx. 1 cm thick segments and the water content on each segment was determined. As the slurry prior to the preconsolidation phase had a uniform water content over depth and a uniform preconsolidation pressure of ≈ 0 kPa, any change in water content over depth would indicate a change in developed void ratio e from the preloading. Any effects of self-weight of the clay have been disregarded. The data obtained for each of the tested samples during the phase of preconsolidating the slurry is presented in table B.2.

Table B.2: *Average values obtained for the tested soils for investigating the homogeneity of the prepared slurries.*

Slurry number	Recipe	h_0 [mm]	e_0 [-]	w_0 [%]	σ'_v [kPa]	h_f [mm]	e_{end} [-]
S013	K100B0	190	2.02	72	163	140	1.23
S014	K91B09	220	2.94	105	163	135	1.42
S016	K80B20	152	3.89	144	163	81	1.61
S031	K40B60	188	11.33	419	163	56	2.67

In figure B.6 the water content is presented as a function of normalised depth, $\hat{Z}$ defined in eq. (B.1).

$$\hat{Z} = \frac{Z_w}{H} \tag{B.1}$$

Z_w is the depth to the middle of a segment used for water content analysis and H is the total height of the sample after preconsolidation. As all segments were approximately 1 cm thick, the normalised depth on slice i depends on the total height of the sample after preconsolidation.

As noted from figure B.6 the water content were fairly homogeneously over the entire depth of the samples. The variation of the water content were in general less than 10 % of the mean water content of the sample, which was assumed to be satisfactory. Thus, the procedures applied for creating the artificial samples were seen to provide homogeneous specimens for further testing.
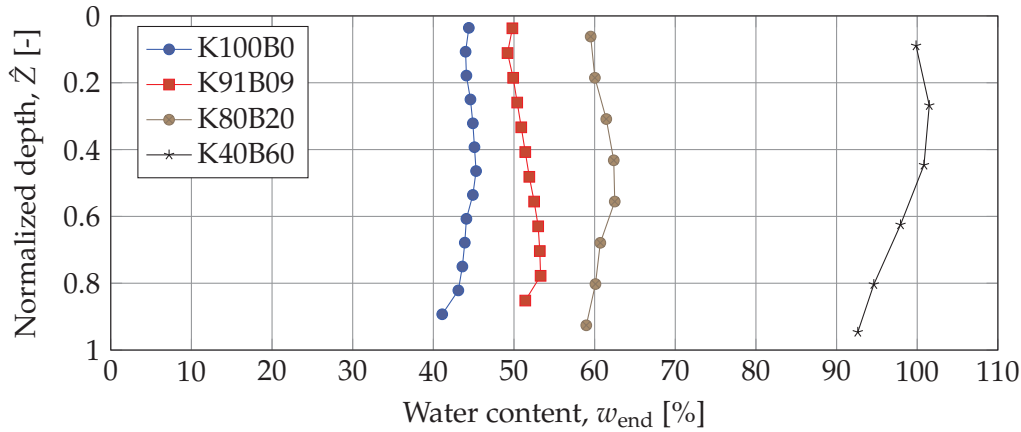
Figure B.6: *Water content after preconsolidation against normalised depth in specimen. Normalised depth of 1 corresponds to bottom of the specimen.*

B.8.3 Conclusion

The procedures for preparing slurries was proven to yield satisfactory homogeneous specimens to be used for oedometer tests. Thus, no significant influence of where an oedometer specimen was trimmed from a sample was expected. This meant that multiple specimens could be trimmed from a single sample.

In the main laboratory programme an initial loading in the normally consolidated stress regime was performed prior to performing the unloading and reloading loops, which were used for model calibration. Thus, a similar state was reached for all specimens of a particular recipe, prior to the unloading-reloading loops, which is why the behaviour of the specimens may be compared directly in terms of void ratio. In case small errors during the trimming procedure decreased the saturation of a specimen, it would have affected only the first load step of the oedometer test.

B.9   Conformity of samples and specimens

To assess the consistency of the determined normally consolidated branch of the compression curves, the curves from two tests, conducted at different stress levels are compared in the present section. According to the *ICL*-framework by Burland (1990) (see section 3.2) the compression curve for normally consolidated specimen should be unique, which is why the normally consolidated branch of the compression curves were expected to be similar in the stress region included in both tests.

B.9.1   Aim of test

The study aims to verify that two specimens of the same recipe, but tested at different stress levels reached the same void ratio for a given stress on the normally consolidated part of the compression curve. Two mixtures were compared to investigate this matter, namely of recipes K60B40 and K0B100. Moreover, it was investigated whether two specimens trimmed from different preconsolidated slurries, but tested with the same loading programmes, yielded comparable compression curves. Two specimens from the main laboratory programme (OE042S034 and OE056S046 (both K80B20)) are presented to investigate this matter.

B.9.2   Test of concordance between slurry and preconsolidated specimen

In figure B.7 the compression curves are plotted together for two mixtures, tested both as slurries and as preconsolidated specimens. As seen from the figure a fairly nice fit is observed for the parts of the curves that are overlapping. Thus, the void ratio developed as expected when the vertical pressure was increased. This in turn means that a unique normally consolidated line may be expected for each mixture of artificial specimens.
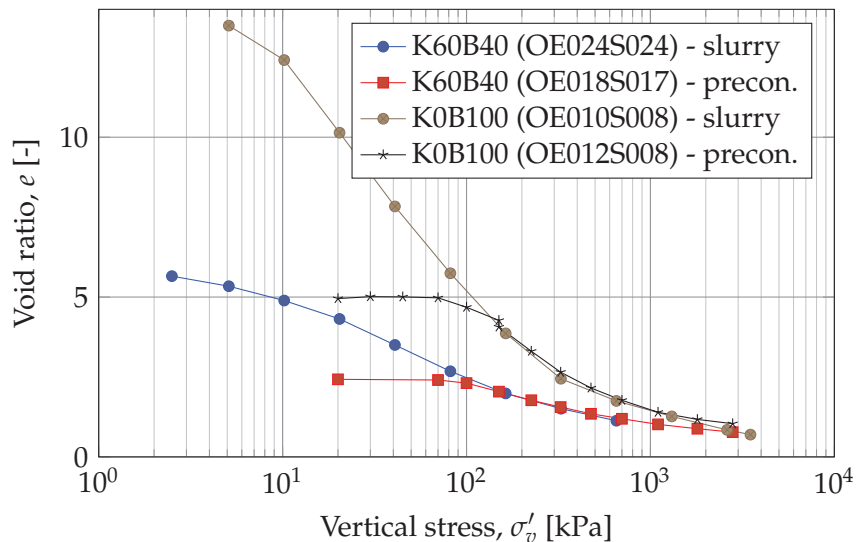

Figure B.7: *Comparison of compression curves for two mixtures with and without preconsolidation in the acrylic tubes. As may be noted, the normally consolidated parts of the compression curves for each mixture are very similar in the stress interval covered in the tests for both preconsolidated and slurry specimens.*

As may be noted from figure B.7 the compression curves are non-linear over the three logarithmic decades of stress where test data is available. Thus, values of the compression index, C_C expectedly will differ dependent on the stress interval provided in the test.

B.9.3 Test of reproducibility of preconsolidated specimens

A test of the reproducibility of the prepared samples are presented in figure B.8 for two load paths on K80B20 specimens. The tested specimens were prepared as two individual slurries, yet as may be noted from the figure, a very close correspondence was observed between the compression curves, except for the first load step. However, the discrepancy in first load step is believed to be introduced as the slurry S034 was stored in the refrigerator at $8\,^{\circ}$C for approx. three months prior to testing due to limited capacity for slurry preconsolidation. Thus, the specimen may have dried out a little (average w = 57.2 % for specimens trimmed from S034 against w = 62.6 % for specimens from S046), which will be reflected in the compression curve. As the initial saturation are high for tests from both slurry S034 and S046 the different behaviour seems to indicate that a slightly higher preconsolidation pressure was induced due to the small desiccation of slurry S034.
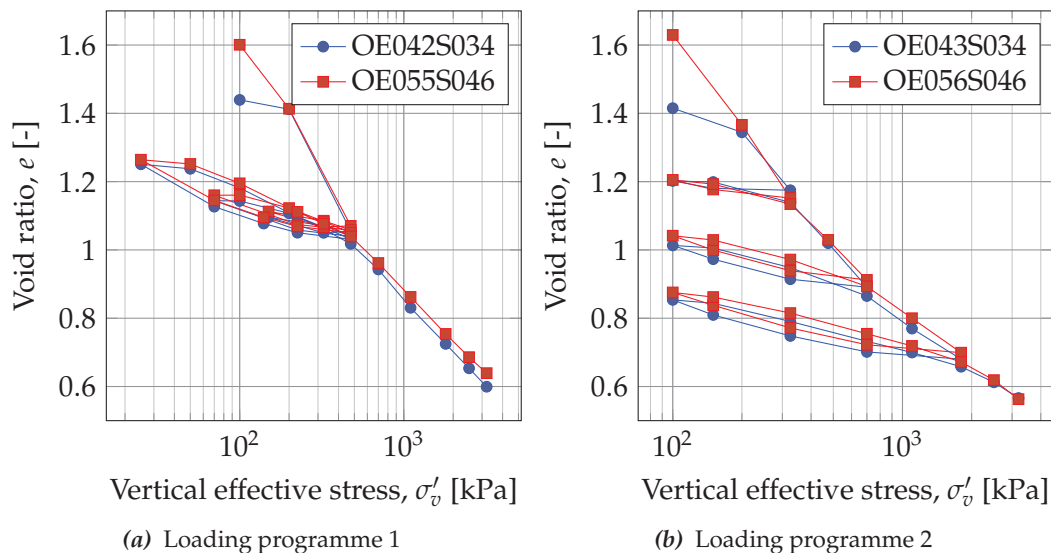
Figure B.8: Comparison of compression curves for four specimens trimmed from two different samples, and subjected to two different loading programmes. Both mixtures were K80B20, and compression curves presented in figure B.8a were tested using loading programme 1 and the curves in figure B.8b using loading programme 2.

B.9.4 Conclusion

The reproducibility of the oedometer specimen trimmed from samples was found to be acceptable, which was documented in tests of specimens trimmed from different samples (of the same recipe) and following the same loading programme.

Moreover, it was found that a smooth transition between tests performed on slurries and on preconsolidated specimens can be found. The reproducibility between spec-

imens trimmed from different samples, but same recipes (reconstituted at $w = 1.5w_L$), shown in subsection B.9.3 seems to suggest that essential identical oedometer specimens were created with the developed procedures for slurry making and the following pre-consolidation phase.

Procedures for oedometer testing and data interpretation

In the following chapter, the applied procedures when performing oedometer test on artificial, reconstitued, preconsolidated specimens are presented. The applied procedures for mixing and preconsolidating the artificial samples, used for specimen-trimming are detailed in appendix B.

In the present project the fixed-ring setup was applied in all the conducted test series. The fixed ring setup allows for a direct comparison with CRS tests and oedometer tests with K_0 measurements, both being carried out in a fixed ring setup. A number of different oedometer cells have been applied for testing. A description of all cells applied during the PhD project is found in chapter 1 of the laboratory report.

C.1 Trimming of test specimens

After the preconsolidation phase, described in chapter B, the samples were trimmed using a cutting ring appropriate for the applied oedometer cell. For each test the cutting ring was rinsed and checked for deformation and sharpness of the cutting edge prior to the trimming process, and the inside of the cutting ring was lubricated with a thin layer of silicon grease. The top and bottom filter discs were thoroughly cleansed and kept in dry state. For all tests in the main laboratory programmes, the porous discs were installed dry in the oedometer cells to avoid swelling of the specimens before the oedometer cells were installed in the oedometer frames. The initial height, h_0, diameter, d, and the weight of the cutting ring, m_{ring}, for the oedometer cell were measured with 0.01 mm accuracy on height and diameter and 0.01 g accuracy on weight.

The preconsolidated sample was extracted from the acrylic tube and transferred to the lathe table for trimming. The ring was pushed down over the sample, while trimmings were removed during the process with a knife. The process was continued until the sample had a stick-up of approximately 1 cm above the cutting ring. The trimmings were used for determination of initial water content, w_0, by drying at 110 °C for at least 24 hours.

C.1.1 Trimming of specimens for the ELE and CRS cells

For specimens tested in the ELE and CRS cells, The upper and lower surface of the sample were trimmed with a knife while in the cutting ring, working towards the middle of the specimen. The specimen was finally levelled with a straight-edge to make the surface of the specimen plane with the sides of the cutting ring. During trimming of the second side of the specimen, the cutting ring was placed on a glass plate to avoid pushing the sample out while trimming. After trimming, the outside of the cutting ring was cleaned, and the weight of the cutting ring and soil sample was recorded. The cutting ring was placed in the oedometer cell on the bottom porous disc and the upper porous disc was installed under the upper pressure head. Thus, the cutting ring also served as oedometer ring during the tests. A fixation ring was placed around the cutting ring to increase the radial stiffness of the ring and the steel ball was placed on top of the upper pressure head.

C.1.2 Trimming of specimens for the COWI and nmGeo cells

Specimens tested in the COWI and nmGeo-cells were levelled on one side while in the cutting ring, and then transferred from the cutting ring to the oedometer ring using the upper pressure head to gently push the specimen out of the cutting ring. The oedometer ring was placed on a flat surface top-down. A spacer was inserted between the flat surface and the upper pressure head to control the specimen height. The height of the specimen was measured beforehand for each test using the spacer, the oedometer ring and the upper pressure head. When the specimen was successfully transferred to the oedometer ring, the other side was levelled using the oedometer ring as guide. The oedometer ring containing the specimen was then weighed and the oedometer cell was assembled.

C.1.3 Procedures after trimming

In all cases measures were taken to avoid evaporation during testing, and any loss of the fluid in the carriage was replenished during testing.

Based on the measurements of h_0 and d, the initial volume, V_0, of the specimen was calculated. The initial mass of the specimen was calculated from $m_0 = m_{tot} - m_{\mathrm{ring}}$. The initial void ratio, e_0, was calculated based along with the initial degree of saturation, S_0. After testing the height, mass and water content of the specimen were recorded to allow calculation of e and S after testing.

C.1.4 Quality of oedometer specimens for main tests

For natural specimens, the degree of sample disturbance from in situ sampling, transport and trimming may be estimated from the sample quality. Lunne et al. (1997) suggests that the specimen quality should be estimated based on the ratio between the change in void ratio, Δe from test initiation to the vertical stress reaches the in situ stress, and the initial void ratio, e_0. A small change in void ratio indicates a high quality specimen. However, larger changes are acceptable for normally consolidated clays than for overconsolidated clays.

In the main laboratory programme, all specimens were initially loaded significantly above the preconsolidation stress achieved in the acrylic tubes, prior to any unloading-reloading loops. Thus, the specimens quality in the loops must be expected to be superb, as all consolidation parameters are estimated based on data points after full sample adaptation to the oedometer ring. The loading to a stress state above the preconsolidation pressure from the acrylic tubes will – with the improved sample preparation procedure presented in section B.4 – secure full saturation of the test specimen during the unloading-reloading loops analysed in the present project, as discussed in the sections B.8 and B.9.

C.2 Conduction of oedometer tests

To account for machine deflection, a compliance test was performed prior to carrying out a series of tests. During the compliance test the actual planned loading programme was performed using a steel disc as a substitute for the soil specimen. The deformations measured during this test originates from deflections in the oedometer frame, oedometer cell, porous discs and filter paper (if applied). All measurements on soil specimens were corrected for deflections of machinery using this procedure. As presented in section 1.6 of the laboratory report, a large part of the compliance were found to be caused by the filter papers. Thus, the main laboratory tests were carried out without filter papers to minimise compliance.

When the oedometer cell was installed in the oedometer frames, the displacement transducer was positioned to enable movement to be recorded in both directions. Moreover, it was ensured that the transducer would not interfere with the movement of the oedometer cell (on the automatic oedometer frames). The displacement transducer was zeroed and the test was initiated. The first load step of the programme was initiated dry, allowing for 5 min of consolidation before adding pore fluid. After 5 min, the carriage is flooded with the selected (de-aired) pore fluid. A few different methodologies were tested in the pilot testing phase for initiating the tests, when the first load step in the oedometer programme was lower than 163 kPa (corresponding to the slurry preconsolidation pressure) to avoid swelling of the high plasticity specimens. However, for the main testing programme the initial load step for the specimens expected to cause swell was 200 kPa, which is why no swelling occurred, as the swelling pressures of the tested mixtures were found below this stress (presented in section 6.8).

During testing a new load step was initiated when the displacement log indicated the end of primary consolidation and onset of secondary consolidation. Thus, when the displacement log indicated that enough data for making the Casagrande-construction was obtained (by visual inspection), a new load step was initiated.

Different loading programmes have been developed for the different type of tests. However, the main laboratory programme were conducted using three different loading paths:

> Three unloading-reloading loops from different σ'_{max} to the same σ'_{min} (Load 1)

> Three unloading-reloading loops from different σ'_{min} to the same σ'_{max} (Load 2)

> Three unloading-reloading loops with same OCR at different stress levels (Load 3)

Moreover, the validation tests were carried out using two different loading paths:

> An unloading-reloading loop reaching a large OCR-value initiated at a relatively low σ'_{max}, followed by an unloading-reloading loop reaching a small OCR-value (Load 4)

> Three unloading-reloading loops from different σ'_{max} to the same σ'_{min}, σ'_{max} = 1100 kPa, which were larger than for load 1 (Load 5)

All specimens are unloaded to 10 kPa in the final step, which was maintained until the tests were manually aborted and the specimens were removed from the oedometer cells. Quickly after the abort of a test, the oedometer cell was removed from the oedometer frame and the carriage was drained for pore fluid. The oedometer ring was dismantled and upper and lower porous discs were dabbed dry using paper towel and removed before the final height of the specimen, h_f, was determined as the average of the three measurements. The mass of the oedometer ring and specimen, m_{end}, was recorded and mass of the specimen, m_f, was calculated. The final water content, w_f, of the specimen was determined and final void ratio and degree of saturation were calculated.

C.3 Post-processing of the data

After testing, the time-strain curves were analysed to identify t_{50}, t_{100}, ε_{50}, ε_{100} and ε_{end} using the method proposed by Casagrande (1938). A discussion of other available methods for interpretation the time curves are presented in appendix D. ε_0 was obtained utilizing the parabolic shape of the initial approx. 60 % of the consolidation phase (Terzaghi et al. 1996) as proposed by BS 1377-5 (1990). The compression curve was constructed by plotting ε_{100} (and the corresponding e) against σ'_v. The magnitude of creep developed on each load step was illustrated by also plotting ε_{end} against σ'_v in the compression curve. For the final load step in (re)loading or unloading, i.e. when the loading direction was changed, the value of ε_{end} was used to construct the compression curve.

The coefficient of consolidation, c_v was calculated based on values of t_{50} for each load step, using eq. (C.1), after BS 1377-5 (1990).

$$c_v = \frac{0.026 \bar{H}^2}{t_{50}} \tag{C.1}$$

In eq. (C.1) the parameter $\bar{H}$ is the average drainage path in the load step. For double sided drainage, this is half the specimen thickness.

For each load step (load step i), except the initial load step, the stiffness was calculated as the secant stiffness from the former (load step $i-1$) to the current load step according to eq. (C.2). For load steps after a stress reversal, the value of $\varepsilon_{v,i}$ was selected as $\varepsilon_{v,i} = \varepsilon_{end,i}$ to avoid including the strain developed during secondary consolidation on the load step before stress reversal.

$$E_{oed,i} = \frac{\sigma'_{v,i} - \sigma'_{v,i-1}}{\varepsilon_{v,i} - \varepsilon_{v,i-1}} \tag{C.2}$$

C.3.1 Identification of vertical yield stress

During the initial work on the Fehmarn Fixed-link project, the Janbu method (Janbu 1969) was the recommended method for estimating σ'_{vy} on the undisturbed high plasticity clays (Femern 2014a). Thus, it was expected that the Janbu method will yield good results on the artificial, reconstituted, preconsolidated clay specimens relevant for the current PhD-project. According to Janbus method, σ'_{vy} is located slightly to the left of the saddle point in a plot of the tangent stiffness, E_{oed}, against the mean effective stress σ'_m. The method is illustrated in figure C.1. For comparison, the compression curve is also analysed applying the method suggested by Casagrande (1936). The method is illustrated in figure C.2 and may be described as:

1. The obtained stress-strain curve is plotted in a $\log(\sigma'_v)$–ε_v-diagram

2. The point of maximum curvature of the curve is determined by eye

3. A horizontal line is extended from the point of maximum curvature

4. A tangent line to the compression curve is drawn from the point of maximal curvature

5. The angle (2α in figure C.2) between the horizontal line and the line fitted to the virgin curve is halved by a third line (the bisector line)

6. The vertical yield stress is determined as the intersection of the bisector line and the line fitted to the virgin part of the curve
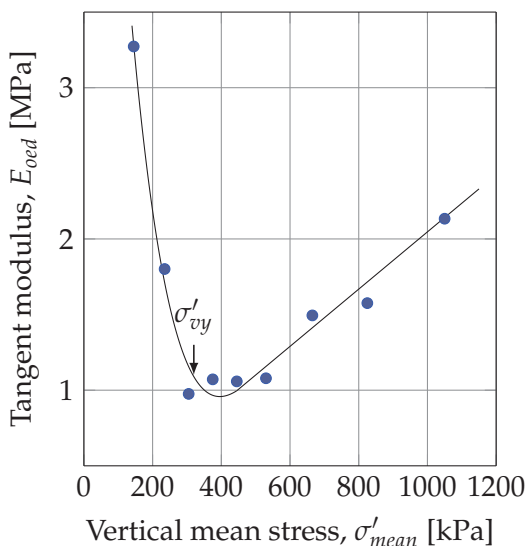

Figure C.1: *Determination of σ'_{vy} after the method of Janbu (1969).*
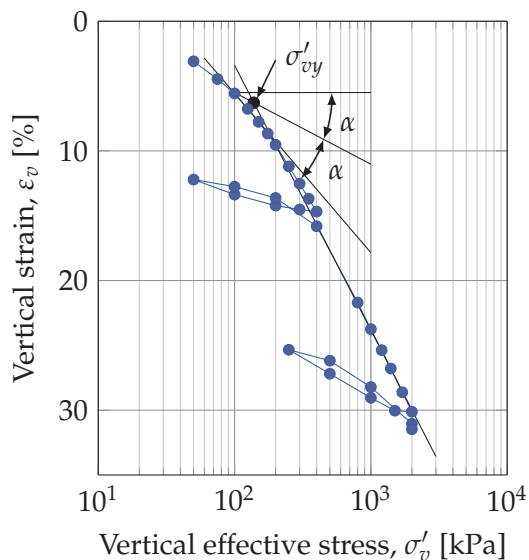
Figure C.2: *Illustration of determination for σ'_{vy} after the method of Casagrande (1936).*

In the present project the procedure presented above was applied when the compression curves were analysed using the method proposed by Casagrande (1936). However,

to minimise the scatter introduced by graphical interpretation, a procedure was adopted where a high-order polynomial was fitted to the measured points and differentiated twice with respect to $\log(\sigma'_v)$ to identify the maximal curvature of the stress-strain curve. The maxima of the double-differentiated curve was then applied as the stress for maximum curvature. This procedure yielded the same position of maximal curvature as would have been identified by the minimum radius of the curve (Conte et al. 2011). Visual inspection of the compression curve and the curvature-curve during the analysis ensured compliance with the original Casagrande approach.

C.3.2 Determination of moduli of specimens

The compression coefficients, except the coefficients of secondary consolidation, C_α and $C_{\alpha\varepsilon}$, of the tested specimen were determined based on fits on the compression curves. For all values of the compression index, C_C, presented in the laboratory reports, the value is representative for the steepest part of the compression curve, which should be accounted for, if applying the values for a different stress range than indicated in the laboratory reports. The swelling and recompression indices were fitted using the largest possible range as presented in figure C.3. As such, C_S and C_R represent secant values. The values presented in figure C.3 are based on strain, which is why the index "ε" is added. For the tested specimens both values based on e and ε_v are presented in the laboratory reports.
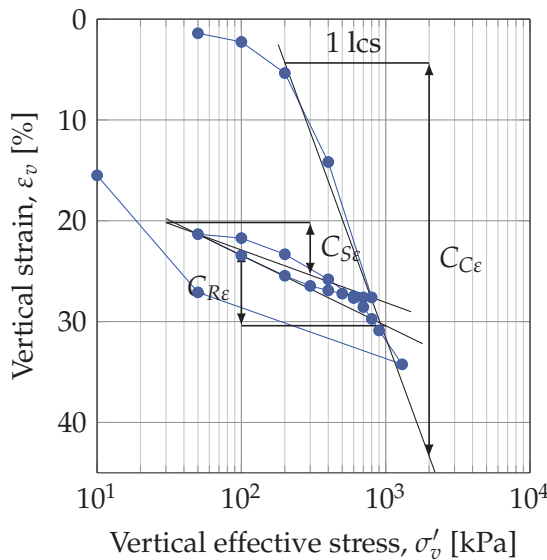
Figure C.3: *Determination of compression, swelling and recompression indices by curve fitting.*
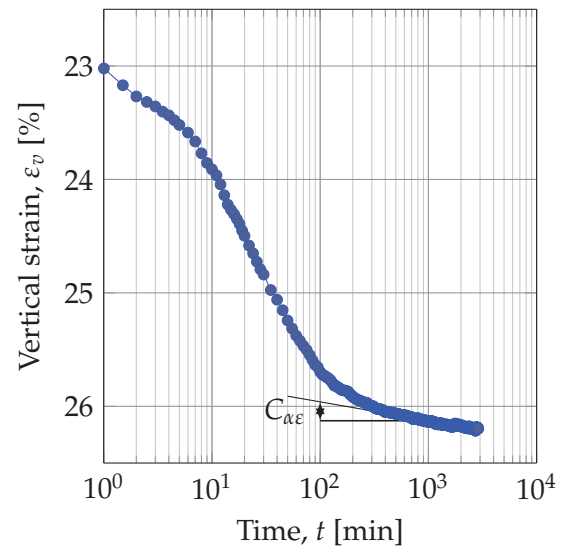
Figure C.4: *Determination of coefficient of secondary consolidation.*

The coefficient of secondary consolidation was determined on the time curves of the load steps containing an appropriately long phase for secondary consolidation. The modulus was determined as the slope over one logarithm of time on the final part of the time-strain curve. As the process of secondary consolidation was not of primary focus

of the present PhD project, the creep coefficients were not routinely determined for the conducted tests.

## C.4 Effect of loading programme on deformation behaviour

A flexible loading schedule was considered beneficial for the sake of time and duration of the tests of the main laboratory programme. Thus, a number of tests were carried out to analyse the influence of the loading programme on the stress-strain behaviour of the artificial specimens.

C.4.1 Aim of study

Two mixtures were tested; namely three K90B10 specimens and three K60B40 specimens. The obtained results were assumed to cover the entire range of plasticity which were tested in the main laboratory programme. During the tests, the effect on the specimens of accelerating the loading and unloading phases of the tests were tested, by not allowing full consolidation on some of the load steps. This did essentially imply that a difference in load increment ratio was introduced between the tests.

C.4.2 Test procedures and analysis

To investigate the effect of different loading paths, three identical specimens were subjected to three different loading paths. One of the loading paths resembling a "normal" oedometer stress sequence, starting from $\approx 40\,\text{kPa}$ utilizing a load increment ratio of 1 to $\sigma'_v = 640\,\text{kPa}$ followed by an unloading branch to $40\,\text{kPa}$. This programme is designated "normal" in the figures C.5 and C.6. Two other loading programmes resembled respectively a quick loading and a quick unloading. These programmes deviated from
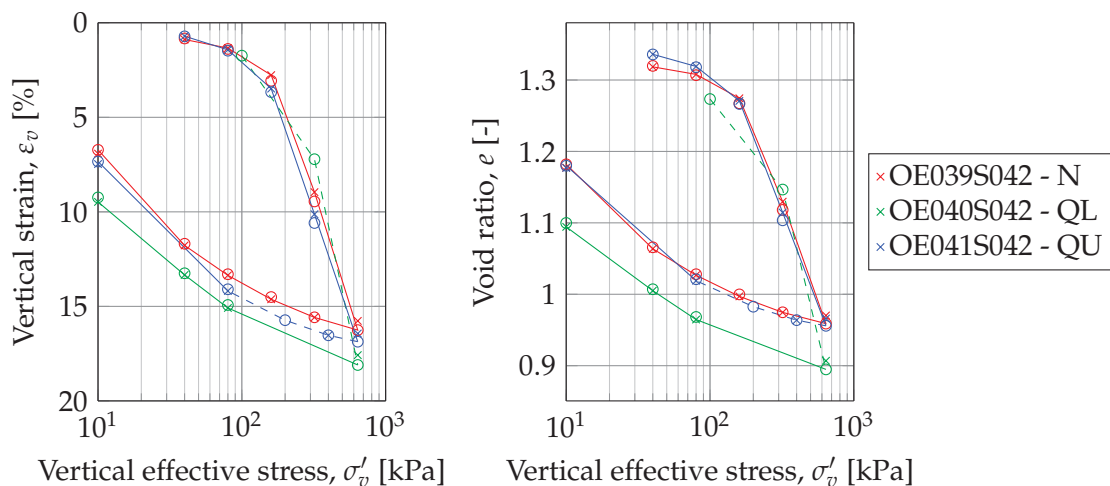
Figure C.5: *Effect of loading programme for K90B10 specimens compared on basis of void ratio. "N" denotes normal loading, "QL" denotes quick loading and "QU" denotes quick unloading. Stress levels where 100 % consolidation was not reached are connected using dashed lines.*

the load increment ratio of 1 on the loading and unloading path respectively. These programmes are designated "Quick loading" and "Quick unloading" in the figures C.5 and C.6. A few temporary load steps were planned on the quick parts of the paths to avoid extreme pore pressure build-up. The duration of the temporary load steps were 15 min for the K90B10 specimens and 2 hours for the K40B60 specimens.
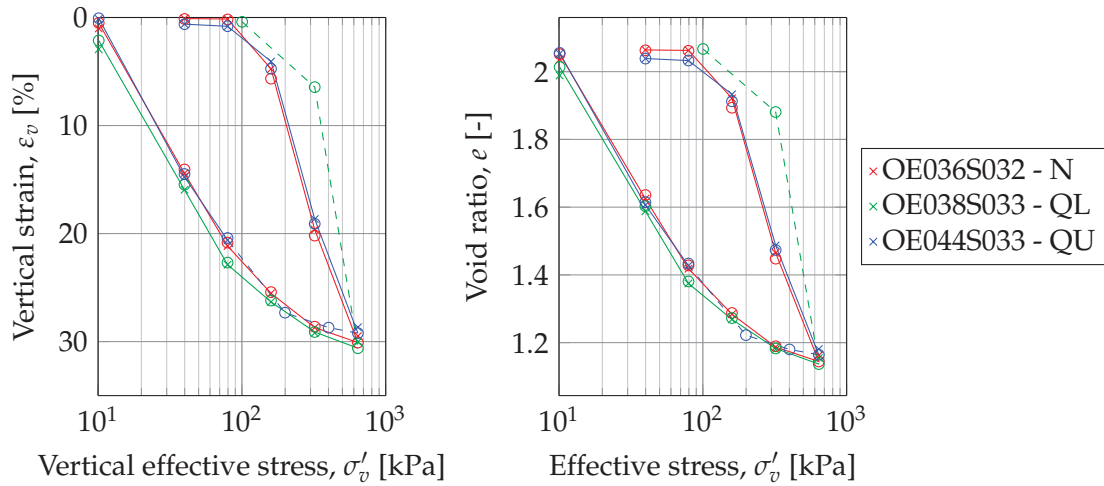
Figure C.6: *Effect of loading programme for K60B40 specimens compared on basis of void ratio. "N" denotes normal loading, "QL" denotes quick loading and "QU" denotes quick unloading. Stress levels where 100 % consolidation was not reached are connected using dashed lines.*

The obtained stress strain curves are presented in figure C.5 for the K90B10-specimens and in figure C.6 for the K60B40-specimens. As may be observed from the figures, a fairly good correspondence is observed between the results obtained from the different loading programmes. This seems to indicate that stiffness parameters are uniquely linked to the mineralogical composition of the specimens regardless of the loading programme. However, it should be noted that all six specimens were loaded past the preconsolidation pressure obtained during the preconsolidation phase. Thus, the intrinsic properties of the specimens were governing the stress-strain behaviour on most of the loading path.

As may be observed the largest deviations from the overall stress-strain curve was obtained on the loading path of the "Quick loading" programme (For the K60B40-specimens), which was due to incomplete consolidation on the temporary steps. On the corresponding temporary steps on the unloading branch, a minor deviation is seen, which was due to the higher stiffness for small unloading stresses.

In figure C.5 the stress strain curves for the different stress paths are illustrated for the K90B10 specimens based on vertical strain and void ratio, respectively. As may be observed from the figure, very close correspondence between the normal loading test and the quick unloading test was observed, especially on the loading path. This was expected, as all three specimens origin from the same sample. However, the curve for the quick loading shows a significant deviation. This may be due to an error in the programming of the load path, where a 640 kPa–320 kPa–640 kPa loop with 15 min duration of each step was incidentally executed before unloading the specimen. The

developed strain during this loop has been subtracted from the following load steps (i.e. during unloading). As may be observed in figure C.5 the shape of the unloading curve follows the other curves closely, which may suggest that the difference in initial void ratio of the specimens is to blame for the discrepancy.

For the K60B40 specimens (Figure C.6) an excellent correspondence between the different stress strain paths were found for all three stress paths. It should be noted that the three tests were performed on specimens from two different slurries. This illustrates the homogeneity of the prepared reconstituted slurry samples as also discussed in section B.9.

C.4.3 Conclusion

From the miniature study presented above, is may be concluded that the deformation behaviour of the artificial reconstituted specimens do not depend on applied load increment ratio. Hence for longer testing series, a load increment ratio of more than unity may be applied in order to save time. Moreover, the tests have indicated that using a number of intermediate steps during loading to a specified stress level will not influence the obtained final void ratio of the specimen. Thus, for tests where a soft specimen is loaded to a very high stress level, a number of intermediate points (i.e. allow only a part of the excess pore pressure to dissipate before progressing to the next load step) may be introduced to avoid squeezing the specimen out between oedometer ring and pressure heads. This procedure will save time, especially for tests on specimens of very high plasticity.

C.5 Effect of creep during testing

One of the unfortunate traits of high plasticity clay is a relatively large coefficient of secondary consolidation, C_α. As will be presented in appendix D, the load is gradually transferred from being carried by the excess pore water pressure to being carried by the soil skeleton as effective stresses during the primary consolidation process. Thus, the parts of the specimen where the excess pore pressure dissipates fastest, actually are subjected to the final effective stress in the load step much before to the identified t_{100}. This must mean that the secondary consolidation process initiates for these elements prior to the t_{100} identified for the specimens. As the boundary of the specimen drains instantly, in reality the process of primary and secondary consolidation runs simultaneously.

If the primary and secondary consolidation process runs simultaneously, prolonged durations of load steps may cause a too stiff response. If the creep isochrones proposed by Bjerrum (1967) is considered, during a too long duration on a load step in virgin loading, the specimen will reach an isochrone corresponding to $t \geq 0$, which will push the vertical yield stress past the actual stress in the load step. This will cause the obtained displacements on the next load step to correspond to a transition from slightly overconsolidated to normally consolidated state, which is why the soil response may be influenced by the secondary consolidation process. On a given load step, where primary and secondary consolidation runs simultaneously, a too large ε_{100} will most likely be obtained, as a part of the secondary consolidation strains cannot be easily separated from the primary consolidation process. Prolonged duration of a load step will on the other

hand cause an apparent (small) preconsolidation pressure on the next load step, which will tend to limit the displacement obtained for that step.

C.5.1 Aim of the study

The current sub-study was undertaken to evaluate the effects of long durations of the load steps on the deformation behaviour of the artificial clays. Moreover, it was sought to detect whether the vertical yield stress was affected by secondary consolidation during the load steps.

C.5.2 Test procedures and analysis

A total of four oedometer tests were analysed to investigate the effect of long durations of the load steps. Two tests on K90B10 and K60B40 respectively have been tested with long and short durations of load steps. The specimens tested under the "normal" loading programme as presented in appendix C.4 was included as the specimens with short load steps and the specimens presented in appendix D.3.1 was included as the specimen with long load steps. Note that tests of long durations were carried out with single-sided drainage and tests of short duration with double sided drainage. Even accounting for the factor of four in consolidation time (eq. (C.1)) when doubling the length of the drainage path, the relative duration of long tests are longer than for short test.
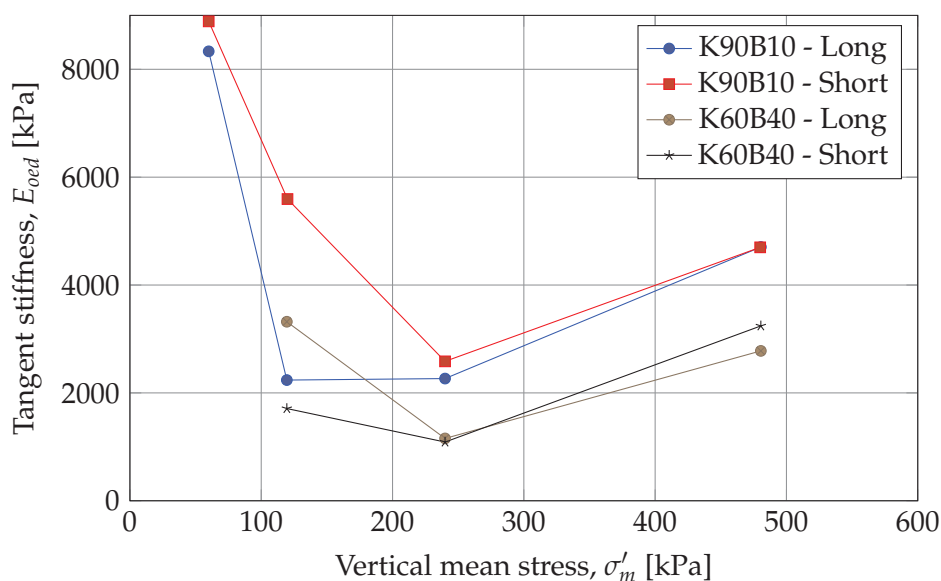

Figure C.7: *Development of tangent stiffness along loading curves for two different mixtures.*

For the loading part of the obtained compression curve, the tangent stiffness was calculated and plotted against the vertical mean stress in figure C.7. In case the prolonged duration of the load steps caused the specimen to yield a stiffer response, the curves in the Janbu plot presented in the figure should be translated upwards for the specimens tested with long load steps compared to the specimens tested with short load steps. This behaviour seem only apparent for the K60B40-specimen, and only to a minor degree. However, as only very limited data was included in the present analysis,

no firm conclusions on the behaviour of secondary consolidation during the oedometer tests may be drawn.

As may be noted from figure C.7 no significant shift of the saddle point, i.e. the σ'_{vy}-value, was observed in the present sub-study.

C.5.3 Conclusion

As may be observed from figure C.7 no significantly increased stiffness is observed from the longer load steps. Specifically, in the normally consolidated part of the curve ($\sigma'_m = 240 - 480 \, \text{kPa}$) the slopes of long and short tests on the same mixture are similar. As a note it may be observed from figure C.7 that the stiffness decreases with increasing smectite content as also observed in other tests presented in the present project.

Methods for determining end of primary consolidation

In the following sections four different methods to identify the duration of the primary consolidation process for oedometer tests are introduced. The four methods are briefly describe individually. Hereafter, the four methods are compared based on analysis of two oedometer tests performed within the present PhD-study. Two tests were performed in the nmGeo oedometer cell, where displacements of upper pressure head, along with excess pore pressure and force at the lower pressure head were logged during testing. A K90B10-specimen and K60B40-specimen were tested to cover a range of plasticities.

D.1 Casagrandes method

The obtained displacement data was corrected for frame compliance and converted to strain, using eq. (D.1). Time-strain curves were plotted on $\log(t)$ scale and the method suggested by Casagrande (1938) was employed to assess the time and strain for 100 % consolidation, t_{100} and ε_{100}, respectively. Moreover, the time and stain for 50 % consolidation was extracted, t_{50} and ε_{50}, respectively. The method is illustrated in figure D.1. For each load step, values of t_{100}, ε_{100} and $\varepsilon_{\mathrm{end}}$ were obtained, and the compression curve was constructed, plotting e_{100} and ε_{100} against $\log(\sigma'_v)$.

$$\varepsilon = \frac{\delta_v}{h_0} \tag{D.1}$$

It should be noted that the t_{100}-value estimated from Casagrandes method do not correspond to a situation of fully dissipated excess pore pressure. This may be seen from figure D.2, where the theoretical consolidation curve for load step 4 of the test on OE035S037 (K90B10 specimen) is presented. As may be observed, the value of T_{100} is located before $U = 100$ % is reached. The theoretical consolidation curve was obtained using eq. (D.2) as presented by Hansen (1961).

$$U^{-6} = 1 + \frac{1}{2}T^{-3} \tag{D.2}$$

Where T is the dimensionless time factor $T = t\,c_v/h^2$, and U is the degree of consolidation. The curves presented in figure D.2 were constructed using the c_v-value for load

189
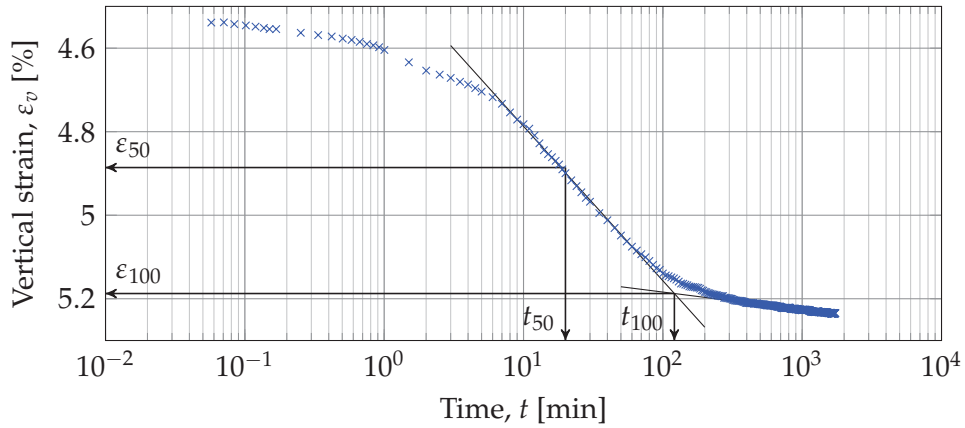
Figure D.1: *Illustration of determination for t_{100}, after Casagrande (1938).*

step 4 on specimen OE035S037. The development of strain with time may be modelled by $\varepsilon(t) = U(t)\varepsilon_{100}$. If a simple creep model is added to the developed strains, an artificial time curve is obtained, resembling the curves extracted during a load step in the oedometer. The following model were used for the data plotted in figure D.2:

$$\varepsilon_{\text{creep}} = C_{\alpha\varepsilon} \log\left(1 + \frac{t}{t_{100}}\right) \tag{D.3}$$

Where $C_{\alpha\varepsilon}$ and t_{100} were assessed from the time-strain curve for the actual test data (load step 4 on OE035S037).
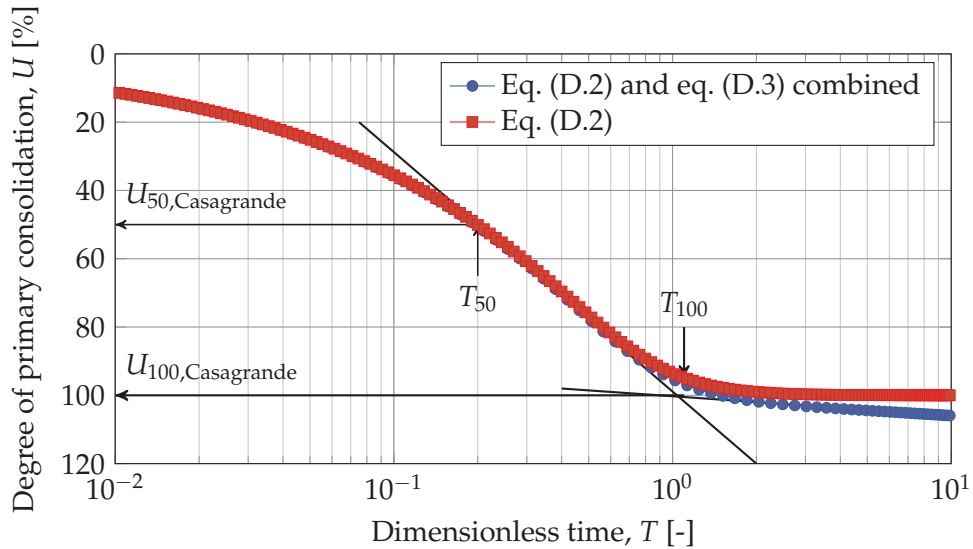
Figure D.2: *Theoretical time-strain curve for load step 4 (Increase in load from 160 kPa to 320 kPa) on OE035S037 obtained by combining eq. (D.2) and eq. (D.3). The Casagrande construction is sketched and the T identified as end of primary consolidation is high-lighted.*

As may be observed from figure D.2 $T_{50} = 0.2$ as expected, while $T_{100} \approx 1.1$. By use of the Casagrandes method $T = 1.1$ indicates that the excess pore pressure is not yet fully dissipated, as a fully consolidated state often is related to $T = 2$. Moreover, as

the volume of the specimen changes under the secondary consolidation process, a small excess pore pressure must be developed and expelled by the creep strains, which is why the excess pore pressure only asymptotically approaches zero.

It should be noted from figure D.2 that the $U_{100,\text{Casagrande}}$ is very close to the value of U_{100}, which is why all parameters based on measurements of displacement and its derivatives (e.g. strain, void ratio and stiffness) are very close to correct. However, basing parameters (e.g. c_v) on T_{100} may introduce an error, which is why these parameters are calculated based on t_{50} in the present project, as described in section C.3.

As figure D.2 indicates the distribution between the applied load carried by excess pore pressure and by the soil skeleton as effective stress, the process of secondary consolidation, e.g. the model presented in eq. (D.3), in reality is running in parallel with the primary consolidation process. As such, the underlying assumption of the Casagrande method (to model the primary consolidation and secondary consolidation as two separate processes with two lines and and find the intersection) is in principle not correct. For highly plastic soils the secondary consolidation process may be significant even prior to the value of t_{100}. For small load steps this may introduce difficulties identifying the value of t_{100} as no distinct bend is observed on the time-strain curves, due to the large values of $C_{\alpha\varepsilon}$ in the highly plastic clays.

D.2 Taylors method

The strains obtained from the corrected displacement logs were plotted on a $\sqrt{t}$ scale, and the method suggested by Taylor (1948) is used for identifying t_{90} and ε_{90}. The method is illustrated in figure D.3. The method employs the parabolic behaviour of the initial part of the time-strain curve by fitting a curve to the initial part, up to approx. $U = 50\%$. The slope of the fitted line was increased by 15% and was used to draw a second line, where t_{90} and ε_{90} were identified as the intersection between the time-strain curve and the second line. ε_0 was obtained as the intersection between the first fitted line and the ordinate, ε_{100} is found from eq. (D.4), and t_{100} as the time value corresponding to ε_{100} from the series of measurements.

$$\varepsilon_{100} = \frac{10(\varepsilon_{90} - \varepsilon_0)}{9} \tag{D.4}$$

As t_{100} and ε_{100} are predicted based on the initial part of the time-strain curve, Taylors method in principle allows for optimal durations of the load steps. Thus, a new load increment could be applied when the value of ε_{100} is obtained on the measurement log. On the other hand, as the slope of the logged $\sqrt{t} - \varepsilon$ curves are very flat at large $\sqrt{t}$-values, the estimation of t_{100} depends heavily on the slope of the initial part of the curve. As the compliance is subtracted from measurement data post-testing, it is difficult to ensure that ε_{100} is obtained in real-time during testing.

Generally, a nice correlation between the values for ε_{100} obtained by Taylors method and by Casagrandes method is found in literature, (BS 1377-5 1990). However, it seems that Taylors method generally indicates higher c_v values compared to Casagrandes method (Sridharan et al. 1987), which suggest that the identified t_{100}-values are slightly smaller.
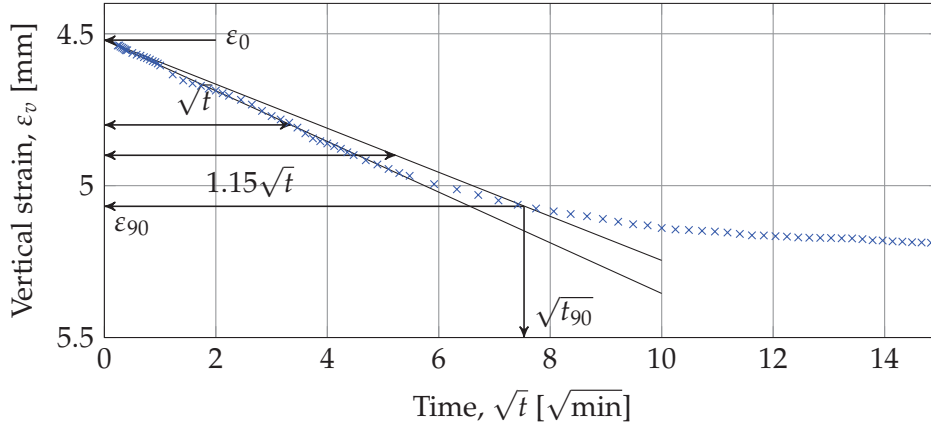
Figure D.3: *Illustration of determination for ε and t_{90} using the method presented by Taylor (1948).*

D.3 Strain rate approach

The 1D consolidation process in oedometer cells may be modelled using the classical consolidation theory as presented by Terzaghi, using the heat equation, illustrated in eq. (D.5).

$$\frac{\partial \Delta u}{\partial t} = c_v \frac{\partial^2 \Delta u}{\partial z^2}, \qquad c_v = \frac{k_{\text{Darcy}} E_{oed}}{\gamma_w} \tag{D.5}$$

The dissipation of the excess pore pressure may be followed by the degree of consolidation $U(t)$:

$$U(t) = \frac{\delta_t}{\delta_{\text{inf}}} = \frac{\varepsilon(t)}{\varepsilon_{100}} \tag{D.6}$$

Hansen (1961) proposed the relation (D.7) to model the degree of consolidation as time progresses, as used in section D.2. The relationship is accurate within 1 % comparing to a Taylor expansion of the solution to eq. (D.5).

$$U^a = b + c\, T^d \tag{D.7}$$

In eq. (D.7) T is the dimensionless time factor $T = t\, c_v / H^2$, a to d is fitting constants. Hansen (1961) proposed $a = -6$, $b = 1$, $c = 0.5$ and $d = -3$. The relationship has been the back-bone of Danish settlement calculations for decades.

Mortensen (2011) applied the relationship to develop an expression of the expected strain rate during dissipation of excess pore pressure during primary and secondary consolidation. Mortensen (2011) combined eq. (D.6) and eq. (D.7) and obtained the following relationship for the strain rate during consolidation.

$$\dot{\varepsilon}(t) = \varepsilon_{100} \frac{\partial U}{\partial T} = \frac{\varepsilon_{100}\, U\, c\, d\, F^d\, t^{d-1}}{a(b + c\, F_t^d\, t^d)} \tag{D.8}$$

where $F_t = c_v / H^2 = 2/t_{100}$ transforms T to t by assuming that full consolidation equals $T = 2$. As seen from eq. (D.8) the theoretical strain rate may be calculated based on ε_{100} and t_{100} for the consolidation process.

Secondary consolidation or creep is often modelled using using a $\log(t)$-model with a fixed coefficient of secondary consolidation, C_α or $C_{\alpha\varepsilon}$ when referring to strains. Thus

strain rate during pure creep will amount to ± 1, dependent on the direction of loading. Thus, the time for 100 % consolidation may be identified as the intersection of the curve defined by eq. (D.8) and the straight line (with slope of ± 1) fitted to the final data points in a $\log(\dot{\varepsilon}(t))$–$\log(t)$ diagram (Mortensen 2011).

D.3.1 Strain rate analysis for oedometer time curves

A small series of tests were carried out in the nmGeo oedometer cell to investigate the applicability of the strain rate approach for assessment of the duration of the primary consolidation. The test programme comprised a K90B10 specimen and a K60B40 specimen, both tested using similar loading programmes. In all tests the excess pore pressure and force below the specimen were logged along with deformation of the upper pressure head and time. Thus, t_{100} may be assessed based on strains, strain rate or dissipation of excess pore pressure. As the tests were executed without applying back pressure, insufficient saturation of filters and drain lines may cause a lag between applied loading at $t \approx 0$ and the peak in the pore pressure response. For the K90B10 specimens, the lag caused a large part of the initial excess pore pressure to dissipate, before the load change was observed in the bottom pore pressure readings. For the K60B40 specimen a smaller part of the excess pore pressure dissipated before the load change was observed in the pore pressure due to the lower permeability of the sample.
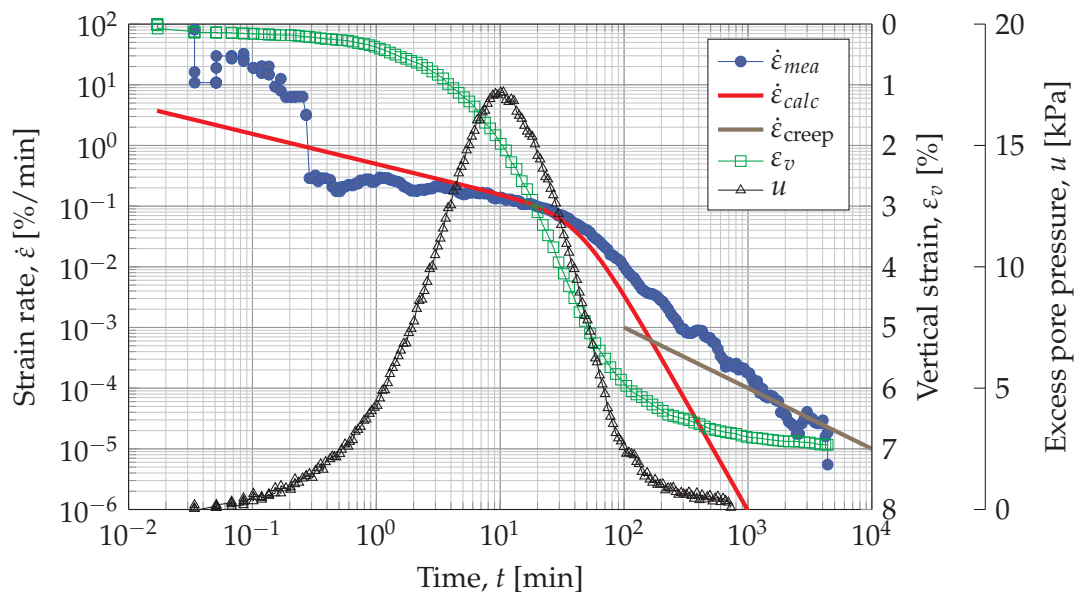
Figure D.4: *Strain rate for load step 5 (loading from 320 kPa to 640 kPa) of OE035S037 tested in the nmGeo cell. Specimen recipe was K90B10. Vertical strain developed during testing and excess pore pressure below specimen are plotted for comparison (right-hand ordinates).*

Results from a selected load step for test OE035S037 on specimen K90B10 are presented in figure D.4. As may be inferred from the figure, the values of t_{100} obtained based on strain (Casagrandes method) and the strain rate method yield similar results. The same correspondence between the strain and strain rate methods for identifying t_{100} may be observed from figure D.5, where data from the K60B40-specimen is presented. However, from both figures it may be observed that the t_{100} identified does not correspond to
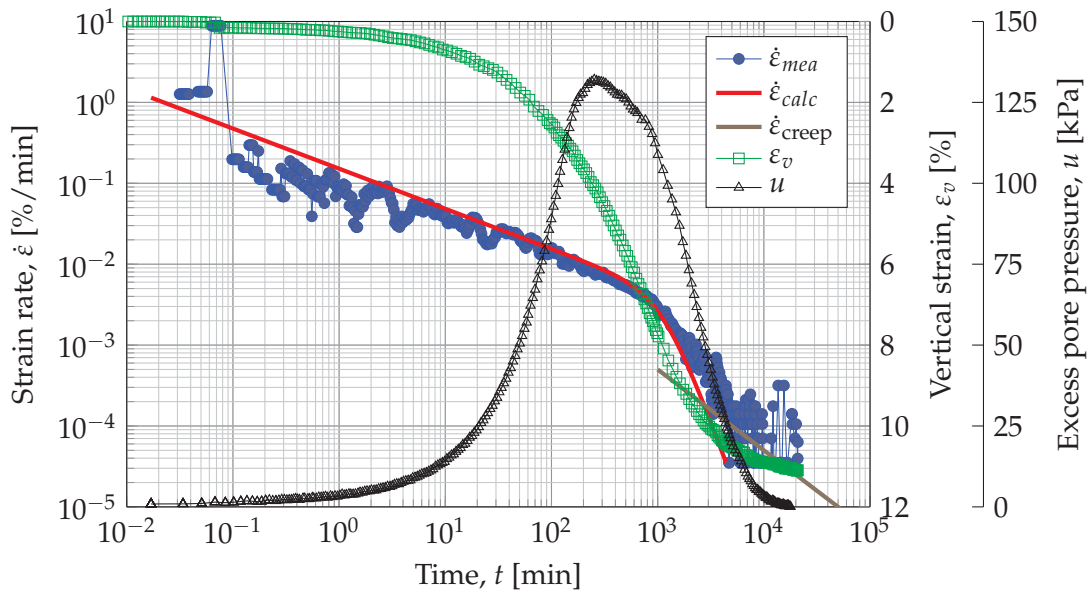
Figure D.5: *Strain rate for load step 4 (loading from 320 kPa to 640 kPa) of OE035S037 tested in the nmGeo cell. Specimen recipe was K60B40. Vertical strain developed during testing and excess pore pressure below specimen are plotted for comparison (right-hand ordinates).*

the excess pore pressure being fully dissipated, $u = 0$ kPa. This is not surprising as the consolidation process in principle is an infinite dissipation of pore pressures which in soils eventually will be over-shadowed by creep. Hence, the strain developed from the t_{100} (determined by Casagrandes method or by the strain rate approach) to the situation $u = 0$ kPa is insignificant for practical purposes when related to stiffness parameters.

D.3.2 Strain rate analysis as a tool for load change

As may be observed from the test series introduced in section D.3.1, an analysis of the strain rate during oedometer testing enables a determination of t_{100} which is agreeable with other known procedures. Thus, it may be speculated that the strain rate approach is applicable to assess whether t_{100} is achieved during a load step in the oedometer test. Contrary to Casagrandes method, t_{100} need not to be passed during a load step, which may reduce testing time. Moreover, the strain rate approach does not rely on extrapolating of data obtained during the first part of the time curve as Taylors method. Thus, the strain rate approach enables t_{100} to be registered at $t \approx t_{100}$, which in principle should allow for a determination of t_{100} more accurately than by Taylors method in a less time-consuming way than by Casagrandes method.

The calculation of the theoretical strain rate during the oedometer testing requires the strain and time for 100 % consolidation, ε_{100} and t_{100} respectively. Thus, the approach requires several iteration to be made for assessing the theoretical strain rate used for evaluating t_{100}. Thus, the procedure for evaluating the time curve for each load step is quite complex compared to e.g. Casagrandes method, where strains plotted against $\log(t)$ directly enables assessment of the consolidation process. As the vertical strain at end of primary consolidation ε_{100} for practical purposes are identical when calculated

from the Casagrande method, the strain rate approach and by analysis of the excess pore pressure, the Casagrandes approach have been used in the present project.

D.4 Full dissipation of excess pore pressure

A simple method of identifying full consolidation is to measure the excess pore pressure in the specimens and allow for full dissipation prior to initiation of a new load step. As this in practise allows only for one-sided drainage during testing, the procedure will cause duration of load steps to be increased by a factor of four, as the drainage path doubles, see eq. (C.1). This will cause the duration of the oedometer tests in the present project to increase significantly. Moreover, as briefly touched upon above, the secondary consolidation process should in principle cause a small excess pore pressure, which will influence the identification of t_{100}.

From the figures D.4 and D.5 it is seen that as the tests were not performed with back-pressure, the pore pressure response was poor in the early parts of the consolidation process. Thus, it is not possible to follow the entire consolidation process nor to see if the load increase in the beginning of a load step is fully registered in the pore pressure transducer. This may introduce significant uncertainty if the full dissipation method was to be used for evaluating duration of the load steps.

D.5 Comparison of methods

The two tests performed in the nmGeo oedometer cell are analysed to assess t_{100} values from the four methods presented above: Casagrandes method, Taylors method, Strain rate approach and full dissipation of excess pore pressure. The two specimens (a K90B10 and a K60B40 specimen) were subjected to the same loading programme, and for each load step, t_{100} was identified from each of the four methods and presented in tables D.1 and D.2 for K90B10 and K60B40 specimens, respectively.

Table D.1: *Comparison of values for t_{100} from four different methods for specimen K90B10, oedometer test OE035S037.*

Initial stress [kPa]	Final stress [kPa]	Casagrande t_{100} [min]	Taylor t_{100} [min]	Strain rate t_{100} [min]	Full dissipation t_{100} [min]
0	40	Swelling	Swelling	Swelling	Swelling
40	80	75	40	95	200
80	160	147	109	182	200
160	320	219	303	950	800
320	640	110	368	380	400
640	320	51	56	40	1800
320	160	91	126	133	2000
160	80	640	318	591	3500
80	40	2648	630	1625	5000
40	10	4219	2466	4550	10 000

Table D.2: *Comparison of values for t_{100} from four different methods for specimen K60B40, oedometer test OE045S036.*

Initial stress [kPa]	Final stress [kPa]	Casagrande t_{100} [min]	Taylor t_{100} [min]	Strain rate t_{100} [min]	Full dissipation t_{100} [min]
0	80	Swelling	Swelling	Swelling	Swelling
80	160	1440	1360	2200	8000
160	320	4090	10501	2500	
320	640	2675	2986	2751	20500
640	320	533	870	793	14000
320	160	2543	1695	2761	20000
160	80	3559	8535	3500	20000
80	40	22187	9226	18000	30000
40	10				

As may be deduced from tables D.1 and D.2, the four investigated methods yield different results for t_{100}. The time for complete dissipation of excess pore pressure naturally is longer than any of the other methods.

It may be somewhat surprising that Casagrandes method and the strain rate approach yields similar results, considering that t_{100} estimated by Casagrandes method corresponds to $T \approx 1.1$, as described in section D.1, whereas the strain rate approach is built on the assumption of full consolidation at $T = 2$, as indicated in section D.3.

D.6 Conclusion

Based on the values of t_{100} tabulated in tables D.1 and D.2 two methods seems to yield roughly similar t_{100}-values, namely the Casagrandes method and the strain rate approach. A low degree of concordance is observed between the Taylor method and the Casagrande method, which is somewhat surprising, as the two methods are expected to yield similar results (BS 1377-5 1990). It should on the other hand be noted that for some time curves the Taylor method yields better estimates than the Casagrande method and vice versa.

For the tests performed in the present project, the times curves identified typically provide a good basis for applying the Casagrande approach, which is why this method was preferred.

Observations from pilot testing

A number of oedometer pilot tests were carried out on artificial clay specimens. The specimens were prepared from mixtures of kaolin and bentonite, following the procedure outlined in appendix B, with $w = 1.25w_L$, according to (Burland 1990), and some were preconsolidated prior to testing in the oedometer cell. Tests with numbers OE006S004, OE007S005 and OE008S006 were carried out by students during the "Experimental Geotechnics" class of Q2 2014. These specimens were selected and prepared by the author, who also provided supervision during testing and analysed and published the results, see (Lodahl and Sørensen 2015), enclosed in appendix G.

In the following, a brief analysis of the conducted pilot tests is presented. The pilot tests served two purposes: Partly the author used the tests to gain experience in conducting the oedometer tests and partly some indications on the duration of the load steps and overall compression behaviour were needed to properly plan the main laboratory programme. As seen from table A.1 the initial saturation of some of the oedometer specimens in the pilot study was rather low. It is believed that the main cause for the low initial saturation was a too stiff consistency of the slurry when installed in the consolidometers, which is why air bobbles may have been present in the preconsolidated samples. This suspicion along with the miniature study presented in appendix B.4 lead to a change in target w for the prepared slurries for the rest of the project as discussed in section 5.3.

E.1   Effects of smectite content on deformation behaviour

A series of compression curves obtained from the pilot tests on specimens prepared from different kaolin-bentonite mixtures are plotted together in figure E.1 for comparison. As seen from the figure, the content of smectite significantly influences the deformation potential of the prepared specimens. Even as different loading programmes were applied for the specimens, a general tendency of increasing deformation potential with increasing content of smectite is observed from the figure. As may also be inferred from figure E.1, the virgin curves grew increasingly upwards concave and the secant parameters $C_{S\varepsilon}$ and $C_{R\varepsilon}$ increased with increasing smectite content.

A test series on slurries built directly in the oedometer ring was conducted to assess the consolidation and stiffness properties of the prepared slurries. From these tests

197
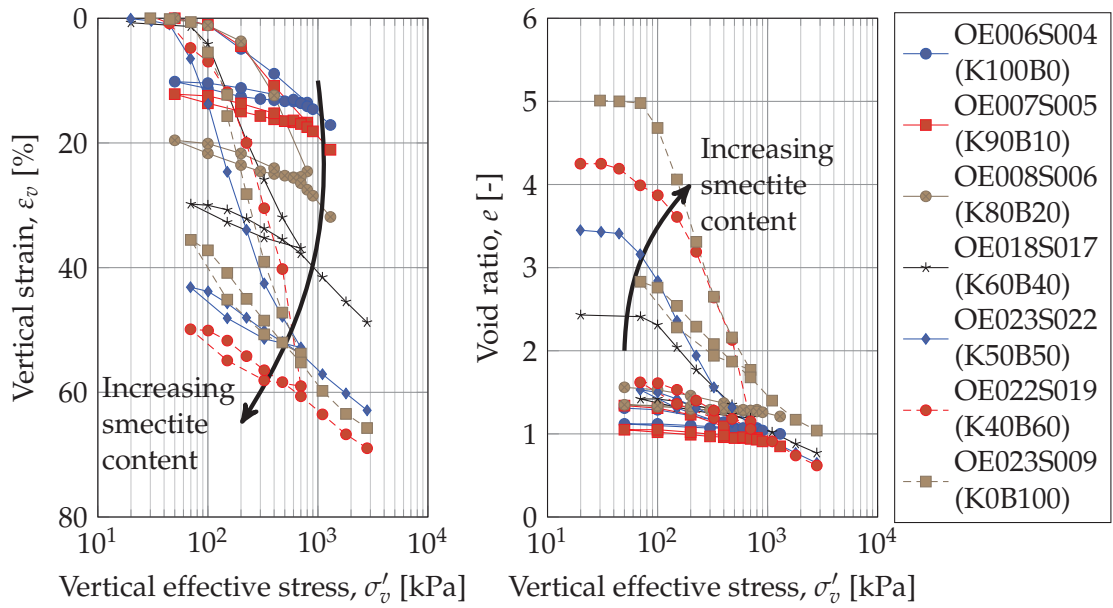
Figure E.1: *Comparison of compression curves for different mixtures of preconsolidated kaolin and bentonite specimens. The compression curves plotted on the vertical strain axis were moved to same origin to allow direct comparison (left figure).*
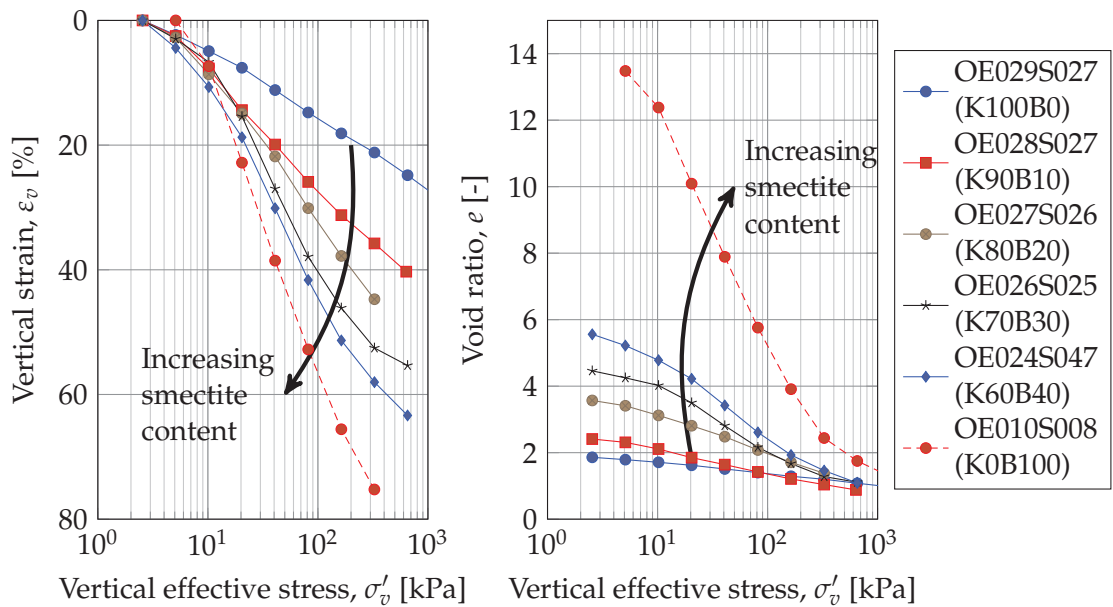

Figure E.2: *Comparison of compression curves for different mixtures of kaolin/bentonite-slurries. The stress-strain curves were moved to same origin to allow comparison (left figure).*

a rough assessment of the necessary initial height of the slurry could be made, to ensure sufficient height of the finished, preconsolidated sample. Moreover, the oedometer tests on the slurries were applied to assess the required duration of the preconsolidation process. The tested slurries are presented in table A.1 and the obtained compression curves are plotted in figure E.2 to allow comparison of deformation behaviour between different mixtures. As may be observed from figure E.1 and E.2, the void ratios of the specimens increased with the content of smectite during testing at low stress levels. As may also be inferred from the figure, the specimens with the highest content of smectite also reflected the largest changes in void ratio during the tests. Thus, the higher content of smectite, the larger ability to absorb water, as a consequence of the diffuse double layers.

As may be inferred from the left hand plot in figure E.2, the stiffness of the tested specimens decrease with increasing smectite content. This may be viewed as a consequence of the large changes in void ratios observed for the specimens of highest plasticity. Mixtures not tested in the pilot testing programme, i.e. the mixtures with bentonite contents between K60B40 and K0B100 are expected to yield compression curves between the curves for K60B40 and K0B100.

As illustrated in figures E.1 and E.2 the content of smectite directly influenced the initial void ratio for the tested specimens. The initial void ratios for the preconsolidated specimens (corresponding to a stress state of 163 kPa) and for the slurry specimens (reconstituted, stress state of approx. 0 kPa) are compared in figure E.3. As observed from the figure, the initial void ratio of the specimens is an essential linear function of the smectite content.
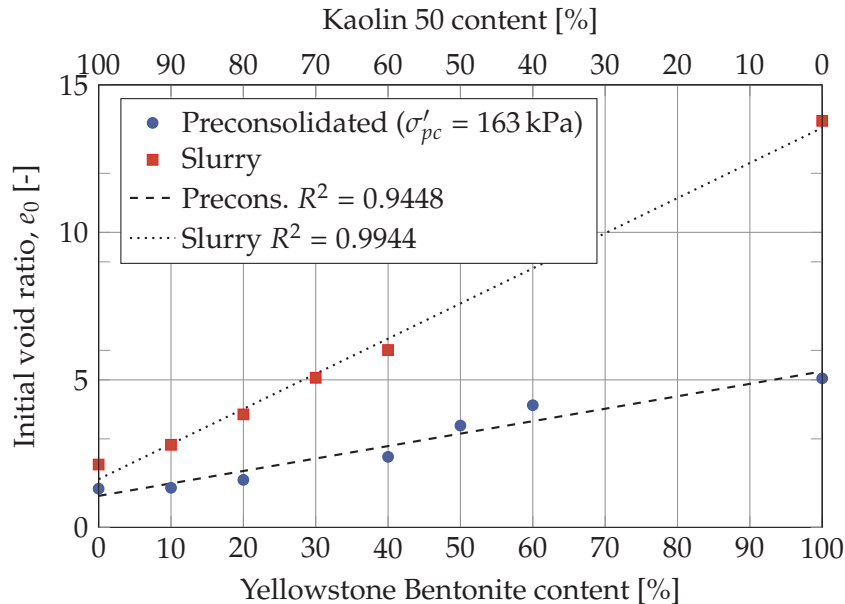
Figure E.3: *Effect of smectite content on the initial void ratio for pilot oedometer tests on slurries and preconsolidated specimens. It should be noted that the initial void ratios presented in the figure represents two different stress states.*

The calculated compression indices for the tests performed on preconsolidated specimens and slurries are presented in figure E.4. As seen from the figure, the compression

indices generally increased with increasing content of smectite, as also discussed above. Small variations were seen around the trend lines, which was most likely caused by the different stress levels used for extracting C_C-values from the individual tests. The compression indices obtained from testing of slurries were generally larger than the values obtained on the preconsolidated specimen of the same recipe. This is also believed to be due to the different stress levels used for extracting the parameters, as the virgin curves are highly non-linear for the high plasticity specimens. In figure E.4 the best linear fits are presented for the populations of slurry and preconsolidated specimens, respectively. As may be observed, the compression index was found to be a linear function of the smectite content with a quite narrow spread, whereas the preconsolidated specimens evidently showed more scatter. However, it should be noted that the two outliers for 50 % and 60 % bentonite were heavily affected by procedure errors during testing and were not included when fitting the trend line for the preconsolidated specimens.
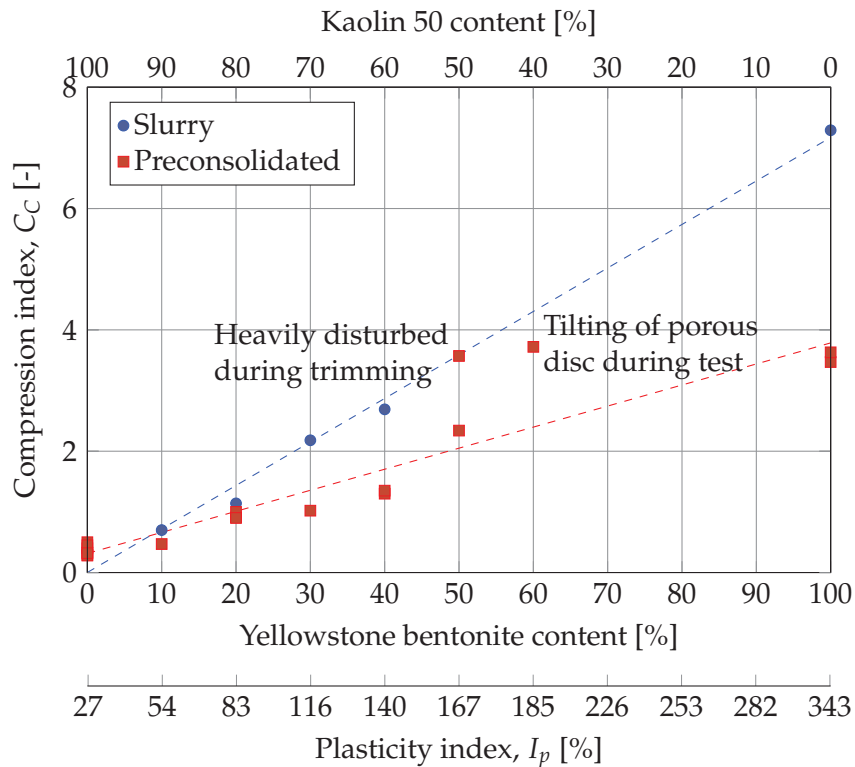
Figure E.4: *Compression indices from tests on artificial specimens as a function of smectite content. The heavily disturbed specimen (K50B50) did reflect consolidation behaviour corresponding to a normally consolidated state and may represent a specimen in a slurry state.*

The preconsolidated specimen K50B50 was dropped on the table during removal from the acrylic tube used for preconsolidation pressure. The drop disturbed the specimen significantly as may also be observed from the rather odd compression curve in the laboratory report. The shearing of the specimen from the drop may have completely erased the internal structure developed during preconsolidation, which may explain that the identified C_C fitted rather nicely with the trend line for slurry specimens in figure E.4. The pilot test carried out on the K40B60 specimen were significantly influenced

by tilting of the upper pressure head. This tilting increased the friction between upper pressure head and oedometer ring, and may have caused an applied stress increase to be carried solely by the ring. At some point – when sufficient additional loading was applied – the upper pressure head may have released, which may have caused a small impact load on the specimen, and induce a larger stress increase than anticipated from the loading programme. Thus, the values of C_C may have been affected my the tilting upper pressure head, as the value was extracted at the steepest part of the compression curve.

E.2 Evaluation of vertical yield stress from pilot tests

The stress-strain curves for the tested artificial specimens presented in figure E.1 were analysed to assess the "stress memory", and determine whether the vertical yield stress and maximal sustained stress showed similar behaviour as found for the natural Palaeogene clay (discussed in section 3.1). In table E.1 the σ'_{vy}-values identified from the pilot tests are compared with the applied stress on the specimens. The specimens were brought to an overconsolidated (OC) state twice during testing: Initially in the oedometer test, for load steps below 163 kPa (i.e. the stress applied on the slurry in the acrylic consolidometer), and in the unloading-reloading loop in the oedometer load programme. As seen from table E.1 the specimens with a smectite content below 20 % yielded $\sigma'_{vy} \approx \sigma'_{max}$, whereas significant differences were observed for smectite content of 40 % and above.

Table E.1: *Comparison of maximal stress sustained by the specimens in IL oedometer tests and the corresponding σ'_{vy} identified along the recompression branch based on the methods proposed by (Casagrande 1936) and (Janbu 1969), designated by "C" and "J" respectively.*

		Initial loading			Reloading		
Specimen	Recipe	σ'_{max} [kPa]	$\sigma'_{vy,C}$ [kPa]	$\sigma'_{vy,J}$ [kPa]	σ'_{max} [kPa]	$\sigma'_{vy,C}$ [kPa]	$\sigma'_{vy,J}$ [kPa]
OE006S004	K100B0	163	127	143	800	853	499[*]
OE007S005	K90B10	163	183	154	800	872	285[*]
OE008S006	K80B20	163	189	143	800[†]	853	478[*]
OE018S017	K60B40	163	70	110	700	270	190
OE023S020	K50B50	163	59	92	700	135	149
OE022S019	K40B60	163	115	114	700	121	149
OE012S008	K100B0	163	131	137	700	130	128

[*] No clear value was identified using this method.
[†] Full consolidation not achieved for this load.

Analysing only part of the compression curves from the oedometer tests, namely recompression from σ'_{min} to σ'_{max} and further normally consolidated compression, the ratio between the vertical yield stress, σ'_{vy} (determined as average values from Casagrandes and Janbus methods) and the previously sustained maximal stress may be plotted against the content of smectite (and hence I_p) as presented in figure E.5. The figure also presents the *OCR*-values calculated from the induced stress paths in the tests. As may

be inferred from figure E.5 the yield stress ratio, the *YSR* was significantly lower than the induced *OCR* when the smectite content reached approx. 20 % to 40 %.
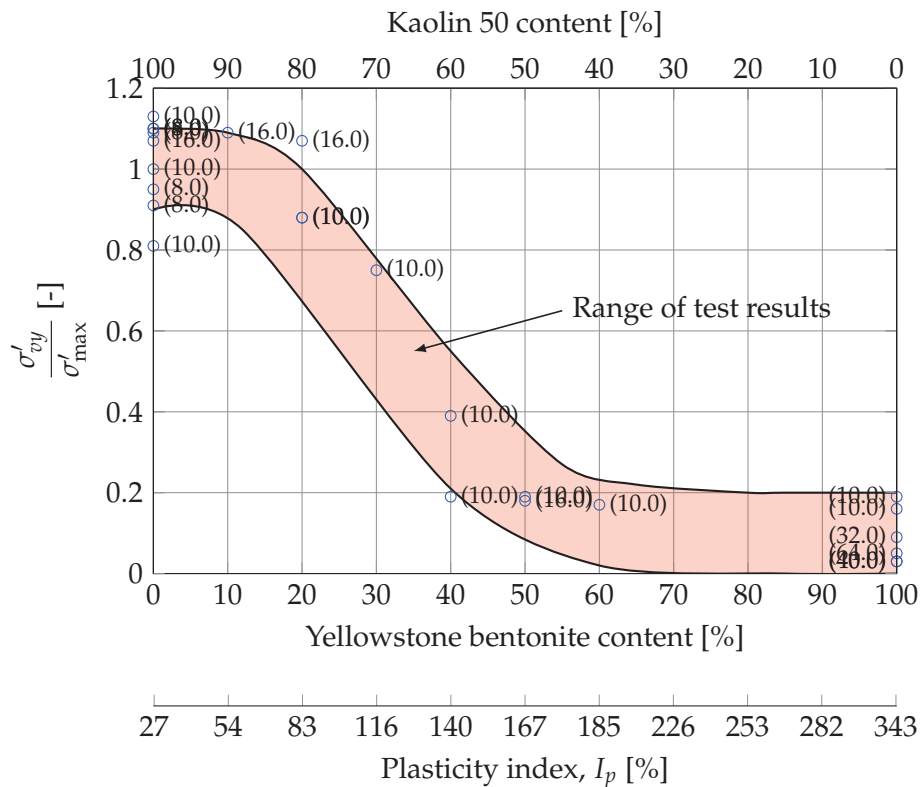

Figure E.5: *Ratio between the derived vertical yield stress and maximal pressure from previous load steps in the pilot oedometer test. Numbers in parenthesis designates OCR for the specific point.*

The data presented on the figure, also suggest that a smectite content of approximately 40 % may be regarded a threshold for stress memory. Below 40 % smectite, the correspondence between the maximal sustained vertical stress and the identified σ'_{vy} was significantly better than above this value. For the K0B100 mixtures, the vertical yield stress was only approx. 5 % to 20 % of the maximal stress sustained prior to unloading. Moreover, it seemed that the larger the *OCR*-value, the smaller the ratio of $\sigma'_{vy}/\sigma'_{max}$. As illustrated in the compression curves for the specimens of pure bentonite (OE010S008, OE011S008 and OE012S008) in the laboratory report, the increase in void ratio during the unloading from σ'_{max} to σ'_{min} was very large, which probably destroyed the internal structure achieved during loading to σ'_{max}. This behaviour was caused by the large content of smectite minerals in the specimens, which absorbed water during unloading and enhanced swelling.

E.3 Observations from natural specimens

As a part of the pilot testing programme, five natural specimens were tested. All five tests were performed using intact Little Belt clay as described in section 4.2.3. Figure E.6 compares the compression curves obtained for each of the five natural specimens.

As may be observed from the figure, an overall trend of highly non-linear compression curves were evident from the five tests. Particular in reloading and virgin loading the curves are upwards convex, whereas the compression curves approached being linear during unloading. This observation is similar to the observation presented by Femern (2014a), as discussed in section 3.6.1. The compression curves are illustrated individually in the respective test reports in the laboratory report.
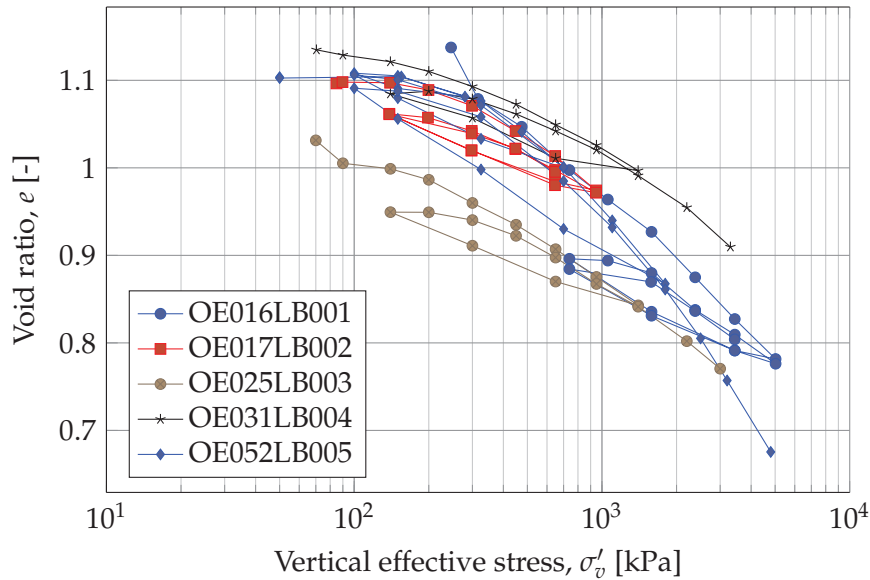

Figure E.6: *Compression curves from the five natural specimens (Little Belt clay) tested within the present PhD-project.*

As may be noted from figure E.6, the initial void ratio of the tested specimens were significantly lower, compared to the artificial specimens of similar plasticity. The closest match for the natural specimens in terms of liquid limits is the artificial mixture K60B40. However, the initial states in the oedometer tests greatly differed. The initial void ratio after preconsolidation for the K60B40 was found in the range e = 2.06–2.29 opposed to the range of the natural Little Belt clay of e = 1.03–1.14. The lower initial void ratios of the natural specimens were most likely caused by intensive loading during past glaciations, as described in section 3.1. Thus, it may be debated whether a state of true virgin compression was reached during the tests presented in figure E.6.

In all tests on natural clays conducted in the present study at least one unloading-reloading loop was performed, and the methods of Casagrande (1936) and Janbu (1969) were applied to assess the vertical yield stress. The specimens were loaded to σ'_{max}, unloaded to σ'_{min} and finally reloaded past σ'_{max}. The vertical yield stress was assessed along the compression curve from σ'_{min} and onwards. The ratio of $\sigma'_{vy}/\sigma'_{max}$ was calculated and is plotted against the plasticity index of the specimens in figure E.7.

As may be inferred from figure E.7 only a limited amount of data on the behaviour of natural, intact Palaeogene clay was obtained from testing with in the present PhD-project. However, it seems that the ratio of $\sigma'_{vy}/\sigma'_{max}$ is dependent on both specimen plasticity and on the induced *OCR*-value. For the test OE052LB005 the ratio was seen to decrease with increasing *OCR*-value in the test. This behaviour is consistent with
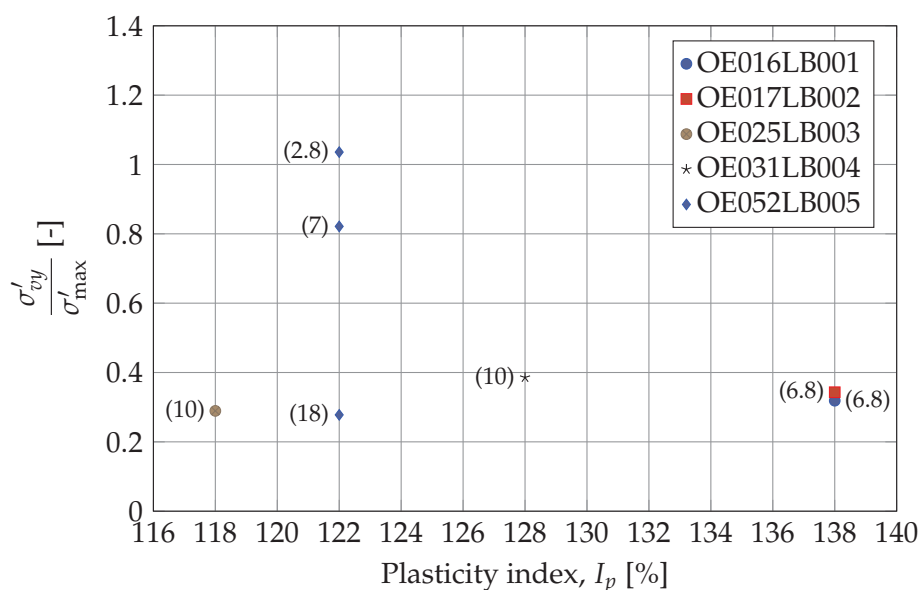
Figure E.7: *Ratio between the derived vertical yield stress and maximal pressure from previous load steps in the pilot oedometer test on natural clays. Numbers in parenthesis designates the induced OCR-value for the specific point.*

an increasing destructuring of the specimen when loaded to larger stress levels prior to unloading. The tests OE016LB001 and OE017LB002 have higher plasticity indices compared to specimens OE052LB005 and the data points for the former two tests are located below the value obtained from test OE052LB005 in figure E.7, despite the similar *OCR*-value.

Comparing figure E.7 with figure E.5 it may be seen that the artificial (pilot tests) and the natural specimens displays similar behaviour when comparing the behaviour at $I_p \approx 140\,\%$. At this level of plasticity, the ratio $\sigma'_{vy}/\sigma'_{max}$ is approximately $20\,\%$ to $40\,\%$ for $OCR = 10$ for the artificial specimens as well as for the natural specimens.

E.3.1 Effects of pore fluid salinity on Atterberg limits of natural clays

Danish geotechnical practice is to use deionised (or tap) water for Atterberg limit testing. As the Danish Palaeogene clays are of marine origin, the in situ pore fluid is saline. As discussed in section 3.5, the pore fluid salinity may be expected to govern the in situ behaviour of the clay. A small sub-study was carried out in the present projects, focusing on the effects of pore fluid salinity on the Atterberg limits of natural Little Belt clay.

A total of five specimens of Little Belt clay were subjected to Atterberg limit testing. For each of the specimens, the liquid limit and the plastic limit were determined using deionised water and the synthetic pore water PC02. Figure E.8 illustrates the effects of diluting the in situ pore fluid on the liquid limits of the five high plasticity specimens. A glacial clay till was also included in the sub-study, to assess the influence of pore fluid composition on the Atterberg limits of low plasticity clays.

As may be noted from figure E.8, the tests performed with deionised water on high plasticity clays yielded significantly higher values compared to the tests performed with the artificial pore fluid, PC02. For the glacial clay till specimens however, no significant

Figure E.8: *Effect of dilution of pore fluid salinity when performing Atterberg limit testing with deionised water. Closed markers denote values obtained with deionised water and open markers denote values obtained using PC02-solution.*

effect of pore fluid was observed. This is noteworthy, as the Danish rules of thumb, which is often based on the Atterberg limits, was derived for specimens of low plasticity, tested using deionised water or tap water, as this is the requirements of the testing standards (DS/CEN ISO/TS 17892-12 2004; BS 1377-2 1990; ASTM D4318 2000). Thus, as no effect of pore fluid salinity was observed in the test for GT001 (representative for clays of low plasticity), the well-known correlations may be assumed to be valid, even if standard procedure is changed to require index tests to be performed with site specific salinity. Expectedly, performing index testing with site specific salinity for high plasticity clays will yield Atterberg limits and results from advanced tests which to a higher degree agrees with the well-known rules of thumb. Thus, it is strongly recommended for industry to shift towards obtaining Atterberg limits based on tests performed with site-specific pore fluid salinity, as this would lead to better correspondence between index parameters and in situ behaviour.

# Simple methods to assess smectite content of specimens

As observed for the main laboratory tests, discussed in chapter 6, the content of smectite in the specimens significantly influences the deformation behaviour. The effects of the smectite minerals include the increasing curvature of unloading-reloading branches and the increasing discrepancy between previously sustained maximal stress and vertical yield stress. Thus, abilities that are highly relevant for foundation engineering work are affected by the smectite content of a clay deposit.

IL oedometer tests on natural, high-plasticity Palaeogene clays are very time consuming and thus quite expensive. Often, e.g. for preliminary studies or small projects, results obtained from oedometer tests will not be available, which is why simple method to assess the smectite content of a clay specimen may prove valuable. In the following a few simple and relatively cheap tests are presented, which were found to correlate well with the smectite content of the artificial specimens, which were tested in the present study.

F.1 Comparison of Atterberg limits

An obvious effect of increasing smectite content is increasing liquid limits and plasticity index. However, as discussed in section 3.4, illite minerals may interact with smectite minerals, which may reduce the liquid limits for illit-smectite mixtures compared to kaolinite-smectite mixtures, with same mass-percentage of smectite. However, as illustrated by Lodahl and Sørensen (2017), the smectite minerals in clays are highly sensitive towards changes in pore fluid salinity. Figure F.1 illustrates the change in plasticity observed for three artificial mixtures, tested with deionised water and the artificial pore fluid PC02. As may be noted from the figure, the reduction of the liquid limit increases with increasing smectite content, which is why the difference between w_L obtained with deionised water and saline water is related to the smectite content.

As observed from figure E.8 a similar effect was observed for the natural specimens tested within the present study. Figure F.2 compares the difference in w_L between tests performed with deionised water and PC02 for the three artificial specimens K100B0, K90B10 and K80B20 and the five natural Little Belt clay specimens. The smectite content
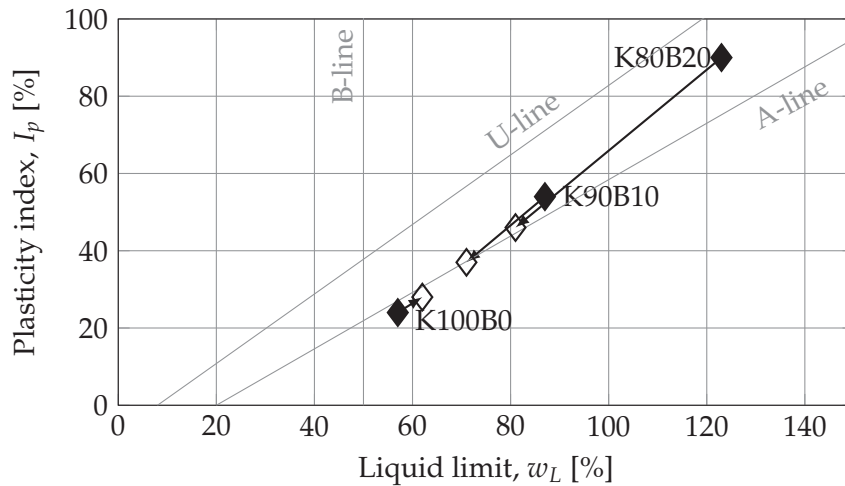
Figure F.1: *Effect of pore fluid salinity on the liquid limit of three artificial specimens. After (Lodahl and Sørensen 2017).*

is known for only two of the natural specimens, as presented in figure 4.4. Moreover, it should be noted that the Little Belt clay specimens were of marine origin, which is why the points in figure F.2 do not represent a fully leached state. Thus, had the specimens been fully leached, a larger change of w_L would have been observed.
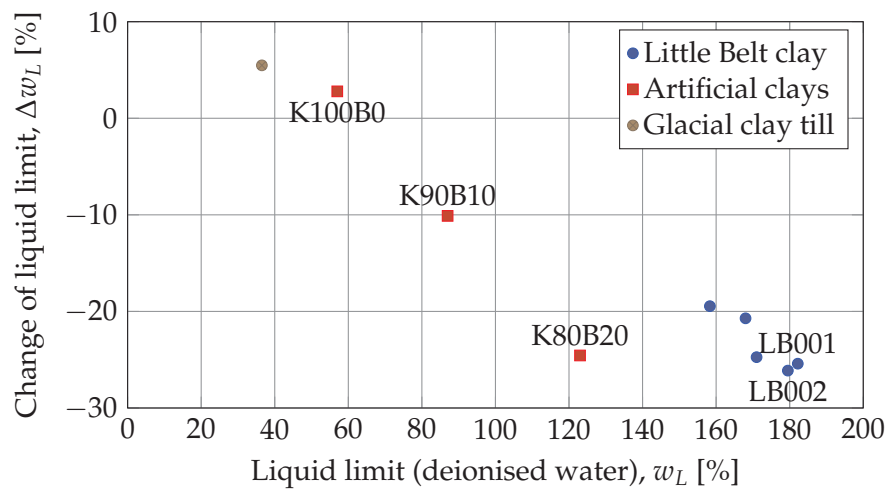

Figure F.2: *Effect of pore fluid salinity on the liquid limit of three artificial specimens. After (Lodahl and Sørensen 2017).*

Based on the observations presented in chapter 6 the smectite minerals starts to dominate clay behaviour when reaching a threshold value of approx. 20 % to 40 %. This value corresponds to a reduction of 20 % of the liquid limit, based on the results presented in figure F.2. As may be noted from the test data on K100B0 and the glacial clay till, uncertainties during testing may introduce variations of a few percent points, which does not reflect a changed behaviour of the clay material.

F.2 Sedimentation volume

A sub-study was carried out on the four mixtures of the main laboratory programme. The study comprised sedimentation of 5 g of oven-dried clay material in water with four different salinities in graduated cylinders. At the beginning of the test, each of the graduated cylinders were stirred with a glass rod to ensure that the clay material was in suspension in the water. Then the clay particles were allowed to settle over 24 hours. After 24 hours the volume of the sedimented clay was read of the graduated cylinder. Figure F.3 presents the volumes of each of the four mixtures tested in the main laboratory programmes after 24 hours sedimentation.
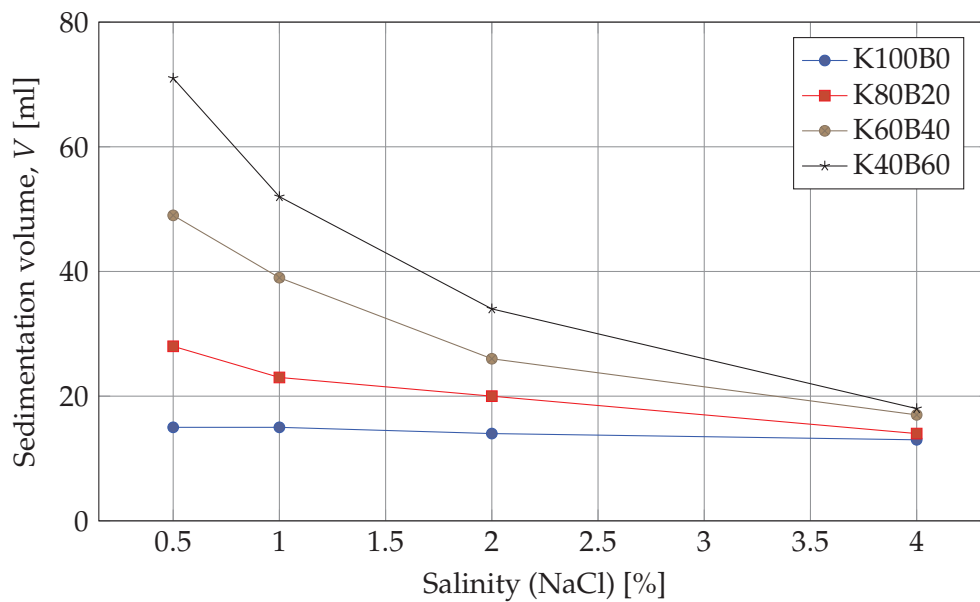
Figure F.3: *Comparison of volumes of four mixtures after 24 hours sedimentation in various pore fluid salinities.*

As illustrated in figure F.3, the sensitivity of the sedimentation volume towards salinity increases with increasing content of smectite minerals in the tested clay. Based on the tests in the main laboratory programme a threshold value was identified, which corresponds to a change of $\approx 20\%$ in the sedimentation volume when comparing results from the 0.5% and 1% tests. It is worth noticing that the sedimentation test is less sensitive towards the inherent salinity of natural samples, as only 5 g of clay is used for the test. Thus, the influence of the salt in the clay is of limited influence on the salinity in the sedimentation fluid (a total of 100 ml was used to obtain the presented results).

A simple test to assess the overall traits of a clay can consist of tests performed with 0.5% and 1% NaCl-solutions. These two tests will last for approx. two days, as the clay is to be sieved and dried, and the sedimentation test must run for 24 hours.

F.3 Fracture pattern after oedometer test

At the end of the main laboratory testing programme, it was noted that the fracture pattern of the oedometer specimens after testing and drying for water content analysis,

differed between the tested recipes. Figure F.4 illustrates the fracture pattern for the three mixtures containing smectite minerals.

(a) K80B20   *(b)* K60B40   *(c)* K40B60
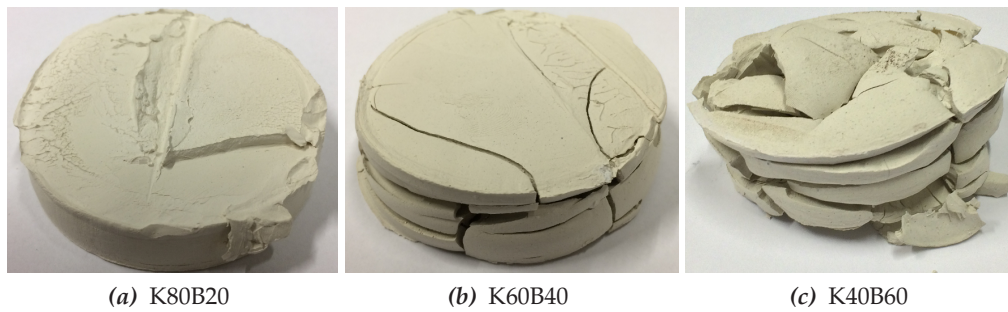
Figure F.4: *Fracture patterns obtained after testing of three mixtures of kaolin and bentonite. All specimens was swelled to 10 kPa prior to drying.*

As indicated in figure F.4 the intensity of the cracks in the dried samples depend on the smectite content of the clay specimen. As the content of smectite minerals increase, so does the intensity of the cracks in the dried samples. This is directly linked to the ability of the smectite to adsorb water, which causes the specimens to shrink significantly when drying.

Based on these observations, a rough estimation of the deformation potential of a clay specimen may be linked to the intensity of the cracks developing when drying.

F.4   Summation of chapter

Three methods of achieving a rough assessment of the deformation potential of clays were proposed above. All three methods is usable for assessing the magnitude of the influence of smectite content on the deformation behaviour of artificial clays tested within the present study. However, the presented methods should be validated for natural specimens, which requires tests, which were not performed within the present study, due to time constraints. In practice it may be found that information on the liquid limit, w_L, is sufficient to estimate the overall deformation behaviour.

For detailed analysis of the diffuse double layer, further analysis may enable an investigation of the clay mineral properties such as the CEC and the SSA of the clay minerals. Knowledge on these parameters enables a prediction to be made base on the diffuse double layer theory, which will yield an expression for the virgin compression line.

Part II

Papers

Influence of Smectite Content on the One-Dimensional Deformation Behavior of Reconstituted High Plasticity Clays

The following paper was presented at the "6th International Symposium on Deformation Characteristics of Geomechanics", held in Argentina in November 2015. The paper focused on the effects of smectite content on the deformation behaviour of clays, and compares behaviour of natural Danish clays with a series of tests performed on artificial clay specimens.

Three IL oedometer tests from the pilot testing phase have been referenced in the paper. The paper presented that the index parameters along with the C_C, C_S and C_R-values were affected by the content of smectite. Moreover tendencies of increasing curvature of the recompression branches with increasing smectite was noted, which was envisioned to affect the vertical yield stress identified via Casagrandes or Janbus methods. The paper also presents that the c_v-values depends on the smectite content in both normally consolidated and overconsolidated state.

The final publication is available at IOS Press through the doi-link presented in the paper details below. A draft version is enclosed in the present appendix.

Oedometer tests with measurement of internal friction between oedometer ring and clay specimen

The following paper was presented at the "Nordic Geotechnical Meeting" in Reykjavik, Iceland held between 25th and 27th May, 2016. The paper focuses on the effects of the interface friction between specimen and oedometer ring developing during testing.

The paper presents results from oedometer tests carried out using a special cell, where a force transducers is fitted between the bottom pressure head and the bottom plate, allowing measurements of the stress at the bottom pressure head. Thus, based on the applied loading at the top pressure head, the stress loss due to friction may be calculated. It is shown that during reloading, an overestimation of up to approx. 30 % is found for the tangent stiffness for the initial load steps in reloading.

The main focus of comments after the presentation at the conference was the choice to use a fixed-ring setup for the tests. Even as the fixed ring is a necessity for measuring the friction between ring and specimen, it was commented that this choice introduced additional friction to the system, which is correct. For oedometer tests the use of floating ring will minimise the developed friction. However, for CRS-testing and oedometer tests with K_0-measurements, the ring is fixed. Thus, the topic of the paper is highly relevant.

The paper may be downloaded from the url presented in the paper details below. The paper is enclosed in the present appendix.

M. R. Lodahl et al. 2016. "Oedometer tests with measurements of internal friction between oedometer ring and clay specimen." In *NGM 2016 Reykjavik - Proceedings of the 17th Nordic Geotechnical Meeting - Challenges in Nordic Geotechnics 25th - 28th of May*, 289–298. ISBN: 978-9935-24-002-6. `http://www.ngm2016.com/papers.html`

Effects of pore water chemistry on the unloading-reloading behaviour of reconstituted clays

The following paper was submitted to the "European Journal of Environmental and Civil Engineering". The paper deals with the effects of pore fluid salinity on the Atterberg limits and deformation potential of high plasticity clays. The data was obtained after Sigurðardóttir and Dobrescu (2016).

The paper presents results from IL oedometer tests on three mixtures of artificial clays, tested with a total of 11 different pore fluids. The pore fluids comprised different solutions of NaCl and $CaCl_2$ and the artificial pore fluid PC02 (Laier 2010).

The results presented in the paper show profound influence of pore fluid salinity on specimens containing smectite minerals. For smectite-rich clays, the deformation potential in virgin loading was shown to be reduced by up to 50 % when the pore fluid salinity was increased from 0 % to 6 %.

The paper also illustrates a very high degree of correlation between C_C and w_L, between C_S and w_L, between C_C and C_S and between c_v and w_L. Moreover the size of the unloading-reloading loops, along with their area, increased with increasing smectite content and decreased with increasing salinity.

The submitted version of the paper may be found on the following pages. The paper details is presented below:

M. R. Lodahl and K. K. Sørensen. 2017. "Effects of pore water chemistry on the unloading-reloading behaviour of reconstituted clays." *European Journal of Environmental and Civil Engineering.* Submitted. ISSN: 2116-7214